coatings

Ion-Substituted Calcium Phosphates Coatings

Edited by
Gabriela Graziani and Enrico Sassoni
Printed Edition of the Special Issue Published in *Coatings*

MDPI

Ion-Substituted Calcium Phosphates Coatings

Ion-Substituted Calcium Phosphates Coatings

Editors

Gabriela Graziani
Enrico Sassoni

Editors
Gabriela Graziani
IRCSS Istituto Ortopedico Rizzoli,
Rizzoli Orthopaedic Institute
Italy

Enrico Sassoni
University of Bologna
Italy

For citation purposes, cite each article independently as indicated on the article page online and as indicated below:

LastName, A.A.; LastName, B.B.; LastName, C.C. Article Title. *Journal Name* **Year**, *Article Number*, Page Range.

Contents

About the Editors

Gabriela Graziani (PhD). Gabriela Graziani is a Researcher at Rizzoli Orthopedic Institute. She conducts research regarding materials science applied to orthopedics, with a special focus on nanostructured materials, 3D printing and 3D bioprinting, and on the development of calcium phosphate-based consolidants for stone and archeological remains. She obtained her master's degree and PhD at University of Bologna, where she also served as a postdoctoral researcher. She was Visiting Student Research Collaborator at Princeton University. Currently, she is PI of the project "A New Strategy to Address Tumor Relapses by Nanostructured Implantable Devices", financed by the Italian Ministry of Health.

Enrico Sassoni (PhD). Enrico Sassoni is tenure track Assistant Professor at the University of Bologna (Italy). Since 2017, he has held the Italian national qualification as Associate Professor in "Materials Science and Technology". In 2015, he was awarded a 3-year Marie Skłodowska-Curie individual fellowship ("HAP4MARBLE" project), thanks to which he worked for 18 months at Princeton University (USA) and 6 months at the University of Göttingen (Germany). He has authored and co-authored +80 scientific publications, including 50 journal articles (+1100 citations in Scopus and h-index = 21). He is member of the Editorial Board of RILEM Technical Letters and Coatings. He is Convener of Cluster E of RILEM ("Masonry, Timber and Cultural Heritage") since 2018. In 2017, he received the "Gustavo Colonnetti Medal 2017", awarded by RILEM to researchers less than 35 years old who have provided "an outstanding scientific contribution to the field of construction materials and structures".

Preface to "Ion-Substituted Calcium Phosphates Coatings"

Calcium phosphates (CaPs) in the form of bulk materials and coatings have found application in numerous fields spanning from biomaterials to cultural heritage conservation and water treatment. In fact, this class possesses particular and versatile characteristics that make them appealing for different applications. Among CaPs, hydroxyapatite is that most widely investigated as it is similar to the mineral phase of bone, which has boosted its application in biomaterials in past decades. Lately, however, attention has also been drawn to other classes of CaPs having different solubility and degradation profiles, thus achieving a wide spectrum of materials to be selected based on the specific need. Brushite, alfa- and beta-tricalcium phosphate, and octacalcium phosphate coatings are generating increasing interest and are being explored by a constantly growing number of papers. In addition, hydroxyapatite and CaPs can easily accommodate foreign ions, either incorporated into the lattice or adsorbed on the surface, all altering hydroxyapatite crystallinity, solubility, and overall properties. This can be exploited to guarantee additional properties (i.e., antibacterial, antiosteoporotic, antitumor efficacy) but can also affect nucleation when undesired, like in the case of substrate contamination. For these reasons, several research efforts have been devoted to the development of ion-substituted calcium phosphate coatings through wet and plasma-assisted techniques as well as on the study of hydroxyapatite nucleation in the presence of substrate contaminants. This Special Issue is a collection of contributions regarding the main advances in the field of ion-doped CaPs and their applications. The synthesis and deposition of ion-substituted calcium phosphate coatings are explored together with nucleation of calcium phosphate coatings in the presence of substrate contamination. The relevance of specific ion substitutions (e.g., magnesium, strontium, silver, zinc) on the properties and/or the behavior of substituted hydroxyapatites is reviewed with a special focus on their exploitation for the development of antibacterial CaPs. To achieve these aims, different techniques are used to improve the control over ion-doping of calcium phosphates, and advanced characterization techniques are proposed to investigate their properties.

Gabriela Graziani, Enrico Sassoni
Editors

A Review on Ionic Substitutions in Hydroxyapatite Thin Films: Towards Complete Biomimetism

Gabriela Graziani, Marco Boi and Michele Bianchi *

IRCSS Istituto Ortopedico Rizzoli, NanoBiotechnology Laboratory (NaBi), Bologna 40136, Italy;
gabriela.graziani2@unibo.it (G.G.); marco.boi@ior.it (M.B.)
* Correspondence: michele.bianchi@ior.it; Tel.: +39-051-6366042

Abstract: Plasma sprayed coatings composed of stoichiometric hydroxyapatite have been extensively used to improve integration of metallic implants in the host bone, as hydroxyapatite (HA) is normally regarded as similar to the mineralized phase of bone. However, these coatings exhibited several drawbacks that limited their success. On the one hand biological apatite is a carbonated-HA, containing significant amounts of foreign ions, having low crystallinity and a small crystals size. This means that it differs from stoichiometric HA in terms of composition, stoichiometry, crystallinity degree, crystal size/morphology and, as a direct consequence, solubility, and ions release in the peri-implant environment. On the other hand, thick plasma sprayed coatings can undergo cracking and delamination and are scarcely uniform. For these reasons, research is pushing into two directions: (i) Increasing the similarity of apatite coatings to real bone, and (ii) exploring deposition by alternative plasma assisted techniques, allowing to achieve thin films, and having superior adhesion and a better control over the coating composition. In this article, we review the latest advances in the field of plasma-assisted deposition of ion-substituted hydroxyapatite thin films, highlighting the state of the art, the limitations, potentialities, open challenges, and the future scenarios for their application.

Keywords: calcium phosphates; ion-substituted apatites; bone regeneration; plasma-assisted deposition; solubility; crystallinity; composition

1. Introduction

Orthopedic implants are still burdened by high failure/revision rates, posing relevant economical and societal challenges [1–13].

To avoid failure, implants must integrate in the host site, which requires the capability to trigger host bone cells response without eliciting any immune reaction [14,15]. However, implants also need to burden physiological loads, which can be high and multiaxial, and must not be fragile, hence why metallic implants are normally used, that are bio-inert. A common route to overcome bio-inert behavior of metallic implants and boost integration is to coat their surface with layers having osseointegrative capabilities, so as to render the implant bio-active [16,17]. These coatings are traditionally manufactured by plasma spraying, and have quite significant thickness (comprised between ~30 and 200 μm) [17].

According to the "biomimetic principle", the biological behavior of a device for bone replacement can be boosted by using a biomaterial as similar as possible to real bone in terms of its composition, crystallinity, lattice dimensions, and Ca/P ratio [18]. This, in the field of bone regeneration, has pushed towards an extensive use of hydroxyapatite ($Ca_{10}(PO_4)_6(OH)_2$, HA), as a bone substitute, in view of its similarity to the inorganic phase of mineralized tissues of vertebrates [16,17,19].

However, clinical results obtained by these traditional coatings are not as promising as expected, and generally not superior to those obtained by bare titanium. This can be ascribed to two main reasons:

(i)   Despite the assumed similarity between biological apatite and stoichiometric apatite having been referred to for decades, they exhibit significant differences, from several points of view. Firstly, in terms of composition, bone apatite is a multi-substituted carbonated HA [18,20,21]. Each substitution can influence the characteristics of the lattice, thus having an impact on its stability, crystallinity degree, crystal size and morphology, all influencing its solubility and, ultimately, ion release in the biological medium [18,20,21]. In addition, several of these ions can have a significant biological role, directly influencing host cells response and/or exerting a therapeutic role, generally in a dose-dependent manner, hence their presence and amount in the peri-implant environment is significant [18,21].

(ii) Due to relatively high thickness, plasma sprayed coatings have a high tendency to cracking and delamination [16,22,23]. In addition, coating manufactured by PS exhibit scarce uniformity in terms of thickness, phase composition and microstructure [16,22,23]. These two aspects have been hampering the performance of these materials.

For this reason, in the last years, research has been pushing into two directions, to overcome these issues:

(i)   Ion-substituted apatites are being investigated, instead of stoichiometric hydroxyapatite.

(ii) Novel plasma-assisted techniques have been emerging, allowing to deposit thin films, with superior adhesion to the substrate and lack of tendency to crack.

In addition, an even more recent route is to deposit coatings directly from bone apatite precursors, which is made possible by plasma-assisted techniques.

Here, we review the literature regarding deposition of ion-substituted apatites by novel thin film plasma-assisted techniques, with special attention to deposition from biological precursors, to highlight the potential, issues and challenges connected to this approach. The focus is on coatings aiming at promoting osseointegration, by a composition as similar as possible to the real bone, hence the Review will be centered on substitution by ions present in the bone. However, because ion-substituted apatites coatings are getting increasing attention for several applications and especially for infections, literature regarding silver-doped hydroxyapatite will be briefly discussed in Section 6, which discusses future perspectives on this topic.

2. Plasma-Assisted Methods for Calcium Phosphate (CaP) Deposition

Plasma-assisted techniques offer some advantaged compared to wet methods and to traditional plasma spraying. Compared to wet synthesis, they allow for much faster coating of the surface thanks to generally high deposition rate, which is an important advantage from an industrial point of view [21]. In addition, they are industrially scalable, which is also boosting their application. Compared to plasma spraying, they allow for an easier transfer of the target composition, a better uniformity in terms of morphology and composition, a lower porosity and a lower tendency to cracking and delamination [16,22].

Among plasma-assisted techniques, the most used in the biomedical field, for manufacturing thin films for bone implants are radio-frequency magnetron sputtering (RF-MS) and pulsed laser deposition (PLD). Matrix-assisted pulsed laser evaporation (MAPLE) and pulsed electron deposition (PED) are emerging techniques, allowing a fine control over film stoichiometry and composition and are gaining increasing interest, hence they will be included in the review.

In magnetron sputtering (MS), deposition takes place starting from the ionization in vacuum of a target material by means of negatively charged magnets [17]. Although two different modes are available, direct current (DC) and radio-frequency (RF); CaP coatings (and, more in general, non-conductive materials), can be deposited only by the latter [17]. MS allows an easy deposition of multi component coatings, by deposition from multi-component ceramic targets or simultaneous deposition from different targets [24]. Coatings can be very thin (average thickness being ~40 nm–3.5 μm) and can effectively cover surface irregularities, while maintaining a uniform thickness.

In addition, they are dense and pore-free [16]. As for all plasma assisted techniques, substrate temperature and deposition time are critical in determining the characteristics of the produced films, but in the case of MS those also have a key role on composition [16]. Films can be deposited at room temperature, which allows coating of heat-sensitive substrates; however, scarce adhesion has been reported for deposition at room temperature, in absence of substrate preparation and/or post deposition treatments. As for all plasma assisted techniques, as-deposited films are amorphous, but both deposition at high temperatures or post deposition annealing are effective strategies to obtain the desired crystallinity degree. Post deposition annealing also allows to tailor surface morphology and roughness to a certain extent. Deposited coatings are generally highly adhesive (bonding strength to the substrate >30 MPa) and exhibit suitable bioactivity. One of the main limitations of this technique is that the coatings composition might differ from that of the deposition target material, also depending on sputtering system and parameters. This, for calcium phosphates, can be very relevant, as significantly different properties can be obtained for slight variations in composition, Ca/P ratio and amount of ionic substitutions. In particular, the Ca/P ratio of the films might vary in a very wide range (1.6 up to 2.6 or even higher) and is normally higher than that of the HA target, due to preferential sputtering of calcium and/or to evaporation of P_2O_5 [16,24].

In PLD, the target to be deposited is ablated by a focused, high power, pulsed laser beam. As a consequence, a plasma plume forms that is accelerated towards the substrate where deposition occurs. Coatings obtained by PLD can be very thin and much below 1 μm. The characteristics of the deposited films are strongly dependent on deposition parameters that determine their morphology, composition and crystallinity. As for MS, as-deposited films are amorphous, but higher crystallinity can be achieved depending on deposition temperature and possible post-deposition heating treatments. However, because deposition can occur at room temperature, coating of heat sensitive substrates is allowed. Substrate temperature and post treatment annealing also have an impact on the final characteristics of the coatings and in particular on the composition and stoichiometry of the coatings. Despite this, PLD allows for a fine transfer of the target composition. This precise control over stoichiometry makes it possible to deposit multicomponent coatings from one same target [16,17,25,26]. Finally, PLD coatings generally exhibit high adhesion to the substrate, good biocompatibility and bioactivity.

When delicate organic or biological matter or thermally unstable phases needs to be deposited, a modification of PLD can be used, namely Matrix-assisted pulsed laser evaporation (MAPLE). MAPLE prevents the laser source from damaging the target, that is a frozen mixture of the "active" biomaterial (up to 5 wt.%) in volatile solvent, gradually removed by a vacuum system as the deposition proceeds [17,27,28]. The solid target is kept frozen during laser irradiation, so as to prevent evaporation; this is achieved by a cooling system inside the chamber and instant-freezing of the targets by immersion in liquid nitrogen. The solvent is chosen to absorb the laser wavelength, that is also tailored to prevent damage of the target, thus avoiding interactions between the laser and the material, allowing the release of the undamaged delicate active matter, that is deposited on the substrate.

More recently, pulsed electron deposition has been proposed as an alternative to PLD also for applications in the biomedical field [29–31]. In PED the target material if ablated by a high energy pulsed electron beam instead of a laser source; a plasma plume is formed at each pulse and the target material is ionized and deposited onto the substrate [32]. Due to the lower cost of the ablation source, PED is more competitive from an economical point of view, compared to PLD. As in the case of PLD, films deposited by PED are composed by globular aggregates and exhibit high roughness, which makes it suitable for promoting host cells behavior [33]. Films obtained are amorphous, but post deposition annealing can be performed to obtain the desired crystallinity degree [34,35]. Films obtained are highly adhesive, adhesion also being influenced by post deposition annealing [36]. Mechanical properties achieved are comparable to those obtained by plasma spraying [36]. Finally, good biocompatibility and bioactivity have been reported [33].

3. The Role of Ionic Substitutions in Hydroxyapatite

The main ionic substitutions present in bone are reported in Table 1. The most diffused substitution is CO_3^{2-} for OH^- (A-type substitution) or for PO_4^{3-} (B-type substitution), followed by and Cl^- and F^- for OH^- [19]. In addition, magnesium, strontium, zinc, and manganese substitutions for calcium, and silicates for phosphates are also present in bone [20,21,37,38]. The amount of these substitutions can significantly vary between different tissues (i.e., bone, dentine, enamel), animal species, types of bone, anatomic sites, etc. [21]. In addition, significant differences can be assessed depending on the patient age, sex, and pathologies.

Ionic substitutions are relevant, as each of them have an influence on HA crystal lattice and hence on its solubility. In addition, some of them have significant biological impact and can have therapeutic effects [19,21]. Those have been largely investigated to obtain substitute HAs for bone regeneration and are their role is reviewed below.

Carbonates cause a decrease in *a*-axis and decrease in *c*-axis of HA, this renders the structure is less crystalline and, as a consequence, more soluble and more bioactive [19,21,39]. Magnesium, the main substitution for calcium in HA, causes a decrease in the *c*-axis of the lattice, acts as an inhibitor of HA nucleation and crystallization and destabilizes its structure. Because Mg-HA is less crystalline than stoichiometric HA, it also has higher solubility [19,21,40]. In addition, Mg is an essential element for living organisms, as it is a key factor in the activity of several enzymes [40]. In bone, Mg influences metabolic activity and growth, by acting on osteoblasts and osteoclasts. As a consequence, scarce concentrations of magnesium can cause osteopenia or fragility [40]. Fluorine substitution for OH^- causes a decrease in the *a*-axis and in the c-axis, the latter being lower by an order of magnitude compared to the first. As a consequence, the lattice gains a strong symmetry, that results in an increased stability and a lower solubility [21]. The effect on bone cells, instead, is controversial, as F^- itself can boost cells attachment, but the lower solubility causes a reduced availability of Ca^{2+} ions decreasing cells proliferation. Lastly, fluorine is expected to be an effective anti-osteoporotic agent [21,41]. Strontium can be incorporated in bone by both ion exchange and ionic substitution [19]. The effect of substitution of Sr for Ca is dose-dependent: High concentrations of Sr increase crystals dimensions and crystallinity, while low concentrations cause an opposite effect (decrease in crystallinity and crystalline length), and a distortion of the lattice, both leading to a significant increase in solubility [19]. Interestingly, solubility can be further increased by Sr substitution in carbonated hydroxyapatite (CHA), instead of HA. From a biological point of view, Sr increases the mechanical strength of bone [21] and has an anti-osteoporotic effect [19–21]. In fact, strontium ranelate, a strontium-based drug used against osteoporosis, can boost osteoblast activity while inhibiting osteoclasts [20,21,24,37,38,42,43]. Sr capability to improve bone regeneration has also been demonstrated by tests in vivo [17,20,37,38,42]. As for the effect on crystallinity and solubility, also in vitro and in vivo behavior of Sr is dose-dependent. Silicon is normally incorporated in biogenic HA because of SiO_4^{4-} substitution for phosphate groups [19]. This substitution increases HA solubility, also because formation of amorphous phosphate phases is promoted, the apatite microstructure becomes finer and, finally, silicates form defects at grain boundaries [19]. Even at concentrations of about 1 wt.%, silicon can exert significant biological impact and it is reported to enhance in vivo bioactivity and bone regeneration [44]. Zinc is a trace element in bone [19,21], that can substitute for calcium, thus acting as a crystallinity inhibitor. Despite its low concentration, it has a key biological role, as it can act as a co-factor for several enzymes, can impact on nucleic acid metabolism and promote bone formation and regeneration by favoring osteoclasts activity and decreasing that of osteoblasts [19,21]. Manganese is also a trace element, acting as a crystallinity inhibitor [19]. Depending on the concentration, it can alter HA morphology to a different extent, which has an impact on the apatite bioactivity [19]. Mn has a role in bone remodeling and the influence of Mn-doped carbonated hydroxyapatite on osteoblasts activity has been demonstrated [19,29,45].

4. Deposition of Ion-Substituted Apatites by Plasma-Assisted Techniques

A scheme of literature about plasma assisted deposition of ion-doped apatites in reported in Table 1.

Table 1. Available literature on ion-substituted coatings realized by thin film deposition techniques. F: Only data relative to coating fabrication and characterization available; V: Data from biological in vitro test available; VV: Data from biological in vivo test available.

Deposition Technique	Carbonate			Mg			F			Sr		
	F	V	VV	F	V	VV	F	V	VV	F	V	VV
MS		[46]		[47]			[48]			[1,38]	[43]	
PLD	[39, 49]	[50]	[51]		[40]	[52]				[42]	[19]	
MAPLE					[27]						[27, 53]	
PED										[36]		

Deposition Technique	Si			Zn			Mn			Biogenic Sources		
	F	V	VV	F	V	VV	F	V	VV	F	V	VV
MS	[54, 55]	[56, 57]	[56]	[47]								
PLD	[53]	[58]					[49]	[45]	[50]	[26, 29]	[27, 28, 33]	[35]
MAPLE												
PED										[34]	[33]	

4.1. Deposition by Magnetron Sputtering

Deposition of carbonated hydroxyapatite (CHA), magnesium-doped hydroxyapatite (Mg-HA), fluorine-doped apatite (FA), strontium-doped apatite (Sr-HA), silicon doped-apatite (Si-HA), and zinc-doped apatite (Zn-HA) has been reported by magnetron sputtering [39,46].

Regarding carbonated hydroxyapatite, high adhesion (measured by pull-out test) has been obtained for different substrates, further increased when co-sputtering of titanium is performed [46]. Quite fine control over stoichiometry of the films has been achieved (Ca/P 1.80) [46].

Sputtered CHAs are biocompatible, as no toxicity is registered towards host cells. Further, suitable adhesion, viability and proliferation of osteoblasts have been reported. In vitro tests showed mineralization after 21 days immersion in simulated body fluid (SBF), and human bone marrow derived MSCs differentiation in human osteoblasts-like cells (hOBs).

Mg-HA coatings have been deposited by targets with variable magnesium content. In vitro tests indicated high adhesion (by pull-out test) and viability of osteoblasts, though not superior to that obtained on pure HA. The authors ascribed this behavior to amorphous nature of both coating, leading to too high a dissolution, making it impossible to discriminate between the effects of the two.

Fluorine-substituted apatite, deposited on Ti and Ti/Si by right-angle MS, indicated a general decrease in HA grain size, independently from the substrate. Crystallinity of the coatings depends on deposition time, as short sputtering times (i.e., 5 min) led to disordered nanocrystalline phases, while longer times allowed for an increase in crystallinity [47]. However, either pre-heating or post treatment annealing (at temperatures up to 300 °C) allowed for significant increases in crystallinity of coatings deposited at room temperature. In particular, by pre-heating, suitable crystallinity can be obtained for temperatures lower than those required for post-deposition annealing [47].

Sr-HA has been deposited both by Sr-HA targets with variable Sr/(Sr + Ca) ratio and by co-deposition from different targets. Deposition on titanium alloys and silicon has been reported [1,24,38,43]. Interestingly, the content of Sr was found to influence sputtering rate.

Scarcely crystalline coatings were obtained, where successful incorporation of Sr in the apatite lattice was achieved [43]. Upon annealing, crystallinity of the films increases and morphology and adhesion experience modifications, as do the (Sr + Ca)/P ratio and the presence of by products (CaO and $Sr(OH)_2$). Coatings obtained are calcium deficient, as a Ca/P ratio of 1.18 was reported.

A (Ca + Sr)/P ratio of 1.26 was found, that also is modified by annealing, that increases Sr content with respect to calcium. The (Ca + Sr)/P ratio is lower than that of the target, due to a preferential sputtering of Ca compared to Sr, deriving from different atomic weight. Deposition from multiple targets results in a generally higher ratio [1,38,43]. Remarkable adhesive strength to titanium has been reported—higher than that of stoichiometric HA [24].

As expected, Sr does effectively increase osteoblasts activity and decrease that of osteoclasts, which is clearly indicated by the fact that proliferation and differentiation is higher compared to pure HA [43].

Sputtered silicon-doped apatite (Si-HA) was deposited by both silicate-substituted HA targets and by co-sputtering of Si and HA targets, as seen for Sr. Different substitutions levels were obtained (i.e., $Ca_{10}(PO_4)_{6-x}(SiO_4)_x(OH)_{2-x}$, $x = 0, 0.25, 0.33, 0.5$) [48]. Silicates can be incorporated in significant amounts, as they can prevent incorporation of carbonates [3].

Even though all deposited coatings are amorphous, crystallinity degree depends on the amount of Si (crystallinity decreases for increasing Si content) [49]. Post deposition annealing does not influence the Si content in apatite, so that the desired crystallinity can be obtained without significantly modifying the coating composition. Deposition at high temperature (with progressive increase of temperature from room temperature up to 200 °C) has also been reported, causing the formation of a nanocrystalline coating, with some amorphous areas [48]. In our opinion, these latter results are significantly dependent on the annealing conditions chosen, and higher crystallinity could be achieved for higher deposition temperature, as reported elsewhere for other substituted apatites.

Despite the expected lattice distortion caused by incorporation of silicates in the lattice [49], no significant differences are detected between HA and Si-HA by X-rays diffraction. In addition to the relatively low amount of Si, this is ascribed by the authors to the proximity of silicon and phosphorous in the periodic table. Presence of secondary Si and CaO phases has been reported [50]. Despite a uniformity in the elemental composition within one coating [3,51], both stoichiometric and calcium deficient coatings have been produced [50,51], indicating that, on one hand, silicon does not tend to accumulate in specific areas, as seen, for example, in the case of magnesium. However, in our opinion, this also evidences a non-perfect and fully reproducible transfer of the target stoichiometry.

Silicates addition also have a dose-dependent impact on the mechanical properties (by nanoindentation) of the coating, as a general decrease in hardness and elastic modulus is registered and failure due to scarce adhesion (measured by scratch test) is reported for high Si concentrations [49]. In vitro, increased dissolution rate is found compared to HA [51], possibly to be ascribed to the decrease in OH- content due to increasing silicates substitution [52], that results in a decrease in HA grain size [49].

Dissolution in SBF was found to be significantly dependent on post deposition annealing [50], which is expected, as solubility strongly depends on crystallinity degree. Nevertheless, suitable mineralization and good activity towards bone cells were found for both annealed and non-annealed coatings [50]. Although the mechanism of interaction of Si with bone cells is yet to be fully understood, Si-Ha coatings were found to boost attachment, proliferation and differentiation of osteoblasts with respect to HA and uncoated implants and to favor the formation of an extracellular matrix [3,51,53]. In vivo tests on mice are reported, indicating that Si-HA coatings are osteoinductive, while stoichiometric HA coatings are not. Both coatings, however, are biocompatible [51].

Zn substituted HA has also been deposited by RAMS, but literature is very scarce in this regard, and no deposition is reported by any other plasma-assisted technique, to the authors' best knowledge. In vitro tests on Zn-HA, however, show promising data, as an increased adhesion and viability of osteoblasts was observed, compared to stoichiometric HA [54].

4.2. Pulsed Laser Deposition

Deposition of carbonated hydroxyapatite (CHA), magnesium-doped hydroxyapatite (Mg-HA) and octacalcium phosphate (Mg-OCP), strontium-doped apatite (Sr-HA) and carbonated

hydroxyapatite (Sr-CHA), silicon doped-apatite (Si-HA), manganese-doped carbonated hydroxyapatite (Mn-CHA), and octacalcium phosphate (Mn-OCP) has been reported by PLD [39,46].

Deposition of carbonated hydroxyapatite allowed to obtain nearly stoichiometric films, Ca/P ratio increasing with deposition temperature (30 up to 700 °C) [43]. As for MS, also crystallinity degree and mechanical properties (Vickers microhardness) increase upon annealing [39]. Instead, no significant alterations in morphology are detected for annealing at temperatures below 500 °C, while they become pronounced at 700 °C and above.

Magnesium-doped hydroxyapatite (Mg-HA) at different magnesium content has also been deposited by PLD. Increasing Mg content was found to cause a parallel decrease in crystallinity and crystal size [40,55]. Effective incorporation of Mg in the lattice was verified. Significantly, Mg distribution is non-homogeneous and tends to form Mg-rich areas, where osteoblasts concentrate, attach and grow [40].

In vivo tests on rabbit models have been reported for both Mg-HA and magnesium doped octacalcium phosphate (Mg-OCP), having the same magnesium content (Mg: 0.6 wt.%) [56]. At sacrifice, 6 months after implantation, good bone growth and integration was found for both coated implants and for the uncoated titanium reference. No inflammatory reactions or failure were reported for any of the implants. Bone volume, bone-implant contact length and contact length ratio to implant surface has been found to be higher for Mg-HA and Mg-OCP implants compared to uncoated implants (μCT). Performances of Mg-HA were found to be higher than those of Mg-OCP, in our opinion also due to differences in solubility of the two compounds.

Strontium substituted hydroxyapatite (Sr-HA) [17] and strontium substituted carbonate apatite (Sr-CHA) [42] have been tested. Thin films of Sr-HA were obtained (200 nm up to 1 μm), that were annealed after deposition [17,42]. The presence of Sr in the coatings, which was verified by EDS, did not significantly impact on coatings morphology, as found elsewhere for plasma sprayed coatings [17].

In vitro, osteoblasts adhesion, proliferation, viability and differentiation were found to be boosted, the increase in adhesion (tensile adhesion by ASTM C633-01(2008) [57], ASTM F1147-05:2011 [58], ISO 20502:2005 [59]) since the early steps being proportional to Sr content [17]. Conversely, osteoclasts proliferation was found to be reduced, again depending on Sr content (3%–7%). Interestingly, spreading of osteoblasts is increased compared to stoichiometric HA coatings.

Deposition of Si substituted hydroxyapatite (Si-HA) has been reported, composition of the targets being successfully and finely transferred to the coatings [60]. In a study by Rau et al., it was found that the Si content must be kept below 2 wt.% to avoid a reduction in the decomposition temperature. This ultimately caused the formation of unwanted unstable phases, such as TCP and/or phosphate silicates [61]. Below 2 wt.%, instead, Si does not significantly alter HA lattice, as denoted by XRD spectra, almost identical to those of HA.

Addition of silica can cause an increase in the Ca/P ratio compared to the target, due to the formation of CaO [60,61]. This formation is relevant, as CaO is cytotoxic, hence compatibility of the coatings must be verified. Ca/P ratio is also dependent on the deposition temperature and/or on post-deposition annealing, as seen for MS [61]. Several temperatures have been tested in the literature for deposition of Si-HA (400, 500, 600, and 750 °C), all leading to deposition of dense and un-cracked films [61]. Films obtained at these temperatures are crystalline and nanostructured, crystallinity degree being obviously depending on annealing temperature. Interestingly, also thickness and Vickers microhardness are affected by deposition temperature [61]. However, despite mechanical properties generally increasing for increasing deposition temperature, when the temperature is brought above 750 °C, formation of byproducts (calcium-titanium mixed phases) hampers adhesion. Also, at these temperatures, Ca/P ratios completely different from those of the target ($\approx$3.5) are obtained, indicating HA decomposition alongside formation of byproducts. As a consequence, deposition temperatures around 500 °C are generally recommended.

In vitro mineralization is reported after 1 day of immersion in alfa-MEM, thickness of the HA-layer increasing for increasing soaking times (up to 28 days) [61].

Mn-substituted CaP coatings have been manufactured exclusively by PLD, to the authors' best knowledge. Deposition of both Mn-CHA and Mn-OCP coatings have been described in [62]. While Mn-CHA is more similar to real bone but has higher crystallinity and consequently slower dissolution rate, Mn-OCP is more soluble and is expected to experience faster dissolution—thus possibly being more effective in boosting bone growth at early stages. When tested in vitro, human osteoclasts and fibroblasts exhibited suitable adhesion, proliferation and viability onto both coatings, without any significant difference being assessed. This is ascribed by the authors to a compensation between the beneficial effects CO_3^{2-} of Mn-CHA, and the lower crystallinity of Mn-OCP.

These coatings were also validated in vivo in rabbit models, in comparison to HA coatings. Tensile strength by pullout test was tested at 8 weeks after implantation [63], indicating that Mn-OCP and, to an even higher extent, Mn-CHA, can better improve implant-bone integration with respect to HA, suggesting a higher osseointegration potential.

4.3. Deposition by Matrix Assisted Pulsed Laser Evaporation

Deposition of Sr-HA and Sr-OCP has been reported by Combinatorial Matrix-Assisted Pulsed Laser Evaporation (C-MAPLE).

The possibility to deposit metastable Sr-OCP and composites of hydroxyapatite and drugs (here alendronate and zoledronate), evidences the strength of this technique, that allows deposition of heat-sensitive material [27,64]. Sr-doping on OCP was found to improves cells proliferation, activity and differentiation and, hence, the overall behavior of the coating. Strontium zoledronate and HA composites, instead, were found to promote osteoblasts adhesion and boosts proliferation, compared to uncoated references.

4.4. Deposition by Pulsed Electron Deposition

Deposition of Sr-HA has been very recently reported by PED (in the novel Ionized Jet Deposition version) for variable Sr content (up to 9 wt.%) [36]. Deposition has been carried out at room temperature on a polymeric substrate (PEEK) leading to an increased in wettability and roughness compared to the bare substrate, and suitable mechanical properties. A good transfer of composition (including Sr content) has been assessed from the target to the deposited coatings [36].

5. Multi-Substituted Coatings and Deposition from Biogenic Sources

Multi substituted HAs have also been explored in the literature, to increase similarity to bone apatite and to exploit the capability of each ion to influence HA lattice, crystallinity and solubility, and the coatings mechanical properties and interactions with cells [24].

In this view, pulsed laser deposition of silicon and strontium co-substituted carbonated hydroxyapatite (SiSrCHA) has been reported [65]. SiSrCHA has been obtained by diatomaceous earth, naturally containing several further foreign ions (Fe, K, Mg, Na, and P), all possibly boosting biological performances [65]. In the study, silica has been kept constant (2.5 at.%), while Sr concentration has been varied in a wide range (0 up to 10 at.%). Deposition has been carried out at high temperature to tune crystallinity and adhesion. Mesenchymal cells adhesion, morphology and osteogenic differentiation and activity have been tested. Results showed that, for multi-substituted coatings, variations in the amount of one of the dopants might affect the content of the others. In fact, aside from an obvious decrease in Ca content, due to a progressive incorporation of Sr, increasing Sr also leads to alterations in carbonates content. This can be seen by a reduction in the intensity of carbonates bands in FT-IR and in the CO_3^{2-} to PO_4^{3-} ratio, compared to pure CHA. We ascribe that to the modifications caused by each substitution to the HA lattice, influencing its capability to host further foreign ions.

Instead, doping with Si and Sr does not influence cells morphology compared to pure CHA reference coatings, as good cells coverage is found at 28 days for all the examined group. Instead, increased cells proliferation and differentiation were found for the multi-doped coating, compared

to references. We speculate that examining growth at lower times could be very useful to assess biological behavior.

A further, crucial step in the direction of obtaining coatings having increasing similarity to bone apatite is deposition directly from biogenic targets. Deposition of apatite coatings from targets from a biogenic source have been reported by PLD [66–69] and PED [33,34]. Deposition of doped bone apatite targets has also been reported [67,68].

In particular, by PLD apatite has been deposited starting from simple, LiO_2- and CIG-doped ovine and bovine bone, MgF_2, and Mg doped bovine bone, simple and titanium doped ovine dentine and human dentine. Further experiments about deposition of "natural apatite" by PLD have also been reported, tested in vitro and in vivo, but without suitable description of the apatite source and the deposition procedures [70,71].

Ovine and bovine bone-derived coatings were obtained by PLD, after calcination of the powders at 850°C for 4 h in air to remove organic components [66]. Characterizations performed on the targets, obtained by compression of the calcinated apatite powders, indicate the presence of brushite and phosphorous fluoride hydroxide traces, alongside HA. HA (calcium deficient) was also found to be the main phase in the coatings. Traces of Na, Mg, Cl, F and Si were detected in the coatings and the targets, suggesting that ion substitutions were preserved. No in vitro and/or in vivo biological tests are reported for these coatings.

HA powders from sheep dentine were also calcinated (6 h at 850° in air) to remove organic components and allow an easy separation between dentine and enamel [67]. After grinding and sieving to obtain particles of a suitable size, part of the powders was admixed with Ti powders. Both Ti-doped and un-doped powders were homogenized and pressed to obtain targets, later heated at 1000 °C for 4 h in air, and deposited by PLD.

Morphology and composition of the coatings were investigated, indicating that HA is the main phase in the coatings, alongside Ti minor phase and, possibly, $MgCO_3$ and $CaMg_2$, possibly resulting from calcination. Traces of Na, Mg, C and Ti (in the doped samples) were detected in the coatings by EDS [67].

Both coatings, respectively 1.8 microns (undoped) and 1.2 microns (doped) thick are composed of granular aggregates, providing a high surface roughness, suitable for cells adhesion. Addition of Ti also has an impact on the coatings morphology, as it causes a reduction in average grain size compared to undoped Ti and a denser particulate. Pull-out test (ASTM D4541-17 [72] and ISO 4624:2016 [73]) indicates a good bonding strength, increased in the case of Ti-doping (55.5 ± 5.5 MPa vs. 63.7 ± 5.2 MPa), due to Ti-Ca segregation at the interface between the coating and the substrate, creating a mingled interlayer. Biocompatibility was assessed by evaluating human mesenchymal stem cells (hMSC) morphology and proliferation, and toxicity assay, showing evidence of good biological behavior for both coatings, with and without titanium addition [67]. Bovine apatite from femoral bones was also used, alone and enriched with MgF_2 and MgO. As for ovine dentine, prior to deposition, bovine bone powders were calcinated (4 h at 850° in air), mixed, pressed in a mold and sintered (4 h at 1000 °C) to obtain the deposition targets. Post deposition annealing was performed to enhance crystallinity of the coatings [68].

Morphology, composition and adhesion (ASTM D4541-17 [72] and ISO 4624:2016 [73]) of the coatings were evaluated, then the influence of the targets and the coatings on HEp-2 cells viability was tested and gene expression and antimicrobial activity of the films were evaluated [68].

A close transfer of composition from the target to the coatings was discovered, with the absence of MgF_2 peaks and weak MgO peaks, that the authors attributed to Mg^{2+} and F^- substitution in the HA lattice. Peaks characteristic of CHA were shown by FT-IR. MgO and MgF_2 enhanced the adhesion to the substrate and to provide anti-biofilm properties to the coatings. All films exhibited good biocompatibility, as none of them exhibited relevant cytotoxicity [68].

Human dentine, bovine-derived HA and ovine-derived HA were also deposited after calcination of the powders (4 h at 850°), pressing and sintering at 1100 °C for 4 h [69]. Deposition was performed

at high temperature (500 °C) and post-treatment annealing at the same temperature (6 h, water vapor) was also carried out. Composition and crystallinity of the deposited coatings were investigated, showing a good transfer of substrate composition, including that of trace elements. Thickness of about 1.1–3.5 microns was obtained, depending on the precursor used. Pull-out tests (ASTM D4541-17 [72] and ISO 4624:2016 [73]) indicated a good adhesion to the substrate [68].

Bovine bone-deriving apatite has also been deposited by PED, including a more recent development of the technique called Ionized Jet Deposition (IJD) [33,34].

Bone apatite-like films were deposited directly from deproteinized bone targets, without any grinding or calcination. Deposition was performed at room temperature and half of the samples were heat treated after deposition, to improve crystallinity (1 h at 400 °C in air) [33,34].

Obtained films were compared to films obtained by sintered stoichiometric-hydroxyapatite targets with the same deposition procedure and parameters, both as deposited and annealed [33,34].

As-deposited and annealed coatings were characterized in terms of composition and crystallinity, microstructure and morphology, and mechanical properties (nanoindentation and micro-scratch, UNI EN ISO 20502:2005 [59]). Obtained coatings are nanostructured and exhibit sub-micrometric thickness. Results showed a close transfer of the targets' composition, including trace elements (Na and Mg and carbonate substitution). As-deposited coatings exhibited low crystallinity, that was significantly increased by post-deposition annealing, up to resembling that of biogenic apatite target. As a result of annealing, mechanical properties increased up to values comparable to those of commercial plasma-sprayed HA-coatings [34].

Biological tests are also reported, evaluating human dental pulp stem cells (hDPSCs) cells attachment, proliferation and the expression of typical osteogenic markers Runx-2, osteopontin, Osx, and Osteocalcin [33].

In vitro biological tests indicated that annealed bone apatite coatings promote hDPSCs proliferation to a higher extent compared to non-annealed bone coating and HA-references. Immunofluorescence and western blot analyses revealed that the typical osteogenic markers were expressed, suggesting that bone apatite-like coatings treated at 400 °C alone can efficiently promote the osteogenic commitment of the cells, even in absence of an osteogenic medium [33].

6. Conclusions and Future Perspectives

Plasma-sprayed (PS) coatings have extensively studied and used in clinical practice but, due some intrinsic limitations, their real effectiveness compared to uncoated implants is still controversial. Instead, good results have been so far obtained for novel plasma-assisted techniques, capable of depositing thin films. In fact, they were found to allow a more controlled transfer of stoichiometry of the deposited coatings and of ionic additions to plasma spraying. However, presence of secondary phases often reported for magnetron sputtering together with preferential sputtering of some ions (i.e., Ca instead of Sr), cause modifications in the Ca/P and substitution rate, and indicates an imperfect transfer of the target composition. Because relatively low changes in the composition of CaPs, especially when substituted can result in significantly different properties, we believe that it is a relevant limitation in the technique, which needs to be addressed. PLD, MAPLE and PED, instead, allow for a more precise transfer of the target composition to the coatings.

Crystallinity degree can also be finely tuned, by deposition at selected temperature or pre/post deposition annealing. Good adhesion and mechanical properties in general, were confirmed by all the examined studies, as well as good behavior in vitro in terms of adhesion, spreading, differentiation, morphology, and osteogenic activity of the cells, although not always higher than those of stoichiometric hydroxyapatite. Some promising results have also been described in vivo, but extremely scarce literature on the topic and differences in trial conditions (animal model, trial time, characteristics of the bone, gap dimensions, etc.) make them scarcely conclusive.

Overall, thin films of ion-substituted apatites are promising materials, having good mechanical properties and biological behavior. Ion-substitution permits the availability of selected ions in selected

concentrations in the peri-implant environment, with both a therapeutic effect and/or the capability to boost host cells response in view of the biomimetic principle. Deposition by plasma-assisted techniques allows to obtain thin films, having high adhesion and a fine control over crystallinity and composition, guaranteeing a tailored release.

Deposition from biogenic coatings has been emerging as a very promising alternative, as it allows to obtain multi-substituted coatings with ion-amounts and stoichiometry very close to those of real bone apatite, which is almost impossible to be achieved by artificial apatites. This new development has been made possible by PLD and PED, that allow a great control over the composition of the obtained targets. We believe that, once in vivo trials will be available for these coatings, this topic will obtain even wider interest and will expand its field of application.

Interestingly, however, despite ion-substituted coatings being generally proposed with the aim to better resemble real bone, mimicking of the real composition of bone is very limited, as generally only one or two ions are substituted simultaneously in doped HAs. In addition, there is a lack of correspondence between the concentrations of ions in biological HA and their biological relevance, and the number of studies devoted to their investigation. This can be partially ascribed to the wide variability in the concentration of trace ions in the bone, depending on the anatomical site, age, sex and to patient-specific characteristics such as, for example, diseases or metabolism. However, some ions, such as magnesium (highly present in bone and having significant biological relevance), is far less studied than Sr, whose concentration is significantly lower. Some other ions, such as Cl, Na and K are not even intentionally substituted. The number of studies, instead, seems more driven by the possible therapeutic role of the ions. This is clarified by intentional addition of specific therapeutic ions in biological apatite, which goes in the opposite direction of biomimetism. We believe that this, however, can be a promising route, further expanding the range of use of ion-substituted coatings.

Another important trend that is emerging regarding ion-substituted hydroxyapatite thin films, is that of antibacterial coatings. To this regard, a wide range, and increasing amount, of literature is available about silver-doped hydroxyapatite, for which deposition by magnetron sputtering [74–78], PLD [79–84] and MAPLE [85] has been reported. Being the study of plasma assisted deposition of Ag-doped hydroxyapatite of more recent introduction, the majority of the studies focus on the influence of deposition parameters on the films characteristics and on the evaluation of antibacterial efficacy, while extensive, comparative in vivo studies are yet to be performed. We believe that plasma-assisted deposition of apatites doped with a variety of ions having antibacterial (such as copper [86] and gallium), antitumor or other therapeutic actions (such as selenium [87] and cerium) will be increasingly pursued in the near future.

Overall, what we believe to be extremely significant is the possibility to pursue both aims, i.e., biomimetism and therapeutic functions, thanks to plasma assisted techniques.

We believe that extensive work still needs to be carried out to fully evaluate properties, potentialities and limitations of ion-doped apatite coatings. The main points that should be explored, in our opinion, are the following:

- A better understanding of the real benefits of ion-doped coatings, compared to un-doped HA. This is still controversial, mainly because effective incorporation of ions in the HA lattice is not always verified and, because direct comparison between doped and un-doped coatings with the same characteristics and deposited in the same conditions is generally non-available. This is important, as several parameters play a key role, together with the composition of the coatings.
- The effects of different ions should be compared, again considering the same deposition and post deposition conditions and/or the same coating properties.
- The number of experiments performed in vivo must significantly increase, as for some coatings, no in vivo literature is available at all.
- Different opinions are found about some parameters that complicate the evaluation of the coatings performance. Among the others, partial verses complete dissolution of the coatings should be addressed. The optimal properties to be preferred must be identified univocally.

- Based on the significant differences existing between different bone sources, a comparative evaluation between different precursors should be carried out.
- To the authors' best knowledge, no clinical trials are available on the topic [88]. Once research will be ready to move to the clinic, a clearer picture will be achieved on the effective potential of these coatings.

Conflicts of Interest: The authors declare no conflict of interest.

References

1. Boyd, A.R.; Rutledge, L.; Randolph, L.D.; Mutreja, I.; Meenan, B.J. The deposition of strontium-substituted hydroxyapatite coatings. *J. Mater. Sci. Mater. Med.* **2015**, *26*, 65. [CrossRef] [PubMed]

2. Tang, Q.; Brooks, R.; Rushton, N.; Best, S. Production and characterization of HA and SiHA coatings. *J. Mater. Sci. Mater. Med.* **2010**, *21*, 173–181. [CrossRef] [PubMed]

3. Thian, E.S.; Huang, J.; Vickers, M.E.; Best, S.M.; Barber, Z.H.; Bonfield, W. Silicon-substituted hydroxyapatite (SiHA): A novel calcium phosphate coating for biomedical applications. *J. Mater. Sci.* **2006**, *41*, 709–717. [CrossRef]

4. Kurtz, S.; Ong, K.; Lau, E.; Mowat, F.; Halpern, M. Projections of primary and revision hip and knee arthroplasty in the United States from 2005 to 2030. *J. Bone Jt. Surg. Am.* **2007**, *89*, 780–785.

5. Hartman, C.W.; Garvin, K.L. Femoral fixation in revision total hip arthroplasty. *J. Bone Jt. Surg. Am.* **2011**, *21*, 2310–2322. [CrossRef] [PubMed]

6. Berni, M.; Lopomo, N.; Marchiori, G.; Gambardella, A.; Boi, M.; Bianchi, M.; Visani, A.; Pavan, P.; Russo, A.; Marcacci, M. Tribological characterization of zirconia coatings deposited on Ti6Al4V components for orthopedic applications. *Mater. Sci. Eng. C* **2016**, *62*, 643–655. [CrossRef] [PubMed]

7. Khatod, M.; Cafri, G.; Inacio, M.C.S.; Schepps, A.L.; Paxton, E.W.; Bini, S.A. Revision total hip arthoplasty: Factors associated with re-revision surgery. *J. Bone Jt. Surg.* **2015**, *97*, 359–366. [CrossRef] [PubMed]

8. Ong, K.L.; Lau, E.; Suggs, J.; Kurtz, S.M.; Manley, M.T. Risk of subsequent revision after primary and revision total joint arthroplasty. *Clin. Orthop. Relat. Res.* **2010**, *468*, 3070–3076. [CrossRef] [PubMed]

9. Fritsche, A.; Haenle, M.; Zietz, C.; Mittelmeier, W.; Neumann, H.G.; Heidenau, F.; Finke, B.; Bader, R. Mechanical characterization of anti-infectious, anti-allergic, and bioactive coatings on orthopedic implant surfaces. *J. Mater. Sci.* **2009**, *44*, 5544–5551. [CrossRef]

10. Peel, T.N.; Dowsey, M.M.; Buising, K.L.; Liew, D.; Choong, P.F. Cost analysis of debridement and retention for management of prosthetic joint infection. *Clin. Microbiol. Infect.* **2013**, *19*, 181–186. [CrossRef] [PubMed]

11. Hanssen, A.D.; Rand, J.A. Evaluation and treatment of infection at the site of total hip or knee arthoplasty. *Instr. Course Lect.* **1999**, *48*, 111–122. [PubMed]

12. Bozic, K.; Ries, M.D. The impact of infection after Total hip arthroplasty on hospital and surgeon resource utilization. *J. Bone Jt. Surg.* **2005**, *87A*, 1746–1750.

13. Sundfeldt, M.; Carlsson, L.V.; Johansson, C.B.; Thomsen, P.; Gretzer, C. Aseptic loosening, not only a question of wear: A review of different theories. *Acta Orthop.* **2006**, *77*, 177–197. [CrossRef] [PubMed]

14. Bonsignore, L.A.; Colbrunn, R.W.; Tatro, J.M.; Messerschmitt, P.J.; Hernandez, C.J.; Goldberg, V.M.; Stewar, M.C.; Greenfield, E.M. Surface contaminants inhibit osseointegration in a novel murine model. *Bone* **2011**, *49*, 923–930. [CrossRef] [PubMed]

15. Branemark, P.-I. Introduction to Osseointegration. In *Tissue-Integrated Prostheses. Osseointegration in Clinical Dentistry*; Branemark, P.-I., Zarb, C., Albrektsson, T., Eds.; Quintessence Publishing Co.: Chicago, IL, USA, 1985; pp. 11–76.

16. Surmenev, R.A. A review of plasma-assisted methods for calcium phosphate-based coatings fabrication. *Surf. Coat. Technol.* **2012**, *206*, 2035–2056. [CrossRef]

17. Dorozhkin, S.V. Calcium orthophosphate coatings, films and layers. *Prog. Biometeorol.* **2012**, *1*, 1. [CrossRef] [PubMed]

18. Boanini, E.; Gazzano, M.; Bigi, A. Ionic substitutions in calcium phosphates synthesized at low temperature. *Acta Biomater.* **2010**, *6*, 1882–1894. [CrossRef] [PubMed]

19. Capuccini, C.; Torricelli, P.; Sima, F.; Boanini, E.; Ristoscu, C.; Bracci, B.; Socol, G.; Fini, M.; Mihailescu, I.N.; Bigi, A. Strontium-substituted hydroxyapatite coatings synthesized by pulsed-laser deposition: In vitro osteoblast and osteoclast response. *Acta Biomater.* **2008**, *4*, 1885–1893. [CrossRef] [PubMed]

20. Li, L.; Lu, X.; Meng, Y.; Weyant, C.M. Comparison study of biomimetic strontium-doped calcium phosphates coatings by electrochemical deposition and air plasma spray: Morphology, composition and bioactive performance. *J. Mater. Sci. Mater. Med.* **2012**, *23*, 2359–2368. [CrossRef] [PubMed]

21. Supova, M. Substituted hydroxyapatites for biomedical applications: A review. *Ceram. Int.* **2015**, *41*, 9203–9231. [CrossRef]

22. Surmenev, R.A.; Surmeneva, M.A.; Ivanova, A.A. Significance of calcium phosphate coatings for the enhancement of new bone osteogenesis—A review. *Acta Biomater.* **2014**, *10*, 557–579. [CrossRef] [PubMed]

23. Fielding, G.A.; Roy, M.; Bandyopadhyay, A.; Bose, S. Antibacterial and biological characteristics of silver containing and strontium doped plasma sprayed hydroxyapatite coatings. *Acta Biomater.* **2012**, *8*, 3144–3152. [CrossRef] [PubMed]

24. Yang, Y.; Kim, K.H.; Ong, J.L. A review on calcium phosphate coatings produced using a sputtering process-an alternative to plasma spraying. *Biomaterials* **2005**, *26*, 327–337. [CrossRef] [PubMed]

25. Bigi, A.; Bracci, B.; Cuisinier, F.; Elkaim, R.; Fini, M.; Mayer, I.; Mihailescu, I.N.; Socol, G.; Sturba, L.; Torricelli, P. Human osteoblast response to pulsed laser deposited calciumphosphate coatings. *Biomaterials* **2005**, *26*, 2381–2389. [CrossRef] [PubMed]

26. Paital, S.R.; Dahotre, N.B. Review of laser based biomimetic and bioactive Ca–P coatings. *Mater. Sci. Technol.* **2008**, *24*, 1144–1161. [CrossRef]

27. Boanini, E.; Torricelli, P.; Fini, M.; Sima, F.; Serban, N.; Mihailescu, I.N.; Bigi, A. Magnesium and strontium doped octacalcium phosphate thin films by matrix assisted pulsed laser evaporation. *J. Inorg. Biochem.* **2012**, *107*, 65–72. [CrossRef] [PubMed]

28. Visan, A.; Grossin, D.; Stefan, N.; Duta, L.; Miroiu, F.M.; Stan, G.E.; Sopronyi, M.; Luculescu, C.; Freche, M.; Marsan, O.; et al. Biomimetic nanocrystalline apatite coatings synthesized by matrix assisted pulsed laser evaporation for medical applications. *Mater. Sci. Eng. B* **2014**, *181*, 56–63. [CrossRef]

29. Bianchi, M.; Gambardella, A.; Berni, M.; Panseri, S.; Montesi, M.; Lopomo, N.; Tampieri, A.; Marcacci, M.; Russo, A. Surface morphology, tribological properties and in vitro biocompatibility of nanostructured zirconia thin films. *J. Mater. Sci. Mater. Med.* **2016**, *27*, 96. [CrossRef] [PubMed]

30. Bianchi, M.; Lopomo, N.; Boi, M.; Gambardella, A.; Marchiori, G.; Berni, M.; Pavan, P.; Marcacci, M.; Russo, A. ceramic thin films realized by means of pulsed plasma deposition technique: Applications for orthopedics. *J. Mech. Med. Biol.* **2015**, *15*, 1540002. [CrossRef]

31. Gambardella, A.; Bianchi, M.; Kaciulis, S.; Mezzi, A.; Brucale, M.; Cavallini, M.; Herrmannsdoerfer, T.; Chanda, G.; Uhlarz, M.; Cellini, A.; et al. Magnetic hydroxyapatite coatings as a new tool in medicine: A scanning probe investigation. *Mater. Sci. Eng. C* **2016**, *62*, 444–449. [CrossRef] [PubMed]

32. Gambardella, A.; Berni, M.; Russo, A.; Bianchi, M. A comparative study of the growth dynamics of zirconia thin films deposited by ionized jet deposition onto different substrates. *Surf. Coat. Technol.* **2018**, *337*, 306–312. [CrossRef]

33. Bianchi, M.; Pisciotta, A.; Bertoni, L.; Berni, M.; Gambardella, A.; Visani, A.; Russo, A.; de Pol, A.; Carnevale, G. Osteogenic Differentiation of hDPSCs on Biogenic Bone Apatite Thin Films. *Stem Cells Int.* **2017**, *2017*, 3579283. [PubMed]

34. Bianchi, M.; Gambardella, A.; Graziani, G.; Liscio, F.; Maltarello, M.C.; Boi, M.; Berni, M.; Bellucci, D.; Marchiori, G.; Valle, F.; et al. Plasma-assisted deposition of bone apatite-like thin films from natural apatite. *Mater. Lett.* **2017**, *199*, 32–36. [CrossRef]

35. Bellucci, D.; Bianchi, M.; Graziani, G.; Gambardella, A.; Berni, M.; Russo, A.; Cannillo, V. Pulsed Electron Deposition of nanostructured bioactive glass coatings for biomedical applications. *Ceram. Int.* **2017**, *43*, 15862–15867. [CrossRef]

36. Bianchi, M.; Degli Esposti, L.; Ballardini, A.; Liscio, F.; Berni, M.; Gambardella, A.; Leeuwenburgh, S.C.G.; Sprio, S.; Tampieri, A.; Iafisco, M. Strontium doped calcium phosphate coatings on poly (etheretherketone)(PEEK) by pulsed electron deposition. *Surf. Coat. Technol.* **2017**, *319*, 191–199. [CrossRef]

37. Xue, W.; Hosick, H.L.; Bandyopadhyay, A.; Bose, S.; Ding, C.; Luk, K.D.K.; Cheung, K.M.C.; Lu, W.W. Preparation and cell–materials interactions of plasma sprayed strontium-containing hydroxyapatite coating. *Surf. Coat. Technol.* **2007**, *201*, 4685–4693. [CrossRef]

38. Boyd, A.R.; Rutledge, L.; Randolph, L.D.; Meenan, B.J. Strontium-substituted hydroxyapatite coatings deposited via a co-deposition sputter technique. *Mater. Sci. Eng. C* **2015**, *46*, 290–300. [CrossRef] [PubMed]

39. Rau, J.V.; Generosi, A.; Laureti, S.; Komlev, V.S.; Ferro, D.; Nunziante Cesaro, S.; Paci, B.; Rossi Albertini, V.; Agostinelli, E.; Barinov, S.M. Physicochemical investigation of pulsed laser deposited carbonated hydroxyapatite films on titanium. *Appl. Mater. Interfaces* **2009**, *1*, 1813–1820. [CrossRef] [PubMed]

40. Mroz, W.; Bombalska, A.; Burdynska, S.; Jedynski, M.; Prokopiuk, A.; Budner, B.; Slosarczyk, A. Structural studies of magnesium doped hydroxyapatite coatings after osteoblast culture. *J. Mol. Struct.* **2010**, *10*, 145–152. [CrossRef]

41. Clemens, J.A.M.; Klein, C.P.A.T.; Sakkers, R.J.B.; Dhert, W.J.A.; de Groot, K.; Rozing, P.M. Healing of gaps around calcium phosphate-coated implants in trabecular bone of the goat. *J. Biomed. Mater. Res.* **1997**, *36*, 55–64. [CrossRef]

42. Pereiro, I.; Rodriguez-Valencia, C.; Serra, C.; Solla, E.L.; Serra, J.; Gonzalez, P. Pulsed laser deposition of strontium-substituted hydroxyapatite coatings. *Appl. Surf. Sci.* **2012**, *258*, 9192–9197. [CrossRef]

43. Ozeki, K.; Goto, T.; Aoki, H.; Masuzawa, T. Characterization of Sr-substituted hydroxyapatite thin film by sputtering technique from mixture targets of hydroxyapatite and strontium apatite. *Biomed. Mater. Eng.* **2014**, *24*, 1447–1456. [PubMed]

44. Bogya, E.S.; Karoly, Z.; Barabas, R. Atmospheric plasma sprayed silica-hydroxyapatite coatings on magnesium alloys substrates. *Ceram. Int.* **2015**, *41*, 6005–6012. [CrossRef]

45. György, E.; Toricelli, P.; Socol, G.; Iliescu, M.; Mayer, I.; Mihailescu, I.N.; Bigi, A.; Werckman, J. Biocompatible Mn^{2+}-doped carbonated hydroxyapatite thin films grown by pulsed laser deposition. *J. Biomed. Mater. Res. A* **2004**, *71*, 353–358. [CrossRef] [PubMed]

46. Sima, L.E.; Stan, G.E.; Morosanu, C.O.; Melinescu, A.; Ianculescu, A.; Melinte, R.; Neamtu, J.; Petrescu, S.M. Differentiation of mesenchymal stem cells onto highly adherent radio frequency-sputtered carbonated hydroxyalapatite thin films. *J. Biomed. Mater. Res. A* **2010**, *95*, 1203–1214. [CrossRef] [PubMed]

47. Lopez, E.O.; Rossi, A.L.; Archanjo, B.S.; Ospina, R.O.; Mello, A.; Rossi, A.M. Crystalline nano-coatings of fluorine-substituted hydroxyapatite produced by magnetron sputtering with high plasma confinement. *Surf. Coat. Technol.* **2015**, *264*, 163–174. [CrossRef]

48. Surmeneva, M.A.; Chaikina, M.V.; Zaikovskij, V.I.; Pichugin, V.F.; Buck, V.; Prymak, O.; Epple, M.; Surmenev, R.A. The structure of an RF-magnetron sputter-deposited silicate-containing hydroxyapatite-based coating investigated by high-resolution techniques. *Surf. Coat. Technol.* **2013**, *218*, 39–46. [CrossRef]

49. Surmeneva, M.A.; Mukhametkaliyev, T.M.; Tyurin, A.I.; Teresov, A.D.; Koval, N.N.; Pirozhkova, T.S.; Shuvarin, I.A.; Shuklinov, A.V.; Zhigachev, A.O.; Oehr, C.; et al. Effect of silicate doping on the structure and mechanical properties of thin nanostructured RF magnetron sputter-deposited hydroxyapatite films. *Surf. Coat. Technol.* **2015**, *275*, 176–184. [CrossRef]

50. Surmeneva, M.A.; Surmenev, R.A.; Pichugin, V.F.; Chernousova, S.S.; Epple, M. In-vitro investigation of magnetron-sputtered coatings based on silicon-substituted hydroxyapatite. *J. Surf. Investig. X-ray* **2011**, *5*, 1202–1203. [CrossRef]

51. Pichugin, V.F.; Surmeneva, M.A.; Surmenev, R.A.; Khlusov, I.A.; Epple, M. Study of physicochemical and biological properties of calcium phosphate coatings prepared by RF magnetron sputtering of silicon-substituted hydroxyapatite. *J. Surf. Investig. X-ray* **2011**, *5*, 863–864. [CrossRef]

52. Surmeneva, M.; Tyurin, A.; Mukhametkaliyev, T.; Teresov, A.; Koval, A.; Pirozhkova, T.; Shuvarin, I.; Chudinova, E.; Surmenev, R. The effect of Si content on the structure and mechanical features of silicon-containing calcium-phosphate-based films deposited by RF-magnetron sputtering on titanium substrate treated by pulsed electron beam. In *IOP Conference Series: Materials Science and Engineering*; IOP Publishing: Bristol, UK, 2015; Volume 98.

53. Thian, E.S.; Huang, J.; Best, S.M.; Barber, Z.H.; Bonfield, W. Silicon-substituted hydroxyapatite: The next generation of bioactive coatings. *Mater. Sci. Eng. C* **2007**, *27*, 251–256. [CrossRef]

54. Hong, Z.; Mello, A.; Yoshida, T.; Luan, L.; Stern, P.H.; Rossi, A.; Ellis, D.E.; Ketterson, J.B. Osteoblast proliferation on hydroxyapatite coated substrates prepared by right angle magnetron sputtering. *J. Biomed. Mater. Res. A* **2010**, *93*, 878–885. [CrossRef] [PubMed]

55. Mroz, W.; Jedynski, M.; Prokopiuk, A.; Slosarczyk, A.; Paszkiewicz, Z. Characterization of calcium phosphate coatings doped with Mg, deposited by pulsed laser deposition technique using ArF excimer laser. *Micron* **2009**, *40*, 140–142. [CrossRef] [PubMed]

56. Mróz, W.; Budner, B.; Syroka, R.; Niedzielski, K.; Golański, G.; Slósarczyk, A.; Schwarze, D.; Douglas, T.E. In vivo implantation of porous titanium alloy implants coated with magnesium-doped octacalcium phosphate and hydroxyapatite thin films using pulsed laser deposition. *J. Biomed. Mater. Res. B Appl. Biomater.* **2015**, *103*, 151–158. [CrossRef] [PubMed]

57. *ASTM C633-01(2008) Standard Test Method for Adhesion or Cohesion Strength of Thermal Spray Coatings*; ASTM International: West Conshohocken, PA, USA, 2008. [CrossRef]

58. *ASTM F1147-05:2011 Standard Test Method for Tension Testing of Calcium Phosphate and Metallic Coatings*; ASTM International: West Conshohocken, PA, USA, 2011. [CrossRef]

59. *ISO 20502:2005 Fine Ceramics (Advanced Ceramics, Advanced Technical Ceramics)—Determination of Adhesion of Ceramic Coatings by Scratch Testing*; ISO: Geneva, Switzerland, 2005.

60. Rau, J.V.; Fosca, M.; Cacciotti, I.; Laureti, S.; Bianco, A.; Teghil, R. Nanostructured Si-substituted hydroxyapatite coatings for biomedical applications. *Thin Solid Films* **2013**, *543*, 167–170. [CrossRef]

61. Rau, J.V.; Fosca, M.; Cacciotti, I.; Laureti, S.; Bianco, A.; Teghil, R. Nanostructured Si-substituted hydroxyapatite coatings on titanium prepared by pulsed laser deposition. *J. Biomed. Res. B* **2015**, *103B*, 1621–1631.

62. Mihailescu, I.N.; Torricelli, P.; Bigi, A.; Mayer, I.; Iliescu, M.; Werckmann, J.; Socol, G.; Miroiu, F.; Cuisinier, F.; Elkaim, R.; et al. Calcium phosphate thin films synthesized by pulsed laser deposition: Physico-chemical characterization and in vitro cell response. *Appl. Surf. Sci.* **2005**, *248*, 344–348. [CrossRef]

63. Mihailescu, I.N.; Lamolle, S.; Socol, G.; Miroiu, F.; Roenold, F.J.; Bigi, A.; Mayer, I.; Cuisinier, F.; Lingstadaas, S.P. In vivo tensile test of biomimetic titanium implants pulsed laser coated with nanostructured calcium phosphate thin films. *J. Optoelectron. Adv. M* **2008**, *2*, 337–341.

64. Boanini, E.; Torricelli, P.; Sima, F.; Axente, E.; Fini, M.; Mihailescu, I.N.; Bigi, A. Strontium and zolendronate hydroxyapatites graded composite coatings for bone prostheses. *J. Colloid Interf. Sci.* **2015**, *448*, 1–7. [CrossRef] [PubMed]

65. Rodríguez-Valencia, C.; Pereiro, I.; Pirraco, R.P.; López-Álvarez, M.; Serra, J.; González, P.; Marques, A.P.; Reis, R.L. Human mesenchymal stem cells response to multi-doped silicon-strontium calcium phosphate coatings. *J. Biomater. Appl.* **2014**, *28*, 1397–1407.

66. Duta, L.; Oktar, F.N.; Stan, G.E.; Popescu-Pelin, G.; Serban, N.; Luculescu, C.; Mihailescu, I.N. Novel doped hydroxyapatite thin films obtained by pulsed laser deposition. *Appl. Surf. Sci.* **2013**, *265*, 41–49. [CrossRef]

67. Duta, L.; Mihailescu, N.; Popescu, A.C.; Luculescu, C.R.; Mihailescu, I.N.; Cetin, G.; Gunduz, O.; Oktar, F.N.; Popa, A.C.; Kuncser, A.; et al. Comparative physical, chemical and biological assessment of simple and titanium-doped ovine dentine-derived hydroxyapatite coatings fabricated by pulsed laser deposition. *Appl. Surf. Sci.* **2017**, *413*, 129–139. [CrossRef]

68. Mihalescu, N.; Stan, G.E.; Duta, L.; Chifiriuc, M.C.; Bleotu, C.; Sopronyi, M.; Luculescu, C.; Oktar, F.N.; Mihailescu, I.N. Structural, compositional, mechanical characterization and biological assessment of Bovine-Derived hydroxyapatite coatings reinforced with MgF2 or MgO for implants functionalization. *Mater. Sci. Eng. C* **2016**, *59*, 863–874. [CrossRef] [PubMed]

69. Duta, L.; Serban, N.; Oktar, F.N.; Mihailescu, I.N. Biological hydroxyapatite thin films synthesized by pulsed laser deposition. *Optoelectron. Adv. Mater.* **2013**, *7*, 1040–1044.

70. Hashimoto, Y.; Kusunoki, M.; Hatanaka, R.; Hamano, K.; Nishikawa, H.; Hosoi, Y.; Hontsu, S.; Nakamura, M. Improvement of hydroxyapatite deposition on titanium dental implant using ArF laser ablation: Effect on osteoblast biocompatibility in vitro. *Adv. Sci. Technol.* **2006**, *49*, 282–289. [CrossRef]

71. Hayami, T.; Hontsu, S.; Higuchi, Y.; Nishijkawa, H.; Kusunoki, M. Osteoconduction of a stoichiometric and bovine hydroxyapatite bilayer-coated implant. *Clin. Oral. Imp. Res.* **2011**, *22*, 774–776. [CrossRef] [PubMed]

72. *ASTM D4541-17 Standard Test Method for Pull-Off Strength of Coatings Using Portable Adhesion Testers*; ASTM International: West Conshohocken, PA, USA, 2017. [CrossRef]

73. *ISO 4624:2016 Paints and Varnishes—Pull-Off Test for Adhesion*; ISO: Geneva, Switzerland, 2016.

74. Ciuca, S.; Badea, M.; Pozna, E.; Pana, I.; Kiss, A.; Floroian, L.; Semenescu, A.; Cotrut, C.M.; Moga, M.; Vladescu, A. Evaluation of Ag containing hydroxyapatite coatings to the Candida albicans infection. *J. Microbiol. Methods* **2016**, *125*, 12–18. [CrossRef] [PubMed]

75. Ivanova, A.A.; Surmeneva, M.A.; Tyurin, A.I.; Pirozhkova, T.S.; Shuvarin, I.A.; Prymak, O.; Epple, M.; Chaikina, M.V.; Surmenev, R.A. Fabrication and physico-mechanical properties of thin magnetron sputtered deposited silver-containing hydroxyapatite films. *Appl. Surf. Sci. Part B* **2016**, *360*, 929–935. [CrossRef]

76. Syromotina, D.S.; Surmeneva, M.A.; Gorodzha, S.N.; Pichugin, V.F.; Ivanova, A.A.; Yu, I.; Grubova, K.; Kravchuk, S.; Gogolinskii, K.V.; Prymak, O.; Epple, M.; et al. Physical-mechanical characteristics of RF magnetron sputter-deposited coatings based on silver-doped hydroxyapatite. *Russ. Phys. J.* **2014**, *56*, 1198–1205. [CrossRef]

77. Ivanova, A.A.; Surmeneva, M.A.; Grubova, I.Y.; Sharonova, A.A.; Pichugin, V.F.; Chaikina, M.V.; Buck, V.; Prymak, O.; Epple, M.; Surmenev, R.A. Influence of the substrate bias on the stoichiometry and structure of RF-magnetron sputter-deposited silver-containing calcium phosphate coatings. *Mater. Sci. Eng. Technol.* **2013**, *44*, 218–225. [CrossRef]

78. Agyapong, D.A.Y.; Zeng, H.; Acquah, I.; Liu, Y. Structural and physical properties of magnetron co-sputtered silver containing hydroxyapatite coatings on titanium substrates. *Integr. Ferroelectr.* **2015**, *163*, 64–72. [CrossRef]

79. Kotoka, R.; Kwame Yamoah, N.; Mensah-Darkwa, K.; Moses, T.; Kumar, D. Electrochemical corrosion behavior of silver doped tricalcium phosphate coatings on magnesium for biomedical application. *Surf. Coat. Technol.* **2016**, *292*, 99–109. [CrossRef]

80. Jelinek, M.; Kocourek, T.; Remsa, J.; Weiserová, M.; Jurek, K.; Mikšovský, J.; Strnad, J.; Galandáková, A.; Ulrichová, J. Antibacterial, cytotoxicity and physical properties of laser—Silver doped hydroxyapatite layers. *Mater. Sci. Eng. C* **2013**, *33*, 1242–1246. [CrossRef] [PubMed]

81. Jelínek, M.; Kocourek, T.; Jurek, K.; Remsa, J.; Mikšovský, J.; Weiserová, M.; Strnad, J.; Luxbacher, T. Antibacterial properties of Ag-doped hydroxyapatite layers prepared by PLD method. *Appl. Phys. A* **2010**, *101*, 615–620. [CrossRef]

82. Jelínek, M.; Weiserová, M.; Kocourek, T.; Zezulová, M.; Strnad, J. Biomedical properties of laser prepared silver-doped hydroxyapatite. *Laser Phys.* **2011**, *21*, 1265–1269. [CrossRef]

83. Eraković, S.; Janković, A.; Ristoscu, C.; Duta, L.; Serban, N.; Visan, A.; Mihailescu, I.N.; Stan, G.E.; Socol, M.; Iordache, O.; et al. Antifungal activity of Ag:hydroxyapatite thin films synthesized by pulsed laser deposition on Ti and Ti modified by TiO$_2$ nanotubes substrates. *Appl. Surf. Sci.* **2014**, *293*, 37–45. [CrossRef]

84. Bell, B.; Scholvin, D.; Jin, C.; Narayan, R.J. Pulsed laser deposition of hydroxyapatite-diamondlike carbon multilayer films and their adhesion aspects. *J. Adhes. Sci. Technol.* **2006**, *20*, 221–231. [CrossRef]

85. Janković, A.; Eraković, S.; Ristoscu, C.; Mihailescu, N.; Duta, L.; Visan, A.; Stan, G.E.; Popa, A.C.; Husanu, M.A.; Luculescu, C.R.; et al. Structural and biological evaluation of lignin addition to simple and silver-doped hydroxyapatite thin films synthesized by matrix assisted pulsed laser evaporation. *J. Mater. Sci. Mater. Med.* **2015**, *26*, 17. [CrossRef] [PubMed]

86. Hidalgo-Robatto, B.M.; López-Álvarez, M.; Azevedo, A.S.; Dorado, J.; Serra, J.; Azevedo, N.F.; González, P. Pulsed laser deposition of copper and zinc doped hydroxyapatite coatings for biomedical application. *Surf. Coat. Technol.* **2018**, *333*, 168–177. [CrossRef]

87. Rodríguez-Valencia, C.; López-Álvarez, M.; Cochón-Cores, B.; Pereiro, I.; Serra, J.; González, P. Novel selenium-doped hydroxyapatite coatings for biomedical applications. *J. Biomed. Mater. Res. Part A* **2013**, *101*, 853–861.

88. Furkó, M.; Balázsi, K.; Balázsi, C. Comparative study on preparation and characterization of bioactive coatings for biomedical applications—A review on recent patents and literature. *Rev. Adv. Mater. Sci.* **2017**, *48*, 25–51.

Article

Pulsed Laser Deposited Biocompatible Lithium-Doped Hydroxyapatite Coatings with Antimicrobial Activity

Liviu Duta [1,*], Mariana Carmen Chifiriuc [2,3], Gianina Popescu-Pelin [1], Coralia Bleotu [4], Gratiela (Pircalabioru) Gradisteanu [3], Mihai Anastasescu [5], Alexandru Achim [6] and Andrei Popescu [6,*]

[1] National Institute for Lasers, Plasma and Radiation Physics, 077125 Magurele, Romania; gianina.popescu@inflpr.ro
[2] Department of Microbiology, Faculty of Biology, University of Bucharest, 060101 Bucharest, Romania; carmen.chifiriuc@gmail.com
[3] Earth, Environmental and Life Sciences Division, Research Institute of the University of Bucharest (ICUB), 060101 Bucharest, Romania; gratiela87@gmail.com
[4] "Stefan S. Nicolau" Institute of Virology, 030304 Bucharest, Romania; cbleotu@yahoo.com
[5] "Ilie Murgulescu" Institute of Physical Chemistry, Romanian Academy, 060021 Bucharest, Romania; manastasescu_ro@yahoo.com
[6] Center for Advanced Laser Technologies (CETAL), National Institute for Lasers, Plasma and Radiation Physics, 077125 Magurele, Romania; alexandru.achim@inflpr.ro
* Correspondence: liviu.duta@inflpr.ro (L.D.); andrei.popescu@inflpr.ro (A.P.)

Abstract: Simple and lithium-doped biological-origin hydroxyapatite layers were synthesized by Pulsed Laser Deposition technique on medical grade Ti substrates. Cytotoxic effects of lithium addition and the biocompatibility of obtained coatings were assessed using three cell lines of human origin (new initiated dermal fibroblasts, immortalized keratinocytes HaCaT, and MG-63 osteosarcoma). Antimicrobial properties of obtained coatings were assessed on two strains (i.e., *Staphylococcus aureus* and *Candida albicans*), belonging to species representative for the etiology of medical devices biofilm-associated infections. Our findings suggest that synthesized lithium-doped coatings exhibited low cytotoxicity on human osteosarcoma and skin cells and therefore, an excellent biocompatibility, correlated with a long-lasting anti-staphylococcal and -fungal biofilm activity. Along with low fabrication costs generated by sustainable resources, these biological-derived materials demonstrate their promising potential for future prospective solutions—viable alternatives to commercially available biomimetic HA implants—for the fabrication of a new generation of implant coatings.

Keywords: lithium-doped hydroxyapatite coatings; renewable resources for implant coatings; pulsed laser deposition; biocompatibility; inhibition of microbial biofilms development

1. Introduction

Microbial biofilms development on medical devices and human tissues represents a serious public health problem at global level, leading to a high diversity of biofilm-associated infections, with increasing incidence, although yet underestimated and high rates of morbidity and mortality. The biofilm growth protects microbial cells from antimicrobials and host immune effectors, enabling pathogens to survive in limited conditions and also to disperse and colonize new niches. The biofilm-embedded microbial cells exhibit a high tolerance to conventional antimicrobial agents, explaining the chronic and relapsing character of the produced infections [1–3]. The increasing

incidence of biomaterial-associated infections is in close relationship with the continuously growing demand for implantable medical devices and other invasive diagnostic and therapeutic maneuvers. Therefore, controlling biofilm formation represents a mandatory feature during medical devices manufacturing and their use [4].

Biofilm development is a dynamic and complex process which occurs in several stages [1]. It starts with a reversible adhesion stage, followed by irreversible adhesion [5], maturation and, in the last stage, detachment. The first stages depend on the physico-chemical properties of the surface, conditioning the interactions with microbial structure involved in the adhesion process [6]. The main pathogens involved in the development of biofilm-associated infections include the Gram-positive bacteria, such as *Staphylococcus aureus* (*S. aureus*), and fungal strains, especially *Candida* spp. Reports from the National Institutes of Health demonstrate that around 80% of human infections are due to biofilms [7]. The biofilm-associated infections are characterized by moderate intensity symptoms, chronic evolution and high resistance to antibiotics [8]. Therefore, one main direction bridging materials science to biomedical research is the development of complex therapeutic strategies, including the association of multiple antimicrobial agents [9–11]. However, one should note that the association of multiple antibiotics might lead to high toxicity effects, correlated with a low efficiency on the cells embedded in biofilms [12]. Therefore, the development of preventive measures, based on the design of novel biomaterials, synthesized in the form of thin layers and used for the fabrication of medical devices which are more resistant to microbial colonization and biofilms development could represent a more effective approach [13,14].

Synthetic hydroxyapatite (HA) represents a well-known biocompatible material used as implantable ceramic due to its great chemical and structural resemblance to the inorganic part of human hard tissues [15,16]. Reports from dedicated literature have demonstrated that biological-derived HA (BHA) has some important advantages over synthetic HA. In this respect, to improve mechanical (anchorage to bone) and biological (osseointegration, resistance to microbial colonization) properties of medical implants, simple BHA materials [17] or BHA doped with specific reagents such as ZnO [18], SiO_2, MgO, Al_2O_3 and ZrO_2 [19], Ti [20], Li_2CO_3 and Li_3PO_4 [21], Li_2O [22], commercial inert glass [22,23], $CaMgSiO_6$ [24], MgF_2 or MgO [25], and CO_2 [26] have been used [27].

The present study is a first attempt in dedicated literature to fabricate, in a single-stage pulsed laser deposition process, BHA coatings to exhibit low cytotoxicity and good biocompatibility, corroborated with an active role in prevention of microbial colonization and biofilm development on prosthetic devices.

2. Materials and Methods

2.1. PLD Experimental Protocol

BHA powders were obtained from the femoral bones of freshly slaughtered cattle (received from a Turkish slaughter house, which uses the other animal parts for general consumption). Bones were delivered on ice to the laboratory and, before usage, they were submitted to a veterinary control. Concisely, both heads of femoral bones were cut off (because they contained too much soft tissue) and only femoral shafts were further processed. Bone marrows were extracted and all other soft tissue residues were removed from shafts. Then, femoral shafts were cut into slices, cleaned and washed with distilled water. Cleaned parts were deproteinized for 14 days in an alkali solution of 1% sodium hypochlorite. After washing and drying, bone pieces were calcinated at 850 °C for 4 h in air, in order to completely eliminate organic components of bone. We emphasize that as-prepared BHA powders are biologically safe due to the high temperature fabrication route, which not only favors the crystallization of the material, but also totally prevents any risk of diseases transmission, as no pathogen can survive to such extreme conditions [20–22,25]. Resulting calcined bone specimens were first crushed with a mortar and pestle and then ball-milled (for 4 h) to fine powders (i.e., with particles of submicron size). The color of the resulting powders was milky-white. One should note that the

experimental procedure for the fabrication of BHA powders was conducted in accordance with the European Regulation 722/2012 [28] and ISO 22442:2015 standard [29]. Batches of BHA powders were admixed with 1 wt.% of Li_2CO_3 or Li_3PO_4 (Sigma-Aldrich GmbH, St. Louis, MO, USA). Sample codes are introduced in Table 1 and will be further used in the text.

Table 1. Sample codes and description.

Sample Code	Sample Description
Ti	Bare Ti control
Si	Simple Si control
Li-0	Simple BHA film deposited on Ti
Li-C	BHA:Li_2CO_3 film deposited on Ti
Li-P	BHA:Li_3PO_4 film deposited on Ti

PLD experiments were carried out inside a stainless-steel deposition chamber. A KrF * excimer laser source COMPex Pro205 (Coherent, Göttingen, Germany) (λ = 248 nm, $\tau_{FWHM} \leq$ 25 ns, υ = 10 Hz) was used for target irradiation.

The laser beam was oriented at 45° in respect with the target surface. The laser fluence incident onto the target surface was set at ~4 J/cm^2 (with a corresponding pulse energy of ~360 mJ).

Before deposition, targets were "cleaned" by short multipulse laser ablation with 1000 pulses. During deposition, the target was continuously rotated with 0.4 Hz and translated along two orthogonal axes to avoid piercing and allow for the growth of uniform films.

The ablated material was collected onto medical-grade titanium (Ti) disks (~0.6 × 0.6 cm^2 and 0.1 cm thickness), that were placed parallel to the target at a separation distance of 5 cm.

All experiments were performed in a 50 Pa water vapor atmosphere. During experiments, substrates were heated and maintained at a constant temperature of 500 °C using a PID-EXCEL temperature controller (Excel Instruments, Gujarat, India). A heating rate of 25 °C/min and a cooling ramp of 10 °C/min have been used. For the deposition of each structure, 15,000 subsequent laser pulses were applied.

So as to improve the crystalline status of synthesized films, all samples have been subjected to a 6 h post-deposition thermal treatment in air (in water vapors), at 600 °C.

2.2. Characterization of Synthesized Structures

2.2.1. Atomic Force Microscopy

The surface topography of synthesized structures was examined in high resolution Atomic Force Microscopy (AFM) (Park Systems, Suwon, Korea), performed in the non-contact mode on a XE-100 apparatus from Park Systems. Sharp tips (PPP-NCHR type from Nanosensors™, Neuchâtel, Switzerland), having 125 μm in length, 30 μm width and radius of curvature of less than 8 nm, were used at surface scanning over areas of 0.5 × 0.5 μm^2. The spring constant was of ~42 N/m and the resonance frequency of ~330 kHz, respectively. All AFM measurements were performed at room temperature.

AFM images were processed using Image Processing Program, XEI–v.1.8.0, developed by Park Systems (Suwon, Korea). The horizontal line by line flattening was used as planarization method for displaying purposes and for subsequent statistical data analysis, including the calculation of the roughness. To have a better view of the surface morphology, 2D-AFM images are displayed in the classical view mode (one color used also for the z-scale bar), while 3D-AFM images are shown as topographic maps in the so-called "enhanced color" view mode (using the change of a pixel color relative to its neighbors).

The textural (amplitude) parameters, namely average roughness (R_a), surface skewness (R_{sk}) and surface kurtosis (R_{ku}) were determined giving information about the roughness and the degree of skewness and kurtosis of investigated surfaces. R_a is the area between the roughness and its mean in

contrast with the root-mean-squared roughness, which is the standard deviation of the height value in the selected region. In statistics, R_{sk} is a measure of the asymmetry of the probability distribution of a real-valued random variable about its mean. In the present case, R_{sk} describes the asymmetry of the height distribution (frequency vs. height histogram). R_{ku} measures the randomness of profile heights and of the "sharpness" of the height distribution, and has a value of 3 in the case of a perfectly random surface [30]. Kurtosis is not related to the geometry of the distribution, but to the shape of it. Kurtosis is a measure of whether data are heavy-tailed or light-tailed, relative to a normal distribution ($R_{ku} = 3$). Thus, data sets with high kurtosis, $R_{ku} > 3$ (sharper height distributions–so called "lepto kurtosis") tend to have heavy tails, or outliers. Data sets with low kurtosis, $R_{ku} < 3$ (flattened height distribution–so called "platy kurtosis"), tend to have light tails, or lack of outliers.

2.2.2. In Vitro Biological Tests

The potential use of synthesized coatings in the biomedical field was appraised by both safety (cytotoxicity and influence on the cellular cycle of three different human cell lines) and anti-biofilm tests (performed on bacterial and fungal strains).

Biocompatibility Assays

(i) Cytotoxicity Assays

The cytotoxicity of obtained coatings was investigated using three different cell lines, i.e., MG-63 osteosarcoma ECACC 86051601, new initiated dermal fibroblasts (FBD) and immortalized keratinocytes HaCaT [31].

The cytotoxicity of samples was investigated after microscopic examination of the unstained monolayers developed on their surface. Changes of the general morphology and monolayer confluence were assessed. The cytotoxicity level of the tested samples was classified in accordance to the ISO standard recommendations [32].

The UV-sterilized samples were placed in duplicate in 24-well plates exposing the coated face. A total of 1×10^5 cells in Dulbecco's Modified Eagle Medium:F12 supplemented with 10% fetal bovine serum were added. Plates were maintained for 24 h at 37 °C and 5% CO_2 atmosphere. After 24 h, samples have been observed with an inverted microscope and photographed in contrast phase with a Zeiss Observer D1 microscope (Zeiss, Oberkochen, Germany). Due to the fact that BHA samples were opaque, the examination and images of cellular monolayers were taken in the vicinity of tested materials. Then, one of the duplicate samples was extracted from the well, fixed in ethanol 70%, stained for 5 min with propidium iodide (PI) (chemical name 3,8-Diamino-5-(3-(diethyl(methyl)ammonio)propyl)-6-phenylphenanthridin-5-ium iodide) 50 µg/mL, and visualized in red channel, using a fluorescence Leica DFC450C microscope (Leica, Allendale, NJ, USA).

(ii) Cellular Cycle Assay

For the investigation of the cellular cycle, samples (treated as mentioned in the previous section) were harvested with trypsin, fixed in 70% cold ethanol over night at −20 °C, and then washed with phosphate-buffered saline (pH 7.5), treated with 100 µg/mL RNase A for 15 min and stained with 10 µg/mL PI for 1 h at 37 °C. After PI staining, the events (number of cells passing through the laser) acquisition was performed with an Epics Beckman Coulter flow cytometer (Beckman Coulter Inc., Indianapolis, IN, USA). The obtained data was analyzed with the FlowJo software 7.6.4 and expressed as fractions of cells found in different cell cycle phases [33].

Antimicrobial Assays

Two microbial strains traceable to American Type Culture Collection (ATTC), belonging to two of the most important species known to be involved in the etiology of medical devices biofilm-associated infections, respectively *S. aureus* and *Candida albicans* (*C. albicans*), were used in the experiments. Fresh cultures were obtained from glycerol stocks of *S. aureus* ATTC 6538 and *C. albicans* ATTC 26790 strains on non-selective solid media. Samples were sterilized by exposure to UV irradiation in a laminar flow chamber for 30 min on each side, placed in duplicate in six-well plates (Nunc) in 2 mL of Luria Broth (LB) nutrient medium and then inoculated with 500 µL of standardized microbial suspensions of 0.5 McFarland density corresponding to $\sim 10^5$–10^6 Colony Forming Units (CFU)/mL. After incubation at 37 °C, for different time periods (1, 6, 12, 24, 48 and 72 h, respectively), colonized samples were gently washed with distilled water to remove unattached microbial cells and then immersed in 1 mL sterile saline buffer in Eppendorf tubes, sonicated for 15 s, and then vortexed for 15 s at 3000 rotations/min. Suspensions resulted from the detached biofilms were then ten-fold diluted and 10 µL of each serial dilution were plated in triplicate on tryptic soy agar. After 24 h of incubation at 37 °C, colonies were counted and the number of CFU/mL was determined.

The surface characterization of inoculated surfaces was carried out using Scanning Electron Microscopy (SEM) with a FEI Inspect S50 apparatus (FEI, Hillsboro, OR, USA). Prior to this investigation, samples were washed three times in PBS and then fixed in ethanol, for 5 min, at RT.

3. Results

3.1. AFM Analysis

Typical bidimensional (2D) and tridimensional (3D) topographic images collected at a scanning area of (0.5×0.5) µm^2 are presented in Figure 1. The 3D AFM images, which are topographic maps of scanned areas, are presented in the Enhanced Color^{TM} view mode (Park Systems) in order to better emphasize the morphological surface peculiarities. In 3D-AFM micrographs, dark color (blue) delineates surface "valleys", whilst the light color (orange) corresponds to the salient features ("hills"). The 2D AFM images are presented in the "classical" view mode, with one color gradient (brown in this case) for the z-scale depth. The first row presents the morphological features of the bare substrate (Si), which are located in a z-scale depth (Δz) of less than 1 nm (typical ~0.7 nm), which leads to a very low R_a value of only 0.1 nm (which is representative for a clean Si wafer), as seen in Table 2. The R_{sk} parameter, describing the asymmetry of the height distribution histogram, has a small value in this case, of 0.9, which is corresponding to a flat surface with random (small) protuberances. The R_{ku} parameter, which represents a measure of the randomness of the profile heights and of the "sharpness" of the surface height distribution, has a value of ~3, which is characteristic for a near perfect random surface (Gaussian distribution) [30].

Li-0 films (Figure 1–second row) exhibit protruding (R_{sk} ~0.46) large particles, randomly distributed (R_{ku} ~3.11), having tens of nm in diameter (~35–50 nm), individually displayed or with a tendency to merge. In this case, the average roughness increases to a value of ~5.9 nm, which is higher than the one registered for the bare substrate.

In the case of Li-C structures (Figure 1–third row), the addition of lithium leads to the formation of much larger particles, almost double as compared to Li-0 films and, accordingly, with a double roughness value (10.3 nm). Though, particles are not much more protruding in z direction, as the R_{sk} parameter is ~0.56, and relatively uniform distributed as the kurtosis parameter being just a bit higher (R_{ku} ~3.49) than in the second case.

Finally, in the case of Li-P structures (Figure 1–last row), the addition of lithium leads to a morphology similar to the one of Li-0 films, but with particles slightly smaller (diameters ~25 nm) and better separated (the fusing tendency being lower). Therefore, it exhibits the highest value for R_{ku} parameter in this series (5.58), pointing to a sharp height distribution [34], but with a lower skewness factor (0.17) as compared with Li-0 (0.46) and Li-C (0.56), which means that particles are less

protuberant for Li-P structures. This leads to an average roughness value (4.32 nm) very close to the one characteristic for Li-0 films (5.9 nm).

Overall, based on the results, one should emphasize that the obtained lithium-based structures could be described as homogeneous and uniform, with a morphology that depends on the preparation route and with (average) roughness values in the nanometric range (R_a ~5–10 nm).

The inferred values of the amplitude parameters, which were discussed above, are summarized in Table 2.
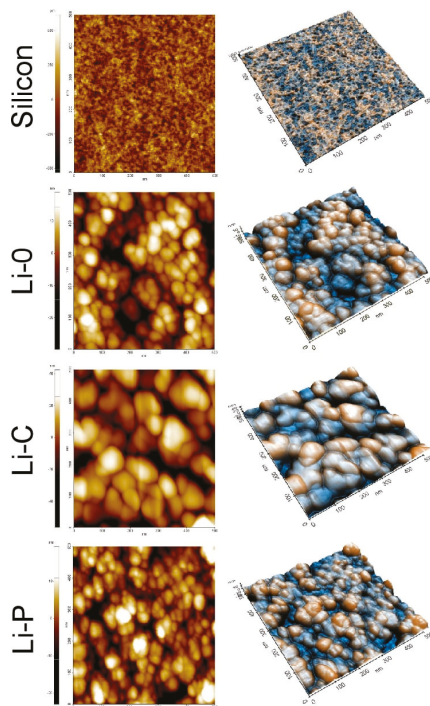
Figure 1. The 2D (classical view mode—left column) and 3D (enhanced color view mode—right column) AFM images of Li-0, Li-C and Li-P structures synthesized at 600 °C on Si(100) wafers.

Table 2. Surface amplitude parameters (R_a, R_{sk} and R_{ku}) for a ($0.5 \times 0.5\ \mu m^2$) scanned surface area of control (Si) and Li-0, Li-C and Li-P structures.

| Sample Code	Amplitude Parameter	Scanning Area ($0.5 \times 0.5\ \mu m^2$)
Si	R_a (nm)	0.10
	R_{sk}	0.09
	R_{ku}	3.03
Li-0	R_a (nm)	5.86
	R_{sk}	0.46
	R_{ku}	3.11
Li-C	R_a (nm)	10.26
	R_{sk}	0.56
	R_{ku}	3.49
Li-P	R_a (nm)	4.32
	R_{sk}	0.17
	R_{ku}	5.58

3.2. Biocompatibility Assays

3.2.1. Cytotoxicity Test

In the current study, the cytotoxicity of obtained coatings was assessed using three cellular lines of human origin, selected for covering their diverse potential applications in the development of medical devices. Thus, MG-63 osteosarcoma cells exhibit common features with human osteoblast precursors or poorly differentiated osteoblasts, producing type I collagen with no or reduced osteocalcin and alkaline phosphatase basal level, making them appropriate for assessing the biocompatibility of biomaterials designed for orthopedic applications [35,36]. The other two cell lines were represented by human skin new initiated dermal fibroblasts and human skin immortalized keratinocytes, considering that many implanted medical devices or next generation wound dressings are coming for short time into contact with the skin.

Concerning the cytotoxicity of synthesized materials, contrast phase microscopy images (Figures 2–4) have shown that cells developed on plastic well, at the limit with the tested disc surface, are unaffected and preserved an unmodified morphology. This suggests that BHA materials do not release toxic substances in the environment, as secondary product. New initiated dermal fibroblasts exhibited a spindle-shaped morphology (Figure 2), the morphological appearance of keratinocytes showed polygonal cells (Figure 3), whilst MG-63 monolayers were composed of elongated and fusiform cells (Figure 4).
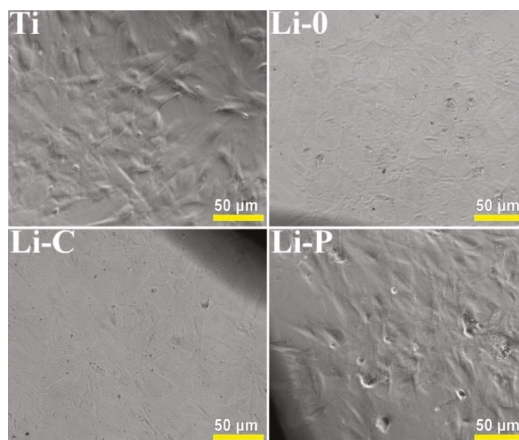
Figure 2. Contrast phase inverted microscopy images of the new initiated dermal fibroblasts monolayer grown in the presence of Ti and simple and doped biological-derived HA coatings (Magnification ×200).
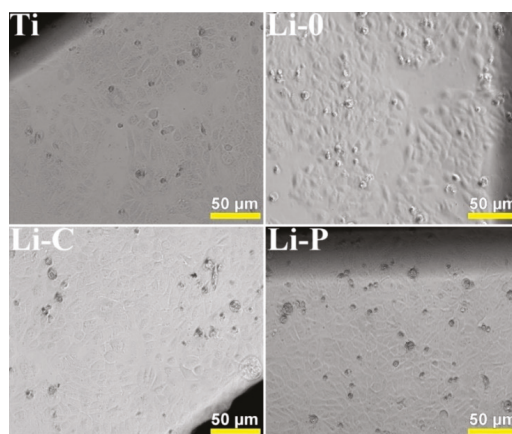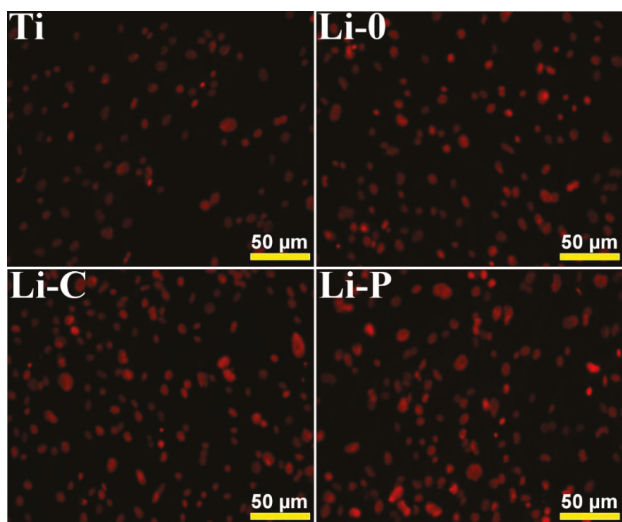
Figure 3. Contrast phase inverted microscopy images of the immortalized keratinocytes HaCaT monolayer grown in the presence of Ti and simple and doped biological-derived HA coatings (Magnification ×200).
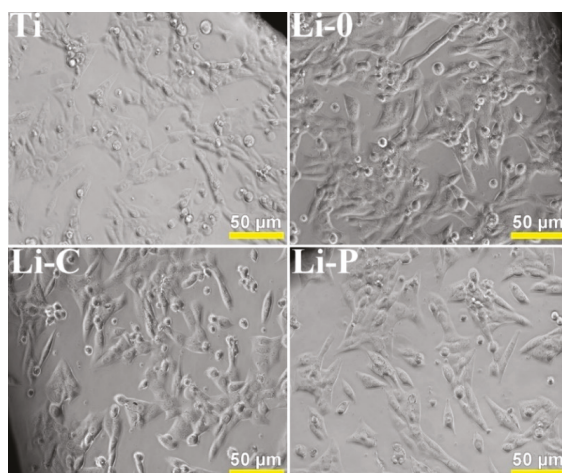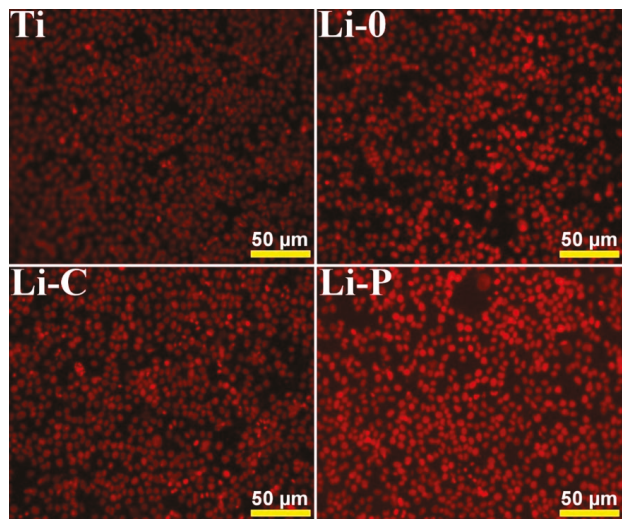

Figure 4. Contrast phase inverted microscopy images of the MG-63 osteosarcoma cells monolayer grown in the presence of Ti and simple and doped biological-derived HA coatings (Magnification ×200).

On the other hand, the fluorescence microscopy images (Figures 5–7) have revealed that the number of adhered cells on the bare Ti was similar between all synthesized layers and depends on type of cell line. This observation suggests that deposited layers are not cytotoxic against human skin or bone cells and allow for an unhindered cell development. According to the ISO standard specifications [32], the cytotoxic effect of synthesized layers can be classified as absent, supporting the potential of fabricated materials to be used as coatings for different biomedical surfaces, such as orthopedic devices, dental materials, or catheters.

Figure 5. Fluorescence microscopy images of new initiated dermal fibroblasts grown for 24 h on the surface of Ti and simple and doped biological-derived HA coatings (Magnification ×200).


Figure 6. Fluorescence microscopy images of immortalized keratinocytes HaCaT grown for 24 h on the surface of Ti and simple and doped biological-derived HA coatings (Magnification ×200).
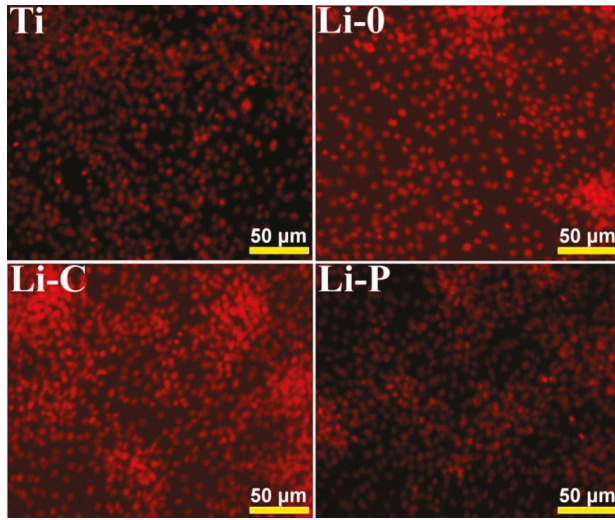
Figure 7. Fluorescence microscopy images of MG-63 osteosarcoma cells grown for 24 h on the surface of Ti and simple and doped biological-derived HA coatings (Magnification ×200).

3.2.2. Cellular Cycle Assay

The cell cycle analysis by flow cytometry revealed that the obtained coatings did not influence the cellular cycle progression of the three type of cells (i.e., new initiated dermal fibroblasts, immortalized keratinocytes and MG-63 osteosarcoma cells) (Figures 8–10), confirming that synthesized layers do not interfere with the typical development of normal and tumoral cells.
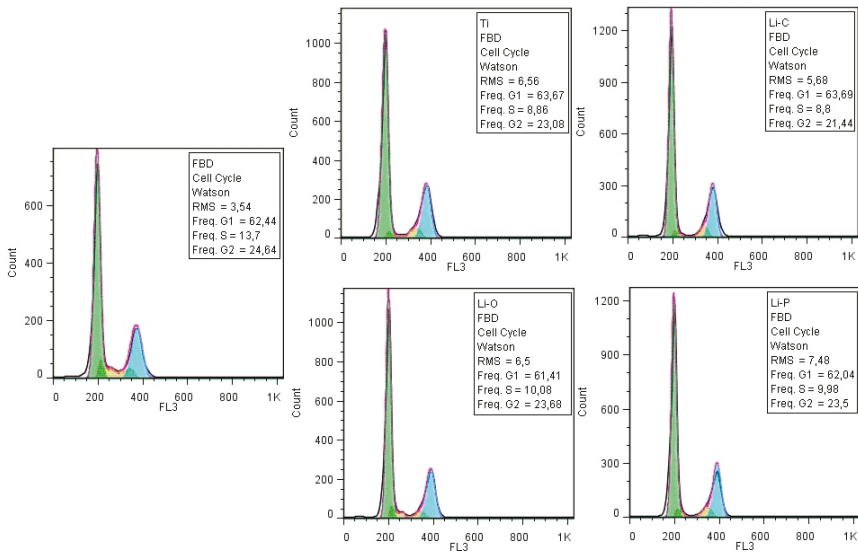
Figure 8. Flow cytometry diagrams of cells cycle analysis of new initiated dermal fibroblasts grown on the tested materials.
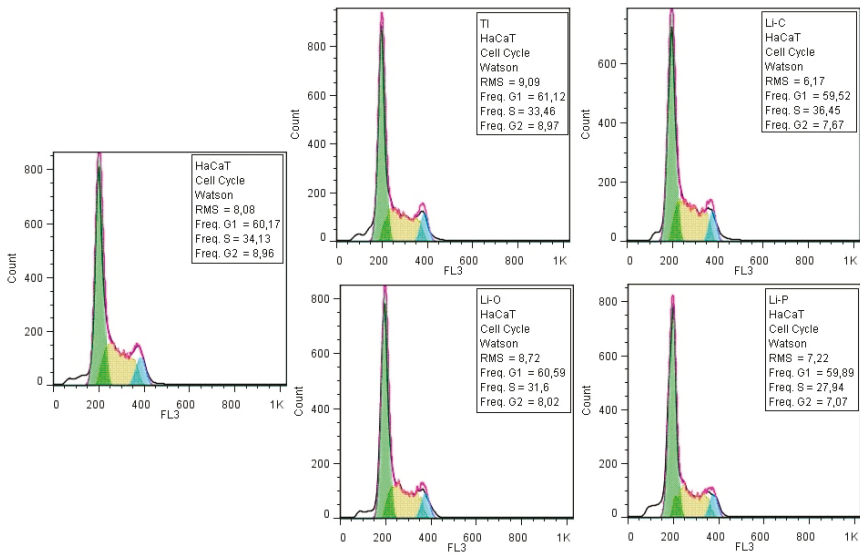
Figure 9. Flow cytometry diagrams of cells cycle analysis of immortalized keratinocytes grown on the tested materials.
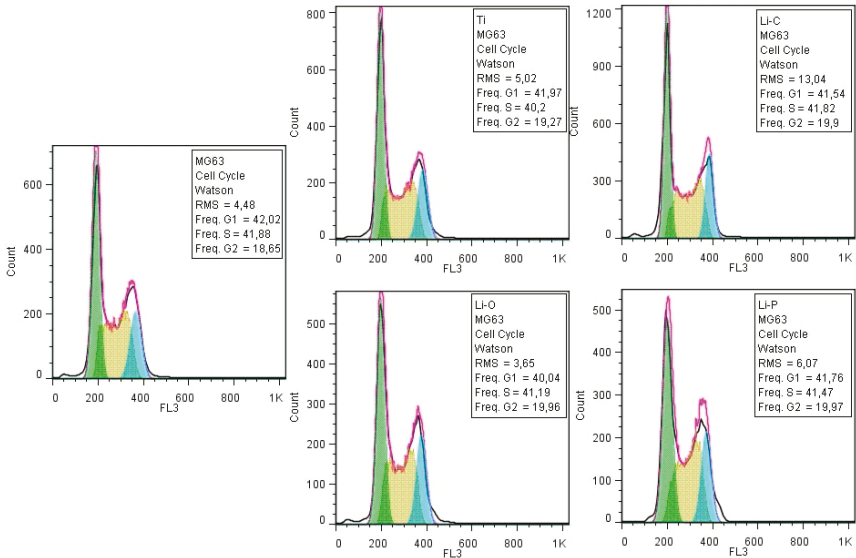

Figure 10. Flow cytometry diagrams of cells cycle analysis of MG-63 osteosarcoma cells grown on the tested materials.

3.3. Anti-Biofilm Activity

3.3.1. Anti-Staphylococcal Biofilm Activity of Obtained Coatings

Compared with Ti, after 24 h of incubation, all tested coatings exhibited a significant inhibitory activity against *S. aureus* biofilm growth, showing a significant increase starting with 48 h of incubation and persisting with high intensity, after 72 h of incubation. This behavior is suggested by the drastic decrease of the number of CFU/mL by 2 to 4 logs at these last two-time intervals (Figure 11b). The

absence of a visible inhibition of the microbial growth in the 1–2 h (Figure 11a) interval reveals that the anti-biofilm effect is possibly due to the slow release of some bioactive components from the synthesized coatings, with potential antimicrobial activity (e.g., oligoelements).

(a)

(b)
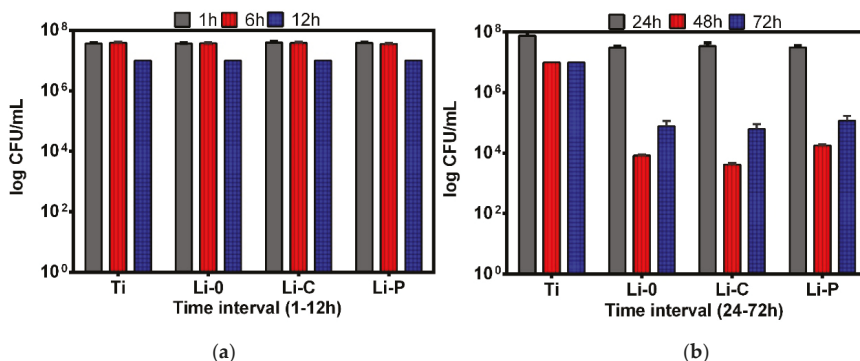
Figure 11. Graphic representation of the logarithmic values of *S. aureus* biofilm cells developed on the surface of Ti and simple and doped biological-derived HA coatings: (**a**) 1–12 h and (**b**) 24–72 h.

Regarding comparative efficiency of the tested materials, one can observe that Li-C coatings exhibited a slightly increased antimicrobial activity against *S. aureus* biofilm after 48 h of incubation, as compared to Li-0 and Li-P ones (Figure 11b).

The SEM images of *S. aureus* biofilm developed on the surface of Ti and simple and doped BHA structures are presented comparatively in Figure 12, at a magnification of 10,000×. For comparison reasons only non-inoculated simple and lithium-doped surfaces are presented by the authors of [21]. Although *S. aureus* adhered to all tested samples, it must be noticed that the density of *S. aureus* cells was significantly more reduced on Li-C > Li-P > Li-0 surfaces as compared to Ti ones, which is in good agreement with the quantitative results presented in Figure 11. SEM images of *S. aureus* biofilms are in concordance with others reported in the literature [1,37,38].
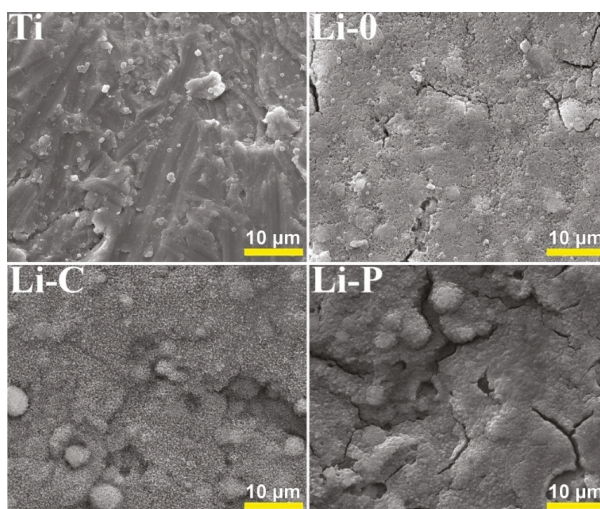
Figure 12. SEM images corresponding to *S. aureus* biofilm after 72 h of development on the surfaces of Ti and simple and doped biological-derived HA coatings.

3.3.2. Anti-Fungal Biofilm Activity of Obtained Coatings

In the case of *C. albicans* strain, a strong anti-biofilm effect was recorded for all tested coatings as compared to Ti, earlier than in the case of *S. aureus* biofilm, i.e., after 12 h of incubation (Figure 13a), followed by a recrudescence of microbial growth at 24 h and a drastic decrease of the biofilm-embedded cells at 48 and 72 h, respectively (Figure 13b). Moreover, Li-C and Li-P coatings proved a slightly better efficiency (as compared to Li-0 samples) against *C. albicans* biofilms incubated for 48 h, whilst Li-0 and Li-P showed the same antimicrobial efficiency at 72 h of incubation (Figure 13b).
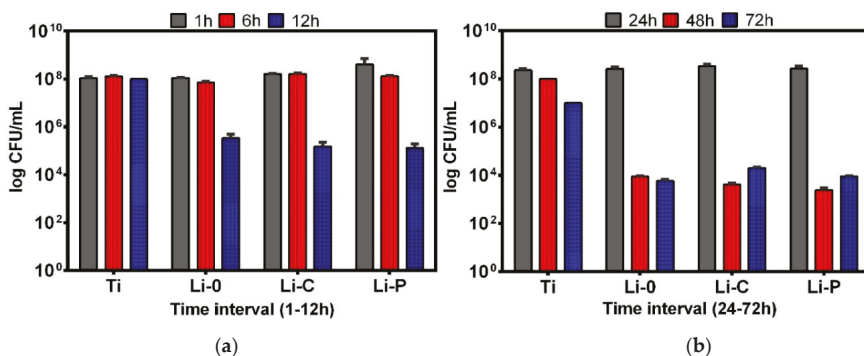

Figure 13. Graphic representation of the logarithmic values of *C. albicans* biofilm cells developed on the surface of Ti and simple and doped biological-derived HA coatings: (**a**) 1–12 h and (**b**) 24–72 h.

The efficiency of the anti-fungal biofilm activity of simple and doped coatings decreased in the order Li-C, Li-P, Li-0, after an incubation time of three days (Figure 13).

Similar to the case of *S. aureus* strain, no visible inhibition of microbial development was obtained in the range of 1–6 h (Figure 13a), most probably due to the slow release from the synthesized films of the active elements responsible for the antimicrobial effect.

Following adherence to abiotic substrates (i.e., catheters and other medical devices), *C. albicans* develops into a three-dimensional community containing round-budding yeast cells, oval pseudo-hyphal cells and elongated hyphal cells embedded in an extracellular polysaccharides' matrix [39]. *C. albicans* biofilm development follows a sequential dynamic over a 24–48 h period, starting with initial adhesion of single fungal yeast cells, continuing with a cellular proliferation and colonization of the surface and the switching to filamentous hyphal forms, a hallmark of the initiation of biofilm formation, followed by maturation, through the accumulation of the protecting extracellular polysaccharide matrix. Dispersion of biofilm-associated cells from the mature biofilm can initiate formation of new biofilms or disseminate into host tissues, therefore being associated with candidemia and invasive fungal infections [40].

SEM images of *C. albicans* biofilm developed on the surface of Ti and simple and doped BHA structures are presented comparatively in Figure 14 at a magnification of 10,000×. In the case of bare Ti, one can observe many ovoidal or round-shaped cells which have the tendency to form micro-colonies, as well as the existence of filamentous, hyphal forms. Ti samples were completely covered by a continuous layer of cells, which is in good correlation with the quantitative results presented in Figure 13. This observation might be indicative not only for cell-surface type interactions, but also for stronger cell-cell type ones.
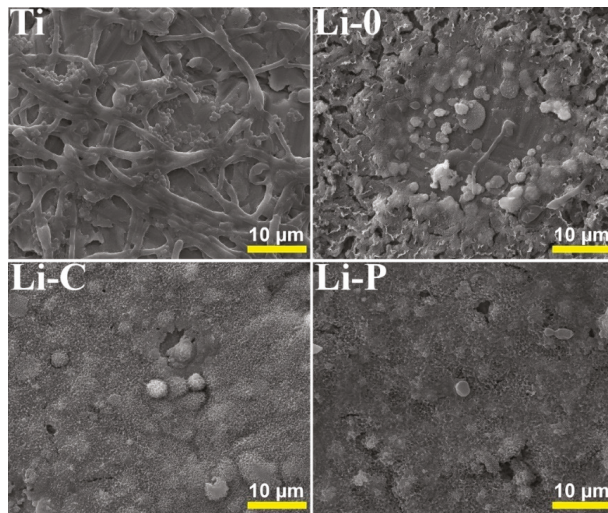
Figure 14. SEM images corresponding to *C. albicans* biofilm after 72 h of development on the surfaces of Ti and simple and doped biological-derived HA coatings.

In exchange, in case of coated surfaces, particularly Li-C and Li-P ones, the number of yeast cells is drastically decreased, they adhere exclusively in isolated, unicellular form, the filaments being completely absent.

The microscopy results demonstrate that the synthesized coatings inhibit the initiation of fungal biofilm development. SEM images of *C. albicans* are in concordance with others reported in literature [1,41].

We note that results of anti-biofilm quantitative assays, which revealed a slightly superior anti-biofilm effect of Li-C and Li-P structures as compared to control Ti and Li-0 ones, are in good agreement with aspects recorded in SEM examination (Figures 12 and 14). Presented SEM images were considered representative for the entire surface of samples and were selected after examining 8–10 different microscopic fields.

4. Discussion

4.1. Biocompatibility

Lithium is considered as a trace metal in organisms and is used for the treatment of bipolar affective disorder [42] and refractory depression [43]. The safe administration of lithium for osteoporosis was reported more than two decades ago [44,45]. When used in the low bone mass and osteoporosis-mice models, lithium was indicated to enhance osteogenesis [46]. Also, in the case of lumbar spine, femoral neck and proximal femur, the corresponding bone mineral density values were reported to be higher than controls [45,47]. Despite its proven efficacy and safety [48], there are cases when lithium administration could be toxic and determine side effects, such as thirst and excessive urination, nausea, diarrhea, tremor, weight gain, sexual dysfunction, dermatological effects, as well as long-term effects on the thyroid gland, kidneys and parathyroid glands [49]. However, recent studies challenge this negative perception of lithium administration, by showing strong evidence that intoxication in patients receiving lithium treatments is rare, it occurs only when the concentration is higher than 1.5 mmol/L, and its main adverse effects can be properly monitored and managed [50–52].

Even though its excellent biocompatibility was proven, the poor mechanical properties of HA limit its applications in implantology to non-load-bearing implants. It has been shown that ion doping represents a good method applied to improve performances of bio-ceramics related to biodegradability,

biocompatibility, strength and toughness. Therefore, when lithium is substituted into the HA structure, it plays an important role because it could induce a decrease in HA solubility [53,54], without affecting its biocompatibility [55,56], and an improvement of biomechanical properties, without altering the HA structure. The reason for the increase of strength of lithium doped HA may be due to the fact that metal ions could decrease the porosity of samples which can result in a more compact and hard structure [57]. Also, one notes that, as a substituted trace element, lithium can positively influence the viability [58], proliferation rates and alkaline phosphatase activity of cells [59,60]. Wang et al. [57] reported that when used in a proper low dose (0.5% and 1%), lithium ions can substitute calcium ones in a HA structure, in order to obtain a biomaterial (LiHA scaffold) characterized by high strength, a higher osteoblast-mediated degradation rate and a superior ability to promote cell proliferation as compared to simple HA and controls. On one hand, the lithium incorporation into HA can change the surface topography of original HA material and make LiHA scaffold possess a more compact bulk, which finally can result in a higher adherence and enhanced growth of osteoblasts [61]. On the other hand, the Li^+ released from LiHA scaffolds could enhance the activity of osteoblasts, a phenomenon also reported by Tang et al. [62]. In another study, Oh et al. [63] assessed the influence of lithium fluoride (LiF) on in vitro biocompatibility and bioactivity of calcium aluminate-polymethylmethacrylate composite cements. The results indicated that there was no cytotoxicity related to LiF and the addition of 1 wt.% LiF enabled composite cements to form HA on their surface within 15 days of soaking in SBF solutions. One can therefore conclude that these enhanced characteristics strengthen the safe use of lithium and could advance lithium-containing structures as promising materials for the fabrication of bone tissue engineering scaffolds.

The literature data on the cytotoxic ions release rates for lithium-substituted HA materials is rather scarce and reported cytotoxic levels are sometimes contradictory due to the fact that release rates are strongly depending on crystallinity or particle morphology and size of the investigated material [42]. In a current study, Miguez-Pacheco et al. [64] reported on lithium-containing bioactive glasses, with Li_2O substituting Na_2O in different amounts. The conclusion of their study, in terms of lithium ion release, was that formulations with 2.5 wt.% and 5 wt.% Li_2O content proved to be within the therapeutic range.

In vitro cytotoxicity assays of newly developed materials should precede in vivo tests, since the results are more reproducible and allow for the evaluation of cellular and molecular responses triggered by an investigated material [65].

We stress upon that results obtained on human skin new initiated dermal fibroblasts and human skin immortalized keratinocytes could be informative for the potential of the tested materials to be used in oral applications, for example in facial reconstruction, dental implants or periodontal pockets filling. A fully differentiated human gingiva equivalent was constructed entirely from keratinocytes and fibroblasts, being considered a valuable surrogate of animal models for testing new therapeutics [66]. Moreover, one could therefore predict the potential orthopedic implant-related adverse effects, related to the occurrence of hypersensitivity reactions to the implant material components. This evaluation is presently recommended for patients with a clear self-reported history of metal reactions and is done by patch testing before device implant [67].

4.2. Possible Mechanisms Explaining the Antimicrobial Activity of Synthesized Structures

We stress that infection still remains a major impediment to the long-term use of many implanted devices. Even though microbial adhesion to biomaterial surfaces represents an essential step in the pathogenesis of these infections, molecular and physical interactions that govern this adhesion have not been yet fully understood. Both specific and non-specific interactions may play an important role in the ability of cells to attach to (or to resist detachment from) the biomaterial surface [68]. In the biomedical field, a great number of implant failures is due to the formation of microbes at the implanted site. Microbes, which are able to cause a wide variety of infections in humans by spreading through common places like bathroom tiles, doorknobs, or packing materials, can be controlled by coating implants

with materials with antimicrobial properties. Antimicrobial implantable materials must locally kill microbes or slow down their growth, without being toxic to host tissue cells. Therefore, if an implant material will possess such characteristics, then the problem of failure will be drastically reduced.

Besides the utility of lithium in the treatment of mood disorders, different studies reported that as well as other antidepressants, it could exhibit an immunostimulant role and antimicrobial activity, as it opposes eicosanoids suppressive action upon the immune system [69]. Recent studies have shown that lithium could limit neurodegeneration and ameliorate symptoms of the trimethyltin poisoning in rodents, by inducing pro-survival and anti-inflammatory effects [70]. Moreover, in concentrations of up to 10 mol.%, lithium could enhance the antibacterial activity of bioactive glass against resistant bacteria, such as methicillin-resistant *S. aureus*. The 58S bioactive glass with 5 mol.% Li_2O substitution for CaO was considered a promising biomaterial in bone repair/regeneration therapies, showing an enhanced biocompatibility and alkaline phosphatase activity, with a negligible loss in the bioactivity compared to the 58S bioglass [71].

The adhesion ability of *S. aureus* to extracellular matrix components and plasma proteins from the pellicle formed on the surface of implanted biomaterials represents one main concern for infections associated to implanted medical devices. *C. albicans* is considered one of the major etiological agents of hospital-acquired infections, being also frequently associated with contamination of indwelling medical devices [72]. The phenotypic plasticity is a unique feature of many fungal species, including *C. albicans*, which is an extremely versatile, dimorphic yeast that can survive as a commensal in various environments, one of the adapting mechanisms being the switching from the yeast to filamentous forms [73]. *S. aureus* and *C. albicans* can be also found in multispecies biofilms, mutually potentiating their tolerance to antibiotics and disinfectants [74]. The mechanism of indirect pathogenesis, which might lead in the end to therapeutic failure, could also occur inside multispecies biofilms, in which genetically resistant microorganisms are the susceptible pathogens [75]. As an example, the coexistence of *S. aureus* and *C. albicans* inside biofilms determines the enhancement of *S. aureus* resistance to vancomycin [76]. Therefore, the decrease of microbial adhesion represents one of the main concerns of the current research in the field of biomaterials and medical devices.

In the following, we propose some relative contributions of specific and nonspecific mechanisms in order to explain, to some extent, the efficiency manifested by our fabricated coatings to prevent the microbial adhesion. Therefore, surface features like wetting behavior and material surface characteristics (topography), corroborated with metal ions release can stand as key-factors able to modulate the adhesion of microbes and their subsequent survival on the surface of the synthesized structures.

Water is considered as a major interfacial host in all living environments, and it can affect the capacity of protein adsorption [77] and cellular adhesion [78]. Therefore, to interpret the microbial behavior, this parameter must be carefully taken into consideration. In this respect, one possible mechanism able to explain the antimicrobial activity of synthesized structures is based on their wetting properties and, consequently, on their surface energy values [38]. Therefore, a hydrophilic behavior and high values of surface energy [21] might enhance the overall antimicrobial properties of our fabricated coatings. In addition, the anti-biofilm activity might be explained by repulsive forces which will occur between anionic-coated surfaces (associated with the presence of hydroxyl hydrophilic functional groups) and the *S. aureus*/*C. albicans* biofilms matrix, which is also negatively charged, due to its main component, represented by self-produced exopolysaccharides [38]. Moreover, coatings will facilitate the formation of a highly alkaline medium, consequently leading to the destruction of lipids, which are the main component of microbial cell membrane, followed by microbial cells lysis [79]. When discussing anti-biofilm properties of obtained coatings, one must also consider that the adhesion of microbial cells from aqueous suspensions follows the thermodynamic model. The surface energy of microbial cells is typically smaller than the surface energy of liquids in which cells are suspended, causing cells to attach preferentially to hydrophobic materials (i.e., materials with lower surface energies). Therefore, a hydrophilic behavior, such that of our coatings, and the subsequent

formation of hydration layers could disrupt the initial step of microbial biofilm formation, represented by the adhesion of microbial cells to a surface [80].

Another factor to explain the adhesion of microorganisms is related to the surface characteristics of the material. Therefore, the reduction of microorganisms can be investigated as a function of surface topographic parameters. Among the surface properties, surface roughness and topography have been the most investigated topics in dental biofilm researches. There exists a general perception according to which an increase in surface roughness can promote bacterial colonization due to the increase in contact area between the material surface and bacterial cells, in other words, due to extended surface area available for attachment [81]. Thus, smoothening the surfaces to nanometer-scale roughness was demonstrated to reduce biofilm formation [82]. We note that a roughness (R_a) value of 0.2 µm was reported to be the threshold for maximum reduction of bacterial adhesion on abutment surfaces [83]. In this respect, R_a values inferred in our cases, which are (19–46) times smaller than this threshold, should be emphasized.

Moreover, it was recognized that R_{ku} and R_{sk} are parameters of key-importance when describing surface roughness of calcified tissue implants [84] because osteogenic cells' adhesion is sensitive to the stress concentrations which derive from the presence of sharp heights at the implant-tissue interface [85], likewise they can be considered against bacterial proliferation [86]. Inferred values for skewness and kurtosis parameters indicated a sharper heights (R_{ku} ~5.6) distribution of surface features in case of Li-P structures as compared with Li-0 and Li-C ones (R_{ku} ~3.1 and ~3.5), with more peaks than valleys ($R_{sk} > 0$) and that these peaks and valleys are much closer in height and depth for Li-P coatings (R_{sk} ~0.17) than those of Li-0 and Li-C (R_{sk} of 0.46 and 0.56, respectively). Thus, the average roughness parameter was found to have a similar value (~5 nm) for Li-0 and Li-P coatings, and a double one (~10 nm), for Li-C structures. The positive values of R_{ku} and R_{sk} coefficients could also be related to less available surface-active sites [78,80], and, consequently, could stay at the origin of the inhibition of microbial development on the surface of synthesized structures.

Last but not least, there are reports in the literature on the antibacterial potential of antibiotics/antibacterial substances-loaded HA, but very few refer to antifungal-loaded cement drug delivery [87]. We stress upon that there are even fewer reports dedicated to the antibacterial activity of lithium [88]. It was demonstrated that the antibacterial/anti-biofilm effect can become more evident when extending the exposure to metal [89]. Therefore, one of the proposed mechanisms of action could be the metal accumulation inside bacterial cells, followed by the cellular wall disruption and, eventually, cellular lysis. By extending the proposed mechanism, we can speculate that the amount of lithium ions released from our synthesized materials was enough to accumulate in the microbial cells and to alter the culture media. By affecting their multiplication and phenotypic switching capacity, their further progress is slowed down. These assumptions were confirmed by the results of our study, the lithium-doped samples showing a more pronounced inhibitory effect after 48 and 72 h of incubation, respectively.

5. Conclusions

Simple and lithium-doped biological-derived hydroxyapatite (BHA) coatings were fabricated by Pulsed Laser Deposition onto medical-grade titanium substrates.

In vitro biocompatibility investigations proved that synthesized layers were non-cytotoxic on all tested cell lines, respectively MG-63 osteosarcoma derived cells, human skin new initiated dermal fibroblasts and immortalized keratinocytes, and did not interfere with their cellular cycle phases. In addition, synthesized structures drastically inhibited the ability of *S. aureus* and *C. albicans*, two microorganisms well-known for their complex genetic resistance mechanisms and involvement in the etiology of medical devices-associated biofilm infections, to develop mature biofilms. The anti-fungal biofilm activity has become significant after 12 h of incubation in the case of *C. albicans* and after 24 h for *S. aureus* biofilm, and persisted with high intensity for 72 h. The anti-biofilm activity of obtained coatings could be explained in terms of their surface characteristics, such as

hydrophilic character, associated to a high value of the surface energy, or low values of surface roughness (in the range of 5–10 nm).

We consider that these combined characteristics can be important for the protection of biomedical equipment against contamination by nosocomial infections of any sort, as well as for the long life exploiting of various implants and could therefore offer guidance towards the suitability of lithium-doped BHA structures for future biomedical applications.

References

1. Rabin, N.; Zheng, Y.; Opoku-Temeng, C.; Du, Y.; Bonsu, E.; Sintim, H.O. Biofilm formation mechanisms and targets for developing anti-biofilm agents. *Future Med. Chem.* **2015**, *7*, 493–512. [CrossRef] [PubMed]
2. Coughlan, L.M.; Cotter, P.D.; Hill, C.; Alvarez-Ordóñez, A. New weapons to fight old enemies: Novel strategies for the (bio) control of bacterial biofilms in the food industry. *Front. Microbiol.* **2016**, *7*, 400–405. [CrossRef]
3. Del Pozo, J.L. Biofilm-related disease. *Expert Rev. Anti-Infect. Ther.* **2018**, *16*, 51–65. [CrossRef] [PubMed]
4. Petrachi, T.; Resca, E.; Piccinno, M.S.; Biagi, F.; Strusi, V.; Dominici, M.; Veronesi, E. An alternative approach to investigate biofilm in medical devices: A feasibility study. *Int. J. Environ. Res. Public Health* **2017**, *14*, 1587. [CrossRef] [PubMed]
5. Renner, L.D.; Weibel, D.B. Physicochemical regulation of biofilm formation. *MRS Bull.* **2011**, *36*, 347–355. [CrossRef] [PubMed]
6. Claessen, D.; Rozen, D.E.; Kuipers, O.P.; Søgaard-Andersen, L.; Van Wezel, G.P. Bacterial solutions to multicellularity: A tale of biofilms, filaments and fruiting bodies. *Nat. Rev. Microbiol.* **2014**, *12*, 115–124. [CrossRef] [PubMed]
7. Joo, H.-S.; Michael, O. Molecular basis of in-vivo biofilm formation by bacterial pathogens. *Chem. Biol.* **2012**, *19*, 1503–1513. [CrossRef] [PubMed]
8. Lazar, V. Quorum sensing in biofilms—How to destroy the bacterial citadels or their cohesion/power? *Anaerobe* **2011**, *17*, 280–285. [CrossRef] [PubMed]
9. Olar, R.; Badea, M.; Marinescu, D.; Chifiriuc, M.C.; Bleotu, C.; Grecu, M.N.; Iorgulescu, E.E.; Lazar, V. *N*,*N*-dimethylbiguanide complexes displaying low cytotoxicity as potential large spectrum antimicrobial agents. *Eur. J. Med. Chem.* **2010**, *45*, 3027–3034. [CrossRef] [PubMed]
10. Limban, C.; Missir, A.V.; Nuta, D.C.; Caproiu, M.T.; Morusciag, L.; Chirita, C.; Cupii, A.; Gurgu, H. Advances in research of new 2-((4-ethylphenoxy)methyl)-*N*-(arylcarbamothioyl)benzamides. *Farmacia* **2015**, *63*, 376–380.
11. Limban, C.; Missir, A.V.; Nuță, D.C.; Căproiu, M.T.; Papacocea, M.T.; Chiriță, C.O. Synthesis of some new 2-((4-chlorophenoxy)methyl)-*N*-(arylcarbamothioyl) benzamides as potential antifungal agents. *Farmacia* **2016**, *64*, 775–779.
12. Boucher, H.W.; Talbot, G.H.; Bradley, J.S. Bad bugs, no drugs: No ESKAPE! An update from the infectious diseases society of America. *Clin. Infect. Dis.* **2009**, *48*, 1–12. [CrossRef] [PubMed]
13. Anghel, I.; Holban, A.M.; Andronescu, E.; Grumezescu, A.M.; Chifiriuc, M.C. Efficient surface functionalization of wound dressings by a phytoactivenanocoating refractory to Candida albicans biofilm development. *Biointerphases* **2013**, *8*, 12. [CrossRef] [PubMed]

14. Chifiriuc, M.C.; Grumezescu, A.M.; Andronescu, E.; Ficai, A.; Cotar, A.I.; Grumezescu, V.; Bezirtzoglou, E.; Lazar, V.; Radulescu, R. Water dispersible magnetite nanoparticles influence the efficacy of antibiotics against planktonic and biofilm embedded enterococcus faecalis cells. *Anaerobe* **2013**, *22*, 14–19. [CrossRef] [PubMed]

15. Dorozhkin, S.V. Calcium orthophosphates: Occurrence properties biomineralization pathological calcification and biomimetic applications. *Biomatter* **2011**, *1*, 121–164. [CrossRef] [PubMed]

16. Graziani, G.; Boi, M.; Bianchi, M. A review on ionic substitutions in hydroxyapatite thin films: Towards complete biomimetism. *Coatings* **2018**, *8*, 269. [CrossRef]

17. Lambert, F.; Angélique, L.; Pierre, D.; Sophie, S.; Pierre, L.; Eric, R. Influence of space-filling materials in subantral bone augmentation: Blood clot vs. autogenous bone chips vs. bovine hydroxyapatite. *Clin. Oral Implant. Res.* **2011**, *22*, 538–545. [CrossRef] [PubMed]

18. Gunduz, O.; Eray, M.E.; Sibel, D.; Serdar, S.; Simeon, A.; Faik, N.O. Composites of bovine hydroxyapatite (BHA) and ZnO. *J. Mater. Sci.* **2008**, *43*, 2536–2540. [CrossRef]

19. Oktar, F.N.; Agathopoulos, S.; Ozyegin, L.S.; Gunduz, O.; Demirkol, N.; Bozkurt, Y.; Salman, S. Mechanical properties of bovine hydroxyapatite (BHA) composites doped with SiO_2, MgO, Al_2O_3, and ZrO_2. *J. Mater. Sci. Mater. Med.* **2007**, *18*, 2137–2143. [CrossRef]

20. Duta, L.; Mihailescu, N.; Popescu, A.C.; Luculescu, C.R.; Mihailescu, I.N.; Cetin, G.; Gunduz, O.; Oktar, F.N.; Popa, A.C.; Kuncser, A.; et al. Comparative physical, chemical and biological assessment of simple and titanium-doped ovine dentine-derived hydroxyapatite coatings fabricated by pulsed laser deposition. *Appl. Surf. Sci.* **2017**, *413*, 129–139. [CrossRef]

21. Popescu, A.C.; Florian, P.E.; Stan, G.E.; Popescu-Pelin, G.; Zgura, I.; Enculescu, M.; Oktar, F.N.; Trusca, R.; Sima, L.E.; Roseanu, A.; et al. Physical-chemical characterization and biological assessment of simple and lithium-doped biological-derived hydroxyapatite thin films for a new generation of metallic implants. *Appl. Surf. Sci.* **2018**, *439*, 724–735. [CrossRef]

22. Duta, L.; Oktar, F.N.; Stan, G.E.; Popescu-Pelin, G.; Serban, N.; Luculescu, C.; Mihailescu, I.N. Novel doped hydroxyapatite thin films obtained by pulsed laser deposition. *Appl. Surf. Sci.* **2013**, *265*, 41–49. [CrossRef]

23. Gunduz, O.; Ahmad, Z.; Ekren, N.; Agathopoulos, S.; Salman, S.; Oktar, F.N. Reinforcing of biologically derived apatite with commercial inert glass. *J. Thermoplast. Compos. Mater.* **2009**, *22*, 407–419. [CrossRef]

24. Khandan, A.; Majid, A.; Neriman, O.; Hamid, G. Study of the bioactivity, wettability and hardness behaviour of the bovine hydroxyapatite-diopside bio-nanocomposite coating. *J. Taiwan Inst. Chem. Eng.* **2016**, *60*, 538–546. [CrossRef]

25. Mihailescu, N.; Stan, G.E.; Duta, L.; Mariana, C.C.; Coralia, B.; Sopronyi, M.; Luculescu, C.; Oktar, F.N.; Mihailescu, I.N. Structural, compositional, mechanical characterization and biological assessment of bovine-derived hydroxyapatite coatings reinforced with MgF_2 or MgO for implants functionalization. *Mater. Sci. Eng. C* **2016**, *59*, 863–874. [CrossRef] [PubMed]

26. Gunduz, O.; Godec, C.; Ahmad, Z.; Gokce, H.; Yetmez, M.; Kalkandelen, C.; Sahin, Y.M.; Oktar, F.N. Preparation and evaluation of cerium oxide-bovine hydroxyapatite composites for biomedical engineering applications. *J. Mech. Behav. Biomed.* **2014**, *35*, 70–76. [CrossRef] [PubMed]

27. Boutinguiza, M.; Pou, J.; Comesaña, R.; Lusquiños, F.; de Carlos, A.; León, B. Biological hydroxyapatite obtained from fish bones. *Mater. Sci. Eng. C* **2012**, *32*, 478–486. [CrossRef]

28. Eisenhart, S. *EU Regulation 722. New EU Animal Tissue Regulations in Effect for Some Medical Devices*; Emergo: Hong Kong, China, 2013; Available online: https://www.emergobyul.com/blog/2013/09/new-eu-animal-tissue-regulations-effect-some-medical-devices (accessed on 16 January 2019).

29. *ISO 22442-1 Medical Devices Utilizing Animal Tissues and Their Derivatives—Part 1: Application of Risk Management*; International Organization for Standardization: Berlin, Germany, 2015.

30. Eaton, P.; West, P. *Atomic Force Microscopy*, 1st ed.; Oxford University Press: Oxford, UK, 2010; pp. 1–256.

31. Boukamp, P.; Petrussevska, R.T.; Breitkreutz, D.; Hornung, J.; Markham, A.; Fusenig, N.E. Normal keratinization in a spontaneously immortalized aneuploid human keratinocyte cell line. *J. Cell Biol.* **1988**, *106*, 761–771. [CrossRef]

32. *ISO 10993-5 Biological Evaluation of Medical Devices—Part 5: Tests for In Vitro Cytotoxicity*; International Organization for Standardization: Berlin, Germany, 2009.

33. Duta, L.; Ristoscu, C.; Stan, G.E.; Husanu, M.A.; Besleaga, C.; Chifiriuc, M.C.; Lazar, V.; Bleotu, C.; Miculescu, F.; Mihailescu, N.; et al. New bio-active, antimicrobial and adherent coatings of nanostructured carbon double-reinforced with silver and silicon by Matrix-Assisted Pulsed Laser Evaporation for medical applications. *Appl. Surf. Sci.* **2018**, *441*, 871–883. [CrossRef]

34. Stan, G.E.; Popescu, A.C.; Mihailescu, I.N.; Marcov, D.A.; Mustata, R.C.; Sima, L.E.; Petrescu, S.M.; Ianculescu, A.; Trusca, R.; Morosanu, C.O. On the bioactivity of adherent Bioglass thin films synthesized by magnetron sputtering techniques. *Thin Solid Films* **2010**, *518*, 5955–5964. [CrossRef]

35. Clover, J.; Gowen, M. Are MG-63 and HOS TE85 human osteosarcoma cell lines representative models of the osteoblastic phenotype? *Bone* **1994**, *15*, 585–591. [CrossRef]

36. Skindersoe, M.E.; Krogfelt, K.A.; Blom, A.; Jiang, G.; Prestwich, G.D.; Mansell, J.P. Dual action of lysophosphatidate-functionalised titanium: Interactions with human (MG63) Osteoblasts and methicillin resistant staphylococcus aureus. *PLoS ONE* **2015**, *10*, e0143509. [CrossRef] [PubMed]

37. Mitik-Dineva, N.; Wang, J.; Truong, V.K.; Stoddart, P.; Malherbe, F.; Crawford, R.J.; Ivanova, E.P. *Escherichia coli*, pseudomonas aeruginosa, and staphylococcus aureus attachment patterns on glass surfaces with nanoscale roughness. *Curr. Microbiol.* **2009**, *58*, 268–273.

38. Chua, P.-H.; Neoh, K.-G.; Kang, E.-T.; Wang, W. Surface functionalization of titanium with hyaluronic acid/chitosan polyelectrolyte multilayers and RGD for promoting osteoblast functions and inhibiting bacterial adhesion. *Biomaterials* **2008**, *29*, 1412–1421. [CrossRef] [PubMed]

39. Paulone, S.; Ardizzoni, A.; Tavanti, A.; Piccinelli, S.; Rizzato, C.; Lupetti, A.; Colombari, B.; Pericolini, E.; Polonelli, L.; Magliani, W.; et al. The synthetic killer peptide KP impairs Candida albicans biofilm in vitro. *PLoS ONE* **2017**, *13*, e0181278. [CrossRef] [PubMed]

40. Tsui, C.; Kong, E.F.; Jabra-Rizk, M.A. Pathogenesis of Candida albicans biofilm. *Pathog. Dis.* **2016**, *74*, ftw018. [CrossRef] [PubMed]

41. Groza, A.; Ciobanu, C.S.; Popa, C.L.; Iconaru, S.L.; Chapon, P.; Luculescu, C.; Ganciu, M.; Predoi, D. Structural properties and antifungal activity against Candida albicans biofilm of different composite layers based on Ag/Zn doped Hydroxyapatite-polydimethylsiloxanes. *Polymers* **2016**, *8*, 131. [CrossRef]

42. Tite, T.; Popa, A.C.; Balescu, L.M.; Bogdan, I.M.; Pasuk, I.; Ferreira, J.M.F.; Stan, G.E. Cationic substitutions in hydroxyapatite: Current status of the derived biofunctional effects and their in vitro interrogation methods. *Materials* **2018**, *11*, 2081. [CrossRef]

43. Cleare, A.; Pariante, C.M.; Young, A.H.; Anderson, I.M.; Christmas, D.; Cowen, P.J.; Dickens, C.; Ferrier, I.N.; Geddes, J.; Gilbody, S.; et al. Evidence-based guidelines for treating depressive disorders with antidepressants: A revision of the 2008 British Association for Psychopharmacology guidelines. *J. Psychopharmacol.* **2015**, *29*, 459–525. [CrossRef]

44. Cohen, O.; Rais, T.; Lepkifker, E.; Vered, I. Lithium carbonate therapy is not a risk factor for osteoporosis. *Horm. Metab. Res.* **1998**, *30*, 594–597. [CrossRef]

45. Nordenstrom, J.; Elvius, M.; Bagedahl-Strindlund, M.; Zhao, B.; Torring, O. Biochemical hyperparathyroidism and bone-mineral status in patients treated long-term with lithium. *Metabolism* **1994**, *43*, 1563–1567. [CrossRef]

46. Satija, N.K.; Sharma, D.; Afrin, F.; Tripathi, R.P.; Gangenahalli, G. High throughput transcriptome profiling of lithium stimulated human mesenchymal stem cells reveals priming towards osteoblastic lineage. *PLoS ONE* **2013**, *8*, e55769. [CrossRef] [PubMed]

47. Zamani, A.; Omrani, G.R.; Nasab, M.M. Lithium's effect on bone mineral density. *Bone* **2009**, *44*, 331–334. [CrossRef]

48. Yang, M.L.; Li, J.J.; So, K.F.; Chen, J.Y.H.; Cheng, W.S.; Wu, J.; Wang, Z.M.; Gao, F.; Young, W. Efficacy and safety of lithium carbonate treatment of chronic spinal cord injuries: A double-blind, randomized, placebo-controlled clinical trial. *Spinal Cord* **2012**, *50*, 141–146. [CrossRef] [PubMed]

49. Gitlin, M. Lithium side effects and toxicity: Prevalence and management strategies. *Int. J. Bipolar Disord.* **2016**, *4*, 27. [CrossRef] [PubMed]

50. Ott, M.; Stegmayr, B.; Salander, R.E.; Werneke, U. Lithium intoxication: Incidence, clinical course and renal function—A population-based retrospective cohort study. *J. Psychopharmacol.* **2016**, *30*, 1008–1019. [CrossRef]

51. Rybakowski, J.K. Challenging the negative perception of lithium and optimizing its long-term administration. *Front. Mol. Neurosci.* **2018**, *11*, 349. [CrossRef]

52. Post, R.M. The new news about lithium: An underutilized treatment in the United States. *Neuropsychopharmacology* **2018**, *43*, 1174–1179. [CrossRef]

53. Mayer, I.; Berger, U.; Markitziu, A.; Gidalia, I. The uptake of lithium ions by synthetic carbonated hydroxyapatite. *Calcif. Tissue Int.* **1986**, *38*, 293–295. [CrossRef]

54. Koutsoukos, P.G.; Nancollas, G.H. The effect of lithium on the precipitation of hydroxyapatite from aqueous solutions. *Colloids Surf.* **1986**, *17*, 361–370. [CrossRef]

55. Shainberg, A.P.M.; Valério, P.; Zonari, A.; Oktar, F.N.; Ozyegin, L.S.; Graça, M.P.F.; Leite, M.F.; Goes, A.M. Attachment and proliferation of osteoblasts on lithium-hydroxyapatite composites. *Adv. Mater. Sci. Eng.* **2012**, *2012*, 650574. [CrossRef]

56. Gough, J.; Notingher, I.; Hench, L.L. Osteoblast attachment and mineralized nodule formation on rough and smooth 45S5 bioactive glass monoliths. *J. Biomed. Mater. Res. Part A* **2004**, *68*, 640–650. [CrossRef] [PubMed]

57. Wang, Y.; Yang, X.; Gu, Z.; Qin, H.; Li, L.; Liu, J.; Yu, X. In vitro study on the degradation of lithium-doped hydroxyapatite for bone tissue engineering scaffold. *Mater. Sci. Eng. C* **2016**, *66*, 185–192. [CrossRef] [PubMed]

58. Meunier, P.J.; Roux, C.; Seeman, E.; Ortolani, S.; Badurski, J.E.; Spector, T.D.; Cannata, J.; Balogh, A.; Lemmel, E.M.; Pors-Nielsen, S.; et al. The effects of strontium ranelate on the risk of vertebral fracture in women with postmenopausal osteoporosis. *N. Engl. J. Med.* **2004**, *350*, 459–468. [CrossRef] [PubMed]

59. Wexler, E.M.; Geschwind, D.H.; Palmer, T.D. Lithium regulates adult hippocampal progenitor development through canonical Wnt pathway activation. *Mol. Psychiatry* **2008**, *13*, 285–292. [CrossRef] [PubMed]

60. Khorami, M.; Hesaraki, S.; Behnamghader, A.; Nazarian, H.; Shahrabi, S. In vitro bioactivity and biocompatibility of lithium substituted 45S5 bioglass. *Mater. Sci. Eng. C* **2011**, *31*, 1584–1592. [CrossRef]

61. Liu, F.; Zhang, X.; Yu, X.; Xu, Y.; Feng, T.; Ren, D. In vitro study in stimulating the secretion of angiogenic growth factors of strontium-doped calcium polyphosphate for bone tissue engineering. *J. Mater. Sci. Mater. Med.* **2011**, *22*, 683–692. [CrossRef]

62. Tang, G.; Xu, J.; Chen, R.; Qian, Y.; Shen, G. Lithium delivery enhances bone growth during midpalatal expansion. *J. Dent. Res.* **2011**, *90*, 336–340. [CrossRef]

63. Oh, S.H.; Choi, S.Y.; Choi, S.H.; Lee, Y.K.; Kim, K.N. The influence of lithium fluoride on in vitro biocompatibility and bioactivity of calcium aluminate-PMMA composite cement. *J. Mater. Sci. Mater. Med.* **2004**, *15*, 25–33. [CrossRef]

64. Miguez-Pacheco, V.; Büttner, T.; Maçon, A.L.B.; Jones, J.R.; Fey, T.; de Ligny, D.; Greil, P.; Chevalier, J.; Malchere, A.; Boccaccini, A.R. Development and characterization of lithium-releasing silicate bioactive glasses and their scaffolds for bone repair. *J. Non-Cryst. Solids* **2016**, *432*, 65–72. [CrossRef]

65. Keong, L.C.; Halim, A.S. In vitro models in biocompatibility assessment for biomedical-grade chitosan derivatives in wound management. *Int. J. Mol. Sci.* **2009**, *10*, 1300–1313. [CrossRef] [PubMed]

66. Buskermolen, J.K.; Reijnders, C.M.A.; Spiekstra, S.W.; Steinberg, T.; Kleverlaan, C.J.; Feilzer, A.J.; Bakker, A.D.; Gibbs, S. Development of a full-thickness human gingiva equivalent constructed from immortalized keratinocytes and fibroblasts. *Tissue Eng. Part C Methods* **2016**, *22*, 781–791. [CrossRef] [PubMed]

67. Schalock, P.C.; Crawford, G.; Nedorost, S.; Scheinman, P.L.; Atwater, A.R.; Mowad, C.; Brod, B.; Ehrlich, A.; Watsky, K.L.; Sasseville, D.; et al. Patch testing for evaluation of hypersensitivity to implanted metal devices: A perspective from the american contact dermatitis society. *Dermatitis* **2016**, *27*, 241–247. [CrossRef] [PubMed]

68. An, Y.H.; Friedman, R.J. Concise review of mechanisms of bacterial adhesion to biomaterial surfaces. *J. Biomed. Mater. Res. (Appl. Biomater.)* **1998**, *43*, 338–348. [CrossRef]

69. Lieb, J. Lithium and antidepressants: Inhibiting eicosanoids, stimulating immunity, and defeating microorganisms. *Med. Hypotheses* **2002**, *59*, 429–432. [CrossRef]

70. Fabrizi, C.; Pompili, E.; Somma, F.; De Vito, S.; Ciraci, V.; Artico, M.; Lenzi, P.; Fornai, F.; Fumagalli, L. Lithium limits trimethyltin-induced cytotoxicity and proinflammatory response in microglia without affecting the concurrent autophagy impairment. *J. Appl. Toxicol.* **2017**, *37*, 207–213. [CrossRef]

71. Moghanian, A.; Firoozi, S.; Tahriri, M.; Sedghi, A. A comparative study on the in vitro formation of hydroxyapatite, cytotoxicity and antibacterial activity of 58S bioactive glass substituted by Li and Sr. *Mater. Sci. Eng. C Mater. Biol. Appl.* **2018**, *91*, 349–360. [CrossRef]

72. Douglas, L.J. Candida biofilms and their role in infection. *Trends Microbiol.* **2003**, *11*, 30–36. [CrossRef]

73. Sadik, O.; Gheorghe, I.; Chifiriuc, M.C. Virulence and pathogenicity aspects in Candida albicans infections. *Rev. Biol. Biomed. Sci.* **2018**, *1*, 11–16. [CrossRef]

74. Kart, D.; Tavernier, S.; Van Acker, H.; Nelis, H.J.; Coenye, T. Activity of disinfectants against multispecies biofilms formed by Staphylococcus aureus. Candida albicans and Pseudomonas aeruginosa. *Biofouling* **2014**, *30*, 377–383. [CrossRef]

75. Jenkinson, H.F.; Lamont, R.J. Oral microbial communities in sickness and in health. *Trend. Microbiol.* **2005**, *13*, 589–595. [CrossRef] [PubMed]

76. Harriott, M.M.; Noverr, M.C. Candida albicans and Staphylococcus aureus form polymicrobial biofilms: Effects on antimicrobial resistance. *Antimicrob. Agents Chemother.* **2009**, *53*, 3914–3922. [CrossRef] [PubMed]

77. D'Elia, N.L.; Gravina, N.; Ruso, J.M.; Marco-Brown, J.L.; Sieben, J.M.; Messina, P.V. Albumin-mediated deposition of bone-like apatite onto nano-sized surfaces: Effect of surface reactivity and interfacial hydration. *J. Colloid Interface Sci.* **2017**, *494*, 345–354. [CrossRef] [PubMed]

78. Giraldez, M.J.; Resua, C.G.; Lira, M.; Oliveira, M.E.C.R.; Magariños, B.; Toranzo, A.E.; Yebra-Pimentel, E. Contact lens hydrophobicity and roughness effects on bacterial adhesion. *Optom. Vis. Sci.* **2010**, *87*, E426–E431. [CrossRef]

79. Tamburic, S.D.; Vuleta, G.M.; Ognjanovic, J.M. In vitro release of calcium and hydroxyl ions from two types of calcium hydroxide preparations. *Int. Endod. J.* **1993**, *26*, 125–130. [CrossRef]

80. Absolom, D.R.; Lamberti, F.V.; Policova, Z.; Zingg, W.; van Oss, C.J.; Neumann, A.W. Surface thermodynamics of bacterial adhesion. *Appl. Environ. Microb.* **1983**, *46*, 90–97.

81. Anselme, K.; Davidson, P.; Popa, A.; Giazzon, M.; Liley, M.; Ploux, L. The interaction of cells and bacteria with surfaces structured at the nanometre scale. *Acta Biomater.* **2010**, *6*, 3824–3846. [CrossRef]

82. Ionescu, A.; Wutscher, E.; Brambilla, E.; Schneider-Feyrer, S.; Giessibl, F.J.; Hahnel, S. Influence of surface properties of resin-based composites on in vitro streptococcus mutans biofilm development. *Eur. J. Oral Sci.* **2012**, *120*, 458–465. [CrossRef]

83. Quirynen, M.; Bollen, C.M.; Papaioannou, W.; Van Eldere, J.; van Steenberghe, D. The influence of titanium abutment surface roughness on plaque accumulation and gingivitis: Short-term observations. *Int. J. Oral Maxillofac. Implant.* **1996**, *11*, 169–178.

84. Hansson, K.N.; Hansson, S. Skewness and kurtosis: Important parameters in the characterization of dental implant surface roughness—A computer simulation. *ISRN Mater. Sci.* **2011**, *2011*, 305312. [CrossRef]

85. Cheng, T.; Chen, Y.; Nie, X. Insertion torques influenced by bone density and surface roughness of HA–TiO$_2$ coatings. *Thin Solid Films* **2013**, *549*, 123–130. [CrossRef]

86. Han, L.; Wang, M.; Sun, H.; Li, P.; Wang, K.; Ren, F.; Lu, X. Porous titanium scaffolds with self-assembled micro/nano hierarchical structure for dual functions of bone regeneration and anti-infection. *J. Biomed. Mater. Res. A* **2017**, *105*, 3482–3492. [CrossRef] [PubMed]

87. Karr, J.C.; Lauretta, J. In vitro activity of calcium sulfate and hydroxyapatite antifungal disks loaded with amphotericin B or voriconazole in consideration for adjunctive osteomyelitis management. *J. Am. Podiatr. Med. Assoc.* **2015**, *105*, 104–110. [CrossRef] [PubMed]

88. Khalid, A.Q.; AlJohny, B.O.; Wainwright, M. Antibacterial effects of pure metals on clinically important bacteria growing in planktonic cultures and biofilms. *Afr. J. Microbiol. Res.* **2014**, *8*, 1080–1088.

89. Harrison, J.C.; Zyla, T.R.; Bardes, E.S.; Lew, D.J. Stress-specific activation mechanisms for the "cell integrity" MAPK pathway. *J. Biol. Chem.* **2004**, *279*, 2616–2622.

Glancing Angle Deposition of Zn-Doped Calcium Phosphate Coatings by RF Magnetron Sputtering

Konstantin A. Prosolov [1,2,*], Olga A. Belyavskaya [1], Juergen Linders [3], Kateryna Loza [4], Oleg Prymak [4], Christian Mayer [3], Julietta V. Rau [5], Matthias Epple [4] and Yurii P. Sharkeev [1,2]

[1] Institute of Strength Physics and Materials Science of SB RAS, 634055 Tomsk, Russia; obel@ispms.tsc.ru (O.A.B.); sharkeev@ispms.tsc.ru (Y.P.S.)

[2] Research School of High-Energy Physics, National Research Tomsk Polytechnic University, 634050 Tomsk, Russia

[3] Physical Chemistry and Center for Nanointegration Duisburg-Essen (CeNIDE), University of Duisburg-Essen, 45117 Essen, Germany; juergen.linders@uni-due.de (J.L.); christian.mayer@uni-due.de (C.M.)

[4] Inorganic Chemistry and Center for Nanointegration Duisburg-Essen (CeNIDE), University of Duisburg-Essen, 45117 Essen, Germany; kateryna.loza@uni-due.de (K.L.); oleg.prymak@uni-due.de (O.P.); matthias.epple@uni-due.de (M.E.)

[5] Istituto di Struttura della Materia, Consiglio Nazionale delle Ricerche (ISM-CNR), 00133 Roma, Italy; giulietta.rau@ism.cnr.it

* Correspondence: konstprosolov@gmail.com; Tel.: +7-961-888-58-33

Abstract: Zn-substituted hydroxyapatite with antibacterial effect was used in radiofrequency (RF) magnetron deposition of calcium phosphate coating onto Ti- and Si-inclined substrates. The development of surface nanopatterns for direct bacteria killing is a growing area of research. Here, we combined two approaches for possible synergetic antibacterial effect by manufacturing a patterned surface of Zn-doped calcium phosphate using glancing angle deposition (GLAD) technique. A significant change in the coating morphology was revealed with a substrate tilt angle of 80°. It was shown that an increase in the coating crystallinity for samples deposited at a tilt angle of 80° corresponds to the formation of crystallites in the bulk structure of the thin film. The variation in the coating thickness, uniformity, and influence of sputtered species energy on Si substrates was analyzed. Coatings deposited on tilted samples exhibit higher scratch resistance. The coating micro- and nano-roughness and overall morphology depended on the tilt angle and differently affected the rough Ti and smooth Si surfaces. GLAD of complex calcium phosphate material can lead to the growth of thin films with significantly changed morphological features and can be utilized to create self-organized nanostructures on various types of surfaces.

Keywords: RF magnetron sputtering; plasma-assisted deposition; biocompatibility; GLAD; ion-substituted apatites

1. Introduction

The demand for implants that can efficiently conduct bone defect regeneration increases significantly with the aging population [1]. It is known that the bioinert metals that are used in implantology and orthopedics do not provide the desired bioactivity and osteoconductivity; therefore, the surface of such medical devices is usually modified with bioactive coatings [2]. Moreover, the demand for antibacterial or bactericidal surfaces and coatings has increased steadily in recent years. It has been noted that the modern approach to surface modification should take into account both coating functions: osteoconduction properties and antibacterial effect [3]. From that perspective,

substituted hydroxyapatites (HAs) are one of the most promising materials in this area of research. It has been shown that the easiness of atomic doping or substitution in HA reveals its potential to be used in various clinical cases [4–6]. Most importantly, it has been shown that inorganic antibacterial metallic ions (e.g., Ag, Cu, Zn, Sr) can be introduced into the HA lattice and improve its antibacterial properties [7–14]. However, there is a physical approach to antibacterial surface production. It has been shown that the creation of nanopatterns is a powerful tool for directing stem cell fate. Another advantage is that high aspect ratio nanopatterns are capable of killing bacteria and preventing biofilm formation [15].

Modern approaches to healthcare are aiming to produce implants with biomimetic properties [16]. These properties are crucial to ensuring a desirable biological response to the newly implanted material, in such a manner that the cells, which are adhered to the surface of such scaffolds, can function in a way that is similar to physiological conditions. From that point of view, the formation of a coating that consists of different types of surface gradient structures and with variations in the level of roughness on the submicro- and nanoscale could be of significant interest for biomimetic purposes [17,18]. The possibility of manipulating nanotopography has attracted much attention in recent years [19–22]. This has fostered the development of film deposition techniques aimed at enhancing these morphological characteristics.

In the field of optics and microelectronics, physical vapor deposition (PVD) of thin films, allowing the deposition of porous and/or columnar-like structured coatings, has been available for some years. For this purpose, the use of an oblique angle geometrical configuration—or as it is also known, glancing angle deposition (GLAD) method—is frequently exploited [23–27].

The GLAD configuration has emerged as a promising tool for the deposition of nanostructured thin films. This method has mostly been applied in the field of metallic coatings or dielectric coatings for optical systems, and the use of such technology in the field of biomaterials started recently [28]. Such coatings are usually represented by inclined columnar-like structures with variations at the nano-roughness level and a direction of growth allowing for the deposition of patterned structures with different shapes and sizes. GLAD has a wide range of applications in various fields, such as sensors [29], optics [30,31], or solar cells [32]. This type of coatings has attracted attention due to the anisotropic nature of the formed films, their peculiar mechanical properties, and the possibility of controlling the level of porosity [33] and roughness [34]. Most researchers who have utilized the GLAD method have used line-of-sight methods of deposition, such as, for example, thermal evaporation. However, the effect of self-shadowing is applicable in many PVD techniques, such as magnetron sputtering.

An emerging method for bioactive coating deposition in the field of PVD is radiofrequency (RF) magnetron sputtering. Magnetron sputtering is widely used in the formation of coatings for various applications. The continuous interest of scientists in this method is due to the possibility of modifying the coating structure and its physicochemical properties by varying the deposition parameters [2]. There is a significant interest in radiofrequency (RF) magnetron sputtering of bioactive calcium phosphate (CaP) thin films [35,36]. This method allows for the deposition of CaP coatings with a high level of adhesion to the substrate. Moreover, RF magnetron sputtering is well known as a highly controllable deposition method. However, to date, a feasible method of calcium phosphate coating deposition in GLAD geometry via RF magnetron sputtering has not yet been reported.

Here, we aimed to develop a method for depositing thin Zn-substituted HA (Zn-HA)-based coatings that are formed by hierarchical gradient surface features with the use of GLAD geometry. This method allows us to manipulate the coating roughness on the submicron and nanoscale level and pursue the possible synergetic antibacterial effect of a nanopattern and the antibacterial activity of Zn.

2. Materials and Methods

Commercially pure titanium samples (99.58 Ti, 0.12 O, 0.18 Fe, 0.07 C, 0.04 N, and 0.01 H wt %) of $10 \times 10 \times 1$ mm^3 size provided by "VSPO-AVISMA" (Perm, Russia) were used as substrates.

The samples were sequentially polished by silicon carbide paper of 120, 480, 600, and 1200 grit. Prior to deposition, the substrates were cleaned in an ultrasonic bath of distilled water for 10 min. Furthermore, commercially available Si wafers (1 0 0) provided by "ELMA" (Zelenograd, Russia) were used as substrates in all the deposition runs.

In Figure 1, the deposition process is schematically shown. The samples were mounted on the custom-made sample holder at different angles to the flux of the sputtered material.
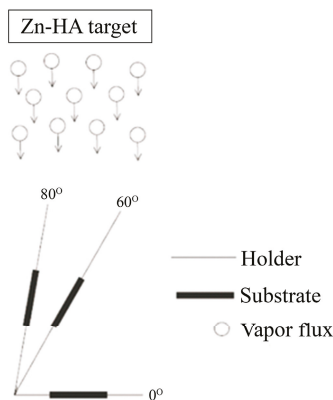
Figure 1. Schematic image of the deposition process of the Ti and Si samples with varying particle incidence angles at 0°, 60°, and 80° during the radiofrequency (RF) magneton sputtering of a Zn-substituted hydroxyapatite (Zn-HA) target with the arrows indicating the direction of the flux.

The sample holder allows for the simultaneous placing of substrates at 0°, 60°, or 80° to ensure the same sputtering conditions for all the deposited samples.

The sputtering target was Zn-substituted hydroxyapatite. This material was chosen because hydroxyapatite resembles the mineral fraction of bone and is used for many implant coatings, while the addition of Zn can provide faster bone growth together with an antibacterial effect [37]. A Zn-HA powder was prepared by mechanochemical synthesis at the Institute of Chemistry and Mechanochemistry, Russian Academy of Sciences, Novosibirsk, Russia. The mechanochemical synthesis was carried out according to the reaction:

$$6CaHPO_4 + (4 - x)CaO + xZnO = Ca_{(10-x)}Zn_x(PO_4)_6(OH)_2 + 2H_2O, \text{ where } x = 0.4.$$
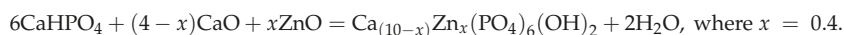
The prepared powder was used as a precursor for the preparation of a target for sputtering. Its detailed characterization can be found in our previous report [38]. The powder was pressed and then sintered in air at 1100 °C for 1 h. The chemical composition of the powder and the target was confirmed by X-ray powder diffraction (XRD) and Fourier transform infrared spectroscopy (FTIR) [39].

To identify the optimal deposition parameters for our experiment, we reviewed the literature dealing with GLAD, considering the substrate material, sputtered material, deposition parameters, and type of formed coatings. In Table 1, the deposition parameters for GLAD of various materials and their properties are summarized.

Table 1. Deposition parameters and coating properties for glancing angle deposition (GLAD) with magnetron sputtering from the literature.

Ref.	Method	Aim of Research	Target	Substrate	Deposition Parameters	Result
[23]	DC magnetron sputtering	The expansion of the well-known model of the Thornton spatial zone, including the inclination angle of the substrate as an additional degree of freedom	Ti	Si (100)	$L = 22$ cm $t = 90$–200 min $P = 0.15$–1.5 Pa $W = 300$ W	For $\alpha = 70°$, a columnar morphology was formed consisting of vertically aligned and well-separated columns with diameters ranging from 50 to 100 nm. For angles of $\alpha = 80°$ and $\alpha = 85°$, the structure was rather similar.
[40]	DC magnetron sputtering	The effect of changing various parameters on the roughness	Mo and Ti/C:H	Silicon and Glass	$L = 7$–10 cm $P = 0.08; 0.16$ Pa	The manipulation of the substrate led to the formation of a zigzag columnar structure. The films prepared in the range of 40–85° showed an increase in the RMS value of roughness from 7 to 55 nm.
[41]	DC magnetron sputtering	Influence on structural and optical properties	ZnO	Si (100)	$L = 15$ cm $t = 180$ min $P = 0.64$ Pa $W = 400$ W	The typical columnar structure was inclined and compact. SEM images showed that the typical columnar structure was inclined, and the column inclination angle was changed from 0 to 34°. From XRD analysis, it was shown that the strains in the ZnO films decreased with the substrate tilt angle.
[42]	Reactive magnetron sputtering	Effect on the refractive index	ZnO	Si (100)	$L = 14; 28.5$ cm $t = 30$ min $P = 0.3$ Pa $W = 100$ W	The films were porous and of an inclined columnar structure, with columns tilting in the direction of the incident flux.
[43]	RF magnetron sputtering	Structural, optical, and electrical properties of zinc oxide (AZO) films doped with aluminum on Si substrate	AZO (aluminum-doped zinc oxide)	Si (100)	$L = 15$ cm $P = 0.67$ Pa $W = 50$–150 W	The deposited AZO films had nanocolumnar structures. In tilted angle sputtering, the nanocolumns were tilted away from the surface normal to the incident AZO flux direction. When the substrate was not rotated, the nanocolumn inclination increased with apparently distinguishable grain boundaries as the tilted angle became larger.
[44]	DC magnetron sputtering	Study of the effect of gas pressure (Ar) on the columnar growth of gold nanostructures, and a comparison of morphology with theoretical modeling.	Au	Si (100)	$L = 19$ cm $t = 30$ min $P = 0.15$–0.4 Pa $W = 100$ W	At low pressures, a ballistic deposition regime dominated, yielding high directional atoms that form tilted nanocolumns. Higher pressure led to a diffusive regime, which gave rise to vertical columnar growth.
[24]	DC magnetron sputtering	To increase the photocatalytic activity	Ti	Si	$L = 11$ cm $P = 0.11$ Pa $W = 200$ W	TiO_2 samples had a discrete columnar nanostructure and efficiently performed a photocatalytic decolorization under UV radiation.

Table 1. *Cont.*

Ref.	Method	Aim of Research	Target	Substrate	Deposition Parameters	Result
[25]	Reactive magnetron sputtering	The influence of collimators on the growth of highly porous structures	Ti	Si and Quartz	$L = 7; 10$ cm $t = 210; 360$ min $P = 0.2; 0.5; 0.8$ Pa	Particle collimators allowed for the growth of highly porous nanocolumnar thin films independently from the thermal degree of the sputtered particles. Using collimators, similar well-defined tilted nanocolumnar structures were prepared independently of the plasma pressure during the deposition.
[45]	DC magnetron sputtering	Identification of the presence of critical zones in certain properties of inclined columnar coatings	Al, Ti, Cr	Si (100)	$L = 10.5$ cm $t = 16; 19; 35$ min $P = 0.09$ Pa $W = 1500$ W	Chromium coatings presented elongated columns perpendicular to the main direction of the incident flux. Titanium coatings had a dense nodular morphology. At an angle of 85°, the aluminum coatings had a rough surface with crystallite columns randomly distributed and oriented towards the target. The high aluminum adatoms mobility explained the dense film at normal deposition and the formation of large crystals with high porosity at an oblique angle. The chromium films still present elongated columns perpendicular to the main direction of the incident flux.
[46]	RF magnetron sputtering	Optical and the structural properties	ZnO	Si (100)	$L = 10$ cm $t = 16; 19; 35$ min $P = 0.67$ Pa $W = 80$ W	The GLAD ZnO films were mixtures of columnar structure and pores. The highly-oriented columnar structure of slanted columns indicated that the GLAD ZnO films were anisotropic with the long axis parallel to the columnar growth direction. This anisotropic structure will introduce an anisotropic dependence into the optical, electrical, thermal, and magnetic properties of the films.

L–target–substrate distance; *t*–deposition time; *P*–pressure; *W*–power.

Even though most GLADs were performed at target-to-substrate distances larger than 70 mm, we decided to perform deposition at a distance of 45 mm, as it is consistent with most published research papers dealing with sputtering of CaPs [47–49] and ensures that the particle-free mean path is significantly higher than the target-to-substrate distance. Moreover, it is known that ZnO and hydroxyapatite share the same type of lattice structure (hexagonal system). Taking into account the fact that there is a correlation between the lattice type of sputtered material and the type of the formed coating structure, we hypothesized that using similar deposition parameters to those used for ZnO would result in the formation of Zn-doped calcium phosphate nanocolumns [42,46,50].

A vacuum installation with a planar magnetron operating at a frequency of 13.56 MHz (TPU, Tomsk, Russia) was utilized for GLAD. The high-quality Zn-HA target was used as the cathode of the magnetron. The sputtering power density was set to 3.15 W/cm^2. Prior to the deposition, the system was pumped to a base pressure of 5×10^{-6} Torr, and then, Ar gas was passed through at a controlled rate to maintain the pressure needed for the experimental deposition. The deposition time was set to 3 h, and the target-to-substrate distance was 45 mm. It is important to note that the target-to-substrate distance varied for tilted samples due to the inclination; therefore, the upper part of the sample was as close to the surface of the magnetron as 35 mm. The samples were deposited at a working gas pressure of 0.8 mTorr at a gas flow of 3.7 sccm. Each set of samples with angles varied from 0 to 80° was deposited in a single run.

The thicknesses of the deposited films were measured using spectroscopic ellipsometry with an ELLIPS-1891 SAG setup (Rzhanov Institute of Semiconductors Physics of SB RAS, Novosibirks, Russia). The surface morphology and composition of the coatings were examined with scanning electron microscopy using an ESEM Quanta 400 FEG scanning electron microscope (SEM, FEI Company, Hillsboro, OR, USA) operating in a high vacuum. The samples were coated with gold–palladium for 15 s before the SEM, which was equipped with energy-dispersive X-ray spectroscopy (EDX; Genesis 4000, SUTW-Si(Li)detector, EDAX, Inc., Mahwah, NJ, USA) and was operating in a high vacuum study in such a way that no alteration of the surface morphology was induced. The estimated thickness of the deposited Au–Pd layer was 4–5 nm. The acceleration voltage for the SEM was 20 kV. To determine the level of crystallinity of the studied samples and estimate the crystallite size of the deposited thin CaP coatings, a Panalytical Empyrean X-ray diffractometer with a Cu Kα radiation source (λ = 1.54 Å; 40 kV and 40 mA) was used. The coatings were investigated by grazing incidence X-ray diffraction (GIXRD) with an incident beam angle of Ψ = 1.0° (with respect to the sample surface) and at 2θ range from 5° to 90° with a step size of 0.05°. For qualitative phase analysis with the Bruker software Diffrac.Suite EVA 4.2.2, the patterns of hydroxyapatite (#09-0432) and titanium (#44-1294) from the ICDD database were used as a reference. After the instrumental correction derived from a standard powder sample LaB6 from the NIST ([51]; a(LaB6) = 4.15689 Å), quantitative Rietveld analysis for the calculation of the lattice parameters and the crystallite sizes was performed with the Bruker software TOPAS 5.0. For the morphology visualization and calculation of the surface roughness level of the samples, a JPK NanoWizard Atomic Force microscope (AFM, JPK, Berlin, Germany) was used. The coating-to-substrate adhesion evaluation was carried out with the scratch-test method on a CSM Macro Scratch Tester Revetest (CSM Instruments, Needham Heights, MA, USA) with an indenter of 20 μm in radius. The maximum indentation load was 10 N. The scratch length was set to 5 mm. In order to obtain statistically meaningful data, each measurement was repeated at least three times per sample.

3. Results and Discussion

3.1. Effect of GLAD on Coating Thickness and Its Uniformity along the Substrate Surface

The key for variation in the coating surface topography when the GLAD method is used lies in the self-shadowing effect [23]. During the film growth, adatoms migrate to the substrate and encounter the surface in a way that causes peak and valley regions to grow. Due to the inclination of the substrate,

the peaks receive more atoms compared with the valleys. As the peaks grow higher, a shadow region, which receives a lower number of atoms, is formed behind them. Consequently, the GLAD coatings have a preferential direction of growth and may even be porous. Also, in most of the reports dealing with GLAD, an increase in root-mean-square (RMS) surface roughness is usually observed when compared with the normal degree deposition [25,26,29].

Even though research on GLAD coatings is evolving extensively, there are few reports on the coating uniformity of the substrate surface and the variation in its thickness. Here, we show the thickness variation on the Si substrates measured by ellipsometry. In Figure 2, the coating thickness of the substrates is placed in parallel to the target of the magnetron (0°), and inclination angles of 60° and 80° are presented.
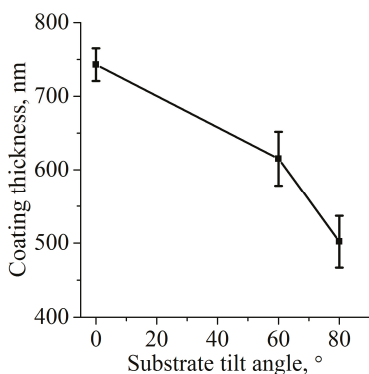

Figure 2. Plot of the coating thickness against the substrate tilt angle.

With the increase in the inclination angle, the coating thickness decreases gradually. We believe that this effect is associated with substrate re-sputtering. It is known that when the substrate is in close proximity to the plasma source, impinging energetic ions of Ar^+ and O^- induce re-sputtering of the coating from the substrate [28]. Moreover, the deposition parameters were chosen in such a way that the mean free path of the sputtered atoms was as large as possible while maintaining a relatively high power density. In this way, the kinetic energy of the sputtered material and the generated ions is close to the original level due to the negligible number of collisions they experience. It not only enables better adatom mobility, but also higher substrate heating and hence higher re-sputtering. In addition, a shorter target–substrate distance will increase the rate of deposition but at the expense of film uniformity [29]. This was the case for the CaP coatings deposited in our experiments. For the samples deposited at less than an inclination angle of 80°, the coating thickness was measured for the upper part (closer to the magnetron source) and the lower part of the sample. Ellipsometry showed that the coating thickness was inhomogeneous along the sample, and the thickness difference between the upper and lower part of the coating was up to 110 ± 25 nm for some samples. Interestingly, the closer the placement of the sample to the plasma source, the thinner the film deposited. We believe that this effect is due to substrate re-sputtering and energetic ions bombardment.

### 3.2. Effect of GLAD on Coating Topography and Roughness

In Figure 3, SEM images show the topography of CaP coatings deposited at different angles of 0°, 60°, and 80°. The coatings deposited without tilting (0°) show globular-like surface features. The samples inclined at 60° during the deposition decreased in size, and the surface structure elements changed their shape. The surface grains were orientated along the incidence direction of the sputtered particles independent of working gas pressure. This effect was even more pronounced for the samples deposited at a tilt angle of 80°. An alteration in the working gas pressure led to a reduction in surface

elements sizes. When the deposition process was performed at a lower working pressure (here: 0.8 mTorr), surface elements tended to be more homogeneously spread on the surface.

(a)   (b)

(c)
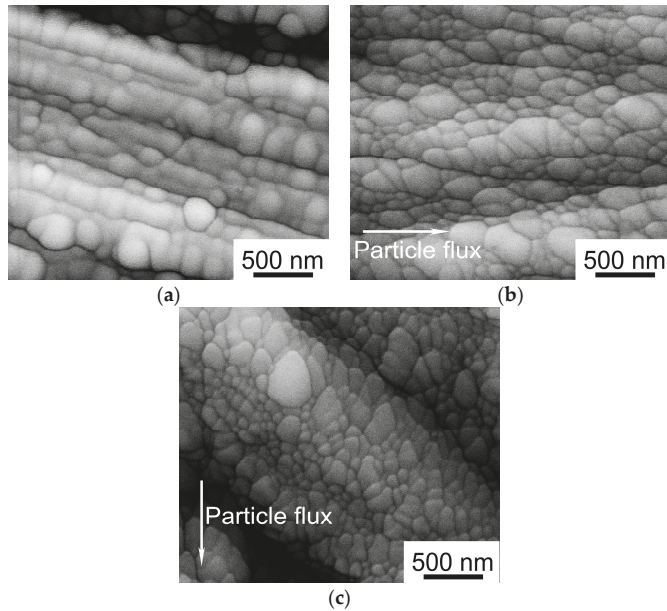
Figure 3. Calcium phosphate (CaP) coatings deposited on Ti at a working gas pressure of 0.8 mTorr under tilt angles of 0° (**a**), 60° (**b**), and 80° (**c**).

In Figure 4, the dispersion of the size of the surface features for the cases of GLAD at 0° and 80° is presented. The mean grain size of the coating decreased from 210 to 190 nm with the increasing tilt angle.

(a)   (b)
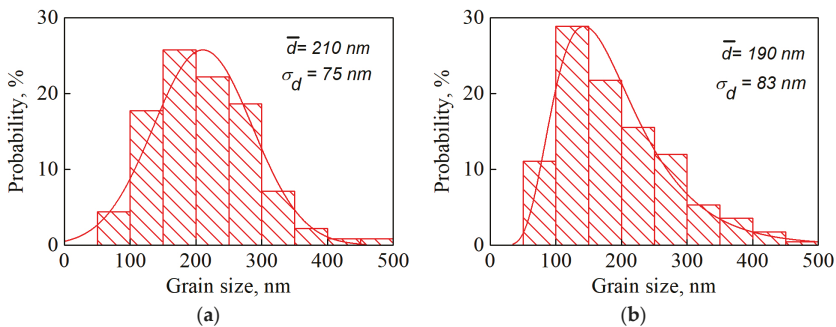
Figure 4. Dispersion of coating surface grain sizes for samples deposited under tilt angles of 0° (**a**) and 80° (**b**) at a working gas pressure of 0.8 mTorr.

It is well known that the coating deposited by magnetron sputtering insignificantly changes the surface topography [52]. In most cases, the deposited coating repeats the topography of the initial substrate surface. Even after polishing, the Ti surface still had some marks after machining that could potentially disturb or alter the growth of the surface coating's elements. Therefore, polished Si samples were used alongside the Ti substrates in all the deposition runs, as they do not provide additional ambiguity in the understanding of coating growth on a non-smooth surface topography.

Figure 5 shows SEM images of CaP on the Si substrate deposited at 0°, 60°, and 80° tilt angles and at a pressure of 0.8 mTorr. This was the pressure that promoted the dispersion of the most homogeneous surface features and minimized the particle collision during deposition most effectively. Interestingly, the deposition of the CaP coating on polished Si resulted in the appearance of surface grains in smaller quantities. Apparently, the Ti surface with defects, cavities, and an overall rougher topography induced more nucleation sites for subsequent grain formation compared with Si.
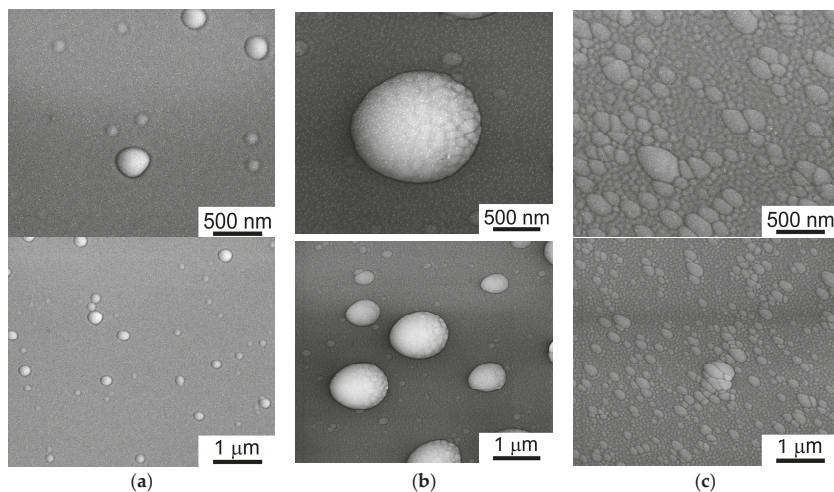

Figure 5. CaP coatings deposited on Si at a working gas pressure of 0.8 mTorr under tilt angles of 0° (**a**), 60° (**b**), or 80° (**c**) on the Si substrates.

Even though the initial surface of the Si samples was smooth and without pronounced defects or impurities, grain nucleation still took place in regions that were energetically favorable. Even though the surface of coated Si deposited at the normal incidence was rather smooth, it was possible to find rare globular-like shaped grains on its surface. In Figure 5, some of the grains that were found on the smooth surface of the sample deposited without tilting are shown. For samples deposited at an angle of 60°, the concentration of surface elements increased together with their size. Moreover, in some cases, grains were comprised of smaller structural elements and had complex topography. We assume that this could be a transition state before the grains coalescence into bigger surface structural elements. With an increase in tilt angle to 80°, the effect of self-shadowing became more pronounced and resulted in the appearance of surface grains of different sizes. In this case, the surface grains covered the whole surface of the sample and left no place for a region without complex topography. From this, we can conclude that an RF magnetron GLAD method for CaP can have a topographical effect on smooth and rough surfaces of different materials. Álvarez et al. [23] performed mathematical modeling with experimental validation for Ti thin films deposited by RF magnetron sputtering. The proposed model correlated well with the experimental results. It was solely based on ballistic deposition phenomena, indicating that the simulations realistically reproduced the competitive growth mechanism involved in GLAD experiments. However, a modeling of a far more complex structure (hydroxyapatite) still needs to be performed.

Figure 6 shows a cross-section SEM of thin films deposited under tilt angles of 0° (a) and 80° (b) at 100,000× magnification and films under tilt angles of 0° (c) and 80° (d) at 200,000× magnification on Si substrates. For the untilted samples, the cross section is presented by an amorphous calcium phosphate layer without any visible structural features. In contrast, coatings deposited at 80° inclination show an anisotropic, elongated type of inner structure orientated towards the particle source represented by small crystallites. EDX data obtained from both types of samples showed that the Ca/P ratio equals

1.8–1.9, while the content of Zn does not exceed 1 at.%. It is worth noting that the inner structure corresponds to the surface topography of the samples. In that way, the surface of the coatings deposited on the untilted samples is smooth with a few globular-like features (Figure 5a), and a cross-section of this sample (Figure 6a,c) is represented by smooth featureless layer. In the case of 80°, tilting small crystallites do not only belong to the surface (Figure 5b) but are also visible throughout the coatings' inner structure (Figure 6b,c). Moreover, predominant growth towards the particle flux is detectable, and the angle of structural inclination β is calculated to be in the range of 60°–65°. As it is mentioned in the literature [53], the tilt angle is always smaller than the vapor incidence angle (β < θ). In the paper by Grüner et al. [53], it is stated that, as a first order approximation, a linear relationship between the tilt angle and the angle of incidence β $\cong$ 0.71θ can be obtained for GLAD of silicon. A similar, linear behavior can be found for obliquely deposited germanium and molybdenum thin films covering a wide range of melting points. However, we could speculate that, in our case, this coefficient is going to be in a range of 0.75–0.8 according to the SEM measurements. Taking into account the fact that the melting point of silicon (1414 °C) is relatively close to the melting point of hydroxyapatite (1570 °C) [54], this coefficient could indicate the differences in the lattices of the sputtered materials. Most published papers dealing with GLAD focused on materials with relatively simple oxide or monocrystal types of structures with a higher level of symmetry when compared with calcium phosphates. In turn, during the sputtering of CaP, various sputtered species travel to the substrate and are later are involved in the condensation step. Therefore, we assume that this fact is responsible for the difference in the calculated coefficient and overall difference in the thin film structure.
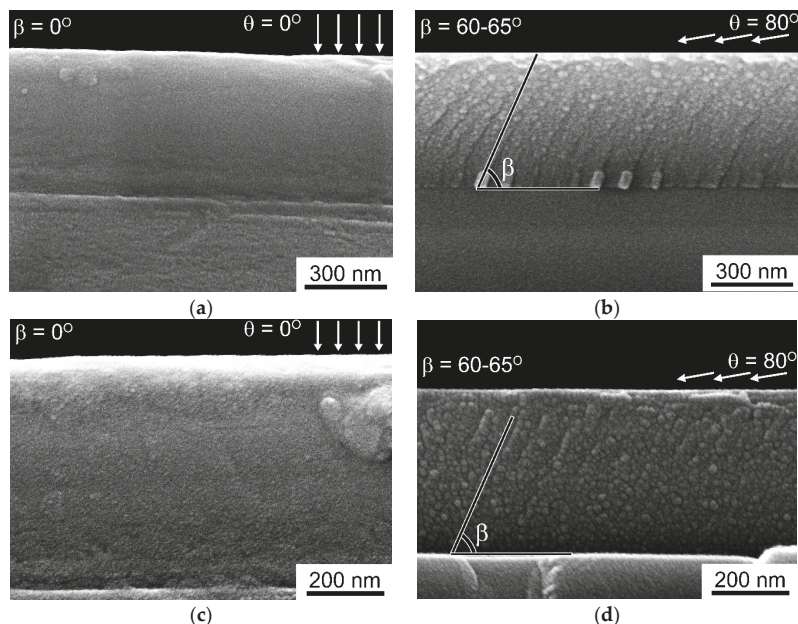
Figure 6. SEM cross-section images of obliquely deposited Zn-doped CaP thin films deposited on Si under tilt angles of 0° (**a**) and 80° (**b**) at 100,000× magnification and films under tilt angles of 0° (**c**) and 80° (**d**) at 200,000× magnification on Si substrates, demonstrating significant changes in the film morphology. The arrows indicate the angle of incidence θ. The columns are tilted by angle β.
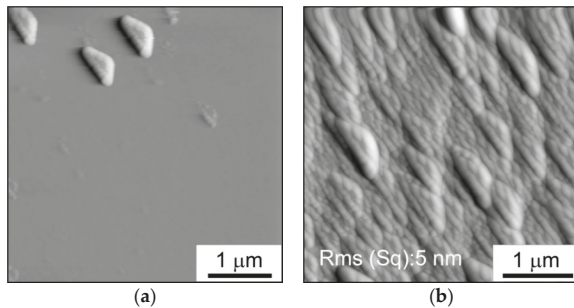
In Figure 7, an AFM visualization of CaP coatings deposited on Ti with and without tilting is shown. According to Sarkar and Pradhan [55], the RMS values of film roughness increase with the increasing oblique angle of deposition. However, in our case, the RMS for tilted samples were smaller than for samples without inclination: 17 nm for the 80° sample and 28 nm for the sample

without inclination (0°), respectively. We believe that this is because small surface grains, which homogeneously cover the initial rough Ti surface, are reducing the RMS compared with the sample without any inclination. In the case of the normal incidence of sputtered particles, round-shaped grains are formed on top of the Ti surface, artificially increasing the RMS. AFM measurements allow us to have a 3D image of the surface topography and reveal an out-of-plane growth of surface grains (Figure 7c).


RMS (Sq): 29 nm   500 nm

(**a**)

RMS (Sq): 18 nm   500 nm

(**b**)

y:0.65μm

x:0.65 μm

(**c**)
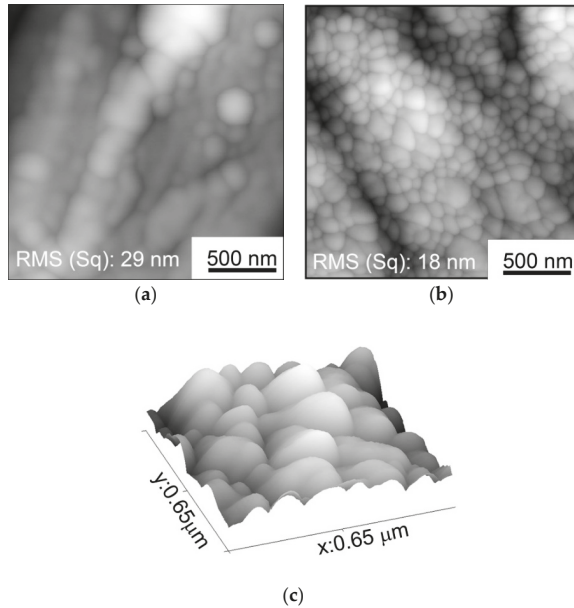
Figure 7. CaP coatings deposited on Ti at a working gas pressure of 0.8 mTorr under tilt angles of 0° (**a**) and 80° (**b**) and three-dimensional (3D) visualization of coating deposited under 80° showing the out-of-plane growth of grains (**c**).

In order to exclude the impact of the substrates' surface topography on the coating's roughness, AFM measurements were performed for polished Si samples as well (Figure 8). For the samples deposited at the normal incidence, it was almost impossible to detect distinct surface features. In an untilted sample, some structural elements were found. Surface elements are represented in the form of pyramids, which possibly represent artifacts rather than the actual shape. Nevertheless, the RMS value for the untilted sample was very low (down to 200 pm).


1 μm

(**a**)

Rms (Sq):5 nm   1 μm

(**b**)

Figure 8. *Cont.*

(**c**)
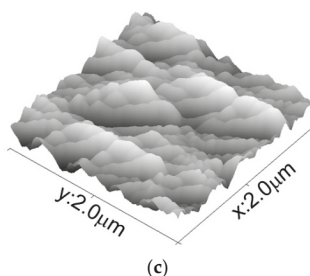
Figure 8. CaP coatings deposited on Si at a working gas pressure of 0.8 mTorr under inclination angles of 0° (**a**) and 80° (**b**) and 3D visualization of coating deposited under 80° (**c**).

However, the RMS of the GLAD sample was 5 nm, i.e., was significantly higher than that of the untilted sample. Moreover, these results are in good correlation with GLAD-related research, as RMS values are usually found to increase with the increasing oblique angle of deposition [24]. Such changes in morphology may lead to a significant decrease in the values of the contact angle of the coatings.

3.3. Effect of GLAD on Coating Crystallinity and Scratch Resistance

It is not rare that CaP coatings deposited by RF magnetron sputtering have a low level of crystallinity [56]. Frequently, CaP-deposited coatings are annealed in order to reveal peaks from crystalline Zn-HA [7]. However, in our case, we decided to perform a GIXRD of the untreated sample, as the temperature treatment will significantly change the internal structure of the CaP. Figure 9 shows representative X-ray powder diffraction patterns of the coatings deposited on Ti substrates at oblique angles of 0° and 80°. The GIXRD measurements indicate a formation of mostly amorphous CaP coating with a broad halo at $2\theta = 30°$, which can be attributed to hydroxyapatite with a crystallite size 2(1) nm as determined by the Rietveld refinement. The slightly increased intensity of the amorphous halo of the hydroxyapatite coating deposited under 80° (Figure 9b) compared with the hydroxyapatite coating under 0° might be caused by the increased crystallinity of the HA coating. The calculated lattice parameters of Ti ($a = 2.951$ and $c = 4.685$ Å) agree well with the ICDD database, confirming that the RF magnetron sputtering does not change the structure of the metallic substrate (as expected). Only a small difference between the Ti substrates was observed in the intensity of diffraction peak (002) at $2\theta = 38.4°$, which was caused by the typical rolling texture in hexagonal metals, including Ti [57–59]. It is worth noting, that the increased crystallinity of the samples inclined to 80° correlates with the formation of small-sized crystallites on the surface and in the cross-section structure of the GLAD samples (Figure 6b,d).


(**a**)
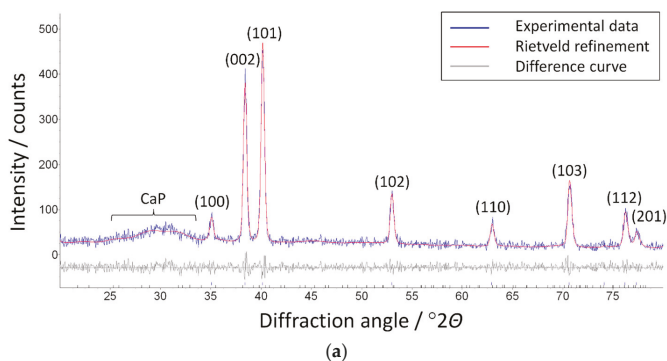
Figure 9. *Cont.*
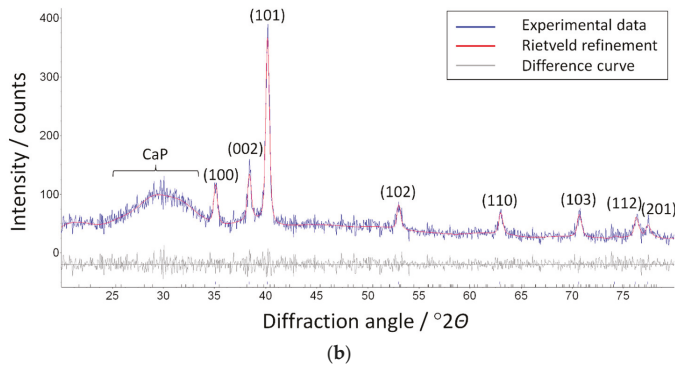
Figure 9. Representative X-ray powder diffractograms (with Rietveld refinement) of CaP coatings deposited on the Ti substrate perpendicular to the flux at 0° (**a**) and inclined at 80° (**b**). The diffraction peaks of HA and Ti (with Miller indices) are shown.

In Figure 10, the results of CaP coating scratching are shown. Thin film adherence is one of the most important aspects when dealing with physical vapor deposition methods. L_c (critical load) is a function of coating–substrate adhesion, but also involves other parameters related to the shape of the stylus, the mechanical properties of the substrate and the coating, the thickness, and the internal stress. In Figure 10a, a micro-scratch on the surface of the Zn-doped CaP coating on the untilted sample is represented. The L_c was determined during the scratch test to be a relatively small load of 10 N. The first adhesive cracks were observed after L_c = 5.3 N for the untilted sample. The average value of the friction coefficient during the measurements was calculated to be 0.3.
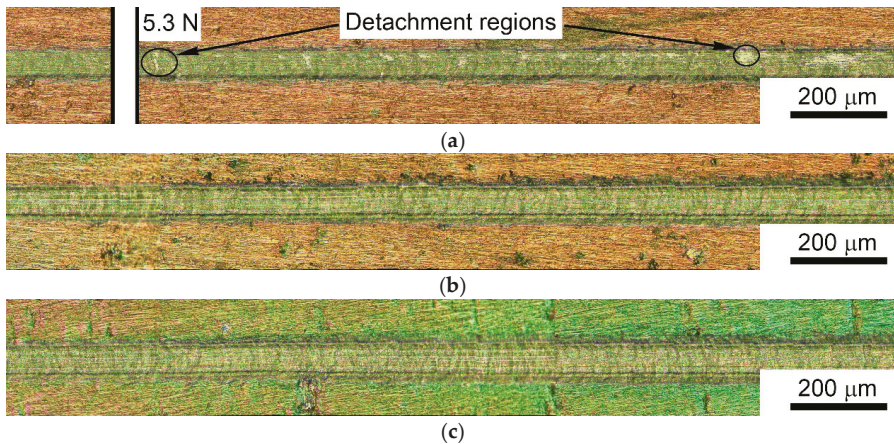
Figure 10. Optical microscopy of the tracks after scratch testing of the CaP coatings deposited on Ti at a working gas pressure of 0.8 mTorr under inclination angles of 0° (**a**), 60° (**b**), and 80° (**c**).

Local detachment of the coating is seen on the side of the track and in several other regions that are identified by arrows in Figure 10a. We concluded that the coating demonstrates sufficient scratch resistance, which is in accordance with the scientific data available in the literature [60,61]. In contrast, samples deposited at inclinations of 60° and 80° (Figure 10b,c) show higher scratch resistance. Thus, coating delamination even at the maximum load of 10 N is not observed. The average value of the friction coefficient for both the tilted substrates during the measurements did not exceed 0.25. This fact also contributed to the observed, improved scratch resistance of the tilted samples. We associate these

results with the high energy of sputtered species impinging the substrate during the condensation phase because of the placement of the inclined substrate closer to the particle source. The influence of bombardment energy on the level of scratch resistance can also be found in the literature [62].

4. Conclusions

Two approaches for achieving a possible synergetic antibacterial effect by manufacturing a patterned surface of Zn-doped calcium phosphate using GLAD technique in RF magnetron sputtering were used. Two types of substrates (Ti and Si) with significantly different roughness were chosen. Variations in coating thickness and uniformity take place starting from a tilt angle of 60°. It was shown that it is possible to manipulate the surface roughness and morphology of the coatings by varying the substrate tilt angle. The columnar structure becomes more prominent at an oblique angle of 80°, and it is made of inclined Zn-doped CaP columns. A significant change in the coating morphology becomes obvious starting from the substrate tilt angle of 60°. An increase in the coating crystallinity for samples deposited at a tilt angle of 80° corresponds to the formation of crystallites in the bulk structure of the thin film. It was shown that GLAD is a powerful technique that allows for the variation of CaP thin film morphology and can be utilized to create self-organized nanostructures that can be used for synergetic antibacterial effect.

References

1. Li, J.; Yang, L.; Guo, X.; Cui, W.; Yang, S.; Wang, J.; Qu, Y.; Shao, Z.; Xu, S. Osteogenesis effects of strontium-substituted hydroxyapatite coatings on true bone ceramic surfaces in vitro and in vivo. *Biomed. Mater.* **2018**, *13*, 015018. [CrossRef]

2. Vladescu, A.; Surmenev, R.; Surmeneva, M.; Braic, M.; Ivanova, A.; Grubova, I.; Cotrut, C.M. Radio frequency magnetron sputter deposition as a tool for surface modification of medical implants. In *Modern Technologies for Creating the Thin-Film Systems and Coatings*; Nikitenkov, N., Ed.; InTech: Rijeka, Croatia, 2017.

3. Raphel, J.; Holodniy, M.; Goodman, S.B.; Heilshorn, S.C. Multifunctional coatings to simultaneously promote osseointegration and prevent infection of orthopaedic implants. *Biomaterials* **2016**, *84*, 301–314. [CrossRef] [PubMed]

4. Šupová, M. Substituted hydroxyapatites for biomedical applications: A review. *Ceram. Int.* **2015**, *41*, 9203–9231. [CrossRef]

5. Rau, J.V.; Cacciotti, I.; De Bonis, A.; Fosca, M.; Komlev, V.S.; Latini, A.; Santagata, A.; Teghil, R. Fe-doped hydroxyapatite coatings for orthopedic and dental implant applications. *Appl. Surf. Sci.* **2014**, *307*, 301–305. [CrossRef]

6. Graziani, G.; Bianchi, M.; Sassoni, E.; Russo, A.; Marcacci, M. Ion-substituted calcium phosphate coatings deposited by plasma-assisted techniques: A review. *Mater. Sci. Eng. C* **2017**, *74*, 219–229. [CrossRef]

7. Robinson, L.; Salma-Ancane, K.; Stipniece, L.; Meenan, B.J.; Boyd, A.R. The deposition of strontium and zinc Co-substituted hydroxyapatite coatings. *J. Mater. Sci. Mater. Med.* **2017**, *28*, 51. [CrossRef]

8. Koo, H.; Allan, R.N.; Howlin, R.P.; Stoodley, P.; Hall-Stoodley, L. Targeting microbial biofilms: Current and prospective therapeutic strategies. *Nat. Rev. Microbiol.* **2017**, *15*, 740–755. [CrossRef] [PubMed]

9. Geng, Z.; Cui, Z.; Li, Z.; Zhu, S.; Liang, Y.; Liu, Y.; Li, X.; He, X.; Yu, X.; Wang, R.; et al. Strontium incorporation to optimize the antibacterial and biological characteristics of silver-substituted hydroxyapatite coating. *Mater. Sci. Eng. C* **2016**, *58*, 467–477. [CrossRef]

10. Huang, Y.; Zhang, X.; Zhao, R.; Mao, H.; Yan, Y.; Pang, X. Antibacterial efficacy, corrosion resistance, and cytotoxicity studies of copper-substituted carbonated hydroxyapatite coating on titanium substrate. *J. Mater. Sci.* **2015**, *50*, 1688–1700. [CrossRef]

11. Peñaflor Galindo, T.G.; Kataoka, T.; Fujii, S.; Okuda, M.; Tagaya, M. Preparation of nanocrystalline zinc-substituted hydroxyapatite films and their biological properties. *Colloids Interface Sci. Commun.* **2016**, *10*, 15–19. [CrossRef]

12. Litvinova, L.S.; Shupletsova, V.V.; Dunets, N.A.; Khaziakhmatova, O.G.; Yurova, K.A.; Khlusova, M.Y.; Slepchenko, G.B.; Cherempey, E.G.; Sharkeev, Y.P.; Komarova, E.G.; et al. Imbalance of morphofunctional responses of Jurkat T lymphoblasts at short-term culturing with relief zinc- or copper-containing calcium phosphate coating on titanium. *Dokl. Biochem. Biophys.* **2017**, *472*, 35–39. [CrossRef]

13. Graziani, G.; Boi, M.; Bianchi, M. A Review on Ionic Substitutions in Hydroxyapatite Thin Films: Towards Complete Biomimetism. *Coatings* **2018**, *8*, 269. [CrossRef]

14. Rau, J.V.; Cacciotti, I.; Laureti, S.; Fosca, M.; Varvaro, G.; Latini, A. Bioactive, nanostructured Si-substituted hydroxyapatite coatings on titanium prepared by pulsed laser deposition. *J. Biomed. Mater. Res. B Appl. Biomater.* **2015**, *103*, 1621–1631. [CrossRef] [PubMed]

15. Modaresifar, K.; Azizian, S.; Ganjian, M.; Fratila-Apachitei, L.E.; Zadpoor, A.A. Bactericidal effects of nanopatterns: A systematic review. *Acta Biomater.* **2018**, *83*, 29–36. [CrossRef]

16. Yu, W.; Sun, T.W.; Qi, C.; Ding, Z.; Zhao, H.; Zhao, S.; Shi, Z.; Zhu, Y.J.; Chen, D.; He, Y. Evaluation of zinc-doped mesoporous hydroxyapatite microspheres for the construction of a novel biomimetic scaffold optimized for bone augmentation. *Int. J. Nanomed.* **2017**, *12*, 2293–2306. [CrossRef] [PubMed]

17. Costa, D.O.; Prowse, P.D.H.; Chrones, T.; Sims, S.M.; Hamilton, D.W.; Rizkalla, A.S.; Dixon, S.J. The differential regulation of osteoblast and osteoclast activity bysurface topography of hydroxyapatite coatings. *Biomaterials* **2013**, *34*, 7215–7226. [CrossRef] [PubMed]

18. Rau, J.V.; Generosi, A.; Laureti, S.; Komlev, V.S.; Ferro, D.; Cesaro, S.N.; Paci, B.; Albertini, V.R.; Agostinelli, E.; Barinov, S.M. Physicochemical investigation of pulsed laser deposited carbonated hydroxyapatite films on titanium. *ACS Appl. Mater. Interfaces* **2009**, *1*, 1813–1820. [CrossRef]

19. Kim, H.N.; Jiao, A.; Hwang, N.S.; Kim, M.S.; Kang, D.H.; Kim, D.H.; Suh, K.Y. Nanotopography-guided tissue engineering and regenerative medicine. *Adv. Drug Deliv. Rev.* **2013**, *65*, 536–558. [CrossRef] [PubMed]

20. Chen, Z.; Bachhuka, A.; Wei, F.; Wang, X.; Liu, G.; Vasilev, K.; Xiao, Y. Nanotopography-based strategy for the precise manipulation of osteoimmunomodulation in bone regeneration. *Nanoscale* **2017**, *9*, 18129–18152. [CrossRef]

21. Lee, L.C.Y.; Gadegaard, N.; de Andrés, M.C.; Turner, L.A.; Burgess, K.V.; Yarwood, S.J.; Wells, J.; Salmeron-Sanchez, M.; Meek, D.; Oreffo, R.O.C.; et al. Nanotopography controls cell cycle changes involved with skeletal stem cell self-renewal and multipotency. *Biomaterials* **2017**, *116*, 10–20. [CrossRef]

22. Karazisis, D.; Petronis, S.; Agheli, H.; Emanuelsson, L.; Norlindh, B.; Johansson, A.; Rasmusson, L.; Thomsen, P.; Omar, O. The influence of controlled surface nanotopography on the early biological events of osseointegration. *Acta Biomater.* **2017**, *53*, 559–571. [CrossRef] [PubMed]

23. Alvarez, R.; Garcia-Martin, J.M.; Garcia-Valenzuela, A.; Macias-Montero, M.; Ferrer, F.J.; Santiso, J.; Rico, V.; Cotrino, J.; Gonzalez-Elipe, A.R.; Palmero, A. Nanostructured Ti thin films by magnetron sputtering at oblique angles. *J. Phys. D. Appl. Phys.* **2015**, *49*, 045303. [CrossRef]

24. Li, Z.; Xing, L.; Zhang, N.; Yang, Y.; Zhang, Z. Preparation and Photocatalytic Property of TiO_2 Columnar Nanostructure Films. *Mater. Trans.* **2011**, *52*, 1939–1942. [CrossRef]

25. Garcia-Valenzuela, A.; Alvarez, R.; Rico, V.; Cotrino, J.; Gonzalez-Elipe, A.R.; Palmero, A. Growth of nanocolumnar porous TiO_2 thin films by magnetron sputtering using particle collimators. *Surf. Coat. Technol.* **2017**, *343*, 172–177. [CrossRef]

26. Sit, J.C.; Vick, D.; Robbie, K.; Brett, M.J. Thin film microstructure control using glancing angle deposition by sputtering. *J. Mater. Res.* **1999**, *14*, 1197–1199. [CrossRef]

27. Zhao, Y.; Ye, D.; Wang, G.-C.; Lu, T.-M. Designing nanostructures by glancing angle deposition. *Proc. SPIE Nanotub. Nanowires* **2003**, *5219*, 59–73. [CrossRef]

28. Barranco, A.; Borras, A.; Gonzalez-Elipe, A.R.; Palmero, A. Perspectives on oblique angle deposition of thin films: From fundamentals to devices. *Prog. Mater. Sci.* **2016**, *76*, 59–153. [CrossRef]

29. Renault, C.; Harris, K.D.; Brett, M.J.; Balland, V.; Limoges, B. Time-resolved UV-visible spectroelectrochemistry using transparent 3D-mesoporous nanocrystalline ITO electrodes. *Chem. Commun.* **2011**, *47*, 1863–1865. [CrossRef]

30. Larsen, G.K.; Fitzmorris, R.; Zhang, J.Z.; Zhao, Y. Structural, optical, and photocatalytic properties of Cr:TiO$_2$ nanorod array fabricated by oblique angle codeposition. *J. Phys. Chem. C* **2011**, *115*, 16892–16903. [CrossRef]

31. Schubert, M.F.; Xi, J.Q.; Kim, J.K.; Schubert, E.F. Distributed Bragg reflector consisting of high- and low-refractive-index thin film layers made of the same material. *Appl. Phys. Lett.* **2007**, *90*, 141115. [CrossRef]

32. Rider, D.A.; Tucker, R.T.; Worfolk, B.J.; Krause, K.M.; Lalany, A.; Brett, M.J.; Buriak, J.M.; Harris, K.D. Indium tin oxide nanopillar electrodes in polymer/fullerene solar cells. *Nanotechnology* **2011**, *22*, 085706. [CrossRef]

33. Jensen, M.O.; Brett, M.J. Porosity engineering in glancing angle deposition thin films. *Appl. Phys. A Mater. Sci. Process.* **2005**, *80*, 763–768. [CrossRef]

34. Lintymer, J.; Martin, N.; Chappe, J.M.; Takadoum, J. Glancing angle deposition to control microstructure and roughness of chromium thin films. *Wear* **2008**, *264*, 444–449. [CrossRef]

35. Hung, K.-Y.; Lai, H.-C.; Feng, H.-P. Characteristics of RF-Sputtered Thin Films of Calcium Phosphate on Titanium Dental Implants. *Coatings* **2017**, *7*, 126. [CrossRef]

36. Surmenev, R.A.; Surmeneva, M.A.; Grubova, I.Y.; Chernozem, R.V.; Krause, B.; Baumbach, T.; Loza, K.; Epple, M. RF magnetron sputtering of a hydroxyapatite target: A comparison study on polytetrafluorethylene and titanium substrates. *Appl. Surf. Sci.* **2017**, *414*, 335–344. [CrossRef]

37. Thian, E.S.; Konishi, T.; Kawanobe, Y.; Lim, P.N.; Choong, C.; Ho, B.; Aizawa, M. Zinc-substituted hydroxyapatite: A biomaterial with enhanced bioactivity and antibacterial properties. *J. Mater. Sci. Mater. Med.* **2013**, *24*, 437–445. [CrossRef] [PubMed]

38. Prosolov, K.A.; Belyavskaya, O.A.; Muehle, U.; Sharkeev, Y.P. Thin bioactive Zn substituted hydroxyapatite coating deposited on ultrafine-grained titanium substrate: Structure analysis. *Front. Mater.* **2018**, *5*, 3. [CrossRef]

39. Prosolov, K.A.; Belyavskaya, O.A.; Rau, J.V.; Sharkeev, Y.P. Thin bioactive Zn-substituted hydroxyapatite coating deposited on Ti substrate by radiofrequency sputtering. *High Temp. Mater. Process.* **2017**, *21*, 3. [CrossRef]

40. Solar, P.; Choukourov, A.; Hanus, J.; Pavlova, E.; Slavinska, D.; Biederman, H. Nanocomposite structured thin films by magnetron sputtering at glancing angle deposition. In Proceedings of the International Plasma Chemistry Society, Bochum, Germany, 27–31 July 2009; p. 226.

41. Pang, H.F.; Zhang, G.A.; Tang, Y.L.; Fu, Y.Q.; Wang, L.P.; Zu, X.T.; Placido, F. Substrate-tilt angle effect on structural and optical properties of sputtered ZnO film. *Appl. Surf. Sci.* **2012**, *259*, 747–753. [CrossRef]

42. Toledano, D.; Galindo, R.E.; Yuste, M.; Albella, J.M.; Sánchez, O. Compositional and structural properties of nanostructured ZnO thin films grown by oblique angle reactive sputtering deposition: Effect on the refractive index. *J. Phys. D Appl. Phys.* **2013**, *46*, 045306. [CrossRef]

43. Leem, J.W.; Yu, J.S. Structural, optical, and electrical properties of AZO films by tilted angle sputtering method. *Thin Solid Films* **2010**, *518*, 6285–6288. [CrossRef]

44. García-Martín, J.M.; Alvarez, R.; Romero-Gómez, P.; Cebollada, A.; Palmero, A. Tilt angle control of nanocolumns grown by glancing angle sputtering at variable argon pressures. *Appl. Phys. Lett.* **2010**, *97*, 173103. [CrossRef]

45. Siad, A.; Besnard, A.; Nouveau, C.; Jacquet, P. Critical angles in DC magnetron glad thin films. *Vacuum* **2016**, *131*, 305–311. [CrossRef]

46. Park, Y.J.; Sobahan, K.M.A.; Nam, H.J.; Kim, J.J.; Hwangbo, C.K. Optical and structural properties of ZnO thin films fabricated by using oblique angle deposition. *J. Korean Phys. Soc.* **2010**, *57*, 1657–1660.

47. Bolbasov, E.N.; Maryin, P.V.; Stankevich, K.S.; Kozelskaya, A.I.; Shesterikov, E.V.; Khodyrevskaya, Y.I.; Nasonova, M.V.; Shishkova, D.K.; Kudryavtseva, Y.A.; Anissimov, Y.G.; et al. Surface modification of electrospun poly-(L-lactic) acid scaffolds by reactive magnetron sputtering. *Colloids Surf. B Biointerfaces* **2018**, *162*, 43–51. [CrossRef]

48. Bolbasov, E.N.; Antonova, L.V.; Stankevich, K.S.; Ashrafov; Matveeva, V.G.; Velikanova, E.A.; Khodyrevskaya, Y.I.; Kudryavtseva, Y.A.; Anissimov, Y.G.; Tverdokhlebov, S.I.; et al. The use of magnetron sputtering for the deposition of thin titanium coatings on the surface of bioresorbable electrospun fibrous scaffolds for vascular tissue engineering: A pilot study. *Appl. Surf. Sci.* **2017**, *398*, 63–72. [CrossRef]

49. Ivanova, A.A.; Surmeneva, M.A.; Surmenev, R.A.; Depla, D. Structural evolution and growth mechanisms of RF-magnetron sputter-deposited hydroxyapatite thin films on the basis of unified principles. *Appl. Surf. Sci.* **2017**, *425*, 497–506. [CrossRef]

50. Chu, J.; Peng, X.; Sajjad, M.; Yang, B.; Feng, P.X. Nanostructures and sensing properties of ZnO prepared using normal and oblique angle deposition techniques. *Thin Solid Films* **2012**, *520*, 3493–3498. [CrossRef]

51. Black, D.R.; Windover, D.; Henins, A.; Filliben, J.; Cline, J.P. Certification of Standard Reference Material 1976B. *Powder Diffr.* **2015**, *30*, 199–204. [CrossRef]

52. Ter Brugge, P.J.; Wolke, J.G.C.; Jansen, J.A. Effect of calcium phosphate coating crystallinity and implant surface roughness on differentiation of rat bone marrow cells. *J. Biomed. Mater. Res.* **2002**, *60*, 70–78. [CrossRef]

53. Gruener, C.; Liedtke, S.; Bauer, J.; Mayr, S.G.; Rauschenbach, B. Morphology of thin films formed by oblique physical vapor deposition. *ACS Appl. Nano Mater.* **2018**, *1*, 1370–1376. [CrossRef]

54. Gross, K.; Berndt, C. Thermal processing of hydroxyapatite for coating production. *J. Biomed. Mater. Res.* **1998**, *39*, 580–587. [CrossRef]

55. Sarkar, S.; Pradhan, S.K. Tailoring of optical and wetting properties of sputter deposited silica thin films by glancing angle deposition. *Appl. Surf. Sci.* **2014**, *290*, 509–513. [CrossRef]

56. Yonggang, Y.; Wolke, J.G.C.; Yubao, L.; Jansen, J.A. The influence of discharge power and heat treatment on calcium phosphate coatings prepared by RF magnetron sputtering deposition. *J. Mater. Sci. Mater. Med.* **2007**, *18*, 1061–1069. [CrossRef] [PubMed]

57. Jiang, H.T.; Liu, J.X.; Mi, Z.L.; Zhao, A.M.; Bi, Y.J. Texture evolution of commercial pure Ti during cold rolling and recrystallization annealing. *Int. J. Miner. Metall. Mater.* **2012**, *19*, 530–535. [CrossRef]

58. Ghosh, A.; Gurao, N.P. Effect of crystallographic texture on ratcheting response of commercially pure titanium. *Mater. Des.* **2017**, *115*, 121–132. [CrossRef]

59. Grubova, I.Y.; Surmeneva, M.A.; Ivanova, A.A.; Kravchuk, K.; Prymak, O.; Epple, M.; Buck, V.; Surmenev, R.A. The effect of patterned titanium substrates on the properties of silver-doped hydroxyapatite coatings. *Surf. Coat. Technol.* **2015**, *276*, 595–601. [CrossRef]

60. Surmeneva, M.A.; Sharonova, A.A.; Chernousova, S.; Prymak, O.; Loza, K.; Tkachev, M.S.; Shulepov, I.A.; Epple, M.; Surmenev, R.A. Incorporation of silver nanoparticles into magnetron-sputtered calcium phosphate layers on titanium as an antibacterial coating. *Colloids Surf. B Biointerfaces* **2017**, *156*, 104–113. [CrossRef]

61. Syromotina, D.S.; Surmeneva, M.A.; Gorodzha, S.N.; Pichugin, V.F.; Ivanova, A.A.; Grubova, I.Y.; Kravchuk, K.S.; Gogolinskii, K.V.; Prymak, O.; Epple, M.; et al. Physical-mechanical characteristics of RF magnetron sputter-deposited coatings based on silver-doped hydroxyapatite. *Russ. Phys. J.* **2014**, *56*, 1198–1205. [CrossRef]

62. Melnik, Y.A.; Metel, A.S. Improvement of the magnetron sputtered coating adhesion through pulsed bombardment by high-energy ions. *J. Phys. Conf. Ser.* **2017**, *830*, 012099. [CrossRef]

Zinc Doped Hydroxyapatite Thin Films Prepared by Sol–Gel Spin Coating Procedure

Daniela Predoi [1,*], Simona Liliana Iconaru [1], Mihai Valentin Predoi [2], Nicolas Buton [3] and Mikael Motelica-Heino [4]

[1] National Institute of Materials Physics, Atomistilor Street, No. 405A, P.O. Box MG 07, 077125 Magurele, Romania; simonaiconaru@gmail.com

[2] Department of Mechanics, University Politehnica of Bucharest, BN 002, 313 Splaiul Independentei, Sector 6, 060042 Bucharest, Romania; predoi@gmail.com

[3] HORIBA Jobin Yvon S.A.S., 6-18, rue du Canal, 91165 Longjumeau cédex, France; nicolas.buton@horiba.com

[4] ISTO, UMR 7327 CNRS Université d'Orléans, 1A rue de la Férollerie, 45071 Orléans CEDEX 2, France; mikael.motelica@univ-orleans.fr

* Correspondence: dpredoi@gmail.com; Tel.: +40-21-241-8154

Abstract: In this study, ZnHAp layers deposited on a Si substrate were obtained by a sol–gel spin-coating procedure. The ZnHAp solutions used to obtain the ZnHAp coatings were investigated by dynamic light scattering (DLS) analysis, ζ-potential, ultrasound measurements, and flame atomic absorption spectrometry (AAS). The average measured hydrodynamic diameter from the DLS analysis, ζ-potential, and ultrasound measurements were analyzed so as to characterize and estimate the stability of the ZnHAp nanoparticles. The AAS results confirmed the presence of zinc in the gels used in the preparation of the ZnHAp layers. The layers were investigated by X-ray diffraction (XRD) and scanning electron microscopy (SEM). The XRD results revealed the diffraction peaks of the hexagonal hydroxyapatite in all of the investigated samples. The morphology of the ZnHAp coatings annealed at 500 °C (ZnHAp-500) and 700 °C (ZnHAp-700), which evidenced that no fissures or cracks formed on the surface of the coatings. The biocompatibility assays indicated that the ZnHAp coatings did not present any toxicity towards the HeLa cells. Furthermore, the study regarding the cytotoxicity of the ZnHAp layers against microorganisms emphasized that ZnHAp coatings exhibited an inhibitory effect towards *S. aureus* bacterial cells and also towards *C. albicans* fungal cells.

Keywords: zinc; hydroxyapatite; ultrasound measurement; sol–gel spin coating; layers; *C. albicans*; *S. aureus*

1. Introduction

Nowadays, the constant and rapid progress registered in the area of technology and engineering has created tremendous opportunities for modern medicine, by creating the premise of developing new and enhanced materials with outstanding properties that could greatly contribute to the improvement of a patient's life quality [1–3]. Nonetheless, even with the constant new developments, there are still difficulties to overcome for some issues in the biomedical field, as a result of medical devices, which could lead to post operatory complications [4]. These days, one of the most distressing complications that could appear after surgery is considered the apparition of a post operatory infection [5,6]. In most cases, the infection appears because of the bacterial cells, which adhere either to an implantable medical device (when is the case), either on the tissue surrounding the surface of the implant, or simply on the surface of the wound [7,8]. These types of bacterial adhesions on implantable devices are some of the most frightening problems that can occur in the dentistry, orthopedic, and cardiovascular field, because they usually lead to severe life treating infections due to the development

of bacterial biofilms, which have been proven to be resilient to conventional antibiotics [9–13]. In most cases, because of the development of bacterial infections, implantable devices are often removed from patients using many costly procedures, which are uncomfortable and even dangerous for the patient [14]. Considering these factors, there has been an increased effort directed towards the development of new materials capable of mimicking the composition and structure of bone, also exhibiting antimicrobial properties [15–17]. Commonly, one of the widely used biomaterials, due to its outstanding biocompatible and osteoconductive properties, is hydroxyapatite (HAp). Synthetic HAp, with the general formula $Ca_{10}(PO_4)_6(OH)_2$, has been widely studied for bone substitution, bone remodeling applications, controlled drug release, bone tissue engineering, bone regeneration as bone graft materials, coatings for implants, or bone fillers [16–18]. Nowadays, HAp is used both in reconstruction and repair surgery, as well as in conservative dentistry, dental implantology, and pharmacy [19,20]. Used as an implant coating, synthetic HAp has been studied because of its excellent biocompatibility and osteoconductivity [20,21]. Despite its great potential, HAp has limitations because of its poor mechanical properties (brittleness, poor tensile strength, and poor fatigue strength) [22,23] and slow biological interaction, and it is because of these factors, which favor the adherence and development of bacterial cells, that the apparition of post operatory infections is caused. Nevertheless, numerous studies have reported that the properties of HAp could be improved by doping with various elements such as Na, Sr, Mg, K, Mn, Ag, Ce, Eu, Cu, Zn, Sm, and so on [24–27]. The structure of HAp allows for both anionic and cationic substitutions [24–27]. Zinc is one of the most widespread trace elements, and is usually considered as a potential substituent in HAp because of its biological properties [28]. Taking into account that almost a third of the amount of zinc that is found in the human body is located in bone tissue, and also that zinc contributes to the proliferation of osteoblast cells and enhances the bone formation process [27,28], the use of zinc as a doping element for HAp will create the premise of obtaining a new biomaterial with outstanding biological properties. Recent studies have also reported that zinc possesses antimicrobial properties and could be used in the development of antimicrobial agents [29–32]. In their study, Radovanović et al. [33] highlighted that zinc exhibited a good antimicrobial activity against *Staphylococcus aureus*, *Escherichia coli*, *Pseudomonas aeruginosa*, and *Candida albicans* microbial strains [33].

Over the years, extensive research has been conducted for the development of uniform, reproducible, and reliable layers using various advanced deposition techniques [34–37]. There are many papers dealing with thin film development, involving several techniques such as vacuum evaporation [38], sputtering [36], laser-assist vacuum evaporation [38], chemical bath deposition [39], electrodepositing [40], dip coating [41], sol–gel [42], the Langmuir Blodgett technique [43], and so on. Among these, the sol–gel spin coating technique is considered to be one of the simplest and most cost-effective techniques for thin film deposition [44]. It has been reported that by using the conventional spin coating technique, the material parameters can be used to determine the final film thickness, which is considered to be a tremendous advantage when developing thin films [45].

The present study is focused on developing ZnHAp coatings based on stable solutions with applications in the biomedical field. Firstly, stable solutions of ZnHAp have been synthesized and characterized. The ZnHAp solutions have been studied using dynamic light scattering (DLS), Zeta potential, and atomic absorption spectroscopy (AAS). On the other hand, studies regarding the stability of the resulting ZnHAp solutions obtained by the sol–gel method were performed using ultrasound measurements. Afterwards, the ZnHAp coatings were deposited on Si discs. The ZnHAp coatings were investigated by X-ray diffraction (XRD) and scanning electron microscopy (SEM). The cytotoxicity of the ZnHAp coatings was studied using a HeLa cell line. Moreover, the antimicrobial activity of the ZnHAp coatings was investigated against *Candida albicans* ATCC 10231 and *Staphylococcus aureus* ATCC 25923 microbial strains.

2. Materials and Methods

2.1. Materials

Reagents such as calcium nitrate (Ca(NO$_3$)$_2$·4H$_2$O, Sigma-Aldrich, St. Louis, MA, USA), ammonium hydrogen phosphate ((NH$_4$)$_2$HPO$_4$), Alfa Aesar, Karlsruhe, Germany; 99.99% purity), silver nitrate (Zn(NO$_3$)$_2$·6H$_2$O, Alfa Aesar, Karlsruhe, Germany; 99.99% purity), triethanolamine (C$_6$H$_{15}$NO$_3$, Sigma-Aldrich; ≥99.0% (GC) purity), and ethanol were used for obtaining the zinc doped hydroxyapatite (ZnHAp) solutions using the sol–gel method, in order to prepare the ZnHAp coatings on the Si substrate using the spin-coating procedure.

2.2. Thin Layer of Zinc Doped Hydroxyapatite

Calcium nitrate (Ca(NO$_3$)$_2$·4H$_2$O), zinc nitrate (Zn(NO$_3$)$_2$·6H$_2$O), and ammonium hydrogen phosphate ((NH$_4$)$_2$HPO$_4$) were used as the starting materials for the preparation of zinc doped hydroxyapatite (Ca$_{10-x}$Zn(PO$_4$)$_6$(OH)$_2$, x_{Zn} = 0.1) thin layers on an Si substrate (ZnHAp), respectively. In order to synthesize the zinc doped hydroxyapatite gel for preparing the thin layers, triethanolamine (C$_6$H$_{15}$NO$_3$) and ethanol (C$_2$H$_5$OH) were also used. Ca(NO$_3$)$_2$·4H$_2$O was dissolved in ethanol and mixed on a magnetic stirrer for 120 min at 40 °C. Triethanolamine was slowly dripped into the solution containing Ca, and the solution was agitated vigorously for 24 h at 40 °C. At the same time, (NH$_4$)$_2$HPO$_4$ and Zn(NO$_3$)$_2$·6H$_2$O were dissolved in the ethanol and mixed on a magnetic stirrer for 120 min at 40 °C. Next, the solution containing Ca was slowly added to the solution containing P and Zn. The final solution was constantly agitated on a magnetic stirrer for 6 h at 100 °C. According to the authors of [18], in the ZnHAp (x_{Zn} = 0.1) sol, [Ca + Zn]/P, the composition ratio was adjusted to be equal to 1.67. The resulting gel was mixing by ultrasound for 6 h. The resulting sol–gel solution was used to obtain, using the spin-coating procedure, the ZnHAp coatings on the Si substrate. For the centrifugation coating, 0.5 mL of the resulting solution was placed on the top of the substrate using a syringe. The centrifugation was carried out for 60 s at 2000 rpm. The Si substrates were repeatedly coated 30 (ZnHAp) times. The Zn:HAp layers were annealed for 2 h at 500 °C (ZnHAp-500) and 700 °C (ZnHAp-700), in order to remove the solvents and to obtain films with a crystalline structure.

2.3. Characterization Methods

The resulting sol–gel solution that was used to obtained the ZnHAp coatings on the Si substrate by the spin-coating procedure was investigated by dynamic light scattering (DLS) analysis, ζ-potential, and ultrasound measurements. Dynamic light scattering (DLS) and ζ-potential were performed at 25 ± 1 °C using a SZ-100 Nanoparticle Analyzer (Horiba, Ltd., Kyoto, Japan. All of the samples were diluted in ethanol before analysis 10 times before the measurements of the DLS and ζ-potential. Three determinations were recorded for each analyzed sample, and the final value was established by mediating the three measurements.

The sample was stirred for 30 min at room temperature. Then, the ultrasonic tests were effectuated using the setup indicated in Figure 1. There are two coaxial ultrasonic transducers distanced by d = 30 mm, of a 5 MHz central frequency, model H5K (General-Electric, Krautkramer, Hürth, Germany), one (marked R) sending and receiving the echoes, and the other (marked T) just receiving the echoes. These were the general purpose longitudinal non-focusing transducers, which attenuated the received echoes by different amounts at different frequencies. In order to minimize the losses in the transducers, we investigated only the echoes received by the T transducer at 5 s intervals.
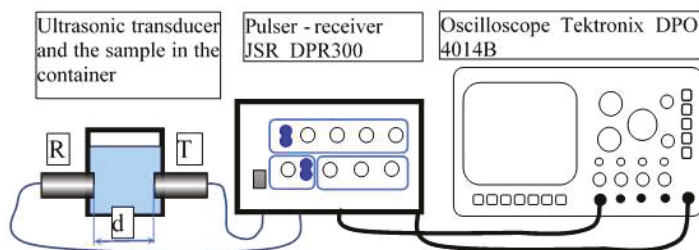
Figure 1. Experimental setup schematic: transducer, pulser-receiver, and oscilloscope.

Quantitative studies regarding the elemental composition of the new zinc-doped hydroxyapatite solutions were performed by flame atomic absorption spectrometry (AAS). The analysis was performed using a Zeeman HITACHI Z-8100 from Japan Hitachi (Tokyo, Japan), using a cavity cathode lamp, specific to the zinc element. The AAS investigations were done using stable solutions of ZnHAp. The AAS measurements were conducted using a zinc hollow cathode lamp under a constant airflow rate of 10.00 L·min^{-1}, at a wavelength of 213.9 nm, according to the manufacturer's operational conditions for zinc.

The resulting sol–gel solution that was used to obtained the ZnHAp coatings on the Si substrate by the spin-coating procedure were dried for 72 h at 100 °C, and preseed into pellets in order to be investiagted by laser ablation-inductively coupled plasma-mass spectrometer (LA-ICP-MS). The studies were conducted in agreement with the procedure described by Motelica-Heino and Donard [46], using an elemental XR Thermo Specific instrument (Waltham, MA, USA) combined with a UV laser probe laser ablation sampling device (Teledyne CETAC Technologies, Omaha, NE, USA). The calibration was done with certified artificial glass, NIST-610. The measurements were reproduced four times.

The morphology of the samples was investigated by scanning electron microscopy (SEM), using a HITACHI S4500 microscope (Hitachi, Ltd., Tokyo, Japan) equipped with an X-ray energy dispersive spectroscopy (EDX) system. In order to establish the crystal structures of the ZnHAp layers, the XRD patterns were recorded using a Bruker D8 Advance diffractometer (Bruker, Karlsruhe, Germany) with a nickel filtered Cu Kα (λ = 1.5418 Å) radiation in the 2θ ranging from 20° to 55°.

2.4. In Vitro Antifungal Activity

The antimicrobial properties of the ZnHAp-500 and ZnHAp-700 layers were assessed using *Candida albicans* ATCC 10231 and *Staphylococcus aureus* ATCC 25923 microbial cells. The evaluation of the antimicrobial activity of the ZnHAp-500 and ZnHAp-700 layers was performed using 1.5×10^8 microbial suspensions of a 0.5 McFarland standard obtained from 15 to 18 h bacterial cultures.

The qualitative antifungal and antibacterial activity of the layers was quantified at 24 and 48 h. For this purpose, microbial suspensions of *C. albicans* ATCC 10231 and *Staphylococcus aureus* ATCC 25923 (500 μL) were grown on the samples in culture medium. After 24 and 48 h the layers were removed from the culture medium, washed with sterile saline solution for the removal of the non-adherent microbial cells. The layers were then introduced into sterile saline (1 mL), vortexed for suspending the microbial cells embedded in the biofilm formed on the surface, washed in saline solution, fixed in cold methanol, and prepared for scanning electron microcopy (SEM) visualization.

The quantitative assays of the antimicrobial activity of the ZnHAp-500 and ZnHAp-700 layers were performed using an adapted method derived from the standard test method for determining the antimicrobial activity of antimicrobial agents under dynamic contact conditions (E2149-10; ASTM International) [47,48]. The layers were added in a Luria-Bertani (LB) broth inoculated with microbial suspensions of 1.5×10^8 CFU/mL. The samples were allowed to incubate at 30 °C for four time intervals (8, 24, 32, and 48 h) in order to assess the temporal dynamics of the microbial biofilms

developed in the presence of the layers. After the incubation of each time interval, the HAp, ZnHAp-500, and ZnHAp-700 layers were removed from the medium, washed using a sterile saline buffer in order to remove the microbial cells that did not adhere to the substrates, and were then immersed in a sterile saline buffer. The quantitative assessment of the antimicrobial activity of the ZnHAp-500 and ZnHAp-700 layers was determined by measuring the absorbance of the recovered suspensions at 620 nm. The experiments were performed in triplicate.

2.5. Hela Cell Viability Assays

The cell viability assays were performed using the first immortal human cell line, known for being one of the most remarkably durable and prolific cell lines (HeLa cells). HeLa cell growth assays were performed as previously described [49], with the following modifications: HeLa were grown in Dulbecco's modified Eagle's medium previously supplemented with fetal calf serum (FCS) 10%, and with 2 mM L-glutamine (GIBCO BRL, Life Technologies, Carlsbad, CA, USA) at a temperature of 37 °C in a humidified atmosphere with 5% CO_2. The culture medium was then renewed every 2 to 3 days. Then, the HeLa cells were seeded in six-well plates, at a density of 5×10^5 cells/mL, and incubated on previously UV-sterilized ZnHAp layers. The cell viability was assessed by microscopic evaluation after 24 and 48 h of incubation. Moreover, a quantitative assay regarding the cell viability was performed on the HeLa cells (~10^4 cells/100 μL) using the conventional 3-(4,5-dimethylthiazolyl-2)-2,5-diphenyltetrazolium bromide (MTT) reduction assay.

2.6. Statistical Analysis

All of the biological investigations were carried out in triplicate. The statistical analysis was carried out using the t-test and analysis of variance (ANOVA). The difference established between the samples was appreciated to be significant at $p < 0.05$.

3. Results and Discussions

3.1. Characterization of Suspension

To achieve uniform coatings, the gels obtained should be stable, and the nanoparticles should be well dispersed. In this regard, the nanoparticles in the solution were studied by DLS, ζ-potential, and ultrasound measurements. If in the DLS studies and zeta potential the final gel was diluted 10 times, the ultrasound measurements allowed for the study of ZnHAp nanoparticles in the final concentrated solution obtained from the sol–gel synthesis method. In agreement with previous studies conducted by Egelhaaf et al. [50], DLS can be used to characterize the hydrodynamic diameter distribution in the range of some hundreds of nm. These results provide important information on colloidal agglomeration. The hydrodynamic diameter distribution determined by DLS is shown in Figure 2. As shown in Figure 2A, the size of the particles was in the range of 10–60 nm. The average hydrodynamic diameter estimated from the hydrodynamic diameter distributions obtained by DLS was 45 ± 4 nm. One distinctive curve was visualized and coincided with one population that could indicate the lack of aggregates in the analyzed solution. The absence of agglomerates is also explained by the high potential of the ζ-potential (Figure 2B,C).

The ζ-potential value of the ZnHAp ($x_{Zn} = 0.1$) nanoparticles in the solution (Figure 2B) was −45.8 mV. The value of the average electrophoretic mobility was −0.00034 cm^2 V^{-1} s^{-1} (Figure 2C). The value obtained for the ζ-potential in the ZnHAp gel was much higher than which has been reported so far [19,31]. This difference may be due to increasing the zinc concentration, and, on the other hand, to the synthesis parameters. In previous studies, Predoi et al. showed that for ZnHAp solutions with $0.01 < x_{Zn} < 0.05$, the zeta potential increased from −8.19 mV ($x_{Zn} = 0.01$) to −15.84 mV when x_{Zn} was 0.05.

Significant information about the Zn:HAp gel used to prepare the ZnHAp layers were achieved from the ultrasound measurements. During the ultrasonic measurements, the recording time was 1000 s, corresponding to 200 records, with each record containing 100k samples (Figure 3).
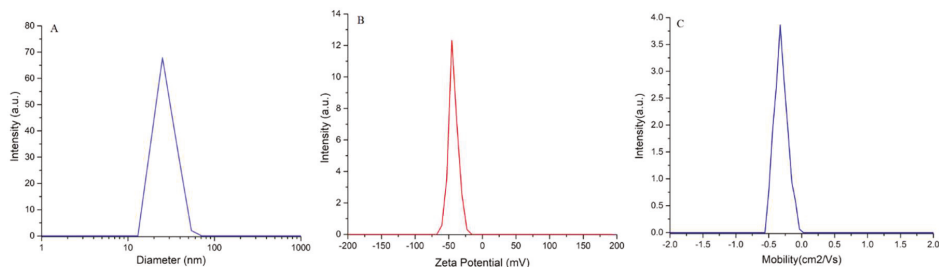
Figure 2. Colloidal characteristics of the ZnHAp and $Ca_{10-x} Zn_x(PO_4)_6(OH)_2$ nanoparticles in the solution ($x_{Zn} = 0.1$): (**A**) hydrodynamic diameter distribution curves images; (**B**) ζ-potential distribution curve; and (**C**) electrophoretic mobility.
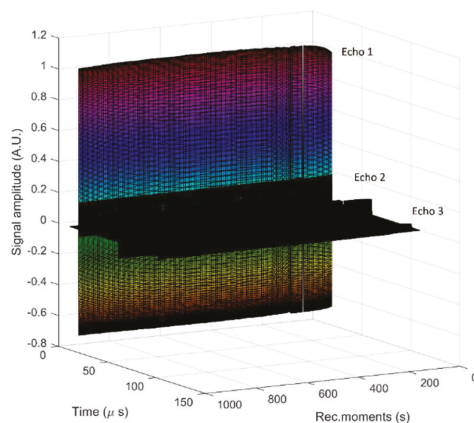
**Figure 3.** Recorded T signals for 1000 s. Each signal includes three echoes.

The three echoes obtained for the ZnHAp sample were each compared with the corresponding echoes in double distilled water in the same setup. This method allows for relative quantitative measurements, which eliminate the influence of the transducers attenuation and frequency spectrum.

Through the intercorrelation of each echo with the corresponding echo in the reference fluid, for which the velocity is $c_0 = 1489.23$ m/s at 22.3 °C, an average velocity in the sample of $c_s = 1489.1$ m/s has been deduced. The velocity of the ultrasonic waves in homogeneous liquids can be calculated with the relation $c = \sqrt{\frac{1}{\kappa\rho}}$, where the adiabatic compressibility, k, is the inverse of the compression elastic modulus ($K = 1/k$), and ρ is the averaged mass density. For the biphasic suspensions, the averaged values can be obtained from the following: $\kappa = \Phi\kappa_2 + (1 - \Phi)\kappa_1$ and $\rho = \Phi\rho_2 + (1 - \Phi)\rho_1$, in which Φ represents the volumetric fraction of the solid particles in the solvent, which was double distilled water in this case.

Consequently, if the volumetric fraction is known, and the elastic properties of the solvent are known (e.g., for water, $\kappa = 4.54 \times 10^{-10}$ Pa^{-1}), one can determine the pairs (κ_2, ρ_2) of the particles in the suspension, and if one of the two parameters is known, then the other can be accurately determined.

The first information is the evolution in time of the echo's amplitudes (Figure 4A). The three recorded signals indicate the stable level of the amplitude, in direct connection with the physical stability of the sample. In our previous studies [24] on bioceramic layers with antifungal properties, we

suggested a stability parameter, measured in s^{-1} and defined as $s = \frac{1}{A_m}\left|\frac{dA}{dt}\right|$. The stability coefficient for this sample is $s = 0.0152$ (1/s), indicating a relatively stable suspension, compared with pure water, for which $s = 0$.
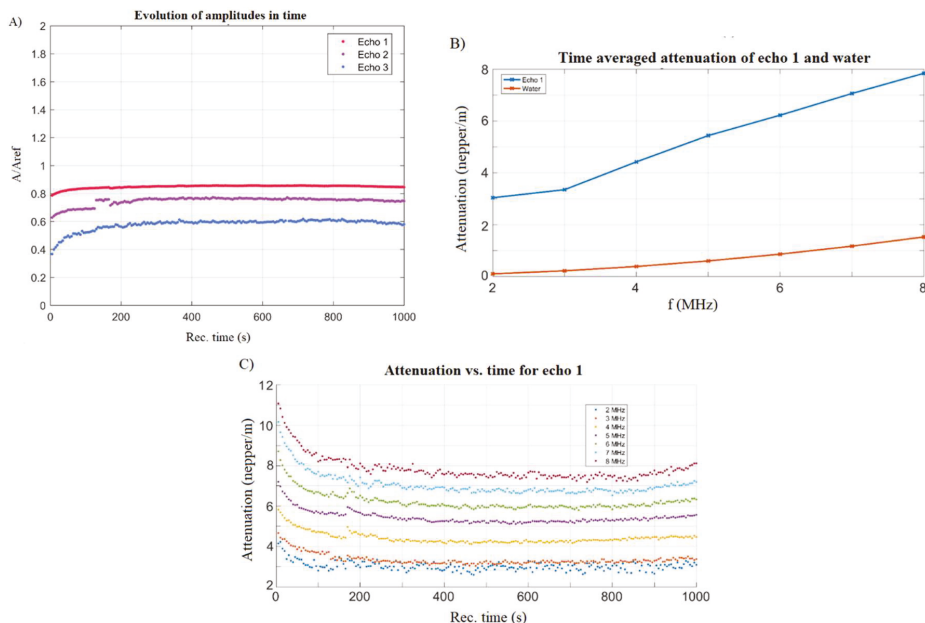
Figure 4. Evolution in time of the echoes amplitudes (**A**), spectral attenuation of echo 1 and reference fluid (**B**), and spectral attenuation vs. time for echo 1 (**C**).

There was an initial period of approximately 100 s during which the suspension reached a stable configuration. The second and third echoes have weaker amplitudes as a result of the attenuation, which will be discussed in the following. The following analysis concerns only the first echo, which was the least affected by the attenuation characteristics of the transducers.

The amplitudes at higher frequencies diminished, a phenomenon that is typical to ultrasound waves. However, this amplitude reduction vs. frequency is typical for each sample. For each echo, an averaged ratio of amplitudes at each frequency in the spectrum, relative to the reference fluid, were determined. The attenuation vs. frequency for the first echo is plotted in Figure 4B.

The attenuation is defined for two successive echoes of amplitudes, A_1 and A_2, determined after traveling a distance, d, as follows: $\alpha = -\frac{1}{d}\ln\frac{A_2}{A_1}$ [Np/m]. For the reference fluid, the attenuation is known from the specialized literature and the attenuation of the sample is determined experimentally.

The attenuation in the sample is considerably higher than in the reference fluid, varying from 3.03 Np/m at 2 MHz, up to 7.84 Np/m at 8 MHz. The slope given by the stability parameter is also very important. For this sample, a change in the attenuation slope for frequencies above 3 MHz is clearly visible, a fact related to the size and concentration of the nanoparticles. More details can be obtained by analyzing the evolution in time of the attenuation for each of the frequencies marked on Figure 4B. The results are plotted on Figure 4C.

There was an initial period of about 100 s, during which the attenuation decreased rapidly, possibly due the sedimentation of the larger size particles in the suspension. Between 100 and 900 s, the attenuation at all of the frequencies remained relatively constant, proving the stability of the suspension. As shown on Figure 4B, the attenuation increased with the increasing frequency.

The amount of zinc incorporated in the HAp lattice from the ZnHAp samples was investigated using flame atomic absorption spectrometry (AAS). For this purpose, stable solutions of ZnHAp were measured and the zinc concentration determined. The results of the AAS investigation revealed that the zinc concentration from the measured samples was of 1.785 ± 2.5 wt %.

More than that, ICP-MS investigations were performed on the ZnHAp powders obtained from the sol–gel solution used in the spin-coating procedure. The results of the ICP-MS studies revealed that the amount of zinc from the ZnHAp powders calculated from the ICP measuremets was 1.57 ± 1.8 wt %. These results are both in good agreement with previous studies reported by Predoi et al. [19].

3.2. Structure and Morphology of the Layers

The XRD patterns of the ZnHAp layers deposited on the Si substrates using the sol–gel spin coating method are shown in Figure 5. The XRD analysis was used for determining the phase composition of the layers. The XRD patterns of the ZnHAp layers deposited on the Si substrates using the sol–gel spin coating method are shown in Figure 5.
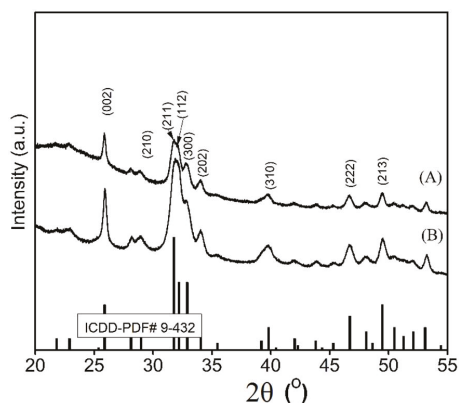
Figure 5. XRD pattern of the ZnHAp layers annealed at 500 °C (**A**) and 700 °C (**B**).

The influence of the annealing temperature on the coating was clearly seen. The peak broadening of the HAp samples decreased upon increasing the temperature, indicating that the crystallinity increased. The XRD patterns revealed the diffraction peaks of hexagonal HAp (space group P63/m) in all of the layers (A and B) according to a standard card of the HAp (ICDD-PDF #9-0432). The relative 2θ position of the diffraction peaks remained virtually unchanged with respect to the application temperatures, up to 700 °C. No impurity peaks of metallic Zn were detected in the XRD patterns. On the other hand, the peaks at about 31° and 47° (2θ), which are characteristic of an amorphous phase, were not observed [51]. The XRD patterns of the ZnHAp-500 and ZnHAp-700 annealed samples revealed two peaks located at 31.7° and 46.7° 2θ, which correspond to the (211) and (222) reflection plans of the hexagonal hydroxyapatite [52]. The results of the XRD studies of the ZnHAp-500 and ZnHAp-700 layers were in good agreement with the previous studies [52].

In order to determine the surface morphology of the ZnHAp-500 and ZnHAp-700 layers, SEM analysis was used. The SEM images of the ZnHAp-500 and ZnHAp-700 layers are presented in Figure 6A,B. The SEM analysis of the coatings did not reveal the pits and fissures on the surface of the ZnHAp-500 and ZnHAp-700 samples. In order to confirm that there were no cracks on the layers' surfaces in Figure 6C,D, the lower magnification images for the investigated samples are presented. Moreover, luminous areas corresponding to the surface of the Si substrate have not been observed. Although, in both cases, a dense layer with a homogeneous structure was observed, but the coating morphology of the surface samples was slightly different. This was due to the higher temperature at

which the heat treatment was carried out. The SEM analysis of the transversal cross section of the investigated layers indicated a thickness equal to 140.1 nm for ZnHAp-500 (Figure 6E), and 138.6 nm for ZnHAp-700 (Figure 6F).
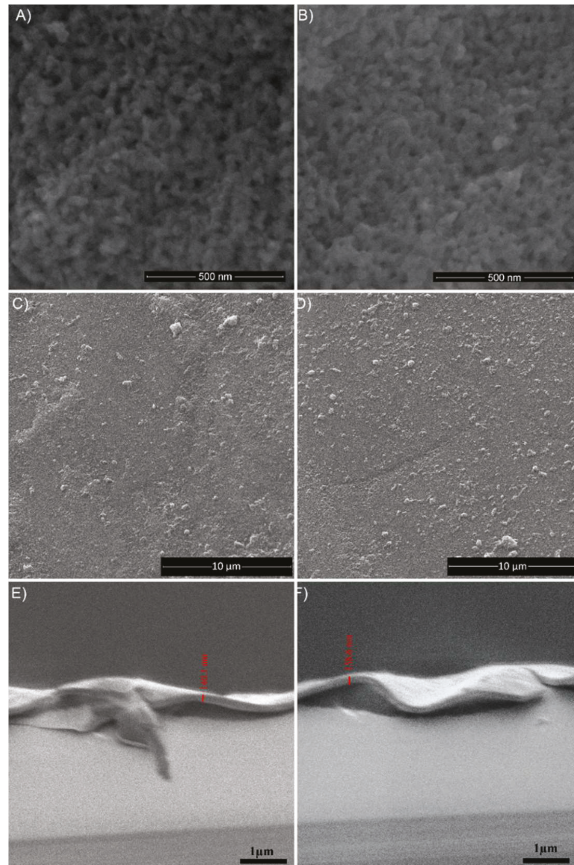

Figure 6. SEM images of the ZnHAp-500 (**A,C**) and ZnHAp-700 (**B,D**) layers at different magnifications. SEM images of the transversal cross section of ZnHAp-500 (**E**) and ZnHAp-700 (**F**) layers.

3.3. Cell Viability

Figure 7A–C shows the morphology of the HeLa cells treated with at 24 h. The morphology of the HeLa cells treated with ZnHAp-500 (Figure 7E) and ZnHAp-700 (Figure 7F) at 48 h are presented in Figure 7E,F. The morphology and size of the HeLa cells did not change after their treatment at 24 and 48 h, relative to the control. The control cells at 24 (Figure 7A) and 48 h (Figure 7D) were represented by HeLa cells grown in the culture medium. MTT assay was used to verify the cell viability of the HeLa cells for incubation times of 24 and 48 h, in presence of ZnHAp-500 and ZnHAp-700 layers. In Figure 8, the percentages of the cell viability are. The cell viability values for the ZnHAp-500 sample were observed to be about 88% and 92% at 24 and 48 h, respectively, relative to the control. The cell viability values for the ZnHAp-700 sample were observed to be about 90% and 95% at 24 and 48 h, respectively. The obtained results for the MTT assay revealed that as the annealing temperature of the layers increased and the incubation time increased, the cell viability gradually increased.
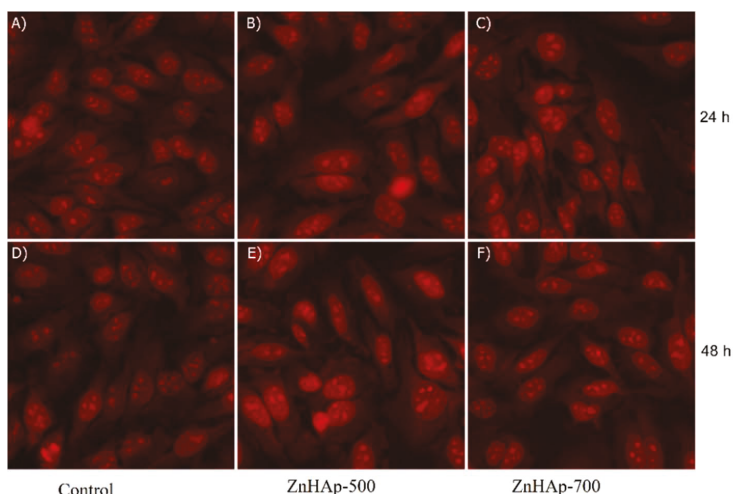
Figure 7. The morphology of the HeLa cells treated with ZnHAp-500 (**B**) and ZnHAp-700 (**C**) at 24 h, relative to the control (**A**). The morphology of the HeLa cells treated with ZnHAp-500 (**E**) and ZnHAp-700 (**F**) at 48 h, relative to the control (**D**).
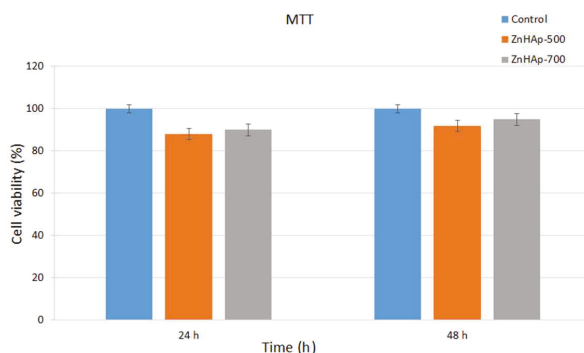
Figure 8. Cell viability of the HeLa cells for incubation times of 24 and 48 h in the presence of ZnHAp-500 and ZnHAp-700 layers.

3.4. Antimicrobial Activity

The antimicrobial activity of the HAp and ZnHAp layers was assessed by studying the cell viability of two significant microbial strains in the presence of the layers.

The results of the antimicrobial activity of the Hap, ZnHAp-500, and AnHAp-700 layers against the two most common microorganisms associated with hospital-related infections are presented in Table 1.

Table 1. Qualitative screening of the antimicrobial activities of the HAp, ZnHAp-500, and ZnHAp-700 layers against *Candida albicans* ATCC 10231 and *Staphylococcus aureus* ATCC 25923.

Sample	*Candida albicans* ATCC 10231				*Staphylococcus aureus* ATCC 25923			
	8 h	24 h	32 h	48 h	8 h	24 h	32 h	48 h
HAp	±	±	±	+	±	+	+	+
ZnHAp-500	+	++	+++	+++	+	++	+++	+++
ZnHAp-700	++	+++	+++	++++	++	+++	++++	++++

The results of the qualitative screening have revealed that all of the tested layers had an inhibitory effect on the tested microbial strains. On the other hand, it was emphasized that the ZnHAp-700 layers were the most efficient in inhibiting both *C. albicans* and *S. aureus* bacterial cells.

The microbial strains chosen for the experiments are some of the most common microorganisms responsible for frequent infections in daily life. The effect of HAp coated Si discs, and ZnHAp-500 and ZnHAp-700 layers against the cell development of the *C. albicans* and *S. aureus* microbial strains are presented in Figure 9. The results of the cell viability studies revealed that a small effect on *C. albicans* and *S. aureus* cells growth was noticed for the HAp coated Si discs. The cell growth of the tested microbial strains in the presence of HAp coated Si discs was comparable with the results obtained for the cell growth of the control, but smaller. Furthermore, the cytotoxicity assay of the ZnHAp layers against the development of the fungal cells of *Candida albicans* revealed that even after 8 h of incubation, the fungal cell growth was inhibited and diminished with time. The results emphasized that both the ZnHAp-500 and ZnHAp-700 layers considerably inhibited the cell growth of the fungal cells of *C. albicans* at all of the tested time intervals. Moreover, the results suggested that the ZnHAp-700 layers exhibited a greater cytotoxic effect on the fungal cell viability than the ZnHAp-500 layers. The most significant cell growth inhibition in the case of the *C. albicans* fungal cells was obtained after 48 h of incubation for both the ZnHap-500 and ZnHAp-700 samples. Furthermore, the cytotoxicity of the ZnHAp layers was also investigated in the case of *S. aureus* bacterial cells. The results of the antibacterial assay highlighted that both ZnHAp layers presented a strong cytotoxic effect on the *S. aureus* bacterial cells growth. Studies regarding the cell viability of the *S. aureus* bacterial cells in the presence of the ZnHAp-500 layers revealed that the samples inhibited cell growth even after a short period of 8 h of incubation. The cytotoxic assays suggested that the inhibition of the cell growth was time depended, and the best cytotoxic effect was registered after 48 h of incubation. Similar results were obtained in the case of the toxicity of the ZnHAp-700 layers against bacterial cell growth. The results emphasized that the ZnHAp-700 layers showed a strong inhibitory effected against the cell growth of the *S. aureus* bacterial cells, even after 8 h of incubation. Moreover, the cytotoxic effect of ZnHAp-700 on the cell growth of the *S. aureus* bacterial cells was greater than the cytotoxic effect of the ZnHAp-500 layers. Nevertheless, both samples proved to exhibit strong antimicrobial properties and had a good inhibitory effect on the cell growth of the tested microorganism.
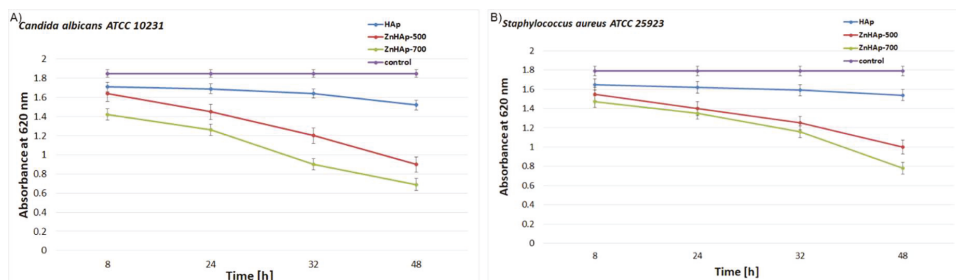
Figure 9. Cell viability assays: (**A**) *Candida albicans* ATCC 10231 cell development for 8, 24, 32, and 48 h in the presence of HAp and ZnHAp layers; (**B**) *Staphylococcus aureus* ATCC 25923 cell development for 8, 24, 32, and 48 h in the presence of ZnHAp composite layers.

The adherence and development of the *C. albicans and S. aureus* microbial cells after 24 and 48 h of incubation on the surface of the ZnHAp-500 and ZnHAp-700 layers were investigated using scanning electron microscopy (SEM). Images of the adherence and development of *C. albicans* fungal cells and *S. aureus* bacterial cells on the surfaces of the Si substrate and the ZnHAp-500 and ZnHAp-700 layers obtained from the SEM investigations are presented in Figures 10 and 11A–F.
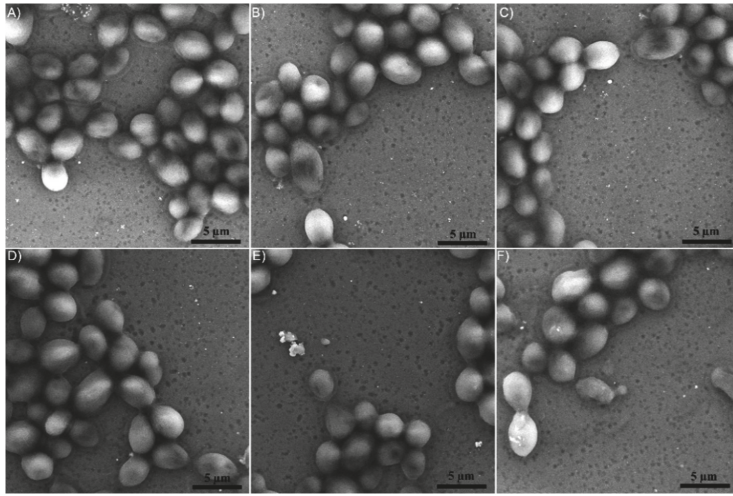
Figure 10. SEM images of *C. albicans* ATCC 10231 cell development on HAp coated Si discs used as the control (**A**,**D**), and the ZnHAp-500 and ZnHAp-700 layers after 24 h (**B**,**C**) and 48 h (**E**,**F**) of incubation.
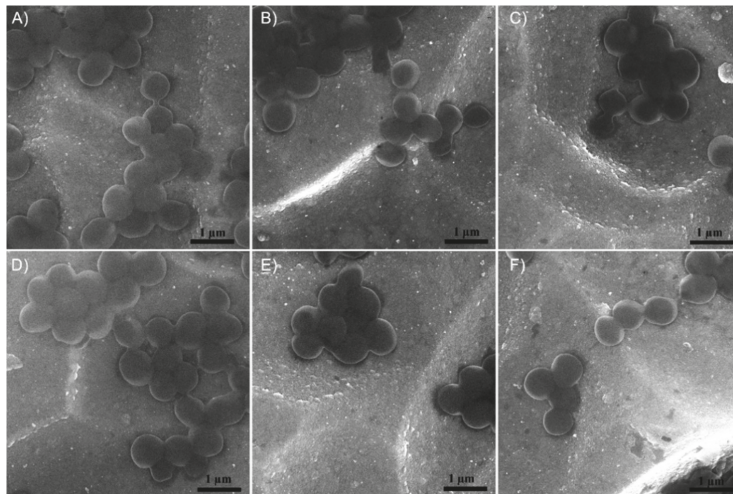
Figure 11. SEM images of *Staphylococcus aureus* ATCC 25923 cell development on HAp coated the Si discs used as the control (**A**,**D**), and the ZnHAp-500 and ZnHAp-700 layers after 24 h (**B**,**C**) and 48 h (**E**,**F**) of incubation.

The SEM visualization highlighted that the morphology of the fungal cells was characteristic to the *C. albicans* fungal strain, with an ovaloid "yeast" shape and sizes ranging from 2.8 to 4.3 μm. More than that, the SEM investigations revealed that the fungal cells had a good adherence on the HAp coated Si discs after 24 and 48 h of incubation. The images also reflect that the ZnHAp-500 and ZnHAp-700 layers presented a good inhibitory effect against the development of *C. albicans* fungal cells. As it can be seen from the SEM images, a better antifungal activity was observed in the case of the ZnHAp-700 layers for both of the tested intervals (Figure 10C,F).

The number of the adhered *Candida albicans* fungal cells on the surface of the HAp, ZnHAp-500, and ZnHAp-700 layers was quantified by performing the count of cells on three different areas of

25 μm × 25 μm of the investigated samples. The results revealed that after 24 h of incubation for the HAp sample, an average of 40 ± 4 bacterial cells were found, while for the ZnHAp-500 and ZnHAp-700 layers, an average of 24 ± 4 cells were found. More than that, after 48 h of incubation, the quantitative results of the cell counting emphasized that for the HAp samples, an average of 33 ± 3 bacterial cells were identified on the surface of the samples. In the case of ZnHAp-500, we identified approximately 18 ± 2 fungal cells, while for the ZnHAp-700 layers, the counting had revealed only approximately 15 ± 2 fungal cells on the investigated surfaces.

The SEM observation in the case of the HAp deposited on the Si discs and the ZnHAp layers incubated for 24 and 48 h with *Staphylococcus aureus* ATCC 25923 microbial suspensions, revealed that on the surface of the investigated samples, round-shaped bacterial cells with sizes between 0.5 and 0.8 μm, typical to *S. aureus* bacterial cells, were found (Figure 11A–F). SEM images in this case that in this case, the HAp deposited Si discs only slightly affected the adherence and development of the *S. aureus* bacterial cells (Figure 11A,D), and presented a small inhibitory activity towards the tested strain after both 24 and 48 h of incubation. Moreover, the SEM images indicated that both ZnHAp layers had a significant antibacterial activity against *S. aureus* ATCC 25923. Even though both of the ZnHAp layers had an inhibitory effect on the development of the bacterial cell, a stronger antibacterial activity was observed in the case of the ZnHAp-700 layers (Figure 11C,F). The SEM images accentuated that for both time intervals, the ZnHAp-700 layer had a strong inhibitory effect on the adherence and development of the *S. aureus* bacterial cells. Nonetheless, a more substantial antibacterial activity of the ZnHAp-700 layers has been identified after 48 h of incubation.

Quantitative investigations by counting the number of *S. aureus* bacterial cells adhered on the surface of HAp, and the ZnHAp-500 and ZnHAp-700 layers were performed on three different areas of 5 μm × 5 μm of the investigated samples. The results have highlighted that in the case of the HAp coating on a surface of 5 μm × 5 μm, approximately 30 ± 2 bacterial cells were counted after 24 h of incubation. Moreover, after 24 h of incubation, a drastically reduced number of bacterial cells were obtained in the case of the ZnHAp-700 layers, which had only 12 ± 2 bacterial cells, comparatively with the ZnHAp-500 layers, which allowed for the development of approximately 20 ± 3 bacterial cells. Furthermore, after 48 h of incubation, the results of the cell counting showed a decrease in the number the bacterial cells that adhered on the ZnHAp-500 sample to 15 ± 4. A small decrease after 48 h of incubation was also observed in the case of the ZnHAp-700 layers. The counted cells in this case were 10 ± 2.

3.5. Discussions

This research aimed at creating a new material with effective antimicrobial properties that could lead to a decrease of infections in implants/bone. Zinc-doped hydroxyapatite layers could help in the prevention and treatment of perioperative and intraoperative bone infections. According to previous studies [19,53–55], the zinc ion substitution in hydroxyapatite includes different aspects regarding the mechanism of inhibition of microbial growth. By bonding with the functional groups and increasing the permeability of the cells, the zinc ions cause the deterioration of the cell membranes.

In accordance with the existing literature, the most common elements used for hydroxyapatite doping are silver and zinc. It is known that silver is used in HAp doping for its antimicrobial properties, while the zinc content can lead also to increased biocompatible properties of the coating, and may contribute to the wound healing process [17,55–59].

The quality of the coatings is heavily influenced by the method of achieving it. The method of surface coating that we proposed in this study is effective because of its low costs and the fact that the most important parameters in the layers acquisition (such as solution stability) are easy to control. In our present study, the sol–gel method was used to synthesize the gel used to prepare the thin films using the sol–gel spin coating method. According to previous studies [56], the gels consist of a solid skeleton that encloses the liquid phase or solvent. The resulting sol–gel solution was evaluated from the point of view of stability using DLS, ζ-potential, and ultrasound measurements. Our studies

regarding the zeta potential value of the ZnHAp nanoparticles in the solution were in good agreement with the previous studies [56]. In previous studies conducted by Fahami et al. [56], it was shown that the ζ-potential of the HAp suspension doped with chlorine and fluorine had a negative value. Moreover, they showed that solutions that have a negative ζ-potential favor osteointegration, apathy nucleation, and bone regeneration. The stability of the ZnHAp undiluted suspension was established using an ultrasound-based technique. The ultrasound measurements gave us clear information about the stability of the suspensions. It is well known that other techniques that allow us to have information on the stability and aggregation of suspended particles require sufficiently diluted suspensions with a solids content of less than 1 vol %. Traditional techniques, despite their popularity, cannot be applied to dense or opaque suspensions. Thus, ultrasound-based technique can provide clear information, regardless of the degree of dispersion or the opacity of the suspensions, as the acoustic fields can serve as an alternative test for the dispersal state. Thus, the ultrasound measurements used to study the ZnHAp solution obtained using the sol–gel method showed a good stability, certified by the calculated stability coefficient. The stability coefficient ZnHAp undiluted suspension showed a relatively stable suspension compared to pure water. The value of the stability coefficient of the ZnHAp solution (undiluted suspension) obtained using the sol–gel method was equal to 0.0152 (1/s) vs. 0 (the coefficient of stability of the pure water).

The results presented in this study are in agreement with previous studies that have shown a good biocompatibility of the ZnHAp on human osteoblast cells MG-63 [59], mesenchymal stem cells derived from human adipose (MSCs) [32], and MRC-5 fibroblast cells [33]. Furthermore, Thian et al. [32], in their studies on "zinc-substituted hydroxyapatite: a biomaterial with enhanced bioactivity and antimicrobial properties", demonstrated that the presence of Zn^{2+} ions in the structure of the hydroxyapatite stimulated the bioactivity of HAp. On the other hand, previous research [32,55–59] provides information on the antimicrobial activity of ZnHAp against various pathogens. Radovanović et al. [33] showed that *E. coli*, *S. aureus*, *P. aeruginosa,* and *C. albicans* were susceptible to Zn–HA, and the degree of reduction was increased when the zinc ion content increased. Moreover, Tank et al. [59] showed that *S. aureus* was the most sensitive strain. Finally, we can say that the studies developed in this paper revealed that coatings based on ZnHAp have the ability to improve the biocompatibility of medical implants.

4. Conclusions

The bio layers were prepared from ZnHAp stable gels using the sol–gel spin coating method. ZnHAp in gel suspensions were evaluated by DLS, ζ-potential, and ultrasound measurements. The stability of the ZnHAp suspensions was demonstrated by both the ζ-potential and ultrasound measurements. As observed by the SEM analysis, the zinc-doped hydroxyapatite gel deposited on the Si substrate had a good crystallinity after heat treatment. The surface of the two samples (ZnHAp-500 and ZnHAp-700) analyzed was homogeneous, without showing breaks.

The cytotoxicity of the ZnHAp layers obtained using the sol–gel spin coating method were investigated using a HeLa cell line. The biocompatibility assays evidenced that the ZnHAp composite layers did not present any toxicity towards the HeLa cells.

The in vitro antimicrobial studies indicated a significantly reduced number of both *S. aures* and *C. albicans* microbial cells on the surface of the ZnHAp layers when compared to the HAp coated Si surface.

The results of this study also emphasized that the annealing temperature of the coatings had a slight influence on the biological properties of the samples. The cytotoxic assays against the microbial cells showed that ZnHAp-700 exhibited a stronger toxicity towards the cells' development for both *S. aures* and *C. albicans* cells. Overall, it was concluded that the ZnHAp layers possess a good biocompatibility and also exhibit strong antimicrobial properties, making them suitable for use in biomedical applications. The results obtained in this study could be extremely useful in the future development of antimicrobial devices with biocompatible properties.

References

1. Darouiche, R.O. Current concepts—Treatment of infections associated with surgical implants. *N. Engl. J. Med.* **2004**, *350*, 1422–1429. [CrossRef] [PubMed]

2. Vallet-Regi, M.; Arcos, D. *Biomimetic Nanoceramics in Clinical Use: From Materials to Applications*, 1st ed.; Royal Society of Chemistry: Cambridge, UK, 2008.

3. Prodan, A.M.; Beuran, M.; Turculet, C.S.; Popa, M.; Andronescu, E.; Bleotu, C.; Raita, S.M.; Soare, M.; Lupescu, O. In vitro evaluation of glycerol coated iron oxide nanoparticles in solution. *Rom. Biotechnol. Lett.* **2018**, *23*, 13901–13908.

4. Kojic, E.M.; Darouiche, R.O. *Candida* infections of medical devices. *Clin. Microbiol. Rev.* **2004**, *17*, 255–267. [CrossRef] [PubMed]

5. Chandra, J.; Guangyin, Z.; Ghannoum, M.A. Fungal biofilms and antimycotics. *Curr. Drug Targets* **2005**, *6*, 887–894. [CrossRef] [PubMed]

6. Von Eiff, C.; Jansen, B.; Kohnen, W. Infections associated with medical devices: Pathogenesis, management and prophylaxis. *Drugs* **2005**, *65*, 179–214. [CrossRef] [PubMed]

7. Predoi, D.; Iconaru, S.L.; Buton, N.; Badea, M.L.; Marutescu, L. Antimicrobial activity of new materials based on lavender and basil essential oils and hydroxyapatite. *Nanomaterials* **2018**, *8*, 291. [CrossRef] [PubMed]

8. Furko, M.; Jiang, Y.; Wilkins, T.; Balázsi, C. Development and characterization of silver and zinc doped bioceramic layer on metallic implant materials for orthopedic application. *Ceram. Int.* **2016**, *42*, 4924–4931. [CrossRef]

9. Bosetti, M.; Massé, A.; Tobin, E.; Cannas, M. Silver coated materials for external fixation devices: In vitro biocompatibility and genotoxicity. *Biomaterials* **2002**, *23*, 887–892. [CrossRef]

10. Jung, W.K.; Koo, H.C.; Kim, K.W.; Shin, S.; Kim, S.H.; Park, Y.H. Antibacterial activity and mechanism of action of the silver ion in *Staphylococcus aureus* and *Escherichia coli. Appl. Environ. Microbiol.* **2008**, *74*, 2171–2178. [CrossRef] [PubMed]

11. Schierholz, J.M.; Lucasj, L.J.; Rump, A. Efficacy of silver-coated medical devices. *J. Hosp. Infect.* **1998**, *40*, 257–262. [CrossRef]

12. Huang, Y.; Zhang, X.; Qiao, H.; Hao, M.; Zhang, H.; Xu, Z.; Zhang, X.; Pang, X.; Lin, H. Corrosion resistance and cytocompatibility studies of zinc-doped fluorohydroxyapatite nanocomposite coatings on titanium implant. *Ceram. Int.* **2016**, *42*, 1903–1915. [CrossRef]

13. Kolmas, J.; Groszyk, E.; Kwiatkowska-Róhycka, D. Substituted hydroxyapatites with antibacterial properties. *BioMed Res. Int.* **2014**, *2014*, 178123. [CrossRef] [PubMed]

14. Kurtjak, M.; Aničić, N.; Vukomanović, M. Inorganic nanoparticles: Innovative tools for antimicrobial agents. In *Antibacterial Agents*; Kumavath, R.N., Ed.; IntechOpen: London, UK, 2017.

15. Liedtke, J.; Vahjen, W. In vitro antibacterial activity of zinc oxide on a broad range of reference strains of intestinal origin. *Vet. Microbiol.* **2012**, *160*, 251–255. [CrossRef] [PubMed]

16. Iconaru, S.L.; Prodan, A.M.; Turculet, C.S.; Beuran, M.; Ghita, R.V.; Costescu, A.; Groza, A.; Chifiriuc, M.C.; Chapon, P.; Gaiaschi, S.; et al. Enamel based composite layers deposited on titanium substrate with antifungal activity. *J. Spectrosc.* **2016**, *2016*, 4361051. [CrossRef]

17. Groza, A.; Ciobanu, C.S.; Popa, C.L.; Iconaru, S.L.; Chapon, P.; Luculescu, C.; Ganciu, M.; Predoi, D. Structural properties and antifungal activity against *Candida albicans* biofilm of different composite layers based on Ag/Zn doped hydroxyapatite-polydimethylsiloxanes. *Polymers* **2016**, *8*, 131. [CrossRef]

18. Ciobanu, C.S.; Massuyeau, F.; Constantin, L.V.; Predoi, D. Structural and physical properties of antibacterial Ag-doped nano-hydroxyapatite synthesized at 100 °C. *Nanoscale Res. Lett.* **2011**, *6*, 613. [CrossRef] [PubMed]

19. Predoi, D.; Iconaru, S.L.; Deniaud, A.; Chevallet, M.; Michaud-Soret, I.; Buton, N.; Prodan, A.M. Textural, structural and biological evaluation of hydroxyapatite doped with zinc at low concentrations. *Materials* **2017**, *10*, 229. [CrossRef] [PubMed]

20. Popa, C.L.; Deniaud, A.; Michaud-Soret, I.; Guégan, R.; Motelica-Heino, M.; Predoi, D. Structural and biological assessment of zinc doped hydroxyapatite nanoparticles. *J. Nanomater.* **2016**, *2016*, 1062878. [CrossRef]

21. Ciobanu, C.S.; Popa, C.L.; Predoi, D. Sm:HAp Nanopowders present antibacterial activity against *Enterococcus faecalis*. *J. Nanomater.* **2014**, *2014*, 780686. [CrossRef]

22. Zebarjad, S.M.; Sajjadi, S.A.; Ebrahimi Sdrabadi, T.; Sajjadi, S.A.; Yaghmaei, A.; Naderi, B. A Study on mechanical properties of PMMA/hydroxyapatite nanocomposite. *Engineering* **2011**, *3*, 795–801. [CrossRef]

23. Prasadh, S.; Wong, R.C.W. Unraveling the mechanical strength of biomaterials used as a bone scaffold in oral and maxillofacial defects. *Oral Sci. Int.* **2018**, *15*, 48–55. [CrossRef]

24. Predoi, D.; Iconaru, S.L.; Predoi, M.V. Bioceramic layers with antifungal properties. *Coatings* **2018**, *8*, 276. [CrossRef]

25. Turculet, C.S.; Prodan, A.M.; Negoi, I.; Teleanu, G.; Popa, M.; Andronescu, E.; Beuran, M.; Stanciu, G.A.; Hristu, R.; Badea, M.L.; et al. Preliminary evaluation of the antifungal activity of samarium doped hydroxyapatite thin films. *Rom. Biotechnol. Lett.* **2018**, *23*, 13928–13932.

26. Andronescu, E.; Iordache, F.; Ciobanu, C.S.; Badea, M.L.; Costescu, A.; Prodan, A. Optical properties of bioactive europium doped hydroxyapatite (HAp:Eu^{3+}). *Optoelectron. Adv. Mat.* **2015**, *9*, 1155–1159.

27. Negrila, C.C.; Predoi, M.V.; Iconaru, S.L.; Predoi, D. Development of Zinc-doped hydroxyapatite by sol–gel method for medical applications. *Molecules* **2018**, *23*, 2986. [CrossRef] [PubMed]

28. Johal, K.K. In vivo response of strontium and zinc-based ionomeric cement implants in bone. *J. Mater. Sci. Mater. Med.* **2002**, *13*, 375–379. [CrossRef] [PubMed]

29. Yamaguchi, M. Role of zinc in bone formation and bone resorption. *J. Trace Elem. Exp. Med.* **1998**, *11*, 119–135. [CrossRef]

30. Ohtsu, N.; Kakuchi, Y.; Ohtsuki, T. Antibacterial effect of zinc oxide/hydroxyapatite coatings prepared by chemical solution deposition. *Appl. Surf. Sci.* **2018**, *445*, 596–600. [CrossRef]

31. Iconaru, S.L.; Prodan, A.M.; Buton, N.; Predoi, D. Structural characterization and antifungal studies of zinc-doped hydroxyapatite coatings. *Molecules* **2017**, *22*, 604. [CrossRef] [PubMed]

32. Thian, E.S.; Konishi, T.; Kawanobe, Y.; Lim, P.N.; Choong, C.; Ho, B.; Aizawa, M. Zinc-substituted hydroxyapatite: A biomaterial with enhanced bioactivity and antibacterial properties. *J. Mater. Sci. Mater. Med.* **2013**, *24*, 437–445. [CrossRef] [PubMed]

33. Radovanović, Ž.; Veljović, D.; Jokić, B.; Dimitrijević, S.; Bogdanović, G.; Kojić, V.; Petrović, R.; Janaćković, D. Biocompatibility and antimicrobial activity of zinc(II)-doped hydroxyapatite, synthesized by a hydrothermal method. *J. Serb. Chem. Soc.* **2012**, *77*, 1787–1798. [CrossRef]

34. Adamiak, B.; Wiatrowski, A.; Domaradzki, J.; Kaczmarek, D.; Wojcieszak, D.; Mazur, M. Preparation of multicomponent thin films by magnetron co-sputtering method: The Cu–Ti case study. *Vacuum* **2019**, *161*, 419–428. [CrossRef]

35. Rajendra Kumar, R.T.; Karunagaran, B.; Senthil Kumar, V.; Jeyachandran, Y.L.; Mangalaraj, D.; Narayandass, S.K. Structural properties of V$_2$O$_5$ thin films prepared by vacuum evaporation. *Mater. Sci. Semicond. Process.* **2003**, *6*, 543. [CrossRef]

36. Wang, X.; Shi, F.; Gao, X.; Fan, C.; Huang, W.; Feng, X. A sol–gel dip/spin coating method to prepare titanium oxide films. *Thin Solid Films* **2013**, *548*, 34–39. [CrossRef]

37. Calnan, S.; Upadhyaya, M.H.; Dann, E.S.; Thwaites, J.M.; Tiwari, N.A. Effects of target bias voltage on indium tin oxide films deposited by high target utilisation sputtering. *Thin Solid Films* **2007**, *515*, 8500–8504. [CrossRef]

38. Yuen, C.; Yu, S.F.; Leong, E.S.P.; Lau, S.P.; Pita, K.; Yang, H.Y.; Chen, T.P. Room temperature deposition of p-type arsenic doped ZnO polycrystalline films by laser-assist filtered cathodic vacuum arc technique. *J. Appl. Phys.* **2007**, *101*, 094905. [CrossRef]

39. Gurav, K.V.; Patil, U.M.; Shin, S.W.; Pawar, S.M.; Kim, J.H.; Lokhande, C.D. Morphology evolution of ZnO thin films from aqueous solutions and their application to liquefied petroleum gas (LPG) sensor. *J. Alloy. Compd.* **2012**, *525*, 1–7. [CrossRef]

40. Jamesh, M.; Kumar, S.; Sankara Narayanan, T.S.N. Electrodeposition of hydroxyapatite coating on magnesium for biomedical applications. *J. Coat. Technol. Res.* **2012**, *9*, 495–502. [CrossRef]

41. Hornberger, H.; Virtanen, S.; Boccaccini, A.R. Biomedical coatings on magnesium alloys—A review. *Acta Biomater.* **2012**, *8*, 2442–2455. [CrossRef] [PubMed]

42. Wen, C.E.; Xu, W.; Hu, W.Y.; Hodgson, P.D. Hydroxyapatite/titania sol–gel coatings on titanium–zirconium alloy for biomedical applications. *Acta Biomater.* **2007**, *3*, 403–410. [CrossRef] [PubMed]

43. Kakimoto, M.-A.; Suzuki, M.-A.; Konishi, T.; Imai, Y.; Iwamoto, M.; Hino, T. Preparation of mono- and multilayer films of aromatic polyimides using Langmuir-Blodgett technique. *Chem. Lett.* **1986**, *15*, 823–826. [CrossRef]

44. Tsay, C.Y.; Fan, K.S.; Wang, Y.W.; Chang, C.J.; Tseng, Y.K.; Lin, C.K. Transparent semiconductor zinc oxide thin films deposited on glass substrates by sol-gel process. *Cermic. Int.* **2010**, *36*, 1791–1795. [CrossRef]

45. Emslie, A.G.; Bonner, F.T.; Peck, L.G. Flow of a viscous liquid on a rotating disk. *J. Appl. Phys.* **1958**, *29*, 858–862. [CrossRef]

46. Motelica-Heino, M.; Donard, O.F. Comparison of UV and IR laser ablation ICP-MS on silicate reference materials and implementation of normalisation factors for quantitative measurements. *Geostand. Geoanal. Res.* **2001**, *25*, 345–359. [CrossRef]

47. *ASTM E2149–13a Standard Test Method for Determining the Antimicrobial Activity of Antimicrobial Agents under Dynamic Contact Conditions*; ASTM International: West Conshohocken, PA, USA, 2013.

48. Fuchs, A.V.; Ritz, S.; Pütz, S.; Mailänder, V.; Landfester, K.; Ziener, U. Bioinspired phosphorylcholine containing polymer films with silver nanoparticles combining antifouling and antibacterial properties. *Biomater. Sci.* **2013**, *1*, 470–477. [CrossRef]

49. Ciobanu, C.S.; Iconaru, S.L.; Gyorgy, E.; Radu, M.; Costache, M.; Dinischiotu, A.; Le Coustumer, P.; Lafdi, K.; Predoi, D. Biomedical properties and preparation of iron oxide-dextran nanostructures by MAPLE technique. *Chem. Cent. J.* **2012**, *6*, 17. [CrossRef] [PubMed]

50. Egelhaaf, S.U.; Wehrli, E.; Muller, M.; Adrian, M.; Schurtenberger, P. Determination of the size distribution of lecithin liposomes: A comparative study using freeze fracture, cryoelectron microscopy and dynamic light scattering. *J. Microsc.* **1996**, *184*, 214–228. [CrossRef]

51. Xu, G.; Aksay, I.A.; Groves, J.T. Continuous crystalline carbonate apatite thin films. A Biomimetic approach. *J. Am. Chem. Soc.* **2001**, *123*, 2196–2203. [CrossRef] [PubMed]

52. Jokanovic, V.; Uskokovic, D. Calcium hydroxyapatite thin films on titanium substrates prepared by ultrasonic spray pyrolysis. *Mater. Trans.* **2005**, *46*, 228–235. [CrossRef]

53. Anwar, A.; Akbar, S.; Sadiqa, A.; Kazmi, M. Novel continuous flow synthesis, characterization and antibacterial studies of nanoscale zinc substituted hydroxyapatite bioceramics. *Inorg. Chim. Acta* **2016**, *453*, 16–22. [CrossRef]

54. Chen, X.; Tang, Q.L.; Zhu, Y.J.; Zhu, C.L.; Feng, X.P. Synthesis and antibacterial property of zinc loaded hydroxyapatite nanorods. *Mater. Lett.* **2012**, *89*, 233–235. [CrossRef]

55. Ren, F.; Xin, R.; Ge, X.; Leng, Y. Characterization and structural analysis of zinc-substituted hydroxyapatites. *Acta Biomater.* **2009**, *5*, 3141–3149. [CrossRef] [PubMed]

56. Ben-Nissan, B.; Choi, A.H. Sol–gel production of bioactive nano-coatings for medical applications. Part 1: An introduction. *Nanomedicine* **2006**, *1*, 311–319. [CrossRef] [PubMed]

57. Fahami, A.; Beall, G.W.; Betancourt, T. Synthesis, bioactivity and zeta potential investigations of chlorine and fluorine substituted hydroxyapatite. *Mater. Sci. Eng. C Mater. Biol. Appl.* **2016**, *59*, 78–85. [CrossRef] [PubMed]

58.	Zhang, J. Biocompatibility and anti-bacterial activity of Zn-containing HA/TiO$_2$ hybrid coatings on Ti substrate. *J. Hard. Tissue Biol.* **2013**, *22*, 311–318. [CrossRef]

59.	Tank, K.P.; Chudasama, K.S.; Thaker, V.S.; Joshi, M.J. Pure and zinc doped nano-hydroxyapatite: Synthesis, characterization, antimicrobial and hemolytic studies. *J. Cryst. Growth* **2014**, *401*, 474–479. [CrossRef]

A Comprehensive Microstructural and Compositional Characterization of Allogenic and Xenogenic Bone: Application to Bone Grafts and Nanostructured Biomimetic Coatings

Gabriela Graziani [1], Marco Govoni [2,*], Leonardo Vivarelli [2], Marco Boi [1], Monica De Carolis [1], Michele Bianchi [3], Enrico Sassoni [4], Maria Chiara Bignozzi [4], Gianluca Carnevale [5], Federico Marmi [2], Maria Cristina Maltarello [6] and Dante Dallari [2]

[1] Laboratory of NanoBiotechnology, IRCCS Istituto Ortopedico Rizzoli, Via di Barbiano 1/10, 40136 Bologna, Italy; gabriela.graziani@ior.it (G.G.); marco.boi@ior.it (M.B.); monica.decarolis2@unibo.it (M.D.C.)

[2] Reconstructive Orthopaedic Surgery and Innovative Techniques–Musculoskeletal Tissue Bank, IRCCS Istituto Ortopedico Rizzoli, Via G.C. Pupilli 1, 40136 Bologna, Italy; leonardo.vivarelli@ior.it (L.V.); federico.marmi@ior.it (F.M.); dante.dallari@ior.it (D.D.)

[3] Center for Translational Neurophysiology of Speech and Communication, Istituto Italiano di Tecnologia, Via Fossato di Mortara 17-19, 44121 Ferrara, Italy; Michele.Bianchi@iit.it

[4] Department of Civil, Chemical, Environmental and Materials Engineering (DICAM), University of Bologna, via Terracini 28, 40131 Bologna, Italy; enrico.sassoni2@unibo.it (E.S.); maria.bignozzi@unibo.it (M.C.B.)

[5] Department of Surgery, Medicine, Dentistry and Morphological Sciences with Interest in Transplant, Oncology and Regenerative Medicine, University of Modena and Reggio Emilia, via del Pozzo 71, 41124 Modena, Italy; gcarneva@unimore.it

[6] Laboratory of Musculoskeletal Cell Biology, IRCCS Istituto Ortopedico Rizzoli, Via di Barbiano 1/10, 40136 Bologna, Italy; mariacristina.maltarello@ior.it

* Correspondence: marco.govoni@ior.it

Abstract: Bone grafts and bone-based materials are widely used in orthopedic surgery. However, the selection of the bone type to be used is more focused on the biological properties of bone sources than physico-chemical ones. Moreover, although biogenic sources are increasingly used for deposition of biomimetic nanostructured coatings, the influence of specific precursors used on coating's morphology and composition has not yet been explored. Therefore, in order to fill this gap, we provided a detailed characterization of the properties of the mineral phase of the most used bone sources for allografts, xenografts and coating deposition protocols, not currently available. To this aim, several bone apatite precursors are compared in terms of composition and morphology. Significant differences are assessed for the magnesium content between female and male human donors, and in terms of Ca/P ratio, magnesium content and carbonate substitution between human bone and different animal bone sources. Prospectively, based on these data, bone from different sources can be used to obtain bone grafts having slightly different properties, depending on the clinical need. Likewise, the suitability of coating-based biomimetic films for specific clinical musculoskeletal application may depend on the type of apatite precursor used, being differently able to tune surface morphology and nanostructuration, as shown in the proof of concepts of thin film manufacturing here presented.

1. Introduction

Bone grafts and bone-based materials are widely used in orthopedic surgery in the form of blocks, granulates and cements, to replace missing bone stock and favor bone regeneration. To this aim, it is widely acknowledged that autografts can guarantee the best efficacy, but lack of availability and need for invasive withdrawal procedure limit their use [1]. For this reason, allografts, xenografts and synthetic substitutes are normally preferred in the clinical practice [2,3]. In addition, synthetic bone-based materials have been engineered to avoid the potential of human disease transmission and immunogenicity, and they have the advantage of being available in unlimited quantities, but they are normally regarded only as osteoconductive. On the other hand, bone derived from human and animal sources is commonly considered both osteoconductive and osteoinductive. In addition, based on the biomimetic principle, a material as similar as possible to the host bone is recommended to allow for the best biological behavior [4–6]. Therefore, both allografts and xenografts are extensively used. The use of bone-derived materials is raising increasing interest in the literature, also for what regards advanced biomedical devices, and in particular for particles, granulates and biomimetic coatings [7–16]. The latter are a newer application of biogenic bone, but they are raising increasing interest, thanks to the increasing capability of plasma-assisted techniques to transfer the composition of the target to the coatings, which makes deposition from biogenic sources one of the fastest and more reliable ways to obtain multi-substituted biomimetic thin films. While human, bovine, equine and, to a lower extent, porcine and ovine bone are used for the grafts and the granulates, coatings are normally obtained by animal bone (ovine and bovine bone).

However, the exact composition of bone is known to be largely dependent on several factors, such as animal species, sex of the donor, age, anatomical site, specific characteristics of the donor, possible pathologies, level of physical activity and alimentation [5,6,17–19]. Several studies focus on the characterization of bone substitutes from a mechanical point of view [20], while only few deals with the characterization of the physico-chemical properties of bone apatite deriving from different human and animal sources. The latter generally take into exam characterization of the effects of calcination or other deproteinization procedures [21–23], materials of interest for dentistry, such as animal and human teeth [24–28] or focus on goals different from medicine [29–32]. At present, to the Authors' best knowledge, no studies exist that carry out an extensive and comparative evaluation of composition of bone grafts used in the biomedical field. In fact, to date, the choice of bone substitutes is mainly based on the surgeon's experience, while understanding the physico-chemical properties of bone would allow a better selection of the most appropriate treating option. Therefore, here, we investigate the physico-chemical and morphological properties of human and animal bone to better understand their main characteristics in terms of composition and their variability, for three main aims:

- Understanding physico-chemical variability among human bone, also depending on the sex of the donor. To this aim, the main parameters influencing the behavior of biological (as well as synthetic) hydroxyapatite (HA—$Ca_{10}(PO_4)_6OH_2$)—i.e., phase composition, crystallinity, Ca/P ratio, content of magnesium—are investigated;
- Comparing the composition of human bone to that of different animal species, commonly used as bone grafts, to understand their effective similarity to host bone;
- Understanding the differences that exist between different sources and how they are translated in clinics when bone is used for biomedical devices. This is particularly relevant for coatings, where obtaining a bone-like composition and the preserving stoichiometry from the deposition target to the film is particularly challenging [6].

To this regard, compared to grafts, powders and granulates, in the coatings, plasma assisted deposition can cause significant alterations in phase composition of the starting material, including formation of decomposition phases [33]. In addition, pre/post deposition thermal treatments are commonly used to tune crystallinity, which can also cause modifications in the composition of the film. This can enhance, or mask, eventual differences between the precursors, in an unpredictable way. For this

reason, here, nanostructured coatings are manufactured starting from different animal precursors and human male/female bone, to understand if the differences in the composition of bone can be translated in differences in the achieved coatings, or can lead to the presence of metastable/decomposition phases.

Ionized Jet Deposition (IJD) is selected for the deposition, which is a plasma assisted technique, recently proposed for the development of biomimetic thin films [12]. Briefly, in IJD, a target material is ablated by a fast pulse, high energy electron beam, causing the formation of a plasma plume, that is accelerate towards a substrate, where it grows as a nanostructured thin film. Previously, the authors have demonstrated that IJD permits to transfer the exact composition of the target to the coatings, without leading to the formation of decomposition phases [7,12]. In addition, when depositing bone-apatite, transfer of trace ions is permitted, so that the films strongly resembles the composition of bone. IJD is very sensitive to the exact composition and mechanical characteristics of the targets, therefore here, the deposition of different biogenic sources is explored, to understand: (i) how the changes in the precursors impact on the characteristics of the coatings and (ii) the suitability of the use of each animal and human source.

2. Materials and Methods

2.1. Sample Collection

Human bone samples were provided by the Muskoloskeletal Tissue Bank of IRCCS Istituto Ortopedico Rizzoli (Bologna, Italy), in accordance with the approval of the Local Ethics Committee (cod. 75/17). In this study, only specimens not suitable for transplantation and considered as waste materials were used, according to the Italian law and National Transplantation Center's guidelines. From 9 human cadaveric donors, 4 male and 5 female, 11 specimens were obtained to have sufficient data while minimizing the number of samples collected. All samples were collected from the same anatomical site, by retrieving a 5 mm thick ring from the lesser trochanter, about 2 cm below the femoral epiphysis. Two femurs were found positive to microbiological controls and irradiated with gamma rays following the Tissue Bank guidelines. Literature studies indicate that significant differences arise in biological and mechanical properties of bones, following gamma irradiation [34–37]. For this reason, samples from these femurs were included in the experimentation, to preliminary assess if and how the irradiation can also cause alterations in bone composition.

Bone tissue from different animal species (ovine, bovine, porcine, equine) was compared. Three samples were selected for each animal species, based on preliminary tests aimed at evaluating variability inside each species. As for humans, for each species, all samples were taken from the same area, i.e., femoral diaphysis, so that the results could be negligent of differences caused by the anatomical site. Animal shafts were obtained by different local butchers from adult animals (age range: ovine, 8–10 months; porcine, 5–7 months; bovine, 8–12 months; equine, 12–15 months). All samples were stored at −80 °C until experimental analysis.

2.2. Sample Preparation

All human and animal samples were thawed overnight at 4 °C and then deproteinized by stirring in 2.6 wt.% solution of NaOCl in deionized water to remove the organic components [38–41].

Efficacy of deproteinization was verified by Fourier-Transform Infrared spectroscopy (FT-IR, Spectrum Two, PerkinElmer, Waltham, MA, USA) at 7, 14 and 21 days of bleaching and thermal gravimetric analysis (TGA, Q50, TA Instrument, New Castle, DE, USA) at 14 and 21 days. Based on the results, all samples were deproteinized by immersion for 14 days, except for ovine bone, for which the deproteinization process was extended up to 21 days.

Samples were labeled in semi-anonymized form by an alphanumeric code, as listed in Table 1.

Table 1. Samples for human donors. Letters F (female) or M (male) indicate the donor gender, while numbers are referred to the batch record of processed tissues. Samples indicated by the letter "γ" were subjected to sterilization with gamma rays.

Gender	Amount	Name	Median Age	Age Range
Female	7	F34, F41, F43, F46, F46γ, F78, F78γ	49.4 years	47–52 years
Male	4	M40, M45, M47, M69	57.8 years	53–60 years

Moreover, as stated above, for two donors (F46 and F78), both femurs were collected and one of each has been treated by gamma rays, as found positive to microbiological controls, according to the procedure normally followed by the Tissue Bank. The minimum validated dose for sterilization by gamma irradiation is 25 kGy, in accordance with ISO 11137-2:2013 [42]. However, this dose is usually exceeded to ensure thorough sterilization. A dosage range of 25.9–34.5 kGy was used in F46γ and F78γ, as reported in the sterility documentation provided by Sterigenics S.p.A (Bologna, Italy) and Gammatom S.r.l (Como, Italy).

2.3. Sample Characterization

Morphology and elemental composition were analyzed by a Scanning Electron Microscope (SEM, EVO/MA10, ZEISS, Oberkochen, Germany) equipped with an Energy Dispersive X-ray (EDS, INCA Energy 200, Oxford Instruments, Abingdon-on-Thames, UK). The EDS analyses were performed on three different zones of each sample and averaged. The spectrum was acquired at an operating voltage of 15 kV. Samples (1 cm × 0.5 cm × 0.5 cm) were left uncoated for the analyses.

Sample composition was assessed by Fourier transform infrared spectroscopy (FTIR-ATR, Spectrum 2, acquisition parameters: resolution 1 cm^{-1}, accumulation 64 scans, data interval 0.5 cm^{-1}, PerkinElmer, Waltham, MA, USA). Phase structure and crystallinity of the samples has been investigated by X-rays diffractometry (XRD, X'Pert PRO, Malvern Panalytical, Malvern, UK, φ = 5°–80°, scan step size 0.017°, time per step 50 s). XRD data were filtered (five-point linear averaging) using the Matlab software (v. R2014b, MathWorks, Natick, MA, USA) to obtain a better graphic representation.

Both FT-IR and XRD were carried out on powders, obtained by manually grinding the samples in an agate mortar.

To highlight differences between the samples, all FT-IR spectra were scaled with respect to the band at 1030 cm^{-1} (phosphate stretching). By doing so, differences in relative amount of phases that constitute the samples (e.g., carbonates vs. phosphates, metastable phases/hydroxyapatite) can be qualitatively evaluated. All XRD spectra were scaled with respect to the peak at 2θ = 31.7° (peak intensity 100% of hydroxyapatite), which is the main peak for all the examined spectra. By doing so, possible differences in the phase composition of the samples (i.e., presence of soluble phases alongside hydroxyapatite), could be qualitatively detected.

Based on these tests, the following parameters were assessed, all being crucial into determining the solubility of biogenic apatite and the type and amount of ions released in the peri-implant environment:

- Ca/P ratio (EDS);
- Magnesium content (EDS);
- Carbonate content (FT-IR);
- Presence/absence of metastable phase different from hydroxyapatite (FT-IR, XRD);
- Crystallinity (XRD).

2.4. Coatings Manufacturing and Characterization

Biomimetic bone apatite coatings have been recently proposed by the authors [8,12], manufactured by an Ionized Jet Deposition (IJD). Here, deposition from different sources is compared.

For deposition of the biomimetic coatings, bone from each source is deproteinized, as described above, to remove organic traces that could hamper coatings uniformity and/or adhesion to the substrate.

Then, they are shaped in the form of disks (2.5 cm diameter, 5 mm thickness), suitable for IJD deposition. After shaping, the disks are mounted on rotating holders in the deposition chamber, to ensure uniformity of deposition. Here, silicon wafers are used as substrates, as they permit a better evaluation of coatings morphology, being atomically flat. Deposition is carried out at room temperature, in the very same way for each precursor, i.e., keeping all deposition parameters constant (substrate-target distance, voltage, frequency, deposition time). Based on preliminary results obtained for bovine bone [7,8], the following deposition parameters are selected: substrate-target distance 8 cm, voltage 18 kV, frequency 7 kHz, deposition time 30 min. Substrate-target distance is selected to ensure uniformity in depositions on the samples, while voltage and frequency must allow optimal ablation and formation of a plasma plume at each pulse of the electron beam. Deposition time, instead, determines film thickness, here corresponding to about 450 nm thickness. This thickness was selected based on the optimization of adhesion to substrate, absence of cracks and delamination and based on in vitro tests on dental pulp stem cells [8]. After deposition, all coatings are annealed for 1 h in air at 400 °C, to tune crystallinity up to resembling that of bone.

After deposition, morphology (SEM) and composition (FT-IR) of the films are examined to detect differences in morphology and/or composition between the different films.

2.5. Statistical Analysis

Statistical analysis is performed using GraphPad Prism ver. 6 (http://www.graphpad.com). EDS data are expressed as mean ± standard deviation and comparison between groups is performed using the two-tailed, unpaired Student's *t*-test. Differences are considered significant for $p < 0.05$.

3. Results

3.1. Human Specimens

3.1.1. Bone Morphology

Human specimens have been characterized in terms of morphology, as shown in Figure 1. For clarity's sake, only a part of the samples is reported in Figure 1, while SEM images for all specimens are in the Supplementary Material, Figures S1 and S2.
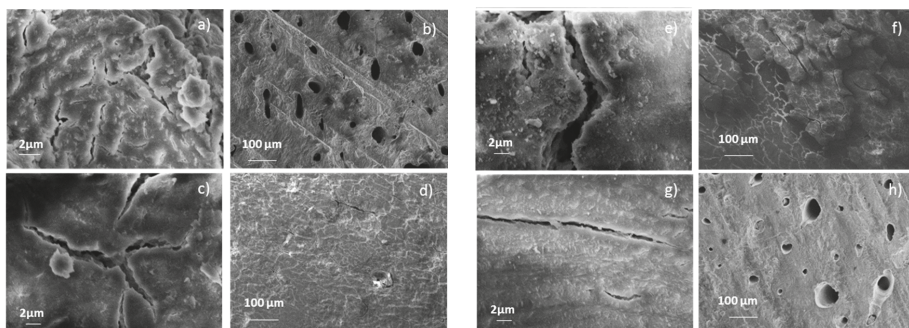
Figure 1. SEM images of representative female and male donor bone samples: F34 (**a**,**b**), F41 (**c**,**d**), M40 (**e**,**f**), M45 (**g**,**h**).

Significant differences are found concerning the morphology of bone samples, as variable amount, dimension and shape of pores are found between different specimens, though not correlated to donor gender. Although mercury intrusion porosimetry would be needed to quantify total open porosity and pore size distribution, a qualitative evaluation can be already obtained by SEM images, as the differences between different samples are significant and highly reproducible.

3.1.2. Phase and Elemental Composition

Phase composition has been investigated by FT-IR and XRD. Results are in Figure 2a,b, respectively.
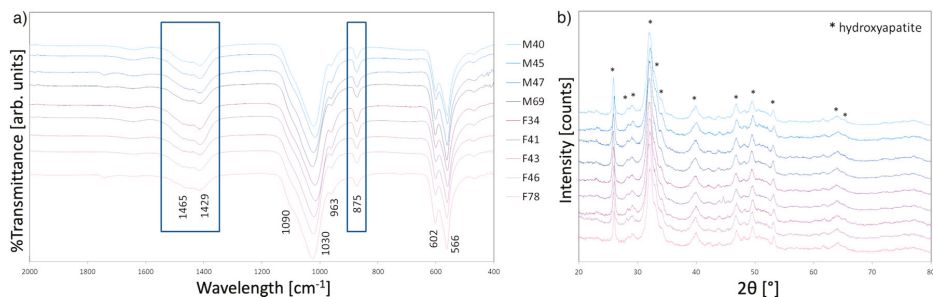
Figure 2. Composition of human bone samples: (**a**) FT-IR and (**b**) XRD spectra. Bands characteristic of CHA (1465, 1429, 875 cm^{-1}) [43,44] and HA (1090, 1030, 963, 602, 566 cm^{-1}) [45,46] are detected in FT-IR graphs, while all peaks detected in XRD patterns are characteristic of hydroxyapatite.

FT-IR spectra exhibit bands characteristic of hydroxyapatite and carbonated hydroxyapatite [43–46]. All samples exhibit bands at 1465, 1429 cm^{-1} (asymmetrical and symmetrical stretching modes of $CO_3\nu_3$), 870 cm^{-1} ($CO_3\nu_2$), 1030 cm^{-1} (antisymmetric stretching mode ν_3PO_4), 963 cm^{-1} (ν_1PO_4 symmetric stretch), 602 and 566 cm^{-1} (ν_4PO_4 antisymmetric bend), 469 cm^{-1} (ν_2PO_4 bend).

FT-IR spectra evidence a non-negligible variability in the amplitude of carbonate bands (1465, 1429, 870 cm^{-1}) compared to phosphates (1030 cm^{-1}) between different human donors. This could be ascribed to a different level of carbonate substitutions in the samples. On the other hand, no significant differences are evidenced between bone deriving from female and male donors.

XRD spectra exhibit peaks characteristic of scarcely crystalline hydroxyapatite. No bands relative to octacalcium phosphate (OCP, $Ca_8H_2(PO_4)_6 \cdot 5H_2O$) or other metastable calcium phosphate phases are detected.

In addition, no differences are assessed between the composition of the different samples, regardless sex and age of the donors.

Elemental composition of human specimens has been investigated by EDS and results are summarized in Table 2. Sodium and chloride ions are neglected because could suffer alterations due to deproteinization procedure in NaOCl.

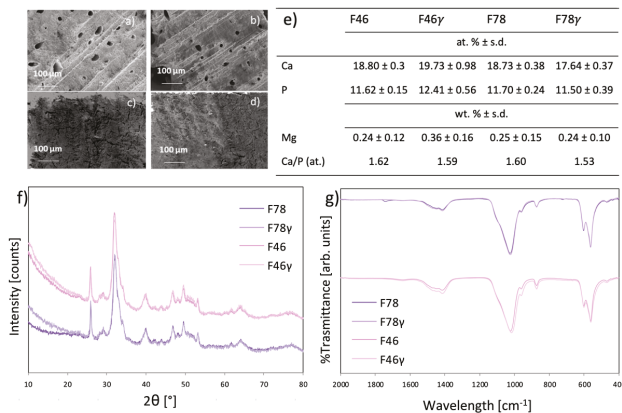**Table 2.** EDS elemental composition of human bone specimens.

Element	F43	F34	F46	F78	M45	M69	M47	M40
	at.%	at.%	at.%	at.%	at.%	at.%	at.%	at.%
Ca	18.61 ± 0.34	20.29 ± 1.41	18.80 ± 0.30	18.78 ± 0.38	17.04 ± 0.23	19.72 ± 0.84	17.57 ± 1.05	19.02 ± 1.08
P	11.47 ± 0.7	12.43 ± 0.75	11.62 ± 0.16	11.70 ± 0.24	11.08 ± 0.11	12.43 ± 0.35	10.19 ± 1.32	11.40 ± 0.30
Ca/P(at.)	1.62	1.63	1.62	1.6	1.54	1.58	1.72	1.67
Element	wt.%	wt.%	wt.%	wt.%	wt.%	wt.%	wt.%	wt.%
Ca	33.40 ± 0.54	35.48 ± 1.78	33.65 ± 0.41	33.31 ± 0.62	31.17 ± 0.35	34.62 ± 1.12	31.64 ± 1.43	33.95 ± 1.54
P	15.91 ± 0.93	16.81 ± 0.69	16.07 ± 0.24	16.09 ± 0.30	15.66 ± 0.19	16.88 ± 0.34	14.17 ± 1.62	15.74 ± 0.42
Mg	0.30 ± 0.08	0.22 ± 0.02	0.24 ± 0.12	0.25 ± 0.15	0.33 ± 0.11	0.39 ± 0.15	0.26 ± 0.16	0.37 ± 0.18
Element	All Female wt.% ± s.d.				All Male wt.% ± s.d.			
Mg	0.26 ± 0.10				0.34 ± 0.14			
Ca/P(at.)	1.62 ± 0.01				1.63 ± 0.08			

Human bone exhibits relevant differences in terms of trace content of magnesium ions, as also indicated by the high values of standard deviation. To this regard, a significant difference ($p = 0.0436$) is highlighted between female donors and male donors, the latter exhibiting a high content of magnesium.

Ca/P ratio, instead exhibits negligible variations between female and male donors, although the latter have higher internal variability.

3.1.3. Gamma Irradiation Effect

The effect of gamma irradiation on morphology and composition of two human bone specimens has also been investigated, and results are reported in Figure 3.


e)	F46	F46γ	F78	F78γ
	at. % ± s.d.			
Ca	18.80 ± 0.3	19.73 ± 0.98	18.73 ± 0.38	17.64 ± 0.37
P	11.62 ± 0.15	12.41 ± 0.56	11.70 ± 0.24	11.50 ± 0.39
	wt. % ± s.d.			
Mg	0.24 ± 0.12	0.36 ± 0.16	0.25 ± 0.15	0.24 ± 0.10
Ca/P (at.)	1.62	1.59	1.60	1.53

Figure 3. Representative SEM images of human samples F46 (**a**), F46γ (**b**), F78 (**c**), F78γ (**d**) and (**e**) EDS elemental composition, (**f**) FT-IR and (**g**) XRD spectra of the irradiated and not irradiated samples.

Gamma irradiation results in an increase in samples fragility, causing a significant mass loss. This significantly alters morphology at the macro-scale. However, morphology at the microscale (SEM) is not affected by the process. Quite alterations are present in sample composition in terms of magnesium content and Ca/P ratio. Instead, phase composition remains substantially unaltered.

3.2. Animal Specimens

3.2.1. Bone Morphology

Animal bone morphology is shown in Figure 4. First, animal bone exhibits a significant difference in morphology, depending on the animal species. For instance, ovine bone is much less compact than bovine and equine bone (Figure 4g,h).
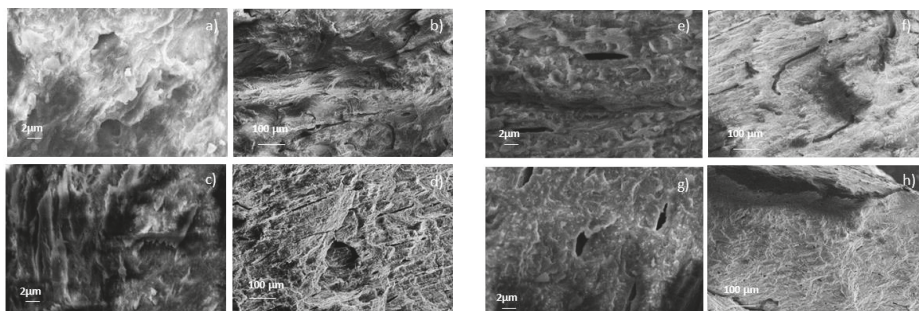
Figure 4. SEM images of bovine bone (**a**,**b**), porcine bone (**c**,**d**), equine bone (**e**,**f**) and ovine bone (**g**,**h**). Right (magnitude = 200×), left (magnitude = 5000×).

3.2.2. Phase and Elemental Composition

Animal bone composition is shown in Figure 5. Only two spectra are reported for each animal species, i.e., those exhibiting the most marked differences (for FT-IR, the spectra having the carbonates bands of lowest and highest intensity, for XRD those exhibiting the main differences in the intensity of secondary peaks).
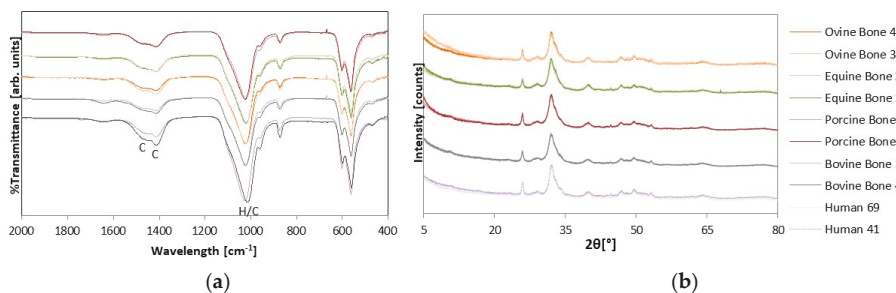
Figure 5. (**a**) FT-IR spectra of the animal and human precursors: bands characteristic of CHA (1455, 1419, 875 cm^{-1}) [43,44] and HA (1090, 1030, 600, 570 cm^{-1}) [45,46] and HA (1090, 1030, 963, 602, 566 cm^{-1} [47,48] are detected); (**b**) XRD patterns of the animal and human precursors: all peaks detected are characteristic of hydroxyapatite.

All samples exhibit almost the same phase composition, regardless of the animal source. As reported in Figure 5, the content of carbonate is lower for bovine bone. On the other hand, content of magnesium is maximum for bovine and ovine and minimum for equine (Table 3), showing a significant difference between ovine vs. equine ($p = 0.0173$) and bovine vs. equine ($p = 0.0018$). No significant differences are assessed when porcine bone is compared to the other animal sources.

Table 3. Differences in EDS elemental composition (at.% and wt.% with standard deviation, s.d.) between animal and human samples.

| Element	Equine Bone	Ovine Bone	Porcine Bone	Bovine Bone	Human
	at.% ± s.d.	at.% ± s.d.	at.% ± s.d.	at.% ± s.d.	at.% ± s.d.
Ca	17.01 ± 3.06	17.43 ± 3.13	18.24 ± 3.82	16.50 ± 5.15	18.80 ± 1.23
P	10.87 ± 0.68	11.49 ± 2.05	11.78 ± 1.78	10.49 ± 0.98	11.58 ± 0.89
Element	**wt.% ± s.d.**	**wt.% ± s.d.**	**wt.% ± s.d.**	**wt.% ± s.d.**	**wt.% ± s.d.**
Ca	31.07 ± 3.78	31.61 ± 4.44	31.55 ± 5.24	30.06 ± 7.14	33.52 ± 1.66
P	15.41 ± 0.63	15.51 ± 0.98	16.29 ± 1.68	14.98 ± 1.51	15.96 ± 1.04
Mg	0.33 ± 0.02	0.64 ± 0.07	0.47 ± 0.07	0.57 ± 0.02	0.29 ± 0.02
Ca/P (at.%)	1.56	1.52	1.55	1.57	1.62

Regarding crystallinity, although slight not significant differences are appraised between specimens, Ca/P ratio is lower for ovine bone (Table 3).

3.3. Coatings Characterization

All bone sources were deposited and thermally treated, then films were analyzed in composition pre and post thermal treatment and morphology post thermal treatment.

Results show that deposition can be carried out by all the examined sources, without any significant drawback, even though easiness of shaping and target duration are bigger for bovine and equine bone.

All as-deposited coatings (Figure 6a) are highly amorphous, negligent of the deposition target. As a consequence of thermal treatments (Figure 6b), crystallinity increases for all, in a similar way, up to resembling that of real bone.
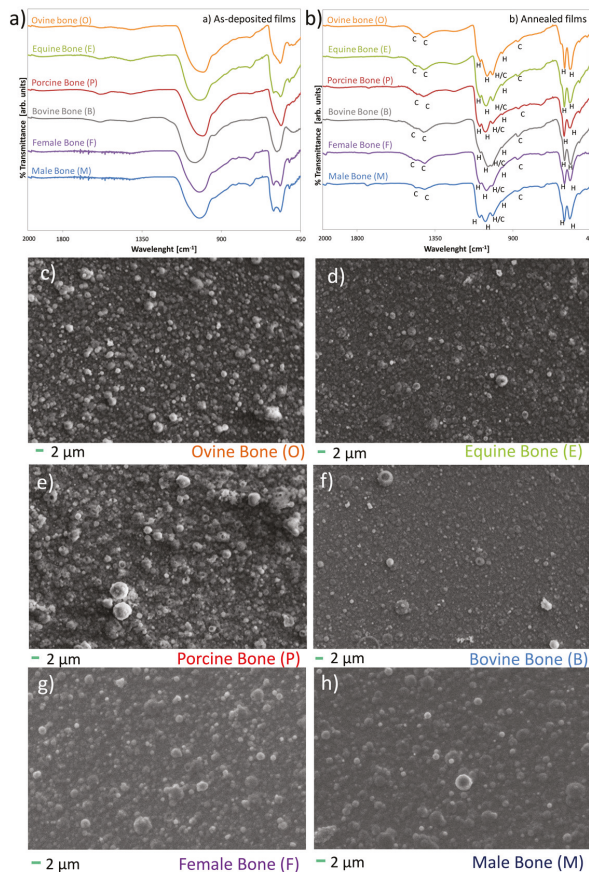
Figure 6. Composition of the coatings before (**a**) and after (**b**) thermal treatment. (**c–h**) Morphology of the coatings deposited from different sources. All as-deposited coatings are amorphous, as demonstrated by the broad and ill-defined shape of the bands in the area 1000–1500 and 560–600 cm^{-1}.

All coatings are composed by carbonated hydroxyapatite and no metastable or decomposition phases are assessed for any of the deposited films, indicating that all sources can be used for manufacturing of biomimetic films.

Morphology of the films (Figure 6c–h), instead, significantly depends on the deposition target characteristics, as more compact and harder bone result in finer aggregates and more homogeneous films.

4. Discussion

Bone grafts and substitutes are significantly used to treat bone defects and local bone loss. It is estimated that in the US, approximately 500,000 bone graft procedures are performed annually [49]. Moreover, the increasing number of musculoskeletal conditions such as osteoarthritis, rheumatoid arthritis, osteoporosis, osteopenia and traumatic fractures is a leading factor to further stimulate the global bone grafts and substitutes market over the years.

Ideally, a bone graft should have some biological properties such as the absence of immunogenicity, rapid incorporation and stable fixation capability. In addition, it should mediate recruitment of mesenchymal stem cells derived from host site (osteoinduction) and promote the bone growth on its surface or down into pores, channels or pipes (osteoconduction). Finally, some clinical particularities

such as cost-effectiveness, indefinite storage capability and easy handling properties are needed. To date, each type of bone graft has its own unique advantages and disadvantages and the relationship between bone healing and various aspects of biological, mechanical and compositional properties should be well-considered.

Among the available grafts, although autografts are still considered as the gold standard since all biological properties in terms of bone regeneration are exhibited, the concerns of limited supply and donor site complications limit their use. This is a clear indication that the use of alternative bone grafting is often necessary. Thus, allografts, xenografts and synthetic substitutes are normally preferred in the clinical practice. However, synthetic bone-based materials are normally regarded only as osteoconductive. In addition, as reported above, a material as similar as possible to the host bone is recommended to allow for the best biological behavior [4–6]. As a consequence, both allografts and xenografts are extensively used despite it is still not clear which is better for clinical purposes, because opposing results have been reported. In fact, despites some authors demonstrated that allografts outperform xenografts, others showed no significantly different outcomes.

As an example, Cook et al. [50] asserted that xenograft implantation was avoided in the past in foot and ankle surgery because of concerns about antigenicity and graft rejection, suggesting that advances in processing and sterilization techniques are needed in order to reduce immunogenicity. In 2015, Shibuya et al. [2] compared incorporation rate of allograft with bovine-based xenograft. Results showed that bovine bone was not adequate for the purpose of foot and ankle reconstructive surgery in both union rate and incorporation time. Sousa et al. [51] investigated the osteoconduction and bioresorption properties of bone allograft vs. anorganic bovine xenograft by a histomorphometric study in humans. Volume density of connective tissue was similar between groups, although greater osteoconductivity and faster bioresorption were noticeable in the allograft group. Recently, Rhodes et al. [52] compared the use of bovine xenograft and cadaveric allograft for calcaneal lengthening osteotomy in patients with cerebral palsy. Authors affirmed that allograft incorporated better than xenograft, yet both groups retained postoperative improvement.

In addition, whilst many studies focus on the allografts and xenografts based on their biological or mechanical [53–55] properties, there is a lack of information regarding the physico-chemical properties of bone apatite deriving from different human and animal sources. Instead, the properties of the mineral phase of bone can significantly impact on its biological behavior as trace ions incorporated in the lattice change the solubility of hydroxyapatite and can have important therapeutic effects (as in the case of magnesium). As a consequence, the use of hydroxyapatites with different type/amount of substitutions results in a different type and concentration of ions released in the peri-implant environment, which in turn, significantly influences the biological behavior of the graft. Lack of similarity between stoichiometric and biological apatite, in fact, is among the main reasons of the scarce behavior of hydroxyapatite-based materials, and in particular of coatings [5,6,33,56].

Stoichiometric HA is basically composed of calcium and phosphorus with molar ratio of Ca/P equal to 1.67 [57]. This ratio has been proven to be the most effective in promoting bone regeneration [30]. However, the mineral component of bone is a non-stoichiometric hydroxyapatite with trace amounts of ions such as Na^+, Mg^{2+} and Al^{3+} substituted in the calcium positions. The trace elements are essential in the regeneration of the bone and accelerates the process of bone formation. Moreover, carbonate is present in biological apatites by substitution at phosphate and hydroxide sites, tending to increase its solubility and the amount of in vivo osseointegration in comparison with pure hydroxyapatite [58].

As shown in Figure 2a,b, FT-IR and XRD analyses have not reported significant differences between human samples regarding both the age and sex of the donors. Specifically, FT-IR spectra highlighted a non-negligible variability in the amplitude of carbonate bands compared to phosphates, while XRD spectra showed peaks characteristic of a scarcely crystalline HA. These differences in crystallinity between stoichiometric and biogenic apatite are significant, as stoichiometric apatite would be essentially insoluble at the pH ranges present in the human body, also in the case of inflammation.

Although information about the elemental composition obtained by EDS analysis (Table 2) exhibited slight variation between female and male donors, they highlighted a significant difference in terms of magnesium trace ($p < 0.05$). In particular, male donors displayed the higher content. Magnesium has an important role on hydroxyapatite crystal and a significant biological relevance. In fact, it causes a decrease in the c-axis of the lattice, acting like a suppressor for HA nucleation and crystallization and destabilizing the apatitic structure [5,6,13,19]. Mg-substitutions make HA less crystalline, therefore its solubility increases. From a biological point of view, magnesium is an essential element for living organisms, as it is a co-factor for over 100 enzymes, influences the metabolic activity and growth of bone by acting on osteoblasts and osteoclasts activity [5,6,13,19]. As a consequence, even though a composition as similar as possible to the host bone is recommended based on the biomimetic principle, magnesium is frequently added in biomaterials in concentrations higher than those of bone [6], to improve its biological behavior and increase the dissolution rate. As a consequence, a high level of magnesium can be preferred; thus, for regenerative medicine intent, male donors may be preferred since the high content of magnesium makes this bone material more degradable and resorbable, in order to be replaced gradually by the new bone after implantation. Obviously, bone regeneration quality is decided by many factors, despite the in vitro solubility of the graft is an important parameter in the evaluation of its biodegradability and in vivo performance.

Therefore, these data highlight the need, that is increasingly emerging in the Literature, for specific in vitro and in vivo studies based on the donor's gender. More attention should be paid for female that are commonly neglected in clinical studies in orthopedics, that tend to take into exam tissues deriving from male donors only. This also indicates that specific biomaterials and grafts (both synthetic and from biogenic sources) could be addressed to male and female patients. A characterization of differences in soft tissues between male and female donors could be of interest as well.

When morphology of human and animal specimens is compared (SEM, Figures 1 and 4), significant differences are assessed regarding variation between the species and within one same species. In fact, human bone has shown a more marked morphological heterogeneity, especially about porosity, than animal sources. A higher porosity results in scarcer mechanical properties, but also in increased specific surface and higher host cells adhesion and proliferation. As a consequence, porosity and morphology shall be taken into consideration when selecting a graft.

As expected, also animal bone exhibits a significant difference in morphology between different species. Specifically, bovine and equine bone is more compact than the other specimens and appears scarcely porous, although more detailed analyses must be carried out to investigate this point. This suggests that bovine bone and equine is more adequate for grafts of medium-big dimensions, as higher porosity results in scarcer mechanical properties, but could be less prone to dissolution and to favoring cells adhesion.

When compared to human bone, all specimens within one same species exhibit a much lower variability in phase-composition. In addition, FT-IR and XRD spectra and EDS (Figure 5 and Table 3) indicate that differences exist in terms of all the investigated parameters. First, on average, the content of carbonates is maximum for human bone (FT-IR) and lower for animal specimens, especially for bovine bone. On the other hand, content of magnesium is significantly higher for ovine, bovine and porcine bone as compared to human bone ($p = 0.002$, $p = 0.0001$, $p = 0.0122$, respectively). No statistical difference is assessed between equine and human bone. Regarding Ca/P ratio, although slight differences are appreciated when human and animal sources are compared, the maximum value (closer to stoichiometric value of HA) is assessed for human bone and minimum for ovine. Bovine, equine and porcine bone exhibit similar Ca/P ratio.

Regarding crystallinity, negligible differences are assessed between the specimens, although crystallinity is maximum for human bone, consistently with Ca/P ratio. In addition, no appreciable differences are assessed in the dimension of crystallites, different from what was reported in some literature data [47,48].

This indicates that different animal sources can be used to address different aims: (i) a higher or lower content of magnesium can be selected depending on therapeutic needs and/or patient gender; (ii) a bone with higher or lower Ca/P ratio can be used to achieve faster or slower dissolution rate; (iii) a greater porosity can be selected to facilitate cell infiltration and adhesion through the 3D environment; (iv) when specific mechanical properties, such as compressive strength and shear force resistance are needed, a more compact bone structure could be indicated.

These considerations are not only valid for bone grafts, but for any bone-based or biomimetic biomaterial.

A detailed in vitro characterization is currently in progress to determine how these differences translate into a modulation of host cell behavior.

In addition, preliminary results on the effect of gamma irradiation on human female samples show quite significant alterations in terms of magnesium content and Ca/P ratio, possibly correlated to material loss. On the other hand, phase composition remains substantially unaltered suggesting that gamma irradiation does not cause alterations in bone tissue composition, that could affect its biological behavior, but causes a significant reduction in processability, given by increased fragility and tendency to pulverization, possibly leading to inflammation. Obviously, a more detailed characterization, based on an increased number of samples is suggested, to also include male donors.

The reported data, summarized in Table 4, provide information beside the published scientific papers in the literature regarding allograft and xenograft composition but do not address certain issues, such as indications, specifications, dosage, limitations and contraindications of bone grafts and substitutes. The goal of achieving an optimal bone-implant interface should be approached considering several parameters such as implant surface topography, chemistry, bulk material composition, resistance in the physiologic milieu, acceptable strength [59]. Nevertheless, these results may be considered, together with biological and mechanical properties of different bone sources, as the basis to design multicenter prospective randomized studies focused on the choice of the most appropriate graft for a specific clinical application.

Table 4. Overview of the main characteristics of the investigated specimens. All values are compared to male human bone (reference), and differences are visually indicated in terms of sign (higher/lower/similar: $+/-/\approx$) and magnitude ($+/++$, $-/--$).

Element	Human Male	Human Female	Human Female γ	Equine	Ovine	Porcine	Bovine
Mg	ref	−	−	≈	++	+	+ +
Ca/P	ref	≈	−	− −	− −	− −	−
Carbonates substitution	ref	≈	≈	−	− −	−	− −

When bone from different sources are used to manufacture nanostructured coatings, they all allow achieving nanostructured biomimetic thin films. All deposited films are highly amorphous, but crystallinity can be tuned by post treatment annealing. All coatings are constituted by ion-doped carbonated hydroxyapatites, whose composition closely resembles that of the relevant deposition targets. However, differences in the composition of the films are negligible, thus indicating that initial differences between bone specimens are less important than the alterations caused in composition by the deposition procedure and by thermal treatment. In particular, if results obtained here are compared with previous results from the Authors [12], it is clear that: (i) plasma deposition causes modifications in the Ca/P ratio, which are more significant than those present between bone from different sources and (ii) annealing temperature has a much stronger impact on the content of carbonates than bone source does.

Similarly, because phase composition is substantially the same for all samples, no differences are assessed in the behavior of the films with respect to annealing. In fact, similar increases in crystallinity are observed in the same temperature range, as demonstrated by the narrowing of bands in IR spectra, while no cracking/spalling phenomena are observed for any of the coatings, as a result of heating.

Instead, different precursors allow achieving significantly different surface morphology and nanostructuration, where more compact bone (equine and bovine) permits a more regular morphology constituted by finer aggregates, while softer bone allows achieving coarser but more irregular aggregates. A similar behavior had been observed comparing ceramics with significantly different properties [60], but results achieved here show that slight alterations in the target morphology can be successfully exploited to tune morphology and in turn, specific surface, which determines ion release. This is important as it has been demonstrated that macro-, micro- and, mostly, nano-sized topographical cues can stimulate changes at cellular and tissue level [61]. For this reason, an increasing number of studies investigate surface patterning and tuning of nanostructuration and materials surface roughness to direct cells adhesion and osteogenic differentiation [62]. For nanostructured thin films, Literature studies are being devoted to modifying the shape, orientation and dimensions of the aggregates to tune cells response, for example by applying glancing angle deposition [63]. Here we demonstrate that the characteristics of the target also have a strong importance on the morphological outcome of deposition and can be exploited for a simple and fast tuning of the micro- and nano-structure of the coatings.

5. Conclusions

In this paper, different bone sources are studied and compared to assess possible differences from a compositional point of view.

Although all samples are composed by the same main inorganic phase (carbonated, multi-substituted hydroxyapatite), significant differences are assessed between female and male human samples and between animal and human bone, especially for what regards the content of magnesium, and slight differences in terms of carbonate substitution and Ca/P ratio. These parameters are known to influence solubility and ion release from the different sources, hence could have an impact on the behavior of bone substitutes. Although ovine, porcine and bovine have a greater content of magnesium with respect to human bone, they exhibit scarce similarity to human bone in terms of carbonates content and Ca/P ratio. Thus, although every bone material may have different clinical applications depending on the expected effect that the clinician demands, human bone from male donors emerge as more appropriate for regenerative purposes. In addition, differences existing between biogenic apatite from human and animal bone could be among the reasons allowing a better performance for allografts compared to xenografts, especially when a faster osseointegration is needed. In addition, significant differences assessed in the physico-chemical composition of female and male bone, should push towards a more detailed investigation of gender-specific studies, also to understand gender disparities in some chronic and degenerative musculoskeletal pathologies such as osteoarthritis and osteoporosis.

Finally, bone from different biogenic sources can be successfully used to manufacture biomimetic thin films, having a nanosized surface roughness and a composition strongly resembling that of bone. Negligent of the deposition target, post-treatment annealing at 400° permits to convert highly amorphous coatings, into films having a crystallinity similar to that of bone.

The results presented here indicate that the selection of the animal precursor to be used for the coatings shall be selected based on the desired morphology, rather than to obtain differences in coatings composition. Most importantly, differences in the mechanical properties of the targets permit to tune surface morphology and nanostructuration of the films, obtaining aggregates of different dimensions and uniformity, thus appearing as a potentially promising tool, to tune host cells adhesion and differentiation.

Ethical Statement: All samples were collected and processed by the Muskoloskeletal Tissue Bank of IRCCS Istituto Ortopedico Rizzoli (Bologna, Italy), in accordance with the approval of the Local Ethics Committee (cod.

References

1. Ricciardi, B.F.; Bostrom, M.P. Bone graft substitutes: Claims and credibility. *Semin. Arthroplast.* **2013**, *24*, 119–123. [CrossRef]
2. Shibuya, N.; Jupiter, D.C. Bone graft substitute: Allograft and xenograft. *Clin. Podiatr. Med. Surg.* **2015**, *32*, 21–34. [CrossRef] [PubMed]
3. Campana, V.; Milano, G.; Pagano, E.; Barba, M.; Cicione, C.; Salonna, G.; Lattanzi, W.; Logroscino, G. Bone substitutes in orthopaedic surgery: From basic science to clinical practice. *J. Mater. Sci. Mater. Med.* **2014**, *25*, 2445–2461. [CrossRef] [PubMed]
4. Barinov, S.M.; Rau, J.V.; Fadeeva, I.V.; Cesaro, S.N.; Ferro, D.; Trionfetti, G.; Komlev, V.S.; Bibikov, V.Y. Carbonate loss from two magnesium-substituted carbonated apatites prepared by different synthesis techniques. *Mater. Res. Bull.* **2006**, *41*, 485–494. [CrossRef]
5. Boanini, E.; Gazzano, M.; Bigi, A. Ionic substitutions in calcium phosphates synthesized at low temperature. *Acta Biomater.* **2010**, *6*, 1882–1894. [CrossRef]
6. Graziani, G.; Bianchi, M.; Sassoni, E.; Russo, A.; Marcacci, M. Ion-substituted calcium phosphate coatings deposited by plasma-assisted techniques: A review. *Mater. Sci. Eng. C Mater. Biol. Appl.* **2017**, *74*, 219–229. [CrossRef]
7. Bianchi, M.; Gambardella, A.; Graziani, G.; Liscio, F.; Maltarello, M.C.; Boi, M.; Berni, M.; Bellucci, D.; Marchiori, G.; Valle, F.; et al. Plasma-assisted deposition of bone apatite-like thin films from natural apatite. *Mater. Lett.* **2017**, *199*, 32–36. [CrossRef]
8. Bianchi, M.; Pisciotta, A.; Bertoni, L.; Berni, M.; Gambardella, A.; Visani, A.; Russo, A.; de Pol, A.; Carnevale, G. Osteogenic differentiation of hDPSCs on biogenic bone apatite thin films. *Stem Cells Int.* **2017**, *2017*, 3579283. [CrossRef]
9. Duta, L.; Mihailescu, N.; Popescu, A.C.; Luculescu, C.R.; Mihailescu, I.N.; Cetin, G.; Gunduz, O.; Oktar, F.N.; Popa, A.C.; Kuncser, A.; et al. Comparative physical, chemical and biological assessment of simple and titanium-doped ovine dentine-derived hydroxyapatite coatings fabricated by pulsed laser deposition. *Appl. Surf. Sci.* **2017**, *413*, 129–139. [CrossRef]
10. Duta, L.; Oktar, F.N.; Stan, G.E.; Popescu-Pelin, G.; Serban, N.; Luculescu, C.; Mihailescu, I.N. Novel doped hydroxyapatite thin films obtained by pulsed laser deposition. *Appl. Surf. Sci.* **2013**, *265*, 41–49. [CrossRef]
11. Duta, L.; Serban, N.; Oktar, F.N.; Mihailescu, I.N. Biological hydroxyapatite thin films synthesized by pulsed laser deposition. *Optoelectron. Adv. Mater. Rapid Commun.* **2013**, *7*, 1040–1044.
12. Graziani, G.; Berni, M.; Gambardella, A.; De Carolis, M.; Maltarello, M.C.; Boi, M.; Carnevale, G.; Bianchi, M. Fabrication and characterization of biomimetic hydroxyapatite thin films for bone implants by direct ablation of a biogenic source. *Mater. Sci. Eng. C Mater. Biol. Appl.* **2019**, *99*, 853–862. [CrossRef] [PubMed]
13. Graziani, G.; Boi, M.; Bianchi, M. A review on ionic substitutions in hydroxyapatite thin films: Towards complete biomimetism. *Coatings* **2018**, *8*. [CrossRef]
14. Hayami, T.; Hontsu, S.; Higuchi, Y.; Nishikawa, H.; Kusunoki, M. Osteoconduction of a stoichiometric and bovine hydroxyapatite bilayer-coated implant. *Clin. Oral Implant. Res.* **2011**, *22*, 774–776. [CrossRef]
15. Mihailescu, N.; Stan, G.E.; Duta, L.; Chifiriuc, M.C.; Bleotu, C.; Sopronyi, M.; Luculescu, C.; Oktar, F.N.; Mihailescu, I.N. Structural, compositional, mechanical characterization and biological assessment of bovine-derived hydroxyapatite coatings reinforced with MgF_2 or MgO for implants functionalization. *Mater. Sci. Eng. C Mater. Biol. Appl.* **2016**, *59*, 863–874. [CrossRef]

16. Hashimoto, Y.; Kusunoki, M.; Hatanaka, R.; Hamano, K.; Nishikawa, H.; Hosoi, Y.; Hontsu, S.; Nakamura, M. Improvement of hydroxyapatite deposition on titanium dental implant using ArF laser ablation: Effect on osteoblast biocompatibility in vitro. *Adv. Sci. Technol.* **2006**, *49*, 282–289. [CrossRef]

17. Barinov, S.M.; Fadeeva, I.V.; Ferro, D.; Rau, J.V.; Cesaro, S.N.; Komlev, V.S.; Fomin, A.S. Stabilization of carbonate hydroxyapatite by isomorphic substitutions of sodium for calcium. *Russ. J. Inorg. Chem.* **2008**, *53*, 164–168. [CrossRef]

18. Rau, J.V.; Cesaro, S.N.; Ferro, D.; Barinov, S.M.; Fadeeva, I.V. FTIR study of carbonate loss from carbonated apatites in the wide temperature range. *J. Biomed. Mater. Res. Part B Appl. Biomater.* **2004**, *71*, 441–447. [CrossRef]

19. Supova, M. Substituted hydroxyapatites for biomedical applications: A review. *Ceram. Int.* **2015**, *41*, 9203–9231. [CrossRef]

20. Datta, A.; Gheduzzi, S.; Miles, A.W. A comparison of the viscoelastic properties of bone grafts. *Clin. Biomech.* **2006**, *21*, 761–766. [CrossRef]

21. Figueiredo, M.; Fernando, A.; Martins, G.; Freitas, J.; Judas, F.; Figueiredo, H. Effect of the calcination temperature on the composition and microstructure of hydroxyapatite derived from human and animal bone. *Ceram. Int.* **2010**, *36*, 2383–2393. [CrossRef]

22. Rahavi, S.S.; Ghaderi, O.; Monshi, A.; Fathi, M.H. A comparative study on physicochemical properties of hydroxyapatite powders derived from natural and synthetic sources. *Russ. J. Non-Ferr. Met.* **2017**, *58*, 276–286. [CrossRef]

23. Ramesh, S.; Loo, Z.Z.; Tan, C.Y.; Chew, W.J.K.; Ching, Y.C.; Tarlochan, F.; Chandran, H.; Krishnasamy, S.; Bang, L.T.; Sarhan, A.A.D. Characterization of biogenic hydroxyapatite derived from animal bones for biomedical applications. *Ceram. Int.* **2018**, *44*, 10525–10530. [CrossRef]

24. Figueiredo, M.; Henriques, J.; Martins, G.; Guerra, F.; Judas, F.; Figueiredo, H. Physicochemical characterization of biomaterials commonly used in dentistry as bone substitutes-comparison with human bone. *J. Biomed. Mater. Res. Part B Appl. Biomater.* **2010**, *92b*, 409–419. [CrossRef]

25. de Dios Teruel, J.; Alcolea, A.; Hernandez, A.; Ruiz, A.J. Comparison of chemical composition of enamel and dentine in human, bovine, porcine and ovine teeth. *Arch. Oral Biol.* **2015**, *60*, 768–775. [CrossRef] [PubMed]

26. Haugen, H.J.; Lyngstadaas, S.P.; Rossi, F.; Perale, G. Bone grafts: Which is the ideal biomaterial? *J. Clin. Periodontol.* **2019**, *46*, 92–102. [CrossRef]

27. Sprio, S.; Fricia, M.; Maddalena, G.F.; Nataloni, A.; Tampieri, A. Osteointegration in cranial bone reconstruction: A goal to achieve. *J. Appl. Biomater. Funct. Mater.* **2016**, *14*, e470–e476. [CrossRef]

28. Taschieri, S.; Del Fabbro, M.; Panda, S.; Goker, F.; Babina, K.S.; Tampieri, A.; Mortellaro, C. Prospective clinical and histologic evaluation of alveolar socket healing following ridge preservation using a combination of hydroxyapatite and collagen biomimetic xenograft versus demineralized bovine bone. *J. Craniofacial Surg.* **2019**, *30*, 1089–1094. [CrossRef]

29. Aerssens, J.; Boonen, S.; Lowet, G.; Dequeker, J. Interspecies differences in bone composition, density, and quality: Potential implications for in vivo bone research. *Endocrinology* **1998**, *139*, 663–670. [CrossRef]

30. Akram, M.; Ahmed, R.; Shakir, I.; Ibrahim, W.A.W.; Hussain, R. Extracting hydroxyapatite and its precursors from natural resources. *J. Mater. Sci.* **2014**, *49*, 1461–1475. [CrossRef]

31. Buddhachat, K.; Klinhom, S.; Siengdee, P.; Brown, J.L.; Nomsiri, R.; Kaewmong, P.; Thitaram, C.; Mahakkanukrauh, P.; Nganvongpanit, K. Elemental analysis of bone, teeth, horn and antler in different animal species using non-invasive handheld X-ray fluorescence. *PLoS ONE* **2016**, *11*, e0155458. [CrossRef] [PubMed]

32. Nganvongpanit, K.; Brown, J.L.; Buddhachat, K.; Somgird, C.; Thitaram, C. Elemental analysis of Asian elephant (*Elephas maximus*) teeth using X-ray fluorescence and a comparison to other species. *Biol. Trace Elem. Res.* **2016**, *170*, 94–105. [CrossRef] [PubMed]

33. Surmenev, R.A. A review of plasma-assisted methods for calcium phosphate-based coatings fabrication. *Surf. Coat. Technol.* **2012**, *206*, 2035–2056. [CrossRef]

34. Allaveisi, F.; Mirzaei, M. Effects of high-dose gamma irradiation on tensile properties of human cortical bone: Comparison of different radioprotective treatment methods. *J. Mech. Behav. Biomed. Mater.* **2016**, *61*, 475–483. [CrossRef]

35. Godette, G.A.; Kopta, J.A.; Egle, D.M. Biomechanical effects of gamma irradiation on fresh frozen allografts in vivo. *Orthopedics* **1996**, *19*, 649–653. [CrossRef]

36. Nguyen, H.; Cassady, A.I.; Bennett, M.B.; Gineyts, E.; Wu, A.; Morgan, D.A.; Forwood, M.R. Reducing the radiation sterilization dose improves mechanical and biological quality while retaining sterility assurance levels of bone allografts. *Bone* **2013**, *57*, 194–200. [CrossRef]

37. Nguyen, H.; Morgan, D.A.; Forwood, M.R. Sterilization of allograft bone: Effects of gamma irradiation on allograft biology and biomechanics. *Cell Tissue Bank* **2007**, *8*, 93–105. [CrossRef]

38. Castro-Cesena, A.B.; Sanchez-Saavedra, M.P.; Novitskaya, E.E.; Chen, P.Y.; Hirata, G.A.; McKittrick, J. Kinetic characterization of the deproteinization of trabecular and cortical bovine femur bones. *Mater. Sci. Eng. C Mater. Biol. Appl.* **2013**, *33*, 4958–4964. [CrossRef]

39. Hamed, E.; Novitskaya, E.; Li, J.; Chen, P.Y.; Jasiuk, I.; McKittrick, J. Elastic moduli of untreated, demineralized and deproteinized cortical bone: Validation of a theoretical model of bone as an interpenetrating composite material. *Acta Biomater.* **2012**, *8*, 1080–1092. [CrossRef]

40. Hamed, E.; Novitskaya, E.; Li, J.; Jasiuk, I.; McKittrick, J. Experimentally-based multiscale model of the elastic moduli of bovine trabecular bone and its constituents. *Mater. Sci. Eng. C Mater. Biol. Appl.* **2015**, *54*, 207–216. [CrossRef]

41. Uklejewski, R.; Winiecki, M.; Musielak, G.; Tokłowicz, R. Effectiveness of various deproteinization processes of bovine cancellous bone evaluated via mechano-biostructural properties of produced osteoconductive biomaterials. *Biotechnol. Bioprocess Eng.* **2015**, *20*, 259–266. [CrossRef]

42. ISO 11137-2:2013 Sterilization of Health Care Products—Radiation—Part 2: Establishing the Sterilization Dose. Available online: https://www.iso.org/standard/62442.html (accessed on 27 May 2020).

43. Antonakos, A.; Liarokapis, E.; Leventouri, T. Micro-Raman and FTIR studies of synthetic and natural apatites. *Biomaterials* **2007**, *28*, 3043–3054. [CrossRef] [PubMed]

44. Rehman, I.; Bonfield, W. Characterization of hydroxyapatite and carbonated apatite by photo acoustic FTIR spectroscopy. *J. Mater. Sci. Mater. Med.* **1997**, *8*, 1–4. [CrossRef] [PubMed]

45. Koutsopoulos, S. Synthesis and characterization of hydroxyapatite crystals: A review study on the analytical methods. *J. Biomed. Mater. Res.* **2002**, *62*, 600–612. [CrossRef] [PubMed]

46. Tao, J. FTIR and Raman studies of structure and bonding in mineral and organic-mineral composites. *Methods Enzym.* **2013**, *532*, 533–556. [CrossRef]

47. Al-Akhras, M.A.H.; Qaseer, M.K.H.; Albiss, B.A.; Alebrhim, M.A.; Gezawa, U.S. Investigation of composition and structure of spongy and hard bone tissue using FTIR spectroscopy, XRD and SEM. In *IOP Conference Series: Materials Science and Engineering*; IOP Publishing: Bristol, UK, 2018; Volume 305.

48. Rey, C.; Combes, C.; Drouet, C.; Glimcher, M.J. Bone mineral: Update on chemical composition and structure. *Osteoporos. Int.* **2009**, *20*, 1013–1021. [CrossRef]

49. Sohn, H.S.; Oh, J.K. Review of bone graft and bone substitutes with an emphasis on fracture surgeries. *Biomater. Res.* **2019**, *23*, 9. [CrossRef]

50. Cook, E.A.; Cook, J.J. Bone graft substitutes and allografts for reconstruction of the foot and ankle. *Clin. Podiatr. Med. Surg.* **2009**, *26*, 589–605. [CrossRef]

51. Sousa, S.B.; Castro-Silva, I.I.; da Rocha Coutinho, L.A.C.; Lenharo, A.; Granjeiro, J.M. Osteoconduction and bioresorption of bone allograft versus anorganic bovine bone xenograft: A histomorphometric study in humans. *J. Biomim. Biomater. Tissue Eng.* **2013**, *18*, 85–95. [CrossRef]

52. Rhodes, J.; Mansour, A.; Frickman, A.; Pritchard, B.; Flynn, K.; Pan, Z.; Chang, F.; Miller, N. Comparison of allograft and bovine xenograft in calcaneal lengthening osteotomy for flatfoot deformity in cerebral palsy. *J. Pediatr. Orthop.* **2017**, *37*, e202–e208. [CrossRef]

53. Kubler, N.; Reuther, J.; Kirchner, T.; Priessnitz, B.; Sebald, W. Osteoinductive, morphologic, and biomechanical properties of autolyzed, antigen-extracted, allogeneic human bone. *J. Oral Maxillofac. Surg.* **1993**, *51*, 1346–1357. [CrossRef]

54. Pelker, R.R.; Friedlaender, G.E.; Markham, T.C. Biomechanical properties of bone allografts. *Clin. Orthop. Relat. Res.* **1983**, *174*, 54–57. [CrossRef]

55. Poumarat, G.; Squire, P. Comparison of mechanical properties of human, bovine bone and a new processed bone xenograft. *Biomaterials* **1993**, *14*, 337–340. [CrossRef]

56. Dorozhkin, S.V. Calcium orthophosphate coatings, films and layers. *Prog. Biomater.* **2012**, *1*, 1. [CrossRef] [PubMed]

57. Pu'ad, N.M.; Koshy, P.; Abdullah, H.Z.; Idris, M.I.; Lee, T.C. Syntheses of hydroxyapatite from natural sources. *Heliyon* **2019**, *5*, e01588. [CrossRef]

58. Porter, A.; Patel, N.; Brooks, R.; Best, S.; Rushton, N.; Bonfield, W. Effect of carbonate substitution on the ultrastructural characteristics of hydroxyapatite implants. *J. Mater. Sci. Mater. Med.* **2005**, *16*, 899–907. [CrossRef]
59. Schmidt, C.; Ignatius, A.A.; Claes, L.E. Proliferation and differentiation parameters of human osteoblasts on titanium and steel surfaces. *J. Biomed. Mater. Res.* **2001**, *54*, 209–215. [CrossRef]
60. Gambardella, A.; Berni, M.; Graziani, G.; Kovtun, A.; Liscio, A.; Russo, A.; Visani, A.; Bianchi, M. Nanostructured Ag thin films deposited by pulsed electron ablation. *Appl. Surf. Sci.* **2019**, *475*, 917–925. [CrossRef]
61. de Peppo, G.M.; Agheli, H.; Karlsson, C.; Ekstrom, K.; Brisby, H.; Lenneras, M.; Gustafsson, S.; Sjovall, P.; Johansson, A.; Olsson, E.; et al. Osteogenic response of human mesenchymal stem cells to well-defined nanoscale topography in vitro. *Int. J. Nanomed.* **2014**, *9*, 2499–2515. [CrossRef]
62. Hou, Y.; Yu, L.; Xie, W.; Camacho, L.C.; Zhang, M.; Chu, Z.; Wei, Q.; Haag, R. Correction to surface roughness and substrate stiffness synergize to drive cellular mechanoresponse. *Nano Lett.* **2020**, *20*, 4059. [CrossRef]
63. Prosolov, K.A.; Belyavskaya, O.A.; Linders, J.; Loza, K.; Prymak, O.; Mayer, C.; Rau, J.V.; Epple, M.; Sharkeev, Y.P. Glancing angle deposition of Zn-doped calcium phosphate coatings by RF Magnetron Sputtering. *Coatings* **2019**, *9*, 220. [CrossRef]

Electrodeposition of Hydroxyapatite Coatings for Marble Protection: Preliminary Results

Enrico Sassoni *, Giulia Masi, Maria Chiara Bignozzi and Elisa Franzoni

Department of Civil, Chemical, Environmental and Materials Engineering (DICAM), University of Bologna, Via Terracini 28, 40131 Bologna, Italy; giulia.masi5@unibo.it (G.M.); maria.bignozzi@unibo.it (M.C.B.); elisa.franzoni@unibo.it (E.F.)

* Correspondence: enrico.sassoni2@unibo.it; Tel.: +39-051-2090-429

Abstract: Surface coatings made of hydroxyapatite (HAP) have been proposed to protect marble artworks from dissolution in rain, originated by the aqueous solubility of calcite. However, HAP coatings formed by wet chemistry exhibit incomplete coverage of marble surface, which results in limited protective efficacy. In this study, electrodeposition was explored as a new route to possibly form continuous coatings over the marble surface, leaving no bare areas. Electrodeposition was performed by placing marble samples in poultices containing the electrolyte (an aqueous solution with calcium and phosphate precursors) and the electrodes. The influence of several parameters was investigated, namely the role of the working electrode (cathode or anode), the distance between the marble sample and the working electrode, the deposition conditions (potentiostatic or galvanostatic), the electrolyte composition and concentration, the applied voltage, and time. The coating morphology and composition were assessed by SEM/EDS and FT-IR. The protective ability of the most promising formulations was then evaluated, in all cases comparing electrodeposition with traditional wet synthesis methods. The results of the study suggest that electrodeposition is able to accelerate and improve formation of HAP coatings over the marble surface, even though the obtained protective efficacy is not complete yet.

Keywords: marble; calcite; dissolution; hydroxyapatite; calcium phosphates; electrodeposition; protective coatings; acid attack; potential; current
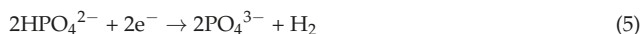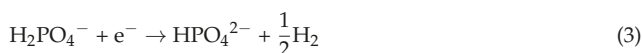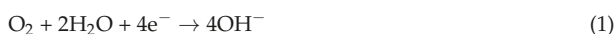
1. Introduction

When exposed outdoors, marble artworks suffer from dissolution in rain because of the aqueous solubility of calcite (the mineral constituting marble, having solubility product K_{sp} = ~5 × 10^{-9} at 25 °C [1] and dissolution rate R_{diss} = ~10^{-10} mol cm^{-2}·s^{-1} [2]). To prevent marble dissolution, a possible strategy is forming a surface coating with reduced solubility, compared to calcite. This has been attempted by several routes, e.g., by treating marble with aqueous solutions of ammonium oxalate, ammonium hydrogen tartrate, and ammonium phosphate to transform calcite into calcium oxalate, calcium tartrate, or calcium phosphates, respectively [2]. Among the investigated minerals, hydroxyapatite (HAP, $Ca_5(PO_4)_3OH$, often written as $Ca_{10}(PO_4)_6(OH)_2$ because the crystal unit cell comprises two formula units) appears as highly promising. Indeed, HAP has solubility product K_{sp} = ~10^{-117} at 25 °C [3] and dissolution rate R_{diss} = ~10^{-14} mol·cm^{-2}·s^{-1} [2], both several orders of magnitude lower than those of calcite. If a continuous and dense coating of HAP is formed over the marble surface, significant protection against dissolution in rain can be expected [2]. Consequently, in recent years, several studies have investigated the feasibility and the effectiveness of forming a protective layer of HAP over marble [2,4–8]. HAP can be formed in a few hours in ambient conditions (necessary to treat monuments in the field), by reacting marble with an aqueous solution of a phosphate salt (typically diammonium hydrogen phosphate, DAP, $(NH_4)_2HPO_4$) [8,9]. Although more effective

than alternative commercial treatments [7], so-formed HAP coatings have nonetheless been found to provide marble with incomplete protection against acid attack, because some cracks and/or pores are present in the coatings [2,5–7]. With the aim of improving the coverage of the marble surface by HAP and reducing cracks and pores in the HAP layer, the effects of several parameters have been investigated, such as DAP concentration, addition of a calcium source, anionic additions, and organic additions [5,7,8]. By tuning such parameters, improved resistance to dissolution in simulated rain has been obtained, but marble dissolution is not completely inhibited yet [7]. The main limiting factor is that some calcite grains, likely having unfavorable crystallographic orientation for HAP epitaxial growth, remain bare after treatment, even though all the surrounding grains are completely covered with the new HAP coating [7]. Although not detrimental, a second factor that might reduce the protective efficacy of the coatings is that, alongside or even instead of HAP, other calcium phosphates (CaP) might form as the result of the DAP-based treatment [8–11]. For instance, octacalcium phosphate (OCP, $Ca_8(HPO_4)_2(PO_4)_4 \cdot 5H_2O$) has been found to form when $CaCl_2$ is added to the DAP solution as a calcium source [12] and when ethanol is added to the DAP solution to increase the reactivity of phosphate ions [7]. Because OCP has lower aqueous solubility than calcite ($K_{sp} = \sim 10^{-97}$ [3]), its formation is not detrimental for the treatment success, but HAP formation would still be preferable, provided that the obtained coating is continuous and non-porous [7,10].

Therefore, in this study, electrodeposition (which is the transport of ions in a solution by application of an electric current and precipitation of material near the surface of an electrode) was explored, as a new route to promote formation of HAP (rather than other CaP) on the whole marble surface, independently of the crystallographic orientation of the underlying calcite grains. In fact, electrodeposition is currently largely used in the biomedical field to deposit HAP coatings over a wide variety of metallic substrates (typically, titanium and magnesium used as implants for bone regeneration) [13–22], with no dependence on the substrate crystallographic orientation. Moreover, the mineralogical composition of the electrodeposited coatings can be controlled, by suitably adjusting the process parameters [17,19].

Electrodeposition of HAP, and CaP in general, is based on the idea of coating a conductive material, such as a metal piece, by immersing it in an aqueous solution containing calcium and phosphate precursors, and then to favor CaP formation by applying an electric potential, using the metal piece as the cathode [13]. At the cathode, several electrochemical reactions can take place [18,19,22], which lead to formation of OH^-, HPO_4^{2-} and PO_4^{3-} ions:

$$O_2 + 2H_2O + 4e^- \rightarrow 4OH^- \tag{1}$$

$$2H_2O + 2e^- \rightarrow H_2 + 2OH^- \tag{2}$$

$$H_2PO_4^- + e^- \rightarrow HPO_4^{2-} + \frac{1}{2}H_2 \tag{3}$$

$$H_2PO_4^- + 2e^- \rightarrow PO_4^{3-} + H_2 \tag{4}$$
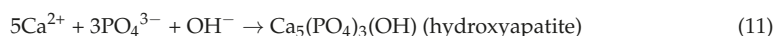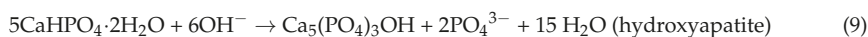
$$2HPO_4^{2-} + 2e^- \rightarrow 2PO_4^{3-} + H_2 \tag{5}$$

Thanks to OH^- formation and the consequent pH increase, deprotonation of phosphate species near the surface of the cathode is promoted, according to the reactions [13,17,18]:

$$H_2PO_4^- + OH^- \rightarrow HPO_4^{2-} + H_2O \tag{6}$$

$$HPO_4^- + OH^- \rightarrow PO_4^{3-} + H_2O \tag{7}$$
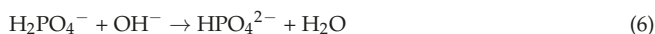
In this environment, precipitation of several CaP phases with low solubility can occur, through the following reactions [13,17,18]:

$$Ca^{2+} + HPO_4^{2-} + 2H_2O \rightarrow CaHPO_4 \cdot 2H_2O \text{ (brushite)} \tag{8}$$

$$5CaHPO_4 \cdot 2H_2O + 6OH^- \rightarrow Ca_5(PO_4)_3OH + 2PO_4^{3-} + 15\ H_2O \text{ (hydroxyapatite)} \tag{9}$$

$$4Ca^{2+} + HPO_4^{2-} + 2PO_4^{3-} + 2.5H_2O \rightarrow Ca_4(HPO_4)(PO_4)_2 \cdot 2.5H_2O \text{ (octacalcium phosphate)} \tag{10}$$

$$5Ca^{2+} + 3PO_4^{3-} + OH^- \rightarrow Ca_5(PO_4)_3(OH) \text{ (hydroxyapatite)} \tag{11}$$

Since the first research on CaP electrodeposition in 1990 [13], numerous studies have been carried out to investigate the effect of several parameters involved in the electrodeposition process on the features of the resulting coatings:

- Nature and concentration of the calcium and phosphate salts used as CaP precursors. Typically, $Ca(NO_3)_2$ and $(NH_4)H_2PO_4$ (ADP) are used, with a molar ratio of 10/6 to reproduce the Ca/P atomic ratio in stoichiometric hydroxyapatite [15,18–31];
- Electrokinetic parameters, namely the electric potential (E) and the current density (i). Typically, these parameters vary in the range $E = -1.4 \div (-3)$ V and $i = 0.5 \div 25\ \text{mA/cm}^2$ [13,14,16,18–25, 29,30,32];
- Possible application of pulsed electric potential. For CaP coating densification, some studies have proposed using pulsed potential, i.e., applying the electric potential by cyclically alternating on/off periods [24,27,29]. According to these studies, during the on-period, OH^- ions are produced at the cathode; during the off-period, Ca^{2+} and PO_4^{3-} ions have the time to diffuse from the bulk solution towards the cathode, where OH^- groups are present so that Reactions (9)–(11) take place [29]. Moreover, pulsed potential reportedly reduces formation of H_2 bubbles (cf. Reactions (3–5)), which might otherwise adhere to the substrate and prevent formation of a dense and well adhering coating [24,27].
- Possible addition of ethanol (EtOH) to the electrolyte solution. To reduce the formation of H_2 bubbles, the possible addition of ethanol to the aqueous solution has been proposed [23,28]. In fact, ethanol addition reduces the conductivity of the solution, thus reducing H_2 bubble formation and promoting coating densification [23,28]. The best results were reported for ethanol additions of about 30–50 vol.% [23,28].
- Possible addition of hydrogen peroxide (H_2O_2) to the electrolyte solution. H_2O_2 is a strong oxidative agent that is reduced before H_2O, hence H_2O_2 addition (about 5–10 vol.% [31]) to the electrolyte can provide an alternative source of OH^- ions, according to Reaction (12) [31]:

$$H_2O_2 + 2e^- \rightarrow 2OH^- \tag{12}$$
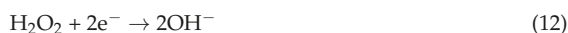
In this way, OH^- ions necessary for HAP formation are obtained with no generation of H_2 bubbles and with consequent improved adhesion of the coating to the substrate [22,32].

Based on the studies summarized above, intended for biomedical applications, in the present study the possible use of electrodeposition to form HAP coatings over marble was investigated. At present, only a few studies have explored the possible use of electrochemical methods for conservation of non-metallic materials, such as marble, stones, and bricks.

In a first group of studies, electrochemical methods were used to *extract* ions from porous materials contaminated by salts [33–35]. The idea is to put the porous material to be desalinated between two poultices, impregnated with water and in contact with two electrodes connected to a power supply (Figure 1a). Then, current is applied and the anions in the material migrate towards the anode and the cations towards the cathode [33]. Because H^+ ions are generated at the anode, which might lead to deterioration of the substrate, clay poultices with pH buffer capacity have been investigated to prevent acidification at the anode [35]. By adopting this electrokinetic method, encouraging desalinating ability has been obtained [33–35].
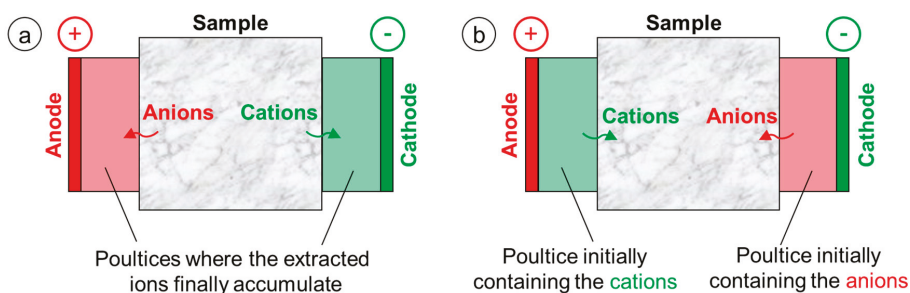
Figure 1. Schemes illustrating the setups adopted for (**a**) ion extraction from porous substrates contaminated with salts and (**b**) ion introduction into porous substrates to be consolidated.

In a second group of studies, electrochemical methods were used to *introduce* ions into porous materials, with the aim of precipitating an insoluble product inside the pore network and providing consolidating action [36–38]. To make the ions penetrate into the porous material, the adopted experimental setup was basically reversed compared to that described above for ion extraction (Figure 1b). The material to be consolidated is in contact with two different solutions, which in turn are in contact with the electrodes connected to a power supply—the solution containing the anions (e.g., HPO_4^{2-} [36] or CO_3^{2-} [37,38]) is in contact with the cathode, while the solution containing the cations (e.g., Ba^{2+} [36] or Mg^+ [37,38]) is in contact with the anode. When current is applied, ions migrate towards the electrode with the opposite sign, thus crossing the sample. When anions and cations encounter inside the material, an insoluble salt precipitates inside the pores (e.g., $Ba_3(PO_4)_2$ [36] or $MgCO_3 \cdot 3H_2O$ [37,38]). Similar to the case of salt extraction, also in this case acidification at the anode occurs, which again led to the use of clay poultices with pH buffer capacity [37].

Moreover, an electrokinetic route has been proposed to deposit a layer of calcium oxalate monohydrate (whewellite) over the marble surface, with protective function [39]. This represents a development of the ammonium oxalate treatment proposed by Matteini in the 1990s [40], which consists of treating carbonate stones (supplying Ca^{2+} ions) with an ammonium oxalate solution (supplying $C_2O_4^{2-}$ ions), so that protective whewellite ($CaC_2O_4 \cdot H_2O$) is formed. In the cited electrokinetic study [39], whewellite formation was reportedly favored by placing the marble piece close to the anode of an electrochemical cell, connected to a power supply, immersed in an ammonium oxalate solution. Because the $C_2O_4^{2-}$ ions are attracted to the anode, a region richer in $C_2O_4^{2-}$ ions is formed near the anode and near the adjacent marble sample, which leads to formation of a thicker whewellite coating over the marble surface compared to simple immersion in an ammonium oxalate solution with no current applied [39].

Based on the studies summarized above, in this study, HAP electrodeposition over marble was explored by first comparing the effect of placing the marble sample close to the cathode (to exploit OH^- formation at the cathode, like in the biomedical studies [27]) or close to the anode (to exploit PO_4^{3-} migration towards the anode, like in the studies on stone consolidation [36–38] and protection [39]). Second, the experimental setup was optimized, by investigating whether direct contact between the electrode and the marble sample is preferable and whether potentiostatic (constant potential) or galvanostatic (constant current) conditions are preferable [27]. Then, the influence of several parameters was investigated, regarding both the electrolyte (concentration of the calcium and phosphate precursors, possible addition of ethanol and/or hydrogen peroxide) and the electrokinetic parameters (pulsing, voltage, and time). Finally, the protective ability of the most promising formulations was evaluated, comparing the acid resistance of untreated and treated marble. To isolate the effect of electrodeposition, a systematic comparison with coatings deposited by simple wet chemistry (with no current application) was carried out. A scheme summarizing the rationale of the study is illustrated in Figure 2.
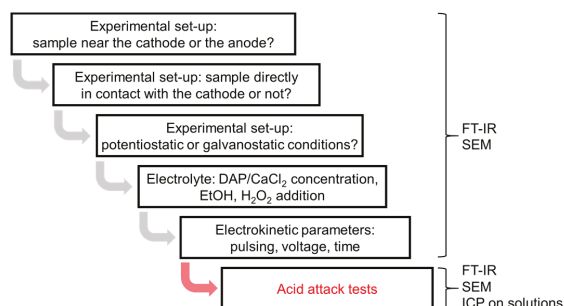
Figure 2. Scheme summarizing the rationale of the study and the adopted analytical techniques.

2. Materials and Methods

2.1. Materials

Carrara marble was used for the tests. Specimens with $20 \times 20 \times 5$ mm^3 size were sawn from a slab supplied by Imbellone Michelangelo S.A.S. (Bologna, Italy). The specimens were subjected to the electrodeposition tests described in the following without preliminary polishing, because a very flat surface would not be representative of marble condition in the field (where prolonged exposure to rain leads to roughening of the surface).

Diammonium hydrogen phosphate (DAP, $(NH_4)_2HPO_4$, assay >99%, Acros Organics, Milan, Italy), calcium chloride ($CaCl_2 \cdot 2H_2O$, assay >99%, Sigma Aldrich, Milan, Italy), ethanol (EtOH, Sigma Aldrich), hydrogen peroxide solution (30 wt% H_2O_2 in D.I. water, Sigma Aldrich), and deionized water were used. Cellulose pulp (MH300, Phase, Florence, Italy) was used to prepare poultices for consolidant application.

2.2. Influence of the Experimental Setup

For the screening tests aimed at identifying the most suitable setup, one of the most recent formulations of the HAP-treatment was considered, namely a solution of 0.1 M DAP + 0.1 mM $CaCl_2$ in 30 vol.% EtOH [7]. Even with no electrodeposition involved, in a previous study this formulation was found to cause basically continuous coverage of the marble surface by CaP after 24 h, although precipitation of some isolated CaP crystals was noticed already in the bulk solution [7]. For the present tests on electrodeposition, the solution was used to prepare a poultice with cellulose pulp, in which the marble samples and the electrodes were embedded. For each test, the poultice was prepared using 100 g of solution and 25 g of dry cellulose fibers.

All the electrodeposition tests were performed using a 3-electrode setup—the working electrode (WE) was a galvanized steel grid, the counter electrode (CE) was a graphite bar, and the reference electrode (RE) was a saturated calomel electrode (SCE) by Amel Electrochemistry (Milan, Italy). Except for the test aimed at comparing potentiostatic and galvanostatic conditions (see below), all the tests were carried out in potentiostatic conditions (i.e., a certain potential was applied and kept constant, while the resulting current was measured [27]), using a potenziostat (7050 Amel Electrochemistry).

First, it was investigated whether the marble sample should be placed close to the cathode (like in the biomedical studies [27]) or the anode (like in the study on ammonium oxalate electrodeposition [39]). The two setups illustrated in Figure 3a,b were adopted, where the only difference was the role of the galvanized steel grid, working either as cathode or anode, respectively. When the marble sample was placed near the cathode (Figure 3a), the expected cathodic reactions

were the electrochemical Reactions (1)–(11), while the anodic reaction was expected to be the oxidation of the graphite bar used as counter electrode, according to the reaction:

$$C + 2H_2O \rightarrow CO_2 + 4H^+ + 4e^-. \tag{13}$$

When the marble sample was placed near the anode (Figure 3b), the expected anodic reaction (necessary to attract the negative PO_4^{3-} ions) was the oxidation of the zinc coating present over the galvanized steel grid, according to the reaction:

$$Zn \rightarrow Zn^{2+} + 2e^- \tag{14}$$

while the cathodic Reactions (1)–(11) were expected at the cathode (the graphite bar). In both cases, the marble sample was kept at a distance of ~3 mm from the grid, the two being separated by a thin layer of poultice. Electrodeposition was carried out applying a constant potential of −2 V or +2 V (depending on whether the grid was working as cathode or anode, respectively) for 3 h.
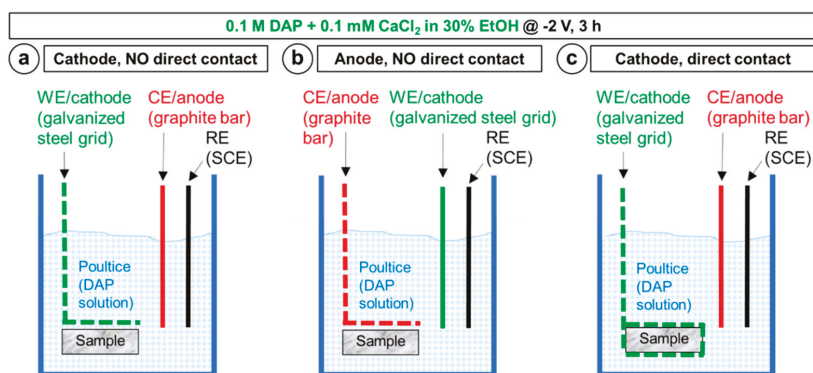
Figure 3. Schemes illustrating the different setups adopted to determine the best setup conditions: In (**a**) and (**b**), the role of the working electrode (the galvanized steel grid) is switched, to determine whether the marble sample should be placed near the cathode or near the anode; in (**a**) and (**c**), the marble sample is always placed near the cathode, but either at ~3 mm distance from the electrode or directly in contact, to determine whether direct contact is preferable or not. The setup in (**a**) was also adopted to compare potentiostatic and galvanostatic conditions.

Second, it was investigated whether direct contact between the marble sample and the steel grid used as cathode might favor the coating formation, expecting the local effect of electrodeposition to be the higher the closer to the electrode. The setup in Figure 3a was compared with the alternative setup illustrated in Figure 3c. The difference consisted in that, in the latter case, the marble sample was directly in contact with the steel grid, wrapped around the sample. In both cases in Figure 3a,c, the steel grid was working as the cathode (*E* = −2 V for 3 h). In the setup in Figure 3c, the same cathodic Reactions (1)–(11) and anodic reaction (13) as in Figure 3a were expected.

Finally, it was investigated whether potentiostatic or galvanostatic conditions are preferable, considering that studies in the biomedical literature have shown that controlling potential or current may lead to significantly different results [30]. For a given setup (Figure 3a) and treatment duration (3 h), the effects of applying a constant potential of −2 or −3 V (potentiostatic conditions) were compared to the effects of applying a constant current of −5 or −20 mA (galvanostatic conditions). In all cases, the variable parameter (current in potentiostatic conditions, potential in galvanostatic conditions) was recorded over time. The adopted current values (−5 and −20 mA) were selected as they correspond to the values recorded in the potentiostatic experiments (at *E* = −2 and −3 V, respectively, cf. Section 3.1.).

Based on the obtained experimental results (cf. Section 3.1.), the setup illustrated in Figure 3a was adopted for all the tests described in the following, as this setup gave the most promising results.

2.3. Influence of the Electrolyte: DAP and CaCl₂ Concentration, Ethanol and/or H₂O₂ Addition

The effects of EtOH and/or H_2O_2 were investigated by comparing the coatings formed using a 0.1 M DAP + 0.1 mM CaCl₂ solution (with no additions) and the coatings obtained when the same solution was added with:

- 30 vol.% EtOH. As mentioned above, this is the maximum concentration not leading to immediate precipitation in the bulk solution at the given DAP and CaCl₂ concentrations (only a few isolated crystals were formed in the bulk solution). Even when no current is applied, EtOH promotes HAP nucleation [5,7], so some benefit compared to the reference 0.1 M DAP + 0.1 mM CaCl₂ solution is already expected. Moreover, when electrodeposition is adopted, EtOH reportedly reduces H_2 bubbling and promotes coating densification [23,28], so an additional benefit is expected.
- 10 vol.% H_2O_2. When electrodeposition is adopted, H_2O_2 is reduced before water, so it can provide the OH^- ions necessary for HAP formation without generation of H_2 bubbles [22,31,32], with a consequent benefit in the coating density and adhesion.
- 30 vol.% EtOH + 10 vol.% H_2O_2. To combine the two effects described above, the double addition was also investigated.

To distinguish between the effect of simply adding EtOH and H_2O_2 to the DAP/CaCl₂ solution (even with no electrodeposition) and the additional benefit resulting from electrodeposition, all the additions were tested without (*E* = 0 V) and with electrodeposition (*E* = −2 V), using the setup illustrated in Figure 3a.

Moreover, the effect of using a higher DAP concentration was also considered. In fact, the higher the DAP concentration, the higher the amount of PO_4^{3-} ions available to form HAP, but also the higher the risk of cracking during drying [7]. A solution of 2 M DAP + 2 mM CaCl₂ in 10 vol.% EtOH was tested. The EtOH concentration was selected as this is the maximum amount not leading to immediate precipitation in the bulk solution at the given DAP and CaCl₂ concentrations. In this case, no H_2O_2 addition was adopted based on the results of the tests described above (cf. Section 3.2). The comparison between the less-concentrated formulation (0.1 M DAP + 0.1 mM CaCl₂ in 30 vol.% EtOH) and the more-concentrated one (2 M DAP + 2 mM CaCl₂ in 10 vol.% EtOH) was carried out by treating marble samples for 30 min and 3 h, without (*E* = 0 V) and with electrodeposition (*E* = −2 V), always using the set up illustrated in Figure 3a.

2.4. Influence of Electrokinetic Parameters: Pulsing, Voltage, and Time

The effect of applying a pulsed potential of −1 V for 3 h was investigated on both the less-concentrated solution (0.1 M DAP + 0.1 mM CaCl₂ in 30 vol.% EtOH) and the more-concentrated one (2 M DAP + 2 mM CaCl₂ in 10 vol.% EtOH), using the setup illustrated in Figure 3a. In addition, for the less-concentrated solution the effect of the pulsed potential was investigated also for a shorter time of 30 min, applying a pulsed potential of −1, −2, and −3 V. The pulsed potential experiments consisted of applying cycles of 1 s on and 2 s off [29].

For both solutions, the effect of applying an increasing negative voltage (without pulsing) was then systematically investigated, again adopting the setup illustrated in Figure 3a. Because, in the literature, HAP was found to be the major phase formed on titanium when a potential of −1.55 V or lower was applied (in that case, the electrolyte being a 42 mM Ca(NO₃)₂ + 25 mM ADP solution [18]), in the present study potential values above and below this threshold were considered: −1, −2, and −3 V in the case of the less-concentrated solution and −1 and −2 V in the case of the more-concentrated one. For the latter solution, *E* = −3 V was not tested, because drying cracks appeared in the coating formed at −2 V, suggesting that the film growth was already excessive at this voltage (cf. Section 3.3). For each voltage value, increasing treatment durations were investigated (30 min, 1, 3, and 6 h). For

all the voltage/time conditions, one sample was also treated without electrodeposition ($E = 0$ V), for comparison's sake.

2.5. Acid Resistance

For the most promising formulations, identified by the screening tests described in the previous paragraphs, the protective ability of the resulting coatings was evaluated. The selected formulations were: (i) 0.1 M DAP + 0.1 mM $CaCl_2$ in 30 vol.% EtOH solution at $E = -2$ V for 3 h and (ii) for 6 h, and (iii) 2 M DAP + 2 mM $CaCl_2$ in 10 vol.% EtOH solution at $E = -1$ V for 6 h. All the electrodeposition treatments were applied adopting the setup in Figure 3a. For comparison's sake, the same solutions were also applied for the same time, but without electrodeposition ($E = 0$ V). An untreated reference was tested too.

After coating deposition, half of the specimens was directly subjected to the acid resistance test, while the other half was subjected to a further preparation step. In fact, previous studies suggested that the sample edges are often incompletely covered with the protective coatings, not because of a scarce performance of the coatings themselves, but because the sample edges are more prone to wear during treatment and handling [7]. For this reason, according to previous studies [6,7] an impermeable coat was applied over the edges of the second half of the samples, to exclude any interference from damage possibly affecting the sample edges. After application of the impermeable coat, two uncovered areas (each measuring 12×12 mm^2) were isolated in the middle of the two square faces of the prismatic specimens (measuring $20 \times 20 \times 5$ mm^3), while the edges and the sides of the prisms were covered with the coat. In this way, only the uncovered central area was exposed to the acidic solution used for the test.

To resemble slightly acidic rain, samples were exposed to aqueous solutions of HNO_3 at pH 5. In fact, thanks to the policies of traffic regulation in the city centers in Europe [41], the average rain pH is currently ~5 in Europe and is predicted to remain at this value in the future [42]. Following a procedure similar to that adopted in previous studies [1,5,7], each sample was submerged in a separated container with 100 mL of solution and left submerged for 15 h, the solution being continuously stirred. At the end of the test, samples were rinsed with D.I. water and dried at room temperature until constant weight. Solutions were collected to determine the Ca and P content by inductively coupled plasma optical emission spectrometry (ICP-OES), using a Serie Optima 3200 XL Perkin Elmer instrument (Milan, Italy).

2.6. Sample Characterization

The composition of the new CaP phases was investigated by Fourier-transform infrared spectrometry (FT-IR), using a Perkin Elmer Spectrum One spectrometer (Milan, Italy). The samples to be analyzed by FT-IR were obtained by scratching from one squared face of the marble specimens, using a spatula. To univocally identify the new CaP phases, combination of FT-IR with other analytical techniques, ideally X-ray diffraction, would be needed [43]. However, given the very low thickness of the new CaP coatings formed over marble (~5 μm [7]), grazing incidence X-ray diffraction (GI-XRD) would be needed, so that the surface layer could be analyzed without the influence from the substrate [7]. However, in the present case, GI-XRD was not available, so the investigation of the new CaP phases was limited to FT-IR, which can provide very important information. In fact, it is true that FT-IR can hardly distinguish between CaP with very similar structure, such as HAP (having strong bands at 1031, 604, and 563 cm^{-1} [43]) and OCP (having strong bands at 1038, 1023, 602, and 560 cm^{-1} [43]). Nonetheless, FT-IR analysis allowed us to conclusively exclude formation of other CaP phases with high aqueous solubility (e.g., brushite, $CaHPO_4 \cdot 2H_2O$, having strong bands at 1136, 1063, 986 cm^{-1} [43]).

The coverage of the marble surface and the morphology of the new CaP phases were evaluated by observation of the other squared face of the specimens (originally close to the steel grid), using a

scanning electron microscope (Philips XL20 SEM, Milan, Italy). The samples to be analyzed by SEM were made conductive by coating them with aluminum (after FT-IR analysis).

3. Results and Discussion

3.1. Influence of the Experimental Setup

The results of the tests aimed at defining the best experimental setup are reported in Figure 4.
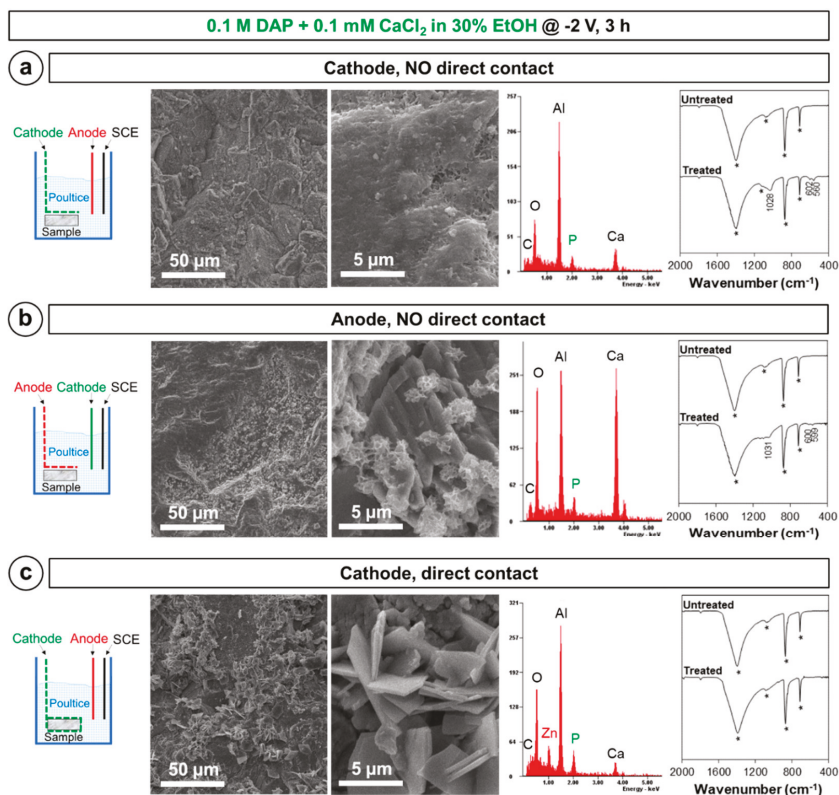
Figure 4. Morphology and composition of the new phases formed by placing the marble sample (**a**) at ~3 mm from the cathode, (**b**) at ~3 mm from the anode, and (**c**) directly in contact with the cathode. EDS spectra were acquired in the whole left SEM image. In the FT-IR spectra, bands owing to the substrate are marked by a star, while the position of the new bands owing to CaP phases is reported.

With regard to the position of the marble sample with respect to the electrodes, new CaP phases were found to form both when the sample was placed near the cathode (Figure 4a) and near the anode (Figure 4b). However, in the former case, the new CaP coating exhibited more promising features. Indeed, ideally the new CaP coating should be continuous (e.g., not leaving uncovered bare areas) and non-porous, which can be more likely achieved when the coating is composed of closely packed small crystals. When the sample was placed near the cathode (Figure 4a), the marble surface appeared as continuously covered with small flower-like crystals, closely following the morphology of the marble surface. Such flower-like morphology is typical of HAP and CaP phases in general [8,12]. Differently, when the sample was placed near the anode (Figure 4b) only few isolated crystals, having significantly bigger size, were visible. Because isolated crystals cannot provide effective protection to the marble

surface, the coating formed in this latter condition was regarded as less promising. Consistently with SEM results, in the FT-IR spectra bands owing to new CaP were definitely more pronounced when the sample was placed near the cathode (Figure 4a). In terms of composition of the new phases, based on the band position (1028–1031, 599–602, and 559–560 cm^{-1}), in both cases formation of HAP seems most likely, even though formation of OCP cannot be completely excluded [43]. The difference in the composition of the new phases in the two cases suggests that the local increase in pH, following formation of OH^{-} ions near the cathode [17], is predominant over the local increase in phosphate ion concentration, occurring near the anode [39].

Once assessed that CaP formation is more abundant when the marble sample is placed near the cathode, the possible advantage of putting the sample directly in contact with the cathode (Figure 4c) rather than at ~3 mm distance (Figure 4a) was investigated. In the case of direct contact, SEM observation disclosed formation of very big crystals, with size reaching 5 μm, which, however, left the marble surface largely uncovered (Figure 4c). EDS analysis revealed that these crystals contained P and also Zn, whereas FT-IR analysis of the marble surface did not detect any new CaP phase. The source of Zn was found to be the galvanized steel grid used as cathode—the basic environment of the DAP solution (initially at pH 8 and further increased by OH^{-} formation near the cathode) led to dissolution of the Zn coating originally present over the steel grid, with consequent Zn release and formation of isolated zinc phosphate crystals. This, in turn, hindered formation of a continuous CaP coating over marble. For this reason, at least in the adopted conditions (i.e., galvanized steel grid used as cathode), direct contact between the marble sample and the cathode is counterproductive, as it leads to formation of zinc phosphates and consequent consumption of phosphate ions. However, in different conditions (e.g., the use of a stainless steel or titanium cathode), direct contact between the sample and the cathode should be re-evaluated. It is worth mentioning that, when the sample was put at ~3 mm from the electrode, no Zn was detected by EDS on the marble surface (Figure 4a).

The results of the test aimed at evaluating whether constant potential or constant current is preferable during electrodeposition are reported in Figure 5.

Both in potentiostatic (Figure 5a) and galvanostatic (Figure 5b) conditions, the variable parameter (current or potential, respectively) exhibits a visible change in the first ~5 min of the test, then it becomes almost stable for the whole duration of the test. In addition to some adjustment in the experimental setup in the initial phase of the test, the registered initial variation is thought to derive from deposition of CaP phase also on the working electrode (the galvanized steel grid). This causes some reduction in the current circulating through the system (Figure 5a) and makes a more negative potential necessary to maintain the same current circulating (Figure 5b). SEM observation of the steel grids at the end of the electrodeposition confirmed that new CaP phases are formed also on the electrode. In terms of features of the new CaP phases formed over marble, SEM observation indicated that, in all cases, complete coverage of the marble surface seems to be achieved by coatings composed of sub-micrometric crystals (Figure 5). However, a significant difference was found in the composition of the new phases obtained in these conditions. While in potentiostatic conditions (Figure 5a), HAP was most likely formed (bands at 1028, 600–602, and 560 cm^{-1} [43]), in the case of galvanostatic conditions (Figure 5b), the identification of the new CaP phase was less straightforward (bands at 1049, 600–602, and 559–560 cm^{-1}), but formation of HAP or OCP seems excluded. Because HAP and OCP are the most desirable phases to form (the other CaP phases having higher aqueous solubility), the coatings formed in potentiostatic conditions were regarded as less promising to provide marble with protection against dissolution in rain, hence they were not adopted further in the prosecution of the study.

Both in potentiostatic and galvanostatic conditions, SEM and FT-IR suggest some increase in the amount of new CaP formed after electrodeposition for increasing negative potential and increasing current, respectively (Figure 5). This confirms the importance of performing a systematic analysis of the influence of the applied potential, which was done in the prosecution of the study (cf. Section 3.3.).
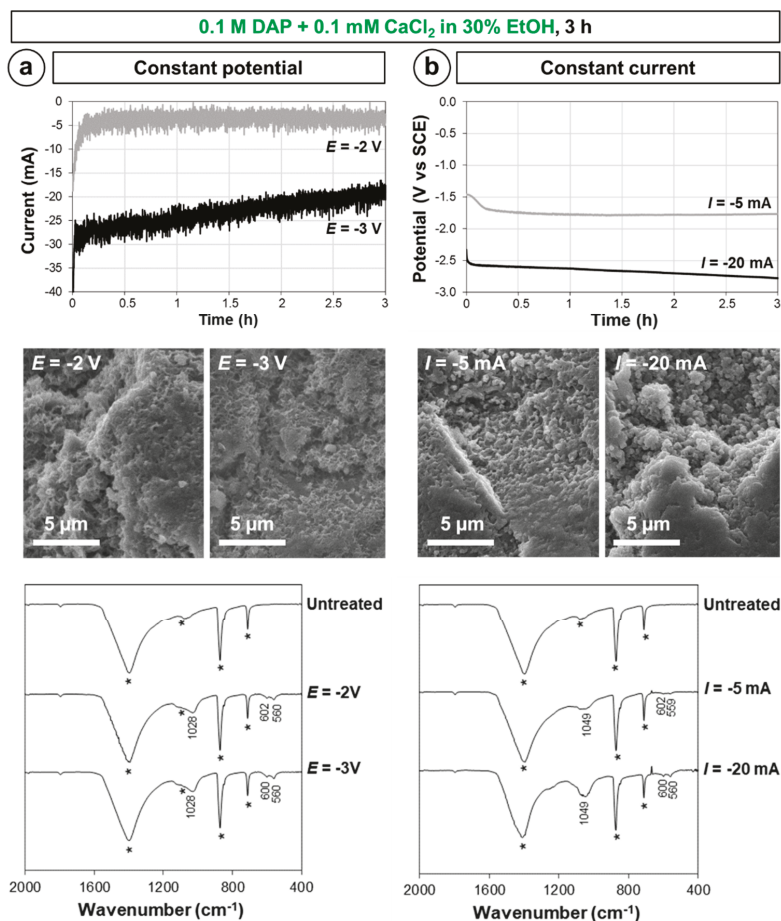
Figure 5. Electrokinetic parameters measured during electrodeposition, morphology, and composition of the new phases formed in (**a**) potentiostatic and (**b**) galvanostatic conditions (in the FT-IR spectra, bands owing to the substrate are marked by a star, while the position of the new bands owing to CaP phases is reported).

3.2. Influence of the Electrolyte: DAP and CaCl$_2$ Concentration, Ethanol and/or H$_2$O$_2$ Addition

The effects of adding EtOH and/or H$_2$O$_2$ to a 0.1 M DAP + 0.1 mM CaCl$_2$ solution are reported in Figure 6. Incomplete coverage of the marble surface was found when no addition was made (either without or with electrodeposition), as the marble surface (dark gray in Figure 6) is clearly visible below isolated CaP crystals. Differently, almost complete coverage of the marble surface was obtained when 30 vol.% EtOH was added, even without electrodeposition (Figure 6). This was possible thanks to the boosting effect of ethanol on CaP nucleation, as assessed in previous studies [5,7]. Indeed, ethanol molecules weaken the hydration sphere of phosphate ions in solution, which makes them more reactive to form CaP [7]. When an electric potential was applied, some increase in the packing of the CaP coating was observed, which can be attributed to the beneficial effect of ethanol on CaP electrodeposition, as previously reported in biomedical studies [23,28]. However, the improvement in the coating was not dramatic.
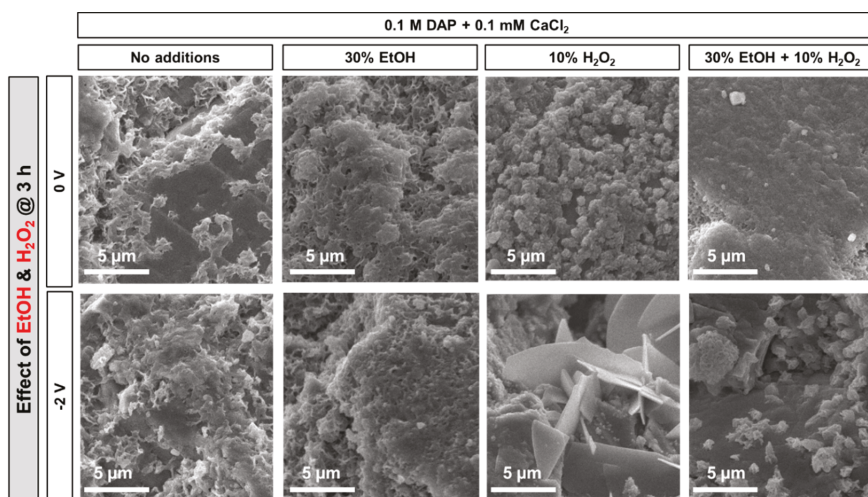
Figure 6. Effect of EtOH and H_2O_2 addition on the morphology of the new CaP phases formed with and without electrodeposition.

In the case of H_2O_2 addition, bigger crystals (size of 0.5–1 µm) were formed even with no electrodeposition (Figure 6). When potential was applied, the crystal size further increased dramatically, leading to formation of isolated crystals with 5–10 µm length. Such huge increase in the crystal size, promoted by the increased availability of OH^- groups induced by H_2O_2 reduction [31], is consistent with previous results available in the literature, reporting even precipitation of CaP directly in the bulk solution upon H_2O_2 addition [32]. However, this huge increase in crystal size is counterproductive towards achievement of a continuous coating, able to protect marble from dissolution in acid. For this reason, H_2O_2 addition was not considered in the prosecution of the study.

By adding both EtOH and H_2O_2 to the solution, when no electrodeposition was used, a coating similar to that obtained using EtOH alone was found (Figure 5). However, when potential was applied, again isolated crystals with 1–2 µm size were formed. Although smaller than in the case of H_2O_2 addition alone, these crystals were unable to completely cover the marble surface (in Figure 6, bare calcite grains are clearly visible as darker zones below the lighter CaP crystals). Therefore, combined EtOH + H_2O_2 addition was discarded in the prosecution of the study.

With regard to the effect of increasing the DAP and, proportionally, the $CaCl_2$ concentrations in the solution (always maintaining a DAP:$CaCl_2$ ratio of 1000:1 and adding the maximum amount of EtOH not leading to immediate CaP precipitation in the solution), the variation in the amount and morphology of the new CaP phases is illustrated in Figure 7.

With no electrodeposition, after 30 min isolated clusters (small lighter particles over the darker marble surface) were found in the case of the solution with the lower concentration and almost no clusters in the case of the more-concentrated solution. This can be explained considering that, in the less-concentrated solution, a much higher amount of EtOH is present (30 vol.%, instead of 10 vol.%), which significantly increases the nucleation of the new CaP phases even at low DAP concentration [7]. Consistently, after 3 h the more-concentrated solution (with lower EtOH addition) caused formation of isolated crystals, relatively big in size (0.5–1 µm), whereas the marble surface was apparently completely covered by a new coating with flower-like morphology in the case of the less-concentrated solution (containing higher EtOH amounts). When potential was applied, formation of new phases was much more abundant for both solutions at both times (Figure 7). After 3 h, in the case of the less-concentrated solution, a very densely packed coating was formed, exhibiting the typical flower-like morphology in a recess in the surface. Also in the case of the more-concentrated solution, almost

complete coverage was obtained after 3 h, but the resulting coating appeared as significantly coarser. In terms of composition of the new phases formed after 3 h at $E = -2$ V, FT-IR spectra exhibit bands attributable to HAP, which were more defined (especially the band at 1028–1031 cm^{-1}) when more EtOH was present in the solution.
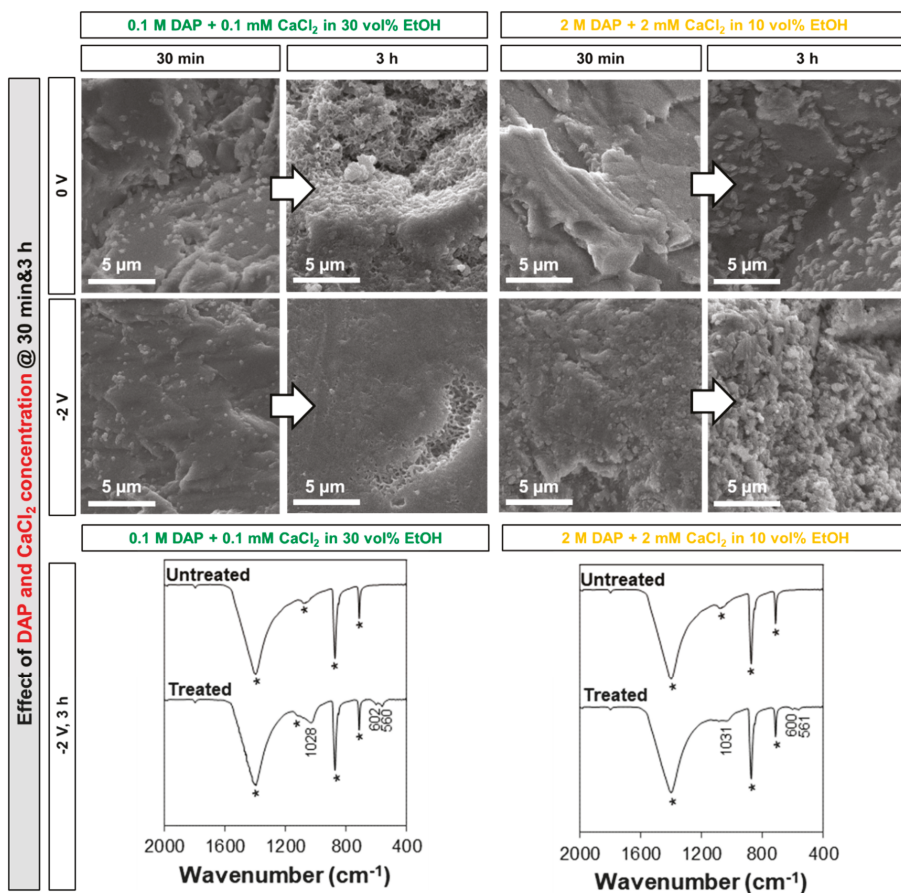
Figure 7. Effect of the different diammonium hydrogen phosphate (DAP) and CaCl$_2$ concentrations on the new calcium phosphate (CaP) phases formed at different times, with and without electrodeposition (in the FT-IR spectra, bands owing to the substrate are marked by a star, while the position of the new bands owing to CaP phases is reported).

For both DAP/CaCl$_2$ concentrations, formation of an almost continuous coating was obtained. Based on the position of the FT-IR bands (Figure 7), it seems most likely that the coatings are composed of HAP, even though formation of OCP cannot be completely excluded. In either case, both formulations were regarded as promising and hence taken into consideration in the prosecution of the study.

3.3. Influence of Electrokinetic Parameters: Pulsing, Voltage, and Time

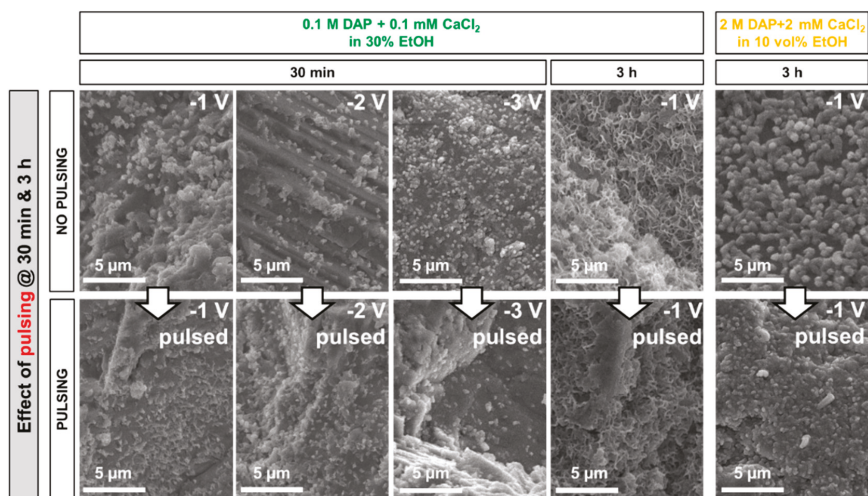The effect of applying a pulsed potential is illustrated in Figure 8.

Figure 8. Effect of pulsed potential on the morphology of the new CaP formed at different times.

In the case of the less-concentrated solution, a limited increase in the density of the new CaP clusters when pulsed potential was applied can be noticed after treatment for 30 min, while the pulsing effect became less evident after 3 h. In fact, after 3 h the flower-like coating was basically complete even with constant potential, so that no increase in coverage thanks to the pulsed potential was visible. In the case of the more-concentrated solution (containing less EtOH), the effect of pulsing was not investigated at 30 min, because almost no coating had been found to form at that time at constant potential (Figure 7). After 3 h, the coating deposited at constant potential appeared to be composed of relatively big, separated crystals, which leave the marble surface partly bare. With pulsed potential, the surface was somewhat improved, although better results were obtained using the less-concentrated solution (containing more EtOH).

Because, in all cases, the effect of pulsing was lower than hoped based on the studies reported in the literature [24,27,29], constant potential was adopted in the prosecution of the study.

The change in the amount and surface coverage of the new phases as a function of the applied voltage and time is illustrated in Figure 9 for the less-concentrated solution and in Figure 10 for the more-concentrated one.

In both cases, it is possible to observe that, at short time (30 min), the number of new phases increased visibly for increasing voltage. In fact, at 30 min, only a few CaP clusters were formed when no voltage was applied (lighter particles over the darker marble surface in Figures 9 and 10). This is consistent with previous results reported in the literature, where CaP formation was found to start to be significant between 3 and 6 h, depending on the formulation of the precursor phosphate solution [12]. When voltage was applied and progressively increased, a progressively more continuous coating was formed. In the case of the more-concentrated solution (Figure 10), the effect was still visible up to 3 h, because the lower amount of EtOH present in this solution (10 vol.%, compared to 30% in the less-concentrated one) implies a longer time for the CaP coating to develop. After 6 h, no significant difference was evident among samples treated with different voltage, including the samples treated without electrodeposition. Apparently, at least in the investigated conditions, after prolonged treatment the effect of time becomes predominant over that of electrodeposition.
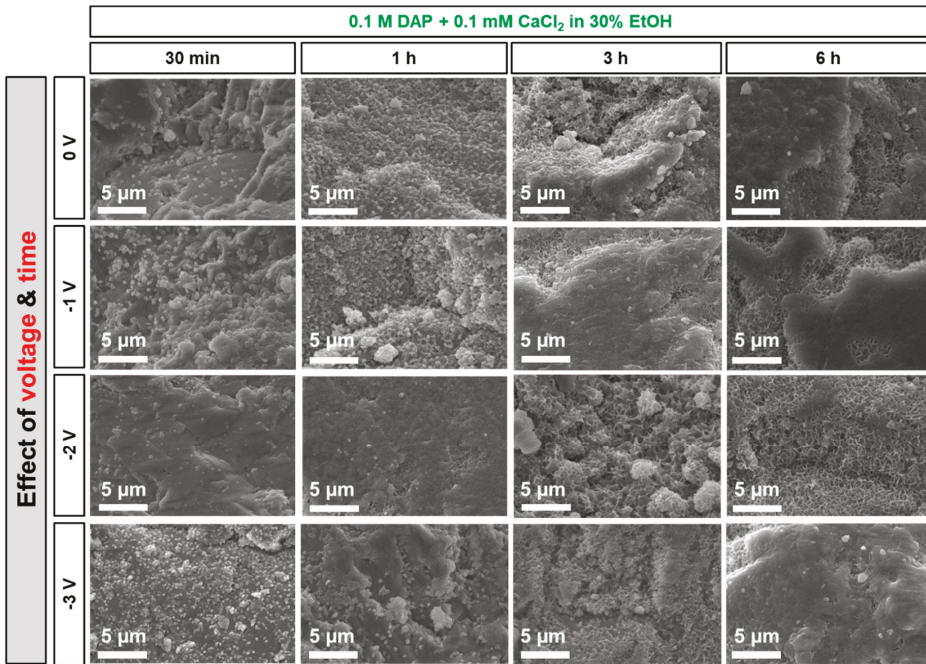
Figure 9. Effect of voltage and time on the morphology of the new CaP phases formed from the less-concentrated solution (0.1 M DAP + 0.1 mM CaCl$_2$ in 30 vol.% EtOH).
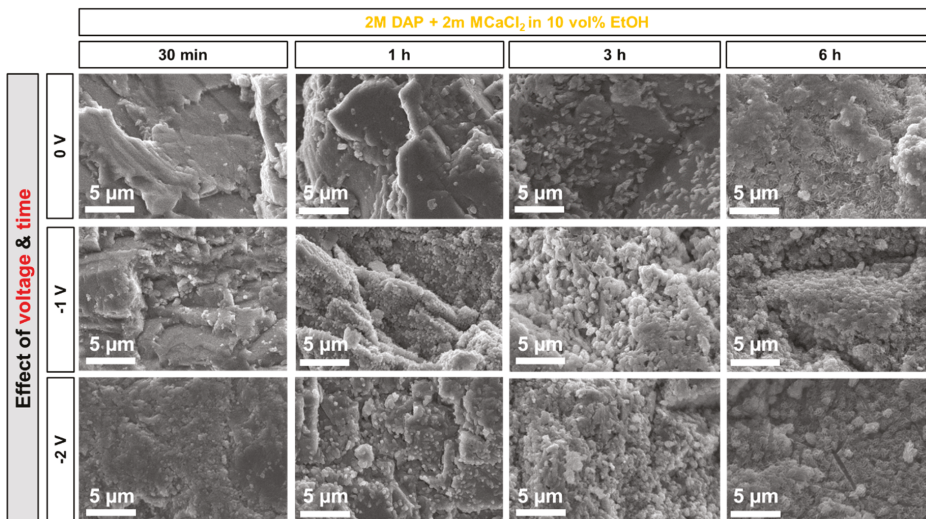

Figure 10. Effect of voltage and time on the morphology of the new CaP phases formed from the less-concentrated solution (2 M DAP + 2 mM CaCl$_2$ in 10 vol.% EtOH).

In the case of the less-concentrated solution (Figure 9), a significant change in the amount and morphology of the new phases was clearly visible passing from 0 to −1 and −2 V. On the contrary,

the difference between coatings formed at −2 and −3 V was less evident. A reason for this might be that, during electrodeposition, the cathode itself is progressively coated with new CaP phases, as already suggested by the change in current measured during potentiostatic deposition (Figure 5a) and confirmed by SEM observation of the steel grids. As a consequence, after a certain time, the amount of current circulating in the system diminishes, so that electrodeposition of the new phases over the marble sample diminishes as well. Consistently, a reduction was found in the current measured during electrodeposition at −2 and −3 V (Figure 5a), whereas no significant change in current was registered during electrodeposition at −1 V (graph not shown). This is consistent with results previously reported in the literature, indicating that HAP was present only in minor amounts when electrodeposition was carried out at −1.25 V and it became the major phase when electrodeposited at −1.55 V or lower [18].

In the case of the more-concentrated solution, micro-cracks with ~5 μm length and ~1 μm width are visible in the flowery coating deposited at −2 V for 6 h (Figure 10, bottom-right image). This suggests that the film formed in these conditions is likely porous and thick, which leads to cracking during drying. In fact, drying cracks do not form when the film is dense and its thickness is below the critical threshold, below which cracking is thermodynamically impeded [44]. Consequently, electrodeposition at −3 V was not considered for the acid resistance tests in the case of the more-concentrated solution.

Based on all the results reported above, the choice of the formulations for the acid attack tests was made. In the case of the less-concentrated solution, treatment at −2 V for 3 and 6 h was selected, because in both cases a basically complete coverage of the marble surface was achieved (Figure 9). In the case of the more-concentrated solution, the treatment at −1 V for 6 h was taken into account, while the treatment at higher voltage (E = −2 V) was discarded, because the resulting coating was heavily cracked (Figure 10). For all these conditions, samples treated for the same time but without electrodeposition were also considered, for comparison's sake.

3.4. Acid Resistance

The amounts of Ca and P released in the acidic solutions, measured by ICP at the end of the acid resistance test, are reported in Table 1.

Table 1. Weight amounts of Ca and P per unit area of surface exposed to the acid attack, dissolved from untreated and treated marble samples, measured by inductively coupled plasma optical emission spectrometry (ICP) in the solutions collected at the end of the acid resistance tests (marble specimens with bare edges and coated edges were tested).

Sample	Voltage, Time	Bare Edges		Coated Edges	
		Ca (mg/cm^2)	P (mg/cm^2)	Ca (mg/cm^2)	P (mg/cm^2)
Untreated reference	–	0.09	–	0.08	–
0.1 M DAP + 0.1 mM CaCl$_2$ in 30 vol.% EtOH	0 V, 3 h	0.10	–	0.03	–
0.1 M DAP + 0.1 mM CaCl$_2$ in 30 vol.% EtOH	−2 V, 3 h	0.08	–	0.02	–
0.1 M DAP + 0.1 mM CaCl$_2$ in 30 vol.% EtOH	0 V, 6 h	0.09	–	0.01	–
0.1 M DAP + 0.1 mM CaCl$_2$ in 30 vol.% EtOH	−2 V, 6 h	0.08	–	0.02	–
2 M DAP + 2 mM CaCl$_2$ in 10 vol.% EtOH	0 V, 6 h	0.11	0.01	0.01	–
2 M DAP + 2 mM CaCl$_2$ in 10 vol.% EtOH	−1 V, 6 h	0.08	0.01	0.02	–

The surface appearance of untreated and treated marble samples, before and after the acid attack test, is illustrated in Figure 11.
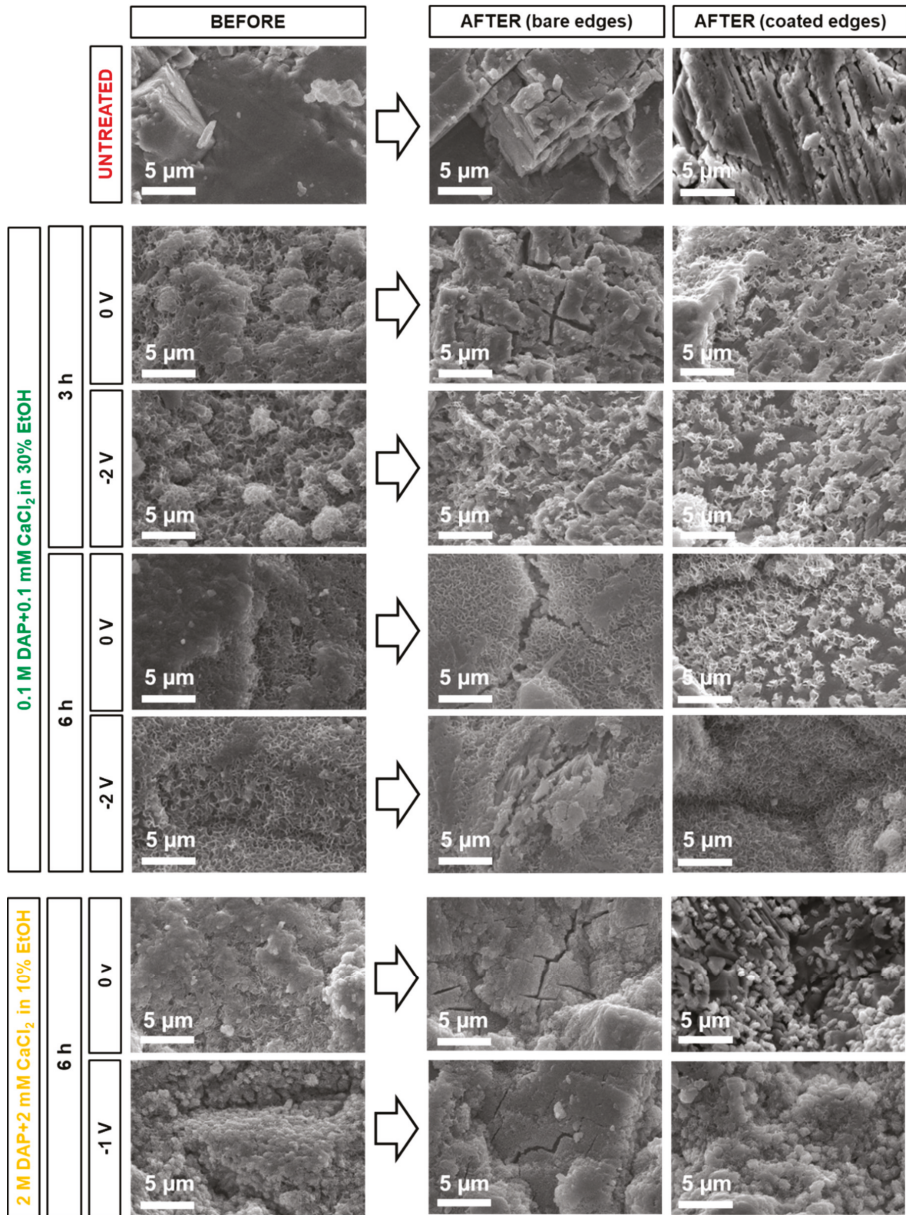

Figure 11. Surface morphology of untreated and treated marble samples, before and after the acid resistance test (samples with either bare or coated edges during the acid test are reported).

As expected, after the acid test, the untreated reference exhibited visible surface etching, in the form of grooves and exposed grain boundaries. As a consequence, Ca ions were detected in the solution (Table 1).

In the case of treated samples, tested with bare edges, no formulation was able to completely prevent dissolution of the marble substrate. In fact, the measured Ca losses had the same order of magnitude as those of the untreated reference (Table 1) and cracking of the protective coatings was clearly visible after the acid attack test (Figure 11). Some limited benefits seem to result from treatments applied by electrodeposition for 6 h, with either concentration of DAP and $CaCl_2$ (Table 1). In these conditions, the lowest Ca losses were registered, and limited damage of the coating was observed after the acid attack test. In the case of the less-concentrated formulation, no P was detected in the solutions analyzed after the acid test, which suggests that the coatings were not dissolved during exposure to acid and that the measured Ca losses mostly originate from dissolution of the marble substrate in uncovered zones or cracks in the coating. Differently, in the case of the more-concentrated solution, some small amounts of P were also detected in the solutions, suggesting that some coating dissolution likely took place.

The reason why cracks were visible after the acid resistance test (Figure 11), while no crack was noticed for the same formulations before the acid attack test (Figures 9 and 10), is thought to be the presence of pores inside the coatings, combined with the specific experimental conditions adopted for these specimens. Indeed, before exposure to acid, the bonding at the interface between the coating and the substrate was strong enough to prevent cracking during drying at the end of the treatment application. However, during the acid test, pores likely allowed acid to reach the substrate/coating interface and to weaken the bonding between the two. As a result, the stress arising in the pores during drying at the end of the acid test now led to cracking. To verify the presence of pores in the coatings, further tests would be needed (e.g., observation of cross sections by a focused ion beam microscope, FIB-SEM). A further reason for the weakening of the coating/substrate interface is thought to be the specific experimental conditions adopted for the first set of specimens, i.e., subjecting them to the acid resistance test without coating their edges. In these conditions, the acid attack can start from the edges (where the coating is often damaged during treatment and handling) and then propagate to the rest of the sample. For this reason, the second set of specimens was treated after coating their edges with an impermeable coat, so that only the central, uniform part of the samples was exposed to acid. In these latter conditions, quite different results were obtained.

In fact, when samples were tested after coating the edges with an impermeable coat, the untreated reference exhibited Ca release much higher than the treated samples (Table 1), which indicates that the coatings were able to provide a better acid protection than in the previous case. Accordingly, SEM images show no sign of cracking in any sample (Figure 11). This confirms that the presence of damaged areas near the sample edges allowed acid to reach the substrate/coating interface, weaken the bonding between the two, and trigger cracking. Nonetheless, the effect of pores in the coatings cannot be excluded and further analyses by FIB-SEM are opportune. In some cases, especially in samples treated without electrodeposition, the calcite substrate is sometimes visible in the SEM images (darker areas beneath the lighter flower-like crystals in Figure 11). This indicates that, also in the case of samples tested after coating the edges, the surface coverage and the resulting protection were not complete. Anyway, all the specimens subjected to the acid attack test clearly exhibited bands attributable to HAP after the test (Figure 12), which confirms that the coatings are still present after exposure to acid.
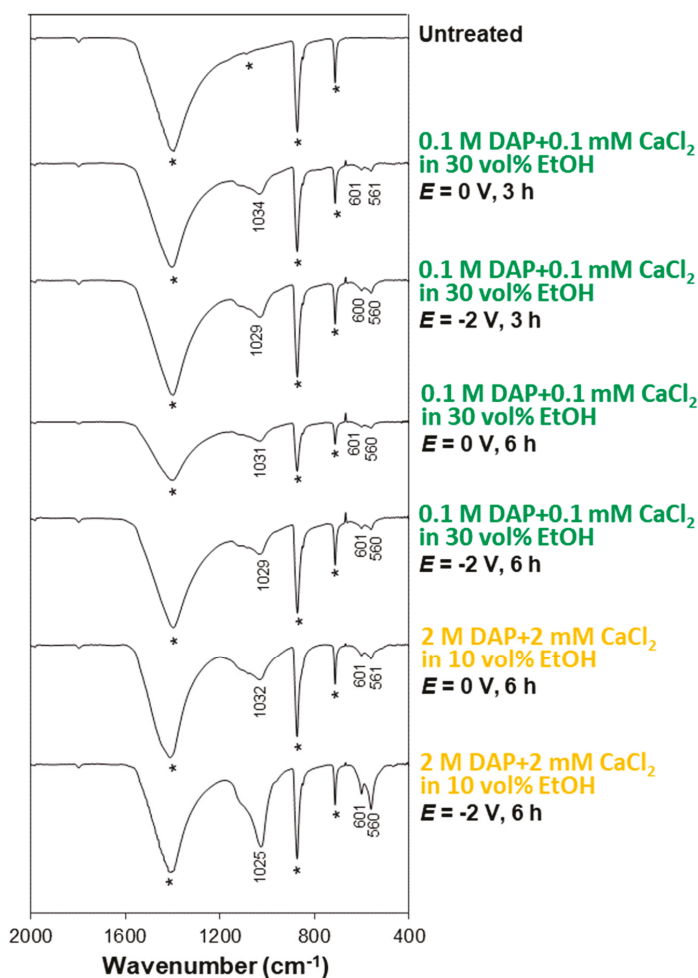
Figure 12. FT-IR spectra of untreated and treated samples (tested with coated edges), after the acid test (in the FT-IR spectra, bands owing to the substrate are marked by a star, while the position of the new bands owing to CaP phases is reported).

4. Conclusions

The results of the present study, aimed at assessing the feasibility of electrodepositing HAP coatings over marble and evaluating the protective ability of the resulting coatings, allow to derive the following conclusions:

- Electrodeposition of HAP over the marble surface can be obtained by placing the marble sample close to the cathode. In these conditions, OH^- groups formed near the cathode during electrodeposition favor HAP formation, compared to the situation when no electric potential is applied. Compared to simple increase in pH of the phosphate solution used as HAP precursor, the local increase in OH^- near the cathode has the advantage that precipitation of CaP in the bulk solution and excessive film growth are prevented.

- At short times (30 min and 1 h), electrodeposition has a significant effect in accelerating and improving marble coverage by the new HAP coating. At longer times, the effect becomes less evident, because HAP nucleation and growth take place even without electrodeposition.

- Among the two formulations investigated in this study (namely, a solution containing 0.1 M DAP + 0.1 mM $CaCl_2$ in 30 vol.% EtOH and a solution containing 2 M DAP + 2 mM $CaCl_2$ in 10 vol.% EtOH), the less-concentrated one, containing a higher amount of ethanol, leads to formation of more uniform coatings in a shorter time. This is possible thanks to the boosting effect of ethanol, which is visible even without electrodeposition and which is further enhanced when electric potential is applied.

- The HAP coatings formed by electrodeposition in the present most promising conditions (-2 V for 3 and 6 h in the case of the less-concentrated solution and -1 V for 6 h in the case of the more-concentrated one) provide some protective efficacy, even though the substrate dissolution is not completely inhibited. In fact, pores are likely present in the electrodeposited coatings, which reduces their protective efficacy and leads to cracking when the coating thickness is excessive. Moreover, possible damaged parts (e.g., the areas near the edges) proved to have a not negligible influence on the coating protective efficacy, which needs to be taken into account when designing acid resistance tests.

All things considered, electrodeposition seems like a technique able to accelerate and improve formation of HAP coatings over the marble surface, even though the resulting protective efficacy is not complete yet. Electrodeposited coatings appear to be mainly composed of HAP, while presence of other CaP was not evidenced. To ascertain the presence of pores in the coatings, further research is needed, for instance observation of cross sections by FIB-SEM.

Author Contributions: Conceptualization, E.S.; Methodology, E.S., G.M, M.C.B. and E.F.; Investigation, E.S. and G.M.; Resources, M.C.B. and E.F.; Data Curation, E.S. and G.M.; Writing-Original Draft Preparation, E.S.; Writing-Review & Editing, E.S., G.M., M.C.B. and E.F.; Supervision, M.C.B. and E.F.; Funding Acquisition, E.S.

Conflicts of Interest: The authors declare no conflict of interest.

References

1. Patnaik, P. *Handbook of Inorganic Chemical Compounds*, 1st ed.; McGraw-Hill: New York, NY, USA, 2003.
2. Naidu, S.; Blair, J.; Scherer, G.W. Acid-resistant coatings on marble. *J. Am. Ceram. Soc.* **2016**, *99*, 3421–3428. [CrossRef]
3. Dorozhkin, S.V. Calcium orthophosphates: Occurrence, properties, biomineralization, pathological calcification and biomimetic applications. *Biomatter* **2011**, *1*, 121–164. [CrossRef]
4. Naidu, S.; Sassoni, E.; Scherer, G.W. New treatment for corrosion-resistant coatings for marble and consolidation of limestone. In *Jardins de Pierres—Conservation of Stone in Parks, Gardens and Cemeteries*; Stefanaggi, M., Vergès-Belmin, V., Eds.; XL Print: Paris, France, 2011; pp. 289–294.
5. Graziani, G.; Sassoni, E.; Franzoni, E.; Scherer, G.W. Hydroxyapatite coatings for marble protection: Optimization of calcite covering and acid resistance. *Appl. Surf. Sci.* **2016**, *368*, 241–257. [CrossRef]
6. Graziani, G.; Sassoni, E.; Scherer, G.W.; Franzoni, E. Resistance to simulated rain of hydroxyapatite- and calcium oxalate-based coatings for protection of marble against corrosion. *Corros. Sci.* **2017**, *127*, 168–174. [CrossRef]
7. Sassoni, E.; Graziani, G.; Franzoni, E.; Scherer, G.W. Calcium phosphate coatings for marble conservation: Influence of ethanol and isopropanol addition to the precipitation medium on the coating microstructure and performance. *Corros. Sci.* **2018**, *136*, 255–267. [CrossRef]

8.   Sassoni, E. Hydroxyapatite and other calcium phosphates for the conservation of cultural heritage: A review. *Materials* **2018**, *11*, 557. [CrossRef] [PubMed]

9.   Sassoni, E.; Naidu, S.; Scherer, G.W. The use of hydroxyapatite as a new inorganic consolidant for damaged carbonate stones. *J. Cult. Herit.* **2011**, *12*, 346–355. [CrossRef]

10.   Possenti, E.; Colombo, C.; Bersani, D.; Bertasa, M.; Botteon, A.; Conti, C.; Lottici, P.P.; Realini, M. New insight on the interaction of diammonium hydrogen phosphate conservation treatment with carbonatic substrates: A multi-analytical approach. *Microchem. J.* **2016**, *127*, 79–86. [CrossRef]

11.   Possenti, E.; Colombo, C.; Conti, C.; Gigli, L.; Merlini, M.; Rikkert Plaisier, J.; Realini, M.; Sali, D.; Diego Gatta, G. Diammonium hydrogenphosphate for the consolidation of building materials. Investigation of newly-formed calcium phosphates. *Constr. Build. Mater.* **2019**, *195*, 557–563. [CrossRef]

12.   Naidu, S.; Scherer, G.W. Nucleation, growth and evolution of calcium phosphate films on calcite. *J. Colloid Interface Sci.* **2014**, *435*, 128–137. [CrossRef] [PubMed]

13.   Redeppening, J.; McIsaac, J.P. Electrocrystallization of brushite coatings on prosthetic alloys. *Chem. Mater.* **1990**, *2*, 625–627. [CrossRef]

14.   Shirkhanzadeh, M. Bioactive calcium phosphate coatings prepared by electrodeposition. *J. Mater. Sci. Lett.* **1991**, *10*, 1415–1417. [CrossRef]

15.   Monma, H. Electrolytic depositions of calcium phosphates on substrate. *J. Mater. Sci.* **1994**, *29*, 949–953. [CrossRef]

16.   Shirkhanzadeh, M. Calcium phosphate coatings prepared by electrocrystallization from aqueous electrolytes. *J. Mater. Sci. Mater. Med.* **1995**, *6*, 90–93. [CrossRef]

17.   Redeppening, J.; Schlessinger, T.; Burnham, S.; Lippiello, L.; Miyano, J. Characterization of electrolytically prepared brushite and hydroxyapatite coatings on orthopedic alloys. *J. Biomed. Mater. Res.* **1996**, *30*, 287–294. [CrossRef]

18.   Yen, S.K.; Lin, C.M. Cathodic reactions of electrolytic hydroxyapatite coating on pure titanium. *Mater. Chem. Phys.* **2002**, *77*, 70–76. [CrossRef]

19.   Kuo, M.C.; Yen, S.K. The process of electrochemical deposited hydroxyapatite coatings on biomedical titanium at room temperature. *Mater. Sci. Eng. C* **2002**, *20*, 153–160. [CrossRef]

20.   Eliaz, N.; Sridhar, T.M. Electrocrystallization of hydroxyapatite and its dependence on solution conditions. *Cryst. Growth Des.* **2008**, *8*, 3965–3977. [CrossRef]

21.   Hu, R.; Lin, C.; Shi, H.; Wang, H. Electrochemical deposition mechanism of calcium phosphate coating in dilute Ca-P electrolyte system. *Mater. Chem. Phys.* **2009**, *115*, 718–723. [CrossRef]

22.   Mokabber, T.; Lu, L.Q.; van Rijn, P.; Vakis, A.I.; Pei, Y.T. Crystal growth mechanism of calcium phosphate coatings on titanium by electrochemical deposition. *Surf. Coat. Technol.* **2018**, *334*, 526–535. [CrossRef]

23.   Bobby Kannan, M. Enhancing the performance of calcium phosphate coating on a magnesium alloy for bioimplant applications. *Mater. Lett.* **2012**, *76*, 109–112. [CrossRef]

24.   Kannan, M.B.; Wallipa, O. Potentiostatic pulse-deposition of calcium phosphate on magnesium alloy for temporary implant applications—An in vitro corrosion study. *Mater. Sci. Eng. C* **2013**, *33*, 675–679. [CrossRef]

25.   Kannan, M.B. Improving the packing density of calcium phosphate coating on a magnesium alloy for enhanced degradation resistance. *J. Biomed. Mater. Res. A* **2013**, *101A*, 1248–1254. [CrossRef]

26.   Walter, R.; Kannan, M.B.; He, Y.; Sandham, A. Influence of the cathodic activity of magnesium alloys on the electrochemical deposition of calcium phosphate. *Mater. Lett.* **2014**, *130*, 184–187. [CrossRef]

27.   Bobby Kannan, M. Electrochemical deposition of calcium phosphates on magnesium and its alloys for improved biodegradation performance: A review. *Surf. Coat. Technol.* **2016**, *301*, 36–41. [CrossRef]

28.   Chen, J.S.; Juang, H.Y.; Hon, M.H. Calcium phosphate coating on titanium substrate by a modified electrocrystallization process. *J. Mater. Sci. Mater. Med.* **1998**, *9*, 297–300. [CrossRef] [PubMed]

29.   Gopi, D.; Indira, J.; Kavitha, L. A comparative study on the direct and pulsed current electrodeposition of hydroxyapatite coatings on surgical grade stainless steel. *Surf. Coat. Technol.* **2012**, *206*, 2859–2869. [CrossRef]

30.   Monasteiro, N.; Ledesma, J.L.; Aranguiz, I.; Garcia-Romero, A.; Zuza, E. Analysis of electrodeposition processes to obtain calcium phosphate layer on AZ31 alloy. *Surf. Coat. Technol.* **2017**, *319*, 12–22. [CrossRef]

31.   Drevet, R.; Benhayoune, H.; Wortham, L.; Potiron, S.; Douglade, J.; Laurent-Maquin, D. Effects of pulsed current and H2O2 amount on the composition on electrodeposited calcium phosphate coatings. *Mater. Character* **2010**, *61*, 786–795. [CrossRef]

32. Blackwood, D.J.; Seah, K.H.W. Electrochemical cathodic deposition of hydroxyapatite: Improvements in adhesion and crystallinity. *Mater. Sci. Eng. C* **2009**, *29*, 1233–1238. [CrossRef]

33. Ottosen, L.M.; Rörig-Dalgård, I. Electrokinetic removal of $Ca(NO_3)_2$ from bricks to avoid salt-induced decay. *Electrochim. Acta* **2007**, *52*, 3454–3463. [CrossRef]

34. Ottosen, L.M.; Rörig-Dalgård, I. Desalination of a brick by application of an electric DC field. *Mater. Struct.* **2009**, *42*, 961–971. [CrossRef]

35. Ottosen, L.M.; Christensen, I.V. Electrokinetic desalination of sandstones for NaCl removal—Test of different clay poultices at the electrodes. *Electrochim. Acta* **2012**, *86*, 192–202. [CrossRef]

36. Bernabeu, A.; Expçsito, E.; Montiel, V.; Ordònez, S.; Aldaz, A. A new electrochemical method for consolidation of porous rocks. *Electrochem. Commun.* **2001**, *3*, 122–127. [CrossRef]

37. Feijoo, J.; Ottosen, L.M.; Nòvoa, X.R.; Rivas, T.; de Rosario, I. An improved electrokinetic method to consolidate porous materials. *Mater. Struct.* **2017**, *50*, 186. [CrossRef]

38. Feijoo, J.; Nòvoa, X.R.; Rivas, T. Electrokinetic treatment to increase bearing capacity and durability of granite. *Mater. Struct.* **2017**, *50*, 251. [CrossRef]

39. Meloni, P.; Manca, F.; Carcangiu, G. Marble protection: An inorganic electrokinetic approach. *Appl. Surf. Sci.* **2013**, *273*, 377–385. [CrossRef]

40. Matteini, M.; Moles, A.; Giovannoni, S. Calcium oxalate as a protective mineral system for wall paintings: Methodology and analyses. In Proceedings of the III International Symposium Conservation of Monuments in the Mediterranean Basin, Venice, Italy, 22–25 June 1994.

41. Sandrolini, F.; Franzoni, E.; Sassoni, E.; Diotallevi, P.P. The contribution of urban-scale environmental monitoring to materials diagnostics: A study on the Cathedral of Modena (Italy). *J. Cult. Herit.* **2011**, *12*, 441–450. [CrossRef]

42. Bonazza, A.; Messina, P.; Sabbioni, C.; Grossi, C.M.; Brimblecombe, P. Mapping the impact of climate change on surface recession of carbonate buildings in Europe. *Sci. Total Environ.* **2009**, *407*, 2039–2050. [CrossRef]

43. Karampas, I.A.; Kontoyannis, C.G. Characterization of calcium phosphates mixtures. *Vib. Spectrosc.* **2013**, *64*, 126–133. [CrossRef]

44. Evans, A.G.; Drory, M.D.; Hu, M.S. The cracking and decohesion of thin films. *J. Mater. Res.* **1988**, *3*, 1043–1049. [CrossRef]

Ion-Substituted Carbonated Hydroxyapatite Coatings for Model Stone Samples

Rodica-Mariana Ion [1,2,†,*], Lorena Iancu [1,2,†], Gabriel Vasilievici [1,†], Madalina Elena Grigore [1,†], Ramona Elena Andrei [1,†], George-Ionut Radu [1,†], Ramona Marina Grigorescu [1,†], Sofia Teodorescu [3,†], Ioan Alin Bucurica [3,†], Mihaela-Lucia Ion [4,†], Anca Irina Gheboianu [3,†], Cristiana Radulescu [3,†] and Ioana Daniela Dulama [3,†]

[1] Research Group "Evaluation and Conservation of Cultural Heritage", National R&D Institute for Chemistry and Petrochemistry–ICECHIM, 202 Splaiul Independentei, 060021 Bucharest, Romania; lorenna77ro@yahoo.com (L.I.); gabi.vasilievici@gmail.com (G.V.); grigore.madalina10@gmail.com (M.E.G.); andreiramona@hotmail.com (R.E.A.); radugeorgeionut@yahoo.com (G.-I.R.); rmgrigorescu@gmail.com (R.M.G.)

[2] Materials Engineering Department, Doctoral School of Materials Engineering, Valahia University of Târgoviște, 130105 Târgoviște, Romania

[3] Institute of Multidisciplinary Research for Science and Technology, Valahia University of Targoviste, 13 Sinaia Alley, 130004 Targoviste, Romania; sofiateodorescu@yahoo.com (S.T.); bucurica_alin@yahoo.com (I.A.B.); anca_b76@yahoo.com (A.I.G.); radulescucristiana@yahoo.com (C.R.); dulama_id@yahoo.com (I.D.D.)

[4] "Atelierul de Creatie" NGO, 12 Liviu Rebreanu, 031786 Bucharest, Romania; lucia.mihaella@gmail.com

* Correspondence: rodica_ion2000@yahoo.co.uk; Tel.: +40-21-316-3094

† These authors contributed equally to this work.

Abstract: Carbonated hydroxyapatite derivatives (CHAp) and its metallic derivatives (Ag, Sr, Ba, K, Zn) have been prepared and characterized in this paper and their coating capacity on some model stone samples have been evaluated and discussed. These compounds were characterized by using several analytical tools, including X-ray diffraction analysis (XRD), thermogravimetric analysis (TGA), Fourier transform infrared spectroscopy (FTIR), to determine the purity of the CHAp sample. The XRD and FTIR results confirmed the presence of AB-carbonated type CHAp. The thermal analysis (TGA) established two stages of weight loss that occured during the heating process: The first weight loss between 30–225 °C corresponding to the partial carbonate release from OH-channel and the second one between 226–700 °C, corresponding to some thermal reactions, possibly to the generation of calcium phosphate. The efficiency and suitability of these products on model stone samples were evaluated by monitoring the resistance to artificial weather (freeze–thaw), and pore structure changes (surface area, pore volume, pore diameter). Meanwhile, optical microscopy (OM) and Scanning Electron Microscopy with Energy Dispersive Spectroscopy (SEM–EDS) techniques showed the particles size and surface morphology of the samples, as well as information on its chemical composition. Also, the compressive strength of these new compounds as coatings revealed a homogeneity and strengthen of these model stone samples.

Keywords: carbonated hydroxyapatite; nanomaterials; coatings

1. Introduction

Nowadays, one of the main difficulties in preserving objects and heritage monuments is to select the most adequate treatment methods for stone protection, able to preserve their original appearance, without any detrimental effect on their aesthetic properties [1]. The protective products must preserve the stones, to bring it to a state like the original one and prevent further damage. In general, to apply a coating to the surface of the stone.

The requirements for the consolidation of products consist of: Good stability, compatibility with the substrate [2] and adequate penetration depth. A good consolidant should first reduce the rate of degradation of the stone surface and then improve its mechanical properties.

The main challenges in stone protection are related to the creation of a barrier against water penetration and protection of the stone surface against pollutants and the deposition of organic/inorganic particles, while ensuring aesthetic compatibility with the substrate (i.e., color changes at acceptable intervals), a minimal change in water vapor permeability and reversibility of the treatment [3]. In this perspective, hydrophobic coatings [4], antifouling treatments [5] and nanoparticle self-cleaning bands [6] are currently at the center of research on stone conservation [7,8].

However, at present, there are no standard procedures and/or unique assessment methods supporting the effectiveness of enhancers and protection products [9].

A good consolidant should have a good penetration depth and adhesion to the substrate. The bonding capacity depends to a large extent, both the chemical composition of the product (including solvent and concentration) and the stone surface. In particular, the products with a composition-like stone are preferred. Among the new products synthesized for preservation of culture heritage materials, some hybrid formulations have been recently proposed for inorganic [10] and organic materials [11,12].

Another aspect concerning the consolidant is the method of application [11,13], which plays a key role, significantly influencing the transfer of laboratory procedures to on-site practice. There are some application methods: Immersion, which can be easily controlled in the laboratory, but is hardly reproducible on site where it maximizes the penetration depth very hard; poulticing, to control even in laboratory conditions [13]; spraying, which delivers high amounts of consolidant at one time, causing a large consolidant runoff and consumption (besides a higher solvent evaporation due to nebulisation) [11], but a limited penetration depth [10]; and brushing, which often lacks an adequate control of all the parameters that finally determine the treatment efficacy [3,12]. Usually, the brushing method is preferred because it assures an efficient application and a relatively controlled balance between penetration and solvent evaporation [13,14]. Nanomaterials exhibit good chemical–physical features for application in the conservation science of artwork, being able to slow down the degradation processes of artifacts, by comparison with traditional methods, widely described in literature [15]. Up to now, the most used consolidants are nano hydroxyapatite, $Ca_{10}(PO_4)_6(OH)_2$, already used for travertine, marble and limestone chalk stone consolidation, and used as models for architectural monuments [16].

The aim of this paper is to synthesize and to test some consolidants based on carbonated hydroxyapatite (CHAp), which is quite similar with hydroxyapatite [17–19]. By comparison with Hap, which has a crystal structure very similar to that of calcite, enabling epitaxial growth over calcareous matrices [20], in carbonated hydroxyapatite (CHAp) the CO_3^{2-} ions can replace both OH^- and PO_4^{3-} ions and thus the last form has a high special surface area than the previous one [21]. In the case of carbonated hydroxyapatite, a decrease in the a-axis and increase in the c-axis in the apatite lattice is registered, due to the incorporation of B-type CO_3^{2-} substitution into the HAp structure [22], a decrease of the crystalinity which suggests a decrease in the crystallite size and crystallinity of the apatite phase [23,24], given by the highest amount of CO_3^{2-} in the apatite structure [25].

Carbonated hydroxyapatite derivatives (CHAp) and its metallic derivatives (Silver (Ag); Strontium (Sr); Barium (Ba); Potassium (K); Zinc (Zn)) have been prepared and characterized by X-ray diffraction analysis (XRD), thermogravimetric analysis (TGA), Fourier transform infrared spectroscopy (FTIR). The efficiency and suitability of these products on model stone samples, applied by brushing (B) and spraying (S), were evaluated by monitoring the resistance to artificial weather (freeze–thaw) and pore structure changes (surface area, pore volume, pore diameter). Also, the mechanical strengths of these new compounds as coatings for model stone samples revealed good adherence, homogeneity and strength of these layers.

2. Materials and Methods

2.1. Specimens Samples Preparation

Different samples were prepared from sand and a mixture of gypsum with lime (95%–5%) (1:4) (40 mm × 40 mm × 40 mm) in order to distinguish the difference between non-treated/treated samples and to observe the influence of consolidant used during the treatment. Cubic specimens (diameter: 4 cm, height: 4 cm) have been prepared in a silicon resin matrice in order to avoid the dispersion of the solid matter or evaporation of the solvent from the lateral sides. All specimens were stored under controlled conditions (T = 20 °C, 65% RH) for 1 month. After the drying process, the substrates were left to cool for two hours in a desiccator and adequately treated with the new prepared compounds, and their appearance was examined.

2.2. Application of the Carbonated Hydroxyapatite Derivatives

The nanoparticles were suspended in distilled water with conductivity <2 s/cm, due to its higher boiling point and higher surface tension, responsible for a low kinetic stability. They were applied by spraying, an application method commonly adopted in the practice of conservation, for a good penetration and deposition in depth. The procedure was repeated with up to 3 consecutive applications, in order to improve the consolidation effect. The interval between consecutive applications was defined at 6 h, for achieving a complete evaporation of the solvent. The applications were performed under controlled conditions (50% RH, T = 20 °C, air speed <0.1 m/s). The treated specimens were then stored at 65% RH, T = 20 °C, air speed <0.1 m/s for over 1 months, in order to enhance the nanoparticles deposition.

2.3. CHAp Synthesis

Carbonated hydroxyapatite (CHAp), as very fine and uniform sized powder, was obtained by a nanoemulsion technique adapted from Zhou et al. [26]. CHAp nanoparticles were synthesized by mixing aqueous solutions of $(NH_4)_2HPO_4$ and NH_4HCO_3, under magnetic stirring. The pH of the aqueous solution was adjusted to 11 using sodium hydroxide 1 M. Then an acetone solution of $Ca(NO_3)_2 \cdot 4H_2O$ at a molar ratio of $Ca^{2+}:PO_4^{3-}:CO_3^{2-}$ = 1.67:1:0.5 was introduced into the flask. The reaction was carried out at room temperature. The precipitate was vacuum filtered using a Buchner funnel and washed with distilled water. The reaction product was freeze-dried overnight and calcined the next day at 900 °C for 4 h. Doped CHAp with different metal ions (Ag^+, Sr^{2+}, Ba^{2+}, Zn^{2+}, K^+) was synthetized by a similar microemulsion method, the metal nitrate solution ($AgNO_3$, $Sr(NO_3)_2$, $Ba(NO_3)_2$, $Zn(NO_3)_2$, KNO_3) being added in the $Ca(NO_3)_2 \cdot 4H_2O$ acetone solution, in concentration of 5 mole% reported to Ca^{2+}. These compounds have been applied by brushing and spraying using an aqueous solution of 0.25g/L on the non-treated samples.

2.4. Chemical Characterization Methods

X-ray diffraction measurements of powder samples were carried out with a Rigaku Ultima IV diffractometer (Rigaku, Tokyo, Japan) using a Cu Kα radiation (λ = 1.54 Å). In this experiment the accelerating voltage of the generator radiation was set at 40 kV and the emission current at 200 mA. The diffractograms were recorded in parallel beam geometry over 2θ = 5° to 100° continuously at a scan rate of 4°/min.

Fourier transformed infrared spectroscopy (ATR–FTIR) was recorded with a Vertex 80 spectrometer (Bruker Optik GMBH, Billerica, MA, USA) equipped with DRIFT accessory, in the range of 2000–400 cm^{-1}, because the range 4000–2000 cm^{-1} did not show major changes for these samples.

Thermogravimetric analyses of CHAp were performed using a Pyris 1 TGA analyzer (Perkin–Elmer TGA-7, Waltham, MA, USA) with a scan range from 50–700 °C and a constant heating rate of 10 °C/min under continuous nitrogen.

For porosity determination, the nitrogen adsorption/desorption isotherms were recorded at 77 K in the relative pressure range p/p_o = 0.005–1.0 using NOVA2200e Gas Sorption Analyzer

(Quantachrome, Boynton Beach, FL, USA). Data processing was performed using NovaWin version 11.03 software. Prior to adsorption measurements, the samples were degassed for 4 h at 180 °C under vacuum. The specific surface area was determined by the standard Brunauer–Emmett–Teller (BET) equation. The total pore volume was estimated from the volume adsorbed at a relative pressure p/p_o close to unity. Pore size distribution and mesopores volume were obtained from desorption branch of the isotherm by applying the Barrett–Joyner–Halenda (BJH) model. The t-plot method was used to estimate the micropore surface area and external surface area.

Also, the OM was recorded by a Primo Star ZEISS optical microscope (Carl Zeiss, Oberkochen, Germany) that offers the possibility of investigating the samples in transmitted light at a magnification between 4–100×. The equipment had a digital video camera attached (Axiocam 105, Carl Zeiss, Oberkochen, Germany) which, by the microscope software (Zen Pro), allowed real-time data acquisition. The obtained images could easily be converted from 2D in 3D format through its software for a better view.

The Scanning Electron Microscopy with Energy Dispersive Spectroscopy (SEM–EDS) was obtained with a SU-70 (Hitachi, Japan) microscope, with a magnification range of 30×–800,000×.

Freeze–thaw aging test: For the freeze-thaw test (20 cycles) STAS 6200/15 83, the sample shall be dried in oven at 105 ± 5 °C for 1 h up to the constant mass (m_1). The samples were immersed in distilled water for 15 min at room temperature. The samples were kept in the freezer for 3 h at −18 ± 5 °C and then thawed in water. The freeze–thaw operation is repeated until 20 cycles are performed, after which the mass losses during the freeze–thaw process is expressed as gelivity coefficient, Equation (1).

$$\mu_g = (m_2 - m_3/m_1) \times 100\% \tag{1}$$

where:

m_1–the initial mass of the sample, determined after drying at 105 °C to the constant mass and before saturation with distilled water, in grams;

m_2–mass of sample saturated with water, determined before the first freeze–thaw cycle, in grams;

m_3–defrost mass of the sample, determined after drying at 105 °C to the constant mass and before saturation with distilled water, in grams.

2.5. Mechanical Testing Method

The mechanical strength test was performed with a Silver Schmidt Hammer Proceq test hammer, type L-0.735 Nm impact energy, according to ASTM C805. The strength range of the Silver Schmidt test hammer is from 10–100 N/mm^2. Ten replicates within the test location with a minimum spacing of 25 mm between each two testing points and a minimum edge distance of 25 mm, have been recorded. The hammer was positioned at 90° downward, and the rebound number value is calculated as the average of the readings within this test location, in order to find a relationship between surface hardness and compressive strength with an acceptable error. The compressive strength was calculated using the Equation (2) (for 10th percentile curve range), after apparatus manual indications.

$$\text{compressive strength} = 2.77 \times e\hat{}(0.048 \times Q) \tag{2}$$

The results have been obtained for the untreated and treated specimens with CHAp, Ag-CHAp, Sr-CHAp, Ba-CHAp, Zn-CHAp, K-CHAp solutions of 0.25 g/L solution applied by brushing and spraying on the stone surface.

3. Results

3.1. Crystal Structure

Table 1 summarizes the results of the phase purity and the average crystallite sizes calculated for the most intense peak of CHAp (0 0 2) for all the investigated samples by XRD and Scherrer Equation (3):

$$L = (K \times \lambda)/(\beta \times \cos\theta) \tag{3}$$

where:

Table 1. Summary of the XRD characterization of pure and substituted CHAp.

Sample	2θ, °	2θ, rad	β, °	β, rad	L, Å	L, nm
CHAp	25.80	0.4503	0.3460	0.006039	229.50	22.50
Ag-CHAp	26.41	0.4609	0.4273	0.007458	185.84	18.58
Sr-CHAp	25.78	0.4499	0.3349	0.005845	237.14	23.71
Ba-CHAp	25.84	0.4510	0.3350	0.005847	237.14	23.71
K-CHAp	25.82	0.4506	0.3454	0.006028	229.50	22.95
Zn-CHAp	25.84	0.4510	0.3271	0.005709	242.77	24.27
HAp	25.81	0.4505	0.186	0.003246	426.99	42.70

L = crystallite size;
K = Scherrer constant (0.9);
λ = X-ray wavelength (1.54 Å);
β = peak width at half maximum intensity (in radians), from the apparatus programme;
θ = Bragg angle, from the apparatus programme;

By analyzing this table, it could be observed that all the samples matched with the standard JCPDS reference (09-432) file for synthetic carbonated hydroxyapatite. XRD confirmed the phase purity of the synthesized carbonate hydroxyapatite [27] and no additional phases (brushite) were identified, this being an indication for these compounds' purity.

Figure 1 shows the characteristic XRD spectra for all samples. When all the prepared samples were analyzed by X-ray diffraction, their patterns were characteristic of the hexagonal apatite phase [28,29]. Few XRD peaks are characteristic of carbonated hydroxyapatite (with 2θ from 26–40) (Figure 1).
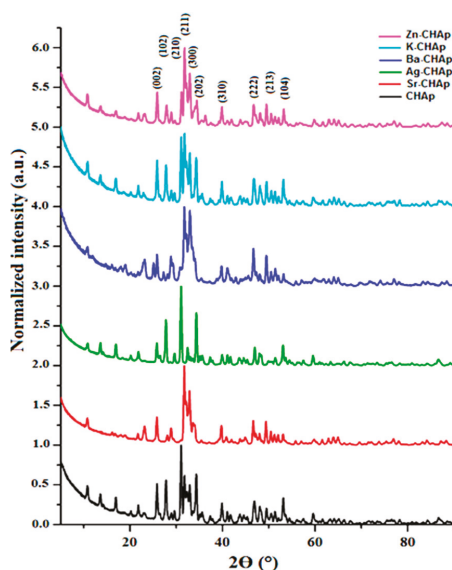
Figure 1. XRD diagrams for CHAp and Me-CHAp (Me = Sr, Ag, Ba, Zn, K).

3.2. Molecular Structure

The major functional groups in this case are the carbonate, hydroxyl, phosphate groups, identified by FTIR. The observed vibrational peaks, summarized in Figure 2, are characteristic of carbonated hydroxyapatite compounds, similar to other literature data [27,30]. For a proper identification of the specific bands of these compounds, the IR region was chosen between 2000–400 cm^{-1}.
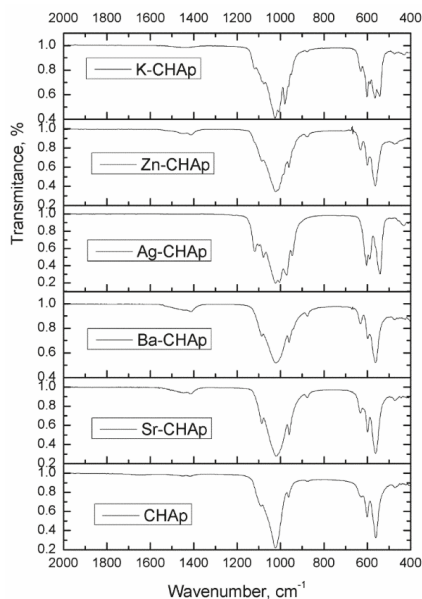

Figure 2. FTIR spectra for CHAp and Me-CHAp (Me = Sr, Ag, Ba, Zn, K).

3.3. Thermal Properties

The thermogravimetric analysis of the samples carried out from 30–1000 °C in air atmosphere using a heating rate of 10 °C/min is shown in Figure 3. The TGA result shows that there are two stages of weight loss that occurs during the heating process: The first weight loss between 30–225 °C and the second one between 226–700 °C, corresponding to some thermal reactions [31].
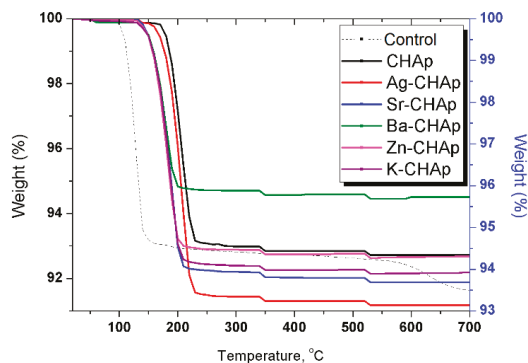

Figure 3. The TGA diagram for CHAp and Me-CHAp (Me = Sr, Ag, Ba, Zn, K).

3.4. The Efficiency and Suitability of These Products on Model Stone Samples

The efficiency and suitability of these products on model stone samples were evaluated by compressive strength, to artificial weather (freeze–thaw), water absorption test in relationship with porosimetry measurements. Except the pore structure changes (surface area, pore volume, pore diameter), the variation of the surface area and pore diameter (by brushing and spraying), is represented in Figure 4.
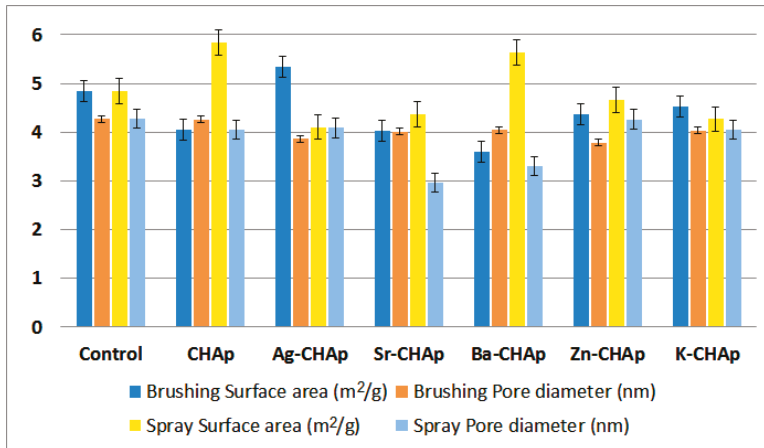

Figure 4. Surface area and pore diameter parameters for CHAp and Me-CHAp (Me = Sr, Ag, Ba, Zn, K).

With the Silver Schmidt test hammer measures the speed of the impact as well as of the rebound immediately before and after the impact, calculating the amount of energy that can be recovered. It is one of the traditionally used methods for evaluating the mechanical properties of the rocks (compressive strength). The rebound number measurements for the untreated and treated with carbonated hydroxyapatite (by brushing and spraying the specimens) are shown in Figure 5. The measurements of rebound number have been taken and then the compressive strength determined as per ASTM C805.
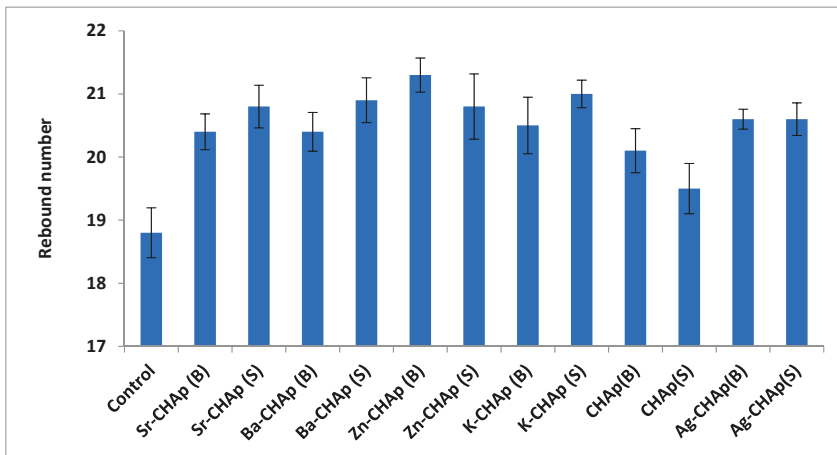

Figure 5. Mechanical strength for control, CHAp and Me-CHAp (Me = Sr, Ag, Ba, Zn, K).

For the water absorption test, the samples were dried in the oven at 40 °C for 8 h, cooled at room temperature and then weighed (W_1). After that, the samples were immersed in distilled water for 24 h. At the end, they were removed from distilled water and weighed (W_2). The water absorption content was calculated with the Equation (4), and graphical represented in Figure 6.

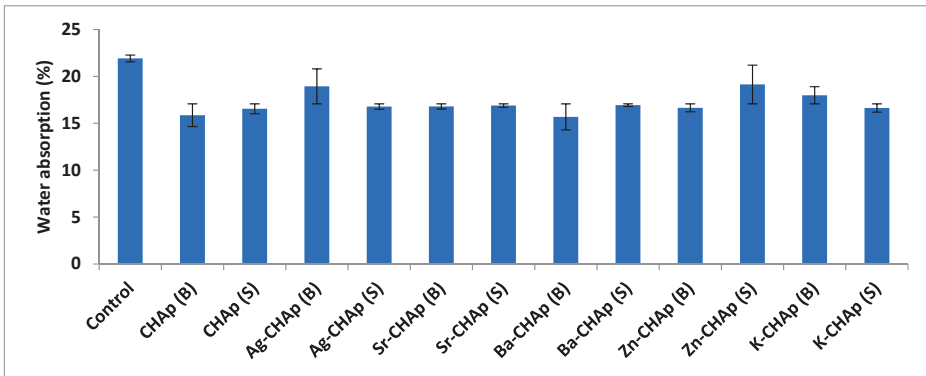$$\text{water absorption} = [(W_2 - W_1)/W_1] \times 100\% \tag{4}$$

Figure 6. Water absorption for control, CHAp and Me-CHAp (Me = Sr, Ag, Ba, Zn, K).

The freeze–thaw operation is repeated until 20 cycles are performed, after which the mass losses during the freeze–thaw process is expressed as gelivity coefficient (Figure 7).
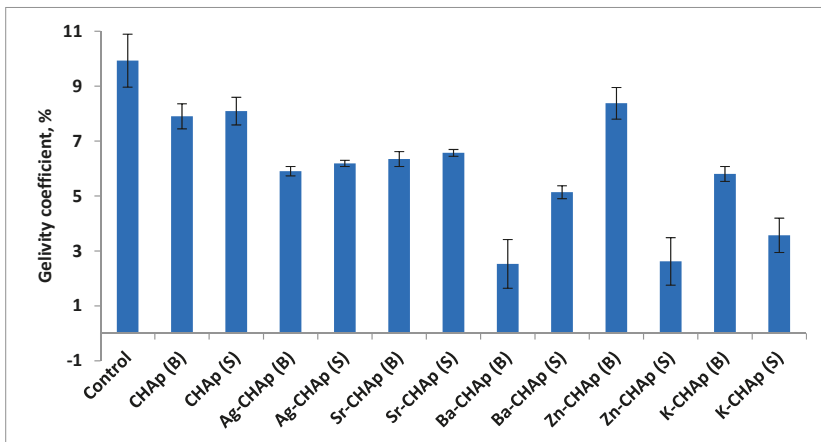

Figure 7. Gelivity coefficient for control, CHAp and Me-CHAp (Me = Sr, Ag, Ba, Zn, K).

4. Discussion

The XRD patterns shown in Figure 1, indicated that Me-CHAp samples are very similar to that of pure CHAPp and were in accordance with ASTM data (Card 9-432). The diffraction peaks (2θ = 25.879° for (002), 31.775° for (211), 31.196° for (112), 32.902° for (300), 33.684° for (202), 35.597° for (301) and 39.853° for (130) respectively), are sharp and well resolved, indicating the obtained phase pure, well crystallized hydroxyapatites [32]. The unit cell parameters of all samples are presented in Table 2.

Table 2. The lattice parameters a and c for synthesized carbonated hydroxyapatites.

Phase Name	a (Å)	c (Å)	Ionic Radius (Å)
CHAp	9.431(8)	6.891(14)	0.99
Ag-CHAp	9.26(9)	6.9(3)	1.26
Sr-CHAp	9.4191(5)	6.8800(4)	1.12
Ba-CHAp	9.421	6.885	1.35
K-CHAp	9.4321	6.9	1.38
Zn-CHAp	9.40	6.8437	0.74

The lattice parameters a and c increased with increasing ionic radium of metallic ions. The substitution of Ca (0.99 Å) with Zn (0.74 Å), Sr (1.12 Å), Ag (1.26 Å), Ba (1.35 Å), and K (1.38 Å) in CHAp lattice could be a cause of increasing of a and c lattice parameters. Changes in cell parameters may imply that all the metals substituted for calcium in the CHAp lattice corresponded with an increase in lattice parameters (except for Zn, which has a smaller ionic radius than Ca). It is also possible that lattice parameter changes occurred due to silver ion and other site substitutions in the crystal lattice. These results are in accordance with previous reports by [30]. Moreover, the inclusion of the metals with a larger ionic radius compared to Ca^{2+}, caused the expansion of the lattice parameters (mainly along the *c* axis) and the increase of cell volume [33–35]. According to results given in Table 2, all Me-CHAp samples have lower crystallinity than pure hydroxyapatite.

On the other hand, the substitution of strontium and silver can cause phase shifting to lower 2θ indicating an increase in the lattice parameters, which can be attributed to the higher ionic radius of Sr (1.12 Å) and Ag (1.26 Å), as compared to Ca^{2+} [35].

Broadening of the peaks due to the reduction in the crystallite size and increase in the lattice disorder, are attributed to the divalent metal$^+$ substitution in the HAp lattice [36]. Also, the average crystallite sizes, calculated after Scherrer equation suggests that the hydroxyapatite samples could be considered as nano-CHAp (Table 1). The results show that insertion of the metals into CHAp lattice led to a higher S_{BET} that is correlated with smaller crystallite sizes of these samples [37].

The bands from 1455 and 1419 cm^{-1} have been ascribed to carbonate and phosphate IR bands. When the carbonate IR bands are at 1455 and 1419 cm^{-1} (ascribed to CO_3^{2-} and PO_3^{4-}) a B type substitution is identified, whereas the bands are at 1550 and 1530 cm^{-1} (ascribed to OH and PO_3^{4-}) a A type substitution is present (Figure 2).

The bands from 879, 873 and 866 cm^{-1} are similar and characteristic of all the samples. This means that the carbonate ions are present in the CHAp structure either carbonate ions substituting OH$^-$ groups (type A–879 cm^{-1}) or carbonate ions substituting the phosphate ions (type B-873 cm^{-1}). Phosphate bands could be identified at 605, 575 and 563 cm^{-1}. The FTIR bands obtained confirm that the synthesized samples could be AB type: CO_3^{2-} is substituting PO_4^{3-}. Similar results have been reported by Padila [30].

The TGA result shows that there are two stages of weight loss that occur during the heating process. The first weight loss of 8.3 wt.% is observed from 30 to 225 °C due to the removal of trapped water in the sample. The second weight loss of approximately 31.6 wt.% occurs from 226 to 700 °C and was attributed to the decomposition of the other components (CO_3^{2-} according to the weight loss observed in TGA curves between 550–950 °C [31,38].

The results obtained for the non-treated and treated specimens with carbonated hydroxyapatite solutions 0.25 g/L concentration, revealed that by brushing, acicular crystals of approximately 500 nm in length and 10 nm in width were obtained (Figure 8); and the second one, when the solution was sprayed on the stone surface, agglomerates of spheroidal crystals of approximately 10 ± 20 nm in diameter were obtained (marked by arrows).
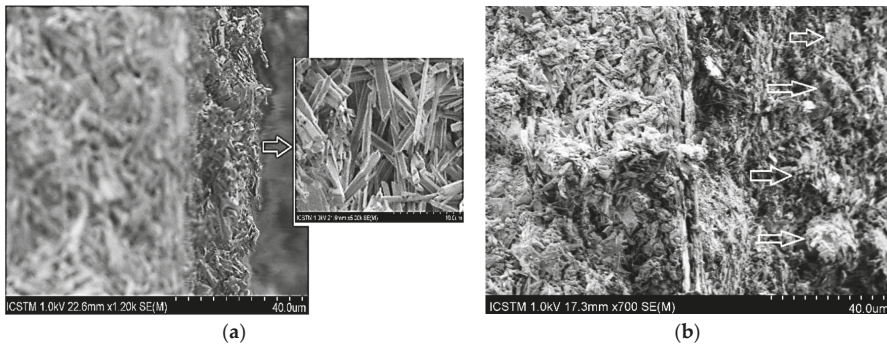
Figure 8. SEM images for BaCHAp applied by brushing and spraying: (**a**) Ba-CHAp applied by brushing, (**b**) Ba-CHAp applied by spraying.

By optical microscopy (Figure 9) it was possible to observe that the untreated specimen presents a whitish, highly porous surface (Figure 9a–c), while the treated specimen shows a more homogeneous surface with no chromatic alteration macroscopically visible. Looking more in detail to the microstructure, it can be observed that the nanoparticles partially filled the superficial pores of the original matrix. The thickness of the deposited layer depends on the consolidant type, higher for Ag-CHAp and mostly similar for Ba-CHAp, Sr-CHAp and CHAp. The layer thickness of the other consolidants is very thin, between 8–10 μm, this being a possible reason for the low efficacy of them.
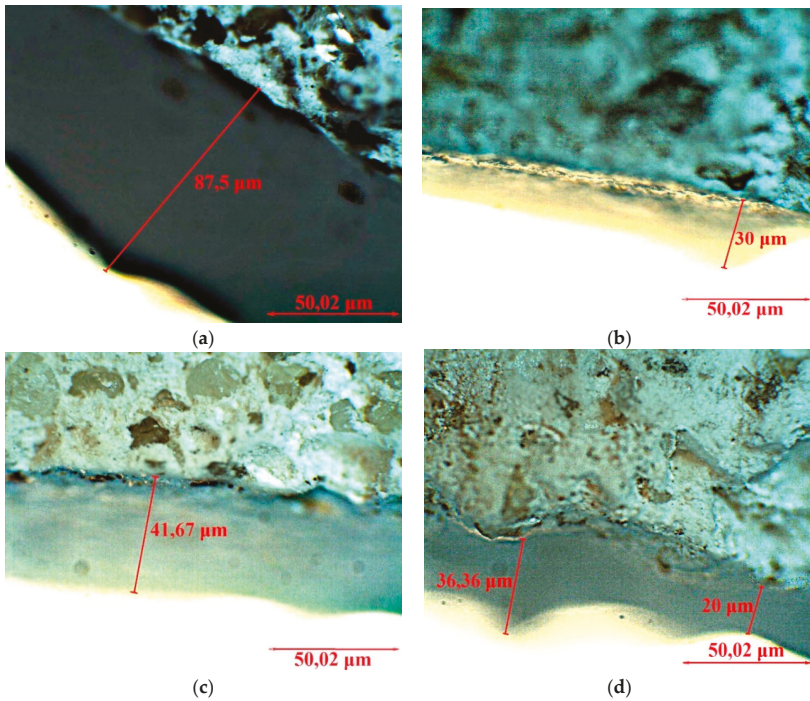
Figure 9. Optical microscopy of the untreated and treated by spraying the specimens: (**a**) Ag-CHAp, (**b**) Ba-CHAp, (**c**) SrCHAp, (**d**) CHAp.

The layer varies between 30–90 μm, which is in good agreement with other literature report [39]. By brushing, the layer is thickened, as SEM images shown (Figure 10a–d).
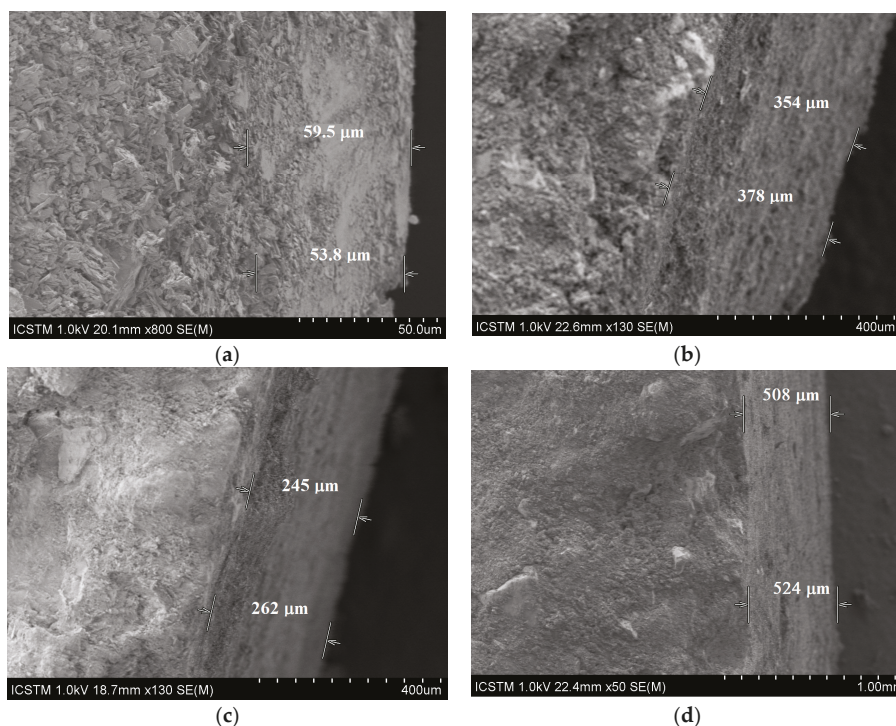
Figure 10. SEM images for brushed specimens: (**a**) CHAp, (**b**) Ba-CHAp, (**c**) Sr-CHAp, (**d**) Ag-CHAp.

As humidity plays a key role in stone deterioration, a detailed understanding of the processes involved and imposed is required. The amount of water presented in a building stone, its actual material moisture, is a function of several parameters. The specific inner surface represents the interface for any process between the atmosphere and the solid material. There is a close interrelation between material moisture and mechanical properties [40].

From the above images it can be observed that the layer obtained by brushing the carbonated hydroxyapatite derivatives on model samples has different thicknesses: 53–59 μm for CHAp (Figure 10a) and thicker from 245 to 524 μm for its metallic derivatives (Figure 10b–d). For CHAp derivatives with divalent metals (Sr, Ba), the layer obtained by application is between 262 and 378 μm, while for the monovalent derivative of CHAp (Ag) the thickest layer of 540 μm is obtained. The reason lies in the tendency to agglomerate of these metallic derivatives, due to the large surface-to-volume ratio (Figure 4), more accentuated at Ag-CHAp than Sr-CHAp and Ba-CHAp.

If the pore volume, determined by porosity, is quite similar (0.008–0.01 cc/g), the surface area and pore diameter are different and depend on the consolidant type: It is highest for Ag-CHAp applied by brushing and for CHAp and Ba-CHAp applied by spraying. Meanwhile, the pore diameter is the smallest for Sr-CHAp and Ba-CHAp applied by spraying. From these data, it could be concluded that the application type is decisive and contribute to the layer homogenity applied on the stone surface. For the control specimens, these values are not different at all. They are similar both for brushing and for spraying (Figure 4).

Measurement of mechanical properties of the samples in all stages (i.e., by brushing and by spraying) was achieved by the test of compression strength. It could be observed that by comparison

with the control samples, all the treated samples presented higher compressive strength values for the samples treated by brushing than those treated by spraying (Figure 11a–d) correlated with an increased rebound number (Figure 5). The addition of the nanoparticles on the specimen surface enhanced the durability of stone compared to the samples not treated, due to the role of nanoparticles in reinforcing the stone, improving their interaction with the stone grains.

It was observed that the results of Zn-CHAp nanoparticles gave the highest values of compressive strength. This can be attributed to the effect of the high reactivity, crystallites size, nanoparticles size and high compatibility with the substrates, similar with other cases reported in the literature [41]. The higher the crystallites size, the higher the compressive strength. The chemical composition of nanosized consolidant can exhibit improvements in thermal, physical, and mechanical properties, because of the strong synergistic effects between the stone surface and CHAp on both the molecular and nanometric scales [42].
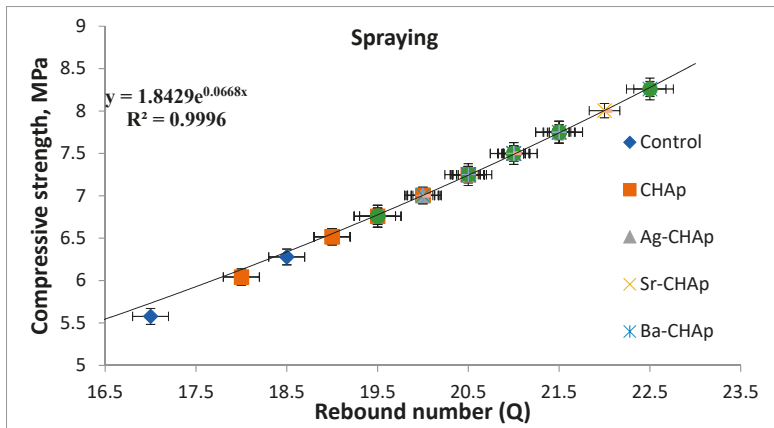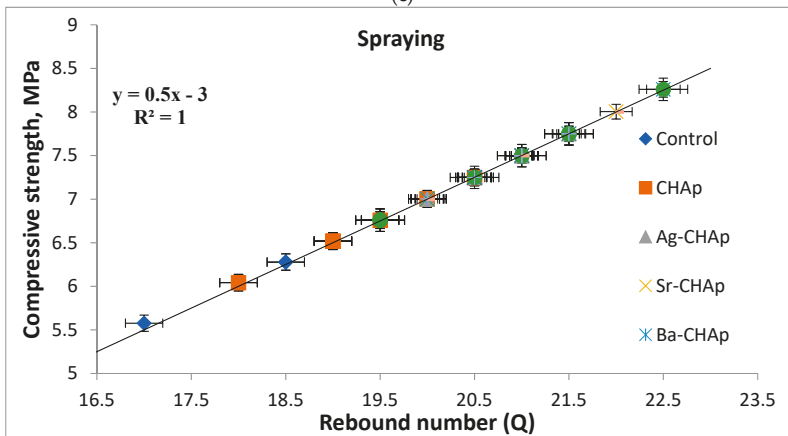

(**a**)

(**b**)
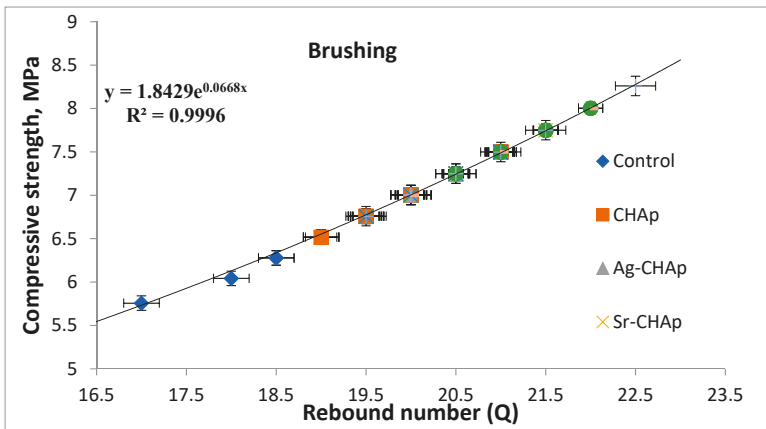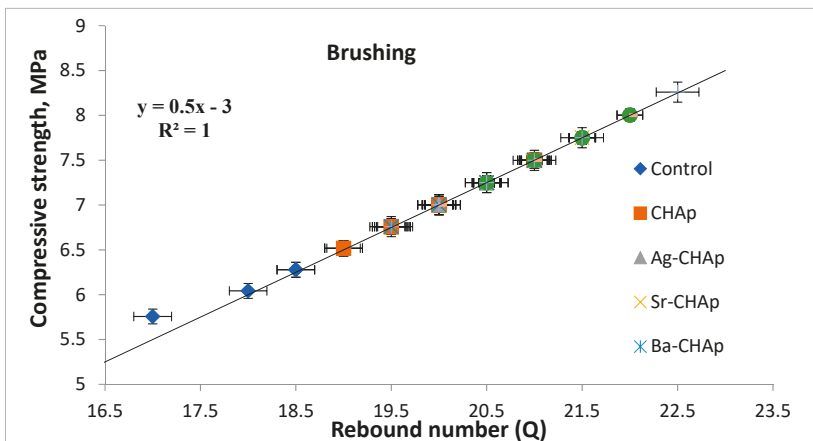
Figure 11. *Cont.*

Figure 11. The compressive strength vs. rebound index relationship for model stones coated with carbonated hydroxyapatite derivatives. (**a**) samples treated by brushing, exponential graphical representation; (**b**) samples treated by brushing, linear graphical representation; (**c**) samples treated by spraying, exponential graphical representation; (**d**) samples treated by spraying, linear graphical representation.

This paper presents the compressive strength vs. rebound index relationship for model stones. Linear and exponential relationship between average rebound number and compressive strength was established using the least square method. The linear model was found to be the better one with a regression coefficient of 1.0 than the exponential model with a regression coefficient of 0.9996, which indicates the acceptability of the linear model for predicting compressive strength of model stones, Figure 11a–d.

As humidity plays a key role in stone deterioration, a detailed understanding of the processes involved and imposed is required. The amount of water presented in a building stone, its actual material moisture, is a function of several parameters. The specific inner surface represents the interface for any process between the atmosphere and the solid material. There is a close interrelation between material moisture and mechanical properties [40].

Transport and distribution of H_2O, fluid water and vapor in porous materials are governed by different processes. In the assumed case of a dry material, as a first step, its surface starts to adsorb single H_2O molecules from the atmosphere to form a layer. The only transport mechanism which occurs is vapor transport. With rising air humidity, the number of layers of water molecules on the surface increases. Within those multimolecular layers of the water, surface flow occurs as a secondary and more efficient transport mechanism. Additionally, at a certain content, the water layers merge into the small pores due to capillary condensation, which is effective up to some 10^{-7} m pore radius. With an increase of water content in the system, capillary forces, which are active in the pore radius range between some 10^{-7}–10^{-3} m, start to govern the internal flow. Finally, when the material is completely filled with water, saturation flow occurs. Similar, but inverse are the processes when a water saturated material is subjected to drying. The removal of H_2O stops when desorption out of the material and adsorption of air humidity reach equilibrium.

When water from the stone surface evaporates faster, a larger active evaporation surface cools occur. Partial saturation enhances this effect. This shows that the surface roughness expressed in the specific inner surface is a determining parameter. The amount of water sorption uptake correlates mainly with the inner surface area, determined by the N_2-BET method.

Samples with medium specific surface areas have a lower uptake and the lowest values can be observed in samples with the lowest specific surface areas. So, the samples with high specific inner surfaces, exhibit the highest moisture uptake values.

The specimens that supported the freeze–thaw cycles were first dried, weighed, and later immersed in H_2O for saturation throughout 48 h, consistent with the standardized procedure represented in EN12371. The freeze–thaw aging was performed on 15 specimens and lasted 20 cycles. At the end of freeze–thaw aging procedure the dry mass of the specimens was assessed (Figure 12).

Sample	Brushing		Spraying	
	Initial	Final-After 20 cycles	Initial	Final-After 20 cycles
Control				
CHAp				
Ag-CHAp				

Figure 12. *Cont*.

Ba-CHAp				
Sr-CHAp				
Zn-CHAp				
K-CHAp				
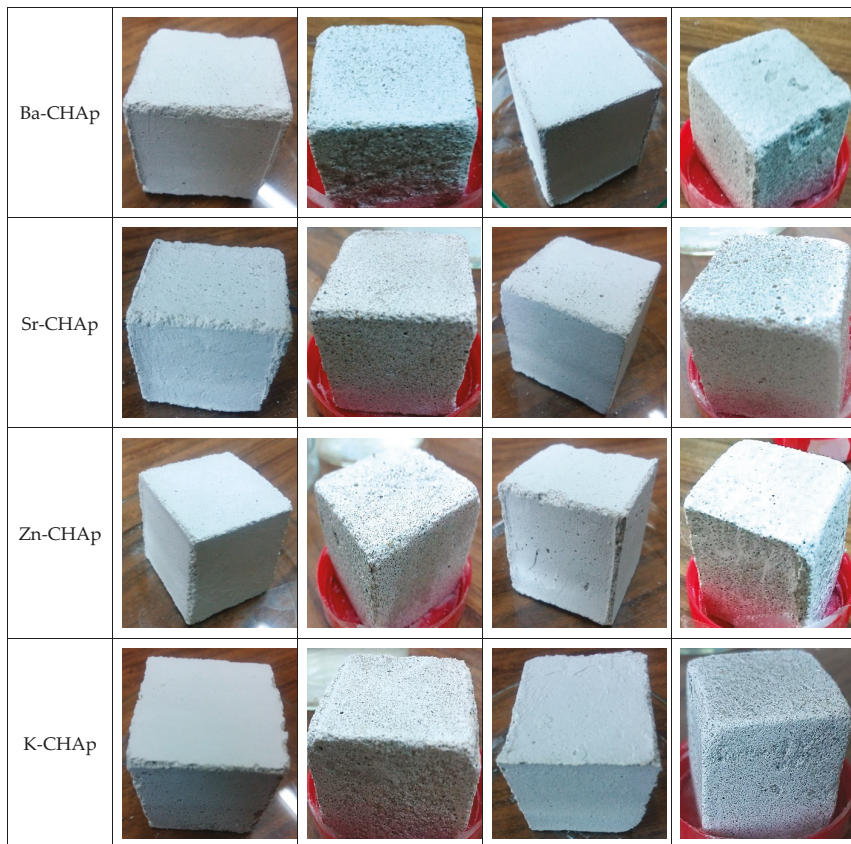
Figure 12. Stone samples with metallic hydroxyapatite applied by brushing and spraying.

The deterioration of the stones involves mechanical ruptures along the edges, fractures due to the weathering, grooves in depth, shrinkage cracks and brown patina. Salt incrustation may cover the stone surface and fill the fissures of blocks. The deterioration/weathering condition could be poorly weathered stone surfaces and extremely weathered stone surfaces.

By correlation between the visual appearances of samples treated with gelivity values for the samples treated with various carbonated hydroxyapatite a similar degradation tendency could be observed. The control samples undergo similar degradations after the 20 freeze–thaw cycles, as shown in Figure 7, and more pronounced in the samples treated by spraying with two exceptions of the samples treated with Zn-CHAp and K-CHAp.

The most pronounced degradations are observed in the case of Ba-CHAp, applied by spraying, most probably due to Ba ionic radium 1.35 Å, too high to cover the homogeneous samples.

The higher the gelivity value, the higher the degradation rate and smaller the protection capacity of the carbonated hydroxyapatite derivatives coatings.

The spraying procedure is a fast application, requires one application, leads to a smooth finish free of brush/roller marks, can get into hard to reach areas, but has some disadvantages: Long prep and clean up time, uneven coverage (sometimes too thick), uses 2–3 times as much paint as brushing, poor adhesion, cannot paint on windy days. By comparison, brushing has an excellent control, very good adhesion, even uniform coverage, gets paint into nooks and crannies better than spraying. But it is a slow and laborious application, can require 2 or more coats, can leave brush marks and obstructions

which make for a difficult application. It is slow, but an even, uniform coat of paint could be obtained and much better adhesion than with spraying alone [20,43,44].

After analyzing these results, it could be concluded that the brushing procedure could offer a more efficient coating of the model stone specimens, while the spraying procedure, evenly induces good compressive strength, produces mechanical ruptures along the edges (Zn-CHAp, Ba-CHAp, Ag-CHAp), fractures (Zn-CHAp, Ba-CHAp, Ag-CHAp), grooves in depth (Zn-CHAp, K-CHAp, Ba-CHAp, Sr-CHAp), shrinkage cracks (CHAp), brown patina (Zn-CHAp).

5. Conclusions

Carbonated hydroxyapatite derivatives (CHAp) and its metallic derivatives (Ag, Sr, Ba, K, Zn) have been prepared and characterized in this paper and their coating capacity has been evaluated and discussed. These compounds were characterized using several analytical tools, XRD, TGA, FTIR, OM and SEM–EDS techniques.

The efficiency and suitability of these products on model stone samples were evaluated by monitoring the resistance to artificial weather (freeze–thaw), and pore structure changes (surface area, pore volume, pore diameter). Also, the mechanical strengths of these new compounds as coatings for model stone samples revealed homogeneous and strong layers deposited on the stone surface. By correlation, between the visual appearance of samples treated with gelivity values and the samples treated with various carbonated hydroxyapatite, a similar degradation tendency could be observed that is more pronounced in the samples treated by spraying with two exceptions of the samples treated with Zn-CHAp and K-CHAp. The higher the gelivity value, the higher the degradation rate and smaller protection capacity of the carbonated hydroxyapatite derivatives coatings.

The brushing procedure could offer a more efficient coating of the model stone specimens, while the spraying procedure, evenly induces good compressive strengths, produces mechanical ruptures along the edges (Zn-CHAp, Ba-CHAp, Ag-CHAp), fractures (Zn-CHAp, Ba-CHAp, Ag-CHAp), grooves in depth (Zn-CHAp, K-CHAp, Ba-CHAp, Sr-CHAp), shrinkage cracks (CHAp) and brown patina (Zn-CHAp).

Author Contributions: Conceptualization, R.-M.I. and M.-L.I.; Formal analysis, R.-M.I. and M.-L.I.; Funding acquisition, R.-M.I.; Investigation, R.-M.I., L.I., G.V., M.E.G., R.E.A., G.-I.R., R.M.G., S.T., I.A.B., M.-L.I., I.D.D., A.I.G. and C.R.; Project administration, R.-M.I.; Software, G.-I.R.; Supervision, R.-M.I. and M.-L.I.; Visualization, R.-M.I. and L.I.; Writing—original draft, R.-M.I.; Writing—review & editing, R.-M.I. and L.I.

References

1. Sassoni, E.; Graziani, G.; Franzoni, E. An innovative phosphate-based consolidant for limestone. Part 1: Effectiveness and compatibility in comparison with ethyl silicate. *Constr. Build. Mater.* **2016**, *102*, 918–930. [CrossRef]

2. Rodrigues, J.D.; Grossi, A. Indicators and ratings for the compatibility assessment of conservation actions. *J. Cult. Herit.* **2007**, *8*, 32–43. [CrossRef]

3. Toniolo, L.; Poli, T.; Castelvetro, V.; Manariti, A.; Chiantore, O.; Lazzari, M. Tailoring new fluorinated acrylic copolymers as protective coatings for marble. *J. Cult. Herit.* **2002**, *3*, 309–316. [CrossRef]

4. Cappelletti, G.; Fermo, P. Hydrophobic and superhydrophobic coatings for limestone and marble conservation. In *Smart Composite Coatings and Membranes*; Montemor, M.F., Ed.; Woodhead Publishing: Cambridge, UK, 2015; pp. 421–452.

5. Ruffolo, S.A.; Macchia, A.; La Russa, M.F.; Mazza, L.; Urzì, C.; De Leo, F.; Barberio, M.; Crisci, G.M. Marine antifouling for underwater archaeological sites: TiO_2 and Ag-Doped TiO_2. *Int. J. Photoenergy* **2013**, *2013*, 251647. [CrossRef] [PubMed]

6. Munafò, P.; Goffredo, G.B.; Quagliarini, E. TiO$_2$-based nanocoatings for preserving architectural stone surfaces: An overview. *Constr. Build. Mater.* **2015**, *84*, 201–218. [CrossRef]

7. Sierra-Fernandez, A.; Gomez-Villalba, L.S.; Rabanal, M.E.; Fort, R. New nanomaterials for applications in conservation and restoration of stony materials: A review. *Materiales de Construcción* **2017**, *67*, 325. [CrossRef]

8. Zendri, E.; Balliana, E.; Izzo, F.C.; Di Crescenzo, M.M.; Falchi, L.; Sgobbi, M.; Biscontin, G. The choise of parameters for the monitoring and the maintenance of architectural stone surfaces. *Int. J. Herit. Digital Era* **2012**, *1* (Suppl. 1), 331–335. [CrossRef]

9. Delgado Rodrigues, J. Stone consolidation: Research and practice. In *Int. Symp. on Works of Art and Conservation Science Today*; Aristotle University of Thessaloniki: Thessaloniki, Greece, 2010.

10. Salazar-Hernández, C.; Cervantes, J.; Puy-Alquiza, M.J.; Miranda, R. Conservation of building materials of historic monuments using a hybrid formulation. *J. Cult. Herit.* **2015**, *16*, 185–191. [CrossRef]

11. Pinto, A.F.; Rodrigues, J.D. Stone consolidation: The role of treatment procedures. *J. Cult. Herit.* **2008**, *9*, 38–53. [CrossRef]

12. Pinna, D.; Salvadori, B.; Porcinai, S. Evaluation of the application conditions of artificial protection treatments on salt-laden limestones and marble. *Constr. Build. Mater.* **2011**, *25*, 2723–2732. [CrossRef]

13. Pinto, A.P.F.; Rodrigues, J.D. Consolidation of carbonate stones: Influence of treatment procedures on the strengthening action of consolidants. *J. Cult. Herit.* **2012**, *13*, 154–166. [CrossRef]

14. Tabasso, M.L.; Simon, S. Testing methods and criteria for the selection/evaluation of products for the conservation of porous building materials. *Stud. Conserv.* **2006**, *51* (Suppl. 1), 67–82. [CrossRef]

15. Ion, R.M.; Turcanu-Caruţiu, D.; Fierăscu, R.C.; Fierăscu, I.; Bunghez, I.R.; Ion, M.L.; Teodorescu, S.; Vasilievici, G.; Rădiţoiu, V. Caoxite-hydroxyapatite composition as consolidating material for the chalk stone from Basarabi–Murfatlar churches ensemble. *Appl. Surf. Sci.* **2015**, *358*, 612–618. [CrossRef]

16. Ion, R.M.; Fierascu, R.C.; Fierascu, I.; Senin, R.M.; Ion, M.L.; Leahu, M.; Turcanu-Carutiu, D. Influence of Fântâniţa lake (chalk lake) water on the degradation of basarabi–murfatlar churches. In *Engineering Geology for Society and Territory-Volume 8*; Springer: Cham, Switzerland, 2015; pp. 543–546.

17. Gibson, I.R.; Bonfield, W. Novel synthesis and characterization of an AB-type carbonate-substituted hydroxyapatite. *J. Biomed. Mater. Res.* **2002**, *59*, 697–708. [CrossRef]

18. Ellies, L.G.; Nelson, D.G.A.; Featherstone, J.D.B. Crystallographic structure and surface morphology of sintered carbonated apatites. *J. Biomed. Mater. Res.* **1988**, *22*, 541–553. [CrossRef]

19. Kovaleva, E.S.; Shabanov, M.P.; Putlyaev, V.I.; Tretyakov, Y.D.; Ivanov, V.K.; Silkin, N.I. Bioresorbable carbonated hydroxyapatite Ca$_{10-x}$Na$_x$(PO$_4$)$_{6-x}$(CO$_3$)$_x$(OH)$_2$ powders for bioactive materials preparation. *Cent. Eur. J. Chem.* **2009**, *7*, 168–174. [CrossRef]

20. Sassoni, E.; Naidu, S.; Scherer, G.W. The use of hydroxyapatite as a new inorganic consolidant for damaged carbonate stones. *J. Cult. Herit.* **2011**, *12*, 346–355. [CrossRef]

21. Yasukawa, A.; Nakajima, M.; Kandori, K.; Ishikawa, T. Preparation and characterization of carbonated barium hydroxyapatites. *J. Colloid Interface Sci.* **1999**, *212*, 220–227. [CrossRef] [PubMed]

22. Nelson, D.G.; Featherstone, J.D. Preparation, analysis, and characterization of carbonated apatites. *Calcif. Tissue Int.* **1982**, *34* (Suppl. 2), S69–S81. [PubMed]

23. Jäger, C.; Welzel, T.; Meyer-Zaika, W.; Epple, M. A solid-state NMR investigation of the structure of nanocrystalline hydroxyapatite. *Magn. Reson. Chem.* **2006**, *44*, 573–580. [CrossRef]

24. Miquel, J.L.; Facchini, L.; Legrand, A.P.; Marchandise, X.; Lecouffe, P.; Chanavaz, M.; Donazzan, M.; Rey, C.; Lernaitre, J. Characterisation and conversion study into natural living bone of calcium phosphate bioceramics by solid state NMR spectroscopy. *Clin. Mater.* **1990**, *5*, 115–125. [CrossRef]

25. Calderin, L.; Stott, M.J.; Rubio, A. Electronic and crystallographic structure of apatites. *Phys. Rev. B* **2003**, *67*, 134106. [CrossRef]

26. Zhou, W.Y.; Wang, M.; Cheung, W.L.; Guo, B.C.; Jia, D.M. Synthesis of carbonated hydroxyapatite nanospheres through nanoemulsion. *J. Mater. Sci. Mater. Med.* **2008**, *19*, 103–110. [CrossRef]

27. Barralet, J.; Knowles, J.; Best, S.; Bonfield, W. Thermal decomposition of synthesised carbonate hydroxyapatite. *J. Mater. Sci. Mater. Med.* **2002**, *13*, 529–533. [CrossRef]

28. Mayer, I.; Apfelbaum, F.; Featherstone, J.D.B. Zinc ions in synthetic carbonated hydroxyapatites. *Arch. Oral Biol.* **1994**, *39*, 87–90. [CrossRef]

29. Kostov-Kytin, V.V.; Dyulgerova, E.; Ilieva, R.; Petkova, V. Powder X-ray diffraction studies of hydroxyapatite and β-TCP mixtures processed by high energy dry milling. *Ceram. Int.* **2018**, *44*, 8664–8671. [CrossRef]

30. Padilla, S.; Izquierdo-Barba, I.; Vallet-Regí, M. High specific surface area in nanometric carbonated hydroxyapatite. *Chem. Mater.* **2008**, *20*, 5942–5944. [CrossRef]

31. Lazić, S.; Zec, S.; Miljević, N.; Milonjić, S. The effect of temperature on the properties of hydroxyapatite precipitated from calcium hydroxide and phosphoric acid. *Thermochim. Acta* **2001**, *374*, 13–22. [CrossRef]

32. Stanić, V.; Janaćković, D.; Dimitrijević, S.; Tanasković, S.B.; Mitrić, M.; Pavlović, M.S.; Krstic, A.; Jovanovic, D.; Raicevic, S. Synthesis of antimicrobial monophase silver-doped hydroxyapatite nanopowder for bone tissue engineering. *Appl. Surf. Sci.* **2011**, *257*, 4510–4518. [CrossRef]

33. Terra, J.; Dourado, E.R.; Eon, J.G.; Ellis, D.E.; Gonzalez, G.; Rossi, A.M. The structure of strontium-doped hydroxyapatite: An experimental and theoretical study. *Phys. Chem. Chem. Phys.* **2009**, *11*, 568–577. [CrossRef]

34. Panda, R.N.; Hsieh, M.F.; Chung, R.J.; Chin, T.S. FTIR, XRD, SEM and solid state NMR investigations of carbonate-containing hydroxyapatite nano-particles synthesized by hydroxide-gel technique. *J. Phys. Chem. Solids* **2003**, *64*, 193–199. [CrossRef]

35. Bianchi, M.; Degli Esposti, L.; Ballardini, A.; Liscio, F.; Berni, M.; Gambardella, A.; Leeuwenburgh, S.C.G.; Sprio, S.; Tampieri, A.; Iafisco, M. Strontium doped calcium phosphate coatings on poly (etheretherketone)(PEEK) by pulsed electron deposition. *Surf. Coat. Technol.* **2017**, *319*, 191–199. [CrossRef]

36. Koutsopoulos, S. Synthesis and characterization of hydroxyapatite crystals: A review study on the analytical methods. *J. Biomed. Mater. Res.* **2002**, *62*, 600–612. [CrossRef]

37. Zyman, Z.; Rokhmistrov, D.; Ivanov, I.; Epple, M. The influence of foreign ions on the crystal lattice of hydroxyapatite upon heating. *Mater. Werkst. Entwickl. Fert. Prüfung Eig. Anwend. Tech. Werkst.* **2006**, *37*, 530–532. [CrossRef]

38. Skwarek, E. Thermal analysis of hydroxyapatite with adsorbed oxalic acid. *J. Therm. Anal. Calorim.* **2015**, *122*, 33–45. [CrossRef]

39. Novoselov, A.; Konstantinov, A.; Leonova, L.; Soktoev, B.; Morgalev, S. Carbonate neoformations on modern buildings and engineering structures in tyumen city, Russia: structural features and development factors. *Geosciences* **2019**, *9*, 128. [CrossRef]

40. Franzen, C.; Mirwald, P. Moisture content of natural stone: static and dynamic equilibrium with atmospheric humidity. *Environ. Geol.* **2004**, *46*, 391–401. [CrossRef]

41. Giorgi, R.; Ambrosi, M.; Toccafondi, N.; Baglioni, P. Nanoparticles for cultural heritage conservation: Calcium and barium hydroxide nanoparticles for wall painting consolidation. *Chem. A Eur. J.* **2010**, *16*, 9374–9382. [CrossRef]

42. Dei, L.; Salvadori, B. Nanotechnology in cultural heritage conservation: Nanometric slaked lime saves architectonic and artistic surfaces from decay. *J. Cult. Herit.* **2006**, *7*, 110–115. [CrossRef]

43. Sandrolini, F.; Franzoni, E.; Cuppini, G. Predictive diagnostics for decayed ashlars substitution in architectural restoration in Malta. *Mater. Eng. Modena* **2000**, *11*, 323–338.

44. Karatasios, I.; Theoulakis, P.; Kalagri, A.; Sapalidis, A.; Kilikoglou, V. Evaluation of consolidation treatments of marly limestones used in archaeological monuments. *Constr. Build. Mater.* **2009**, *23*, 2803–2812. [CrossRef]

Diammonium Hydrogenphosphate Treatment on Dolostone: The Role of Mg in the Crystallization Process

Elena Possenti [1,*], Claudia Conti [1], G. Diego Gatta [2], Marco Realini [1] and Chiara Colombo [1]

[1] Istituto per la Conservazione e la Valorizzazione dei Beni Culturali (ICVBC), Consiglio Nazionale delle Ricerche (CNR), Via R. Cozzi 53, 20125 Milan, Italy; conti@icvbc.cnr.it (C.C.); realini@icvbc.cnr.it (M.R.); colombo@icvbc.cnr.it (C.C.)

[2] Dipartimento di Scienze della Terra, Università degli Studi di Milano, Via Botticelli 23, 20133 Milan, Italy; diego.gatta@unimi.it

[*] Correspondence: possenti@icvbc.cnr.it; Tel.: +39-02-661-73386

Abstract: The diammonium hydrogenphosphate (DAP, $(NH_4)_2HPO_4$) reaction with calcite has been extensively investigated. The availability of free calcium ions in the reaction environment has been acknowledged as a crucial factor in the crystallization of calcium phosphates with a high (hydroxyapatite, Ca/P 1.67) or low Ca/P molar ratio (dicalcium phosphate dihydrate, Ca/P 1.00; octacalcium phosphate, Ca/P 1.33). On the contrary, no data are available on the DAP interaction at room temperature with dolomite in terms of reaction mechanism and composition of the reaction products. Here, a multi-analytical approach based on scanning electron microscopy (SEM) coupled with energy dispersive X-ray spectrometry (EDS) and X-ray powder diffraction before and after heating treatments is proposed to explore how the formation of calcium phosphates occur on Mg-enriched substrates and if the presence of magnesium ions during the reaction influences the crystallization process of calcium phosphates. The DAP reaction with polycrystalline dolomite gives rise to the formation of struvite and of poorly crystalline hydroxyapatite. Calcium and magnesium ions mutually interfered in the crystallization of magnesium and calcium phosphates, respectively, whose effects influenced the properties (size, micro-morphology, composition and crystallinity) of the newly-formed phases.

Keywords: calcium phosphate; hydroxyapatite; magnesium phosphate; struvite; dolomite; consolidating treatment; cultural heritage; ammonium phosphate

1. Introduction

Diammonium hydrogenphosphate (DAP, $(NH_4)_2HPO_4$) is a promising inorganic consolidating treatment for decayed carbonatic stones [1–4]. The DAP consolidating treatment aims at restoring the stone matrix through a partial transformation of the original material in newly-formed phosphate phases. Ideally, crystalline hydroxyapatite (HAP, $Ca_5(PO_4)_3OH$) is formed by combining calcium ions of the substrate with phosphate groups of the reagent [5,6].

The DAP reaction with calcite ($CaCO_3$) of carbonatic stones has been extensively investigated over the last years, [7,8] and recent findings showed that the DAP reaction with polycrystalline calcite of carbonatic stones is non-stoichiometric [9], which implies that many crystalline phases may form in complex mixtures with a nanocrystalline and/or partially-substituted HAP [1,5,6,9–12]. Furthermore, it has been demonstrated that the composition of the new phases depends on several variables, as e.g., the reaction condition (pH, ion strength), the stone substrate (lithotype, microstructure) and the treatment protocol (duration, application method, DAP molarity) [10,13–16].

The DAP reaction in the presence of low amount of calcium ions (e.g., when DAP is used with a low molarity [9] or on calcite substrates with Mg-containing veins [17]) follows a different crystallization process. In particular, the availability of free calcium ions is a crucial factor in the crystallization; phases with a low Ca/P molar ratio (e.g., dicalcium phosphate dihydrate DCPD $CaHPO_4 \cdot 2H_2O$, Ca/P molar ratio 1.00, and octacalcium phosphate OCP $Ca_8(HPO_4)_2 \cdot 5H_2O$, Ca/P molar ratio 1.33 [13,14]) are formed instead of HAP [9,18] (Ca/P molar ratio 1.67) in reaction environments with a low concentration of calcium ions.

Over the centuries, several carbonatic stones with magnesiac nature have been used for artefacts and buildings. A crucial issue is the challenging conservation of Angera stone, a sedimentary dolostone widely used as ornamental lithotype in the North of Italy and severely affected by decay [19]. The literature on the investigation of DAP treatments applied to calcite-based materials of cultural heritage is progressively increasing, while, surprisingly, the DAP reaction with magnesium carbonates is still quite unexplored.

Clearly, the DAP reaction with magnesium carbonates is expected to give rise to a set of crystalline phases different to those formed with calcium carbonate. However, even though the transformation of magnesium carbonates into magnesium phosphates with hydrothermal conditions [20] or by calcination [21] is well-known in literature, only a few studies investigated the carbonate-to-phosphate conversion at room temperature [22,23], which normally is the operative condition of conservation treatments.

This study focused, for the first time, on the reaction of polycrystalline dolomite with DAP solutions at room temperature in order to explore how: (i) DAP treatments react with dolostones; (ii) the nucleation of calcium phosphates occurs in presence of Mg-enriched substrates; (iii) the presence of magnesium and calcium ions during the reaction influences the crystallization process of calcium and magnesium phosphates.

The DAP treatments were carried out by using DAP water solutions with two different molarities on quarry specimens. The formation of specific crystalline phases and their diffusion inside the stone matrix are investigated following a multi-analytical approach (scanning electron microscopy (SEM) coupled with energy dispersive X-ray spectrometry (EDS), X-ray diffraction before and after heating treatments) and critically discussed.

2. Materials and Methods

2.1. Materials

The Angera stone, a dolostone quarried in the northern Italy (Piedmont) and widely used in the Lombard architecture as ornamental building material since the Roman age, was used for this study [24]. The lithotype is characterized by a very fine grain size and a high porosity (18–26%, depending on the Angera stone variety). The stone is mainly composed of dolomite ($CaMg(CO_3)_2$) in association with a low fraction of clay minerals and iron oxides [19,25–28].

The experiments were performed on the white variety of Angera stone, as it is the variety that undergoes the most severe decay processes in the environmental conditions. They were carried out on a set of freshly quarried prismatic specimens (50 mm × 50 mm × 20 mm) in order to explore the crystallization of phosphates from DAP solutions at room temperature on dolostones.

The Angera stone specimens were treated by a 0.76 M or of a 3.00 M aqueous solutions of DAP (CAS Number 7783–28-0, assay ≥99.0%, reagent grade, Merck, Darmstadt Germany). The concentration 0.76 M (corresponding to a 10% w/w) was selected on the basis of previous experiments [10] and on the consolidating practice in conservation worksites [29]; the choice to also include 3.00 M concentration was suggested in previous studies available in the literature [7,30], where this value was used to enhance the crystallization of calcium phosphates. The consolidating DAP solution was applied by poultice (dry cellulose pulp, MH 300 Phase, Italy; ratio ~ 5:1 DAP solution:dry cellulose pulp), as it is one of the most common application methods in the conservation

field. The treatment time was 48 h, during which the specimens were wrapped in a plastic film to avoid the evaporation of the solvent. After 48 h, the plastic film was removed and the specimens were left drying at room temperature for other 24 h with the poultice on top. The DAP poultice was then removed and the specimens were rinsed three times by poultice made with deionized water and dried at room temperature.

2.2. Methods

The crystalline phases of the Angera stone specimens before and after the consolidating treatments were investigated by X-ray powder diffraction (XRD) (Malvern, UK) in Bragg–Brentano geometry with a Panalytical X'Pert PRO diffractometer, equipped with a PW 3050/60 goniometer, anti-scatter slit and divergence slit (1° and 1/2° respectively), a PW3040/60 generator and a X'Celerator solid state detector PW3015/20 nickel filtered. The samples were finely pulverized and spread on silicon zero background holders. The diffraction patterns were collected with a Cu Kα radiation source (λ ~ 1.54 Å), accelerating voltage 40 kV and electric current at the Cu anode of 40 mA, in the 2 Theta angular range 4.5–65° with a stepsize of 0.17°and time per step of 130 s.

A set of thermal treatments were carried out in order to fully explore the composition of the newly-formed calcium phosphates, which showed ambiguously interpretable X-ray diffraction patterns. For this reason, untreated and treated specimens were initially analyzed at room temperature (rT); after that, the samples were heated at 400, 600 and 900 °C, and re-analyzed at rT after each heating process. The selection of the temperature steps used to investigate the *T*-induced "parent-to-product" phase transformation is driven by literature data [9,16,31–36].

The micro-morphology of the specimens before and after the DAP treatments were investigated by zenithal observations using a JEOL 5910 LV scanning electron microscope (SEM) (Tokyo, Japan) coupled with energy dispersive X-ray spectrometer (EDS) IXRF-2000 (0–20 keV) (Austin, Texas) in high vacuum mode on carbon coated samples.

3. Results

3.1. Analysis of the Newly-Formed Phases on Angera Stone

Figure 1 shows the X-ray diffraction patterns of quarry Angera stone before and after the DAP consolidating treatment. The XRD pattern of the untreated substrate shows well-defined peaks of dolomite (main peak at 31.02° and secondary peaks at 24.13°, 33.61°, 35.33°, 37.42°, 41.18°, 44.96°, 50.59° and 51.11° of 2Theta, λ = Cu Kα) and weaker peaks of secondary minerals (quartz at 26.60° of 2Theta, phyllosilicates at 9.41° and 25.37°, feldspar at 26.96° and plagioclase at 27.48°).
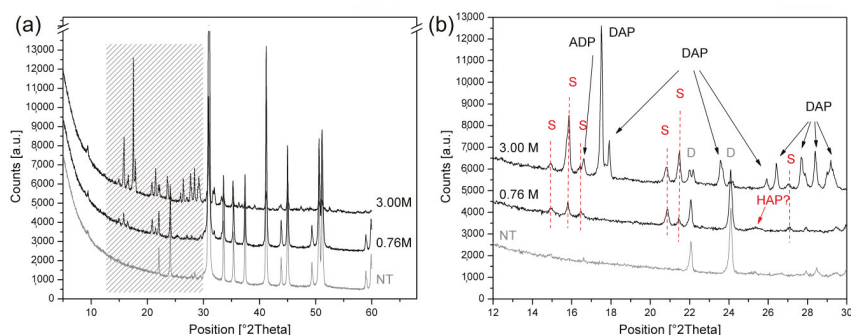
Figure 1. (**a**) X-ray powder diffraction(XRD) patterns of untreated Angera stone (NT) and Angera stone treated by poultice with 0.76 M and 3.00 M DAP solutions. (**b**) Detail in the range 12–30 ° showing the phase variations occurred after the consolidation. D = dolomite, S = struvite, HAP? = possible hydroxyapatite, DAP = diammonium hydrogen phosphate, ADP = ammonium dihydrogen phosphate.

The XRD patterns of the Angera stone treated with 0.76 M and with 3.00 M DAP solution exhibit the formation of magnesium phosphates and calcium phosphates. In fact, the XRD peaks of struvite ($MgNH_4PO_4 \cdot 6H_2O$, peaks at 14.99°, 15.81°, 16.47°, 20.85°, 21.45°, 27.07° and 31.94°) and most likely apatite (peak at ~25.90 °) were revealed in mixture with the phases of the substrate.

The XRD peaks of struvite were sharp and well-resolved, indicating the formation of a well crystalline phase, whereas the peak of the possible apatite was extremely weak and broad, most likely due to a poorly-ordered structure. No other peaks ascribable to calcium phosphates were detectable in the XRD patterns, likely due to overlapping with the peaks of other phases or to their severe weak intensity. Several calcium phosphate phases had a peak at ~25.90° of 2Theta, as many of them were characterized by a similar crystalline structure (e.g., hydroxyapatite; calcium-deficient hydroxyapatite and its partially-substituted forms; octacalcium phosphate; amorphous calcium phosphates, ACPs, $Ca_xH_y(PO_4)_z \cdot nH_2O$, with n = 3–4.5 and 15–20% H_2O) [13,37–41]. The peaks of struvite were more intense in the XRD patterns of the specimens treated with the 3.00 M DAP, while the peak of the possible apatite was more visible in the 0.76 M ones.

Moreover, the XRD pattern of the specimens treated with the 3.00 M DAP solution showed evidence of residual traces of the reagent (DAP peaks at 17.55°, 17.94°, 23.56°, 26.43°, 27.70°, 28.41° and 29.16°) and of ammonium dihydrogen phosphate (ADP, $NH_4H_2PO_4$, at 16.63°), a by-product of the reaction; these two phases were still present within the specimens even though they were rinsed. No peaks of DAP and ADP were detected on the specimens treated with the 0.76 M DAP solution.

In order to further explore the microstructural-crystallographic feature of these poorly-ordered calcium phosphate phases, a sequence of investigations were carried out by electron backscatter diffraction (EBSD), Fourier Transform Infrared spectroscopy (FTIR) and Raman spectroscopy. However, the outcomes of these supplementary techniques did not supply any further information and their results are not reported in this paper.

In particular: (i) for EBSD, it was not possible to obtain the XRD patterns of the investigated area due to the poorly crystalline nature of the phases, their nanometric size and the boundary effects, deriving from the alteration during the sample preparation of the interface between the new phases and the substrate; (ii) for Raman spectroscopy, phosphate phases had a weak Raman scatter, especially when submicrometric and/or poorly ordered, and in mixture with carbonates (phases characterized by a very high Raman cross section); (iii) as for FTIR data, the superimposition of the characteristic stretching and bending PO_4 vibrational bands of both the phosphate phases prevented their unambiguous identification.

3.2. Micro-Morphological Investigations of the Stone Surface

The micro-morphology of untreated Angera stone, showing the well-shaped rhombohedral crystals habit of dolomite is appreciable in Figure 2a, while that of the reacted dolomite is shown in Figure 2b,c. After the DAP treatments, the stone surface showed the presence of a newly-formed coating characterized by a pseudo-amorphous aspect. This coating was prevalently adherent to the stone matrix together with the crystallization of spherical particles agglomerates. Both of them covered the characteristic morphological features of the lithotype.

In the case of the specimens treated with the 0.76 M DAP solution; the newly-formed phases appeared as a pseudo-amorphous thin film (thickness ~ 0.6 μm) that covered the micritic dolomite (Figure 2b, left). On the film profiles, an incipient formation of spherical particles in an elongated arrangement was detected. On dolomite rhombohedral grains (dolomite crystal size ~ 15–20 μm), a shell of spherical crystallites with a bigger size was distinguishable (Figure 2b, right).

In the case of the specimens treated by DAP 3.00 M, the profiles of the dolomite crystals appeared affected by pronounced corrosion marks, with the consequent crystal nucleation of spherical structures combined to form elongated chain individuals (detail of Figure 2c).

Phosphorous is detected by EDS microanalysis in correspondence of the crystals overgrown on the substrate and morphologically different from the dolomite grains of the substrate. By measuring

these newly-formed phases, calcium, magnesium and phosphorous are always present, even though the ratio of their elemental abundance varies.

The SEM investigations suggested the presence of two different phosphates phases: a magnesium and a calcium phosphate, which exhibited differences in morphology and particle size (Figure 2b,c). These phases (struvite and a possible apatite, as suggested by the XRD data) did not show their typical orthorhombic and rose-like morphologies [9,42]. However, on the basis of XRD results and on literature data about the mutual influence of Ca^{2+} and Mg^{2+} ions on the size and habit of hydroxyapatite and struvite, it is possible to hypothesize the following correlation: (i) the pseudo-amorphous aspect of the coating could be ascribed to nano-sized agglomerates of Ca-phosphate spherical particles; (ii) the spherical particles (consistently in the range of 10–50 nm; dimension slightly affected by the treatment concentration) often characterized by an aggregate prismatic aspect (Figure 2c, right) could be correlated to the formation of magnesium phosphate nuclei.
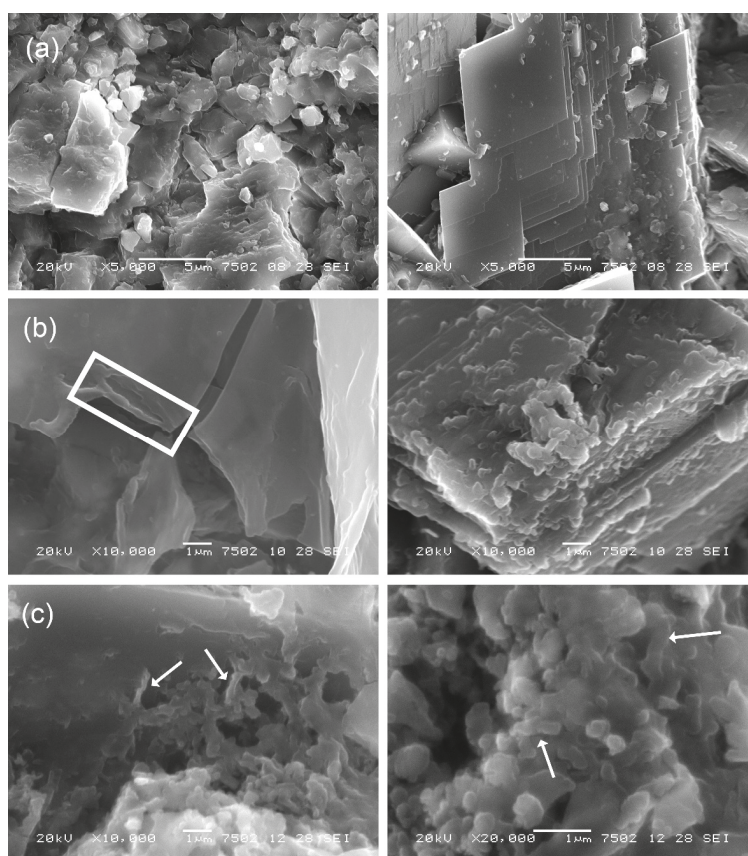
Figure 2. SEM images of Angera stone. (**a**) Untreated substrate, showing micritic dolomite on the left and bigger grains of well-shaped rhombohedral dolomite on the right; (**b**) treated lithotype after the poultice with a 0.76 M DAP solution. On the left, pseudo-amorphous coating formed on micritic dolomite and incipient formation of spherical structures in an elongated arrangement (white rectangle); on the right, big dolomitic crystal with the overgrowth of crystal agglomerates in spherical structures, some of them having prismatic elongations; (**c**) treated Angera stone after the poultice with a 3.00 M DAP solution, showing detail of spherical crystallites and their aggregation in chains - elongated arrangement (arrows).

3.3. Evidence of HAP Formation by Thermal Treatments

Thermal treatments are an acknowledged tool to investigate the nature of calcium phosphate phases showing at room conditions (rT) hardly distinguishable X-ray diffraction patterns [31], by promoting *T*-induced phase transitions.

More specifically, heating of: (i) poorly-crystalline stoichiometric HAP generated crystalline stoichiometric HAP; (ii) partially-substituted HAP (e.g., carbonated-hydroxyapatite) produced crystalline HAP in mixture with β-tricalcium phosphate (β-TCP, β-Ca$_3$(PO$_4$)$_2$), and with β-TCP predominant versus HAP; (iii) OCP did not generates HAP, but only β-TCP in mixture with β-calcium pyrophosphate (β-CPP, Ca$_2$P$_2$O$_7$) [9,31].

Figure 3 shows the parent-to-product phase transformations occurred in Angera stone treated with the 0.76 M DAP solutions. Identical results are obtained on the specimens treated with the 3.00 M one. Thermal treatments were carried out also on untreated Angera stone for comparison and the principal XRD patterns are provided as well.
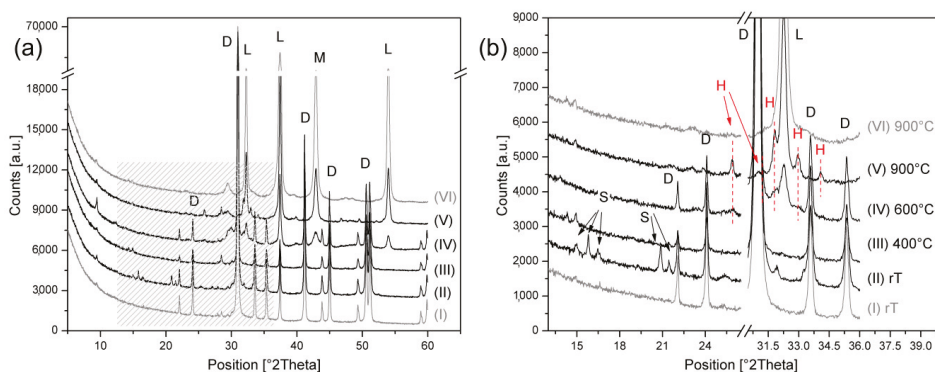
Figure 3. (**a**) XRD patterns of untreated (grey patterns) and treated (black patterns) Angera stone at room temperature (rT) and after heating at 400, 600 and 900 °C. (**b**) zoom of (a) showing the phase transformation occurred with heating. D = dolomite, L = lime, M = MgO, S = struvite, H = hydroxyapatite.

The heating at 400 °C induces the first phase variation, namely the total disappearance of the XRD peaks of struvite, due to the collapse of struvite into amorphous magnesium phosphate phases. Previous studies describe that heating induces a chain decomposition, involving the initial formation of amorphous magnesium hydrogen phosphate hydrate (MgHPO$_4$·3H$_2$O [36]), followed by its transformation into amorphous anhydrous magnesium hydrogen phosphate (MgHPO$_4$ [32,35,36]). In this study, it was not possible to discriminate between the two amorphous products; thus, they are referred to a generic amorphous magnesium phosphate phases.

The heating at 600 °C acts on poorly-crystalline calcium phosphates, as the weak broad peak at ~25.90° of 2Theta becomes more pronounced. The principal phase transformation occurs after heating at 900 °C, where dolomite of the substrate is decomposed into magnesium oxide (MgO, peaks at 42.92° and 62.30°) and lime (CaO, peaks at 32.27°, 37.48° and 53.97°; phase transformation probably occurred between 600–820 °C [33,34]) and the peaks of calcium phosphates become more defined. More precisely, the growth of sharp, well-defined peaks at 2Theta of 25.90° (d_{002}), 31.77° (d_{211}), 32.96° (d_{300}) and 34.08° (d_{202}) unambiguously identify crystalline HAP as heating by-product. Only the very weak peak at 28.09° could be attributed to β-TCP.

Magnesium oxide and lime, the calcinations by-products of dolomite, are active components that might interact with the calcium phosphates at high temperature, resulting in a further calcium source. However, even if the occurrence of this phenomenon cannot be a priori excluded, there is no evidence

of other high-temperature calcium phosphate phases nor of high-temperature magnesium phosphates formed by the reaction of active oxides with amorphous phosphates.

These results demonstrate that apatite formed after DAP treatments is poorly-crystalline, but mainly stoichiometric. Moreover, the formation of minor fraction of β-TCP indicates that a partially-substituted nonstoichiometric apatite and OCP were formed by the DAP treatment, but with poorly-crystalline stoichiometric HAP predominant versus these phases. No phase variations were observed for silicates and phyllosilicates of the Angera stone matrix.

4. Discussion

The DAP reaction with the Angera stone involves the partial dissolution of the dolomite grains, with the release of calcium and magnesium ions from the stone substrate. It was followed by the interaction of these bivalent ions with the reagent ions, with the consequent nucleation and growth of newly-formed phosphate phases. This dissolution-recrystallization process is topotactic and forms magnesium phosphates and calcium phosphates: (struvite and hydroxyapatite, respectively) arranged in a coating on dolomite grains. The micro-morphology of this coating, which resembles almost the features of polymeric products used for the conservation, is quite different from the crystalline shell observed on calcite-based lithotypes [9,10], even where the reaction occurred in presence of Mg-containing veins [9,16,17]. The crystallization of these phases is not merely a superficial film, but it is a binding network which connects different dolomite grains.

The crystallization of the newly-formed phosphates is influenced by the microstructure and the composition of the lithotype. In particular, the microstructure of the substrate acts on the micro-morphology of the new phases. In fact, the newly-formed phosphates are well shaped when they grow on dolomite in large crystals, while on micritic dolomite, the phosphates mainly develop tiny crystals with irregular morphologies.

Mg-phosphates are crystalline, as demonstrated by the sharp well-defined XRD peaks of struvite. On the contrary, the apatite is formed as poorly ordered partially-substituted crystals. It is worth underlying that hydroxyapatite formed after DAP treatments by using only calcium ions of the substrate is never highly crystalline, even when the reaction occurs on calcium carbonate stones. However, the DAP reaction on dolomite of Angera stone is particularly non-stoichiometric, and the formed apatite is so poorly ordered that its identification before heating is assumed only by a weak broad XRD peak. It is conceivable that Mg^{2+} ions destabilizes the crystalline structure and growth sequence of apatite, which shows a morphology characterized by an amorphous-spherical aspect similar to that reported by Ren et al. [43]. In any case, the thermal treatments shed light on the nature of this phase and, for clarity's sake, the poorly ordered calcium phosphate phase formed after the DAP treatment will be labeled as HAP in the following discussion.

The HAP X-ray diffraction peak is more intense in the specimens treated with the DAP 0.76 M, while struvite peaks are more evident in the specimens treated with the DAP 3.00 M, even though it is only a semi-quantitative evaluation. The higher the DAP molarity, the higher the ion dissolution from the substrate; consequently, the more pronounced the formation of struvite and the more poorly crystalline HAP. Regarding to the DAP molarity, the "coating-like" morphology is more evident in the specimens treated with the DAP 0.76 M, whereas the rounded morphology in elongated chains is prevalent on the specimens treated with the DAP 3.00 M. Considering these features, it is conceivable to hypothesize that these morphological and compositional differences depend on the reaction variables, first of all the pH and the ionic strength. Moreover, dolomite is less reactive than calcite to DAP solutions [20]; thus, the reaction kinetic may be different as well.

The minimum solubility of struvite is documented in the pH range 9–11 [42], while HAP crystallizes in aqueous solutions at pH > 8.5–9 [14].

At the beginning of the reaction the pH is 8.8, which is close to the ideal crystallization pH for both the phases. Actually, even though it is not possible to measure the evolution of pH on grain boundaries, it is reasonable that pH decreases as long as the reaction evolves, due to the: (i) dissociation

of the reagent into PO_4^{3-} and H^+ ions [9,44], (ii) nucleation of HAP which consumes OH^- ions [41]; iii) precipitation of struvite which subtracts NH_4^+ ions [36].

Furthermore, close to dolomite boundaries where the dissolution-recrystallization process is ongoing, Ca^{2+} and Mg^{2+} ions compete for PO_4^{3-} groups to nucleate calcium phosphates or magnesium phosphates. In the microscale variations of the pH and of the ionic strength at the grain boundaries, carbonate and bicarbonate ions are reasonably involved as well [45].

The prediction of struvite/apatite crystallization is particularly challenging when this reaction occurs on dolomite stone. A combination of conditions governed by thermodynamics of solid-liquid equilibrium, kinetics of reaction, pH of the solution from which struvite and hydroxyapatite may precipitate, super saturation and presence of foreign ions influence their nucleation and crystallization process.

In particular, the influence of foreign ions on struvite/hydroxyapatite nucleation and their crystallization is a crucial issue because of Ca and Mg are at the same time "impurities" in that solution from which the two Mg/Ca phosphate phases may precipitate. This mutual interference affects the growth rate, which in turn inhibits the increase of crystal size [36].

This complex ionic equilibrium, with pH fluctuations toward not ideal reaction conditions, generates two effects. The first one is a clear inhibiting effect of Mg^{2+} ions on the crystallinity, morphology and crystal size of HAP, which nucleates as a poorly-crystalline phase and with a pseudo-amorphous coating aspect or in agglomerated structures (depending on the employed DAP molarity). A partial intra-crystalline Mg^{2+} versus Ca^{2+} substitution, as ab initio simulated by [43], is also possible. Referring to previous findings, this phenomenon should induce a slight variation of the unit-cell constants. In the case of HAP formed after the DAP treatment on dolomite, the possible generation of a Mg-HAP is not clearly documented, as it is most likely a very minor phase.

The second aspect is the interference of Ca^{2+} ions in the crystallization of struvite, which occurred in sub-micrometric nuclei of crystals, more than well-structured micrometric prismatic crystallites. The possible presence of ions substitutions in struvite is also highly likely [36].

Focusing on conservation evaluations, the newly-formed crystalline phases nucleate in a coating on dolomite grains by forming a covering that provides new functional properties to the substrate.

Irrespective of their composition, the newly-formed phases nucleate on the dolomite grain surface and among dolomite grains; hence, their crystallization provide a clear bonding action on the stone microstructure. Further experiments are scheduled in order to explore the quantitative ratio of the two phases and their arrangement within the stone pores.

5. Conclusions

The DAP reaction with polycrystalline dolomite of the Angera stone determines an interaction among calcium and magnesium ions, which compete each other to form phosphate phases. The variation of the solution pH and of the ionic strength during the DAP reaction with dolomite generate a complex crystallization processes of the phosphate phases, which are formed as Mg-phosphates and Ca-phosphates crystals with morphologies different from those commonly described in literature. The mutual interference of the ions involved in reaction (NH^{4+}, Mg^{2+}, PO_4^{3-}, Ca^{2+}, CO_3^{2-}, HCO_3^-) determines an irregular crystal growth pattern with respect to the primary nucleation process. The consequence is a clear effect in the crystallization of the new phases (struvite and hydroxyapatite) in terms of crystal size, micro-morphology, composition and crystallinity.

In particular, the Mg^{2+} ions presence destabilizes the hydroxyapatite well-ordered structure, causing a structural variation that inhibits the growth of well-shaped crystals and, on the contrary, promotes the formation of an amorphous coating on the dolomite grains. The higher the DAP molarity, the higher the Mg molar fraction in the solution and the lower the crystallinity of the formed calcium phosphate. In any case, heating treatments demonstrated that the newly-formed apatite is poorly crystalline but mainly stoichiometric; thus, with a Ca/P molar ratio quite close to the ideal one (1.67).

On the other hand, the struvite formation is affected by the presence of free calcium ions, and the descending effects are observed in the crystal morphology and crystal size.

Regarding the effects induced by the DAP treatment on the Angera lithotype, it is important to consider that the new phases formed on the dolomite grains create a crystalline network that likely improves the cohesion of the lithotype.

References

1. Matteini, M.; Rescic, S.; Fratini, F.; Botticelli, G. Ammonium Phosphates as Consolidating Agents for Carbonatic Stone Materials Used in Architecture and Cultural Heritage: Preliminary Research. *Int. J. Archit. Herit. Conserv. Anal. Restor.* **2011**, *5*, 717–736. [CrossRef]
2. Sassoni, E.; Naidu, S.; Scherer, G.W. The use of hydroxyapatite as a new inorganic consolidant for damaged carbonate stones. *J. Cult. Herit.* **2011**, *12*, 346–355. [CrossRef]
3. Yang, F.; Zhang, B.; Liu, Y.; Wei, G.; Zhang, H.; Chen, W.; Xu, Z. Biomimic conservation of weathered calcareous stones by apatite. *New J. Chem.* **2011**, *35*, 887. [CrossRef]
4. Matteini, M.; Colombo, C.; Botticelli, G.; Casati, M.; Conti, C.; Negrotti, R.; Realini, M.; Possenti, E. Ammonium phosphates to consolidate carbonatic stone materials: An inorganic-mineral treatment greatly promising. In *Built Heritage 2013 Monitoring Conservation Management*; Springer International Publishing: Cham, Switzerland, 2013; pp. 1278–1286.
5. Ni, M.; Ratner, B.D. Nacre surface transformation to hydroxyapatite in a phosphate buffer solution. *Biomaterials* **2003**, *24*, 4323–4331. [CrossRef]
6. Kasioptas, A.; Perdikouri, C.; Putnis, C.V.; Putnis, A. Pseudomorphic replacement of single calcium carbonate crystals by polycrystalline apatite. *Mineral. Mag.* **2008**, *72*, 77–80. [CrossRef]
7. Sassoni, E. Hydroxyapatite and Other Calcium Phosphates for the Conservation of Cultural Heritage: A Review. *Materials* **2018**, *11*, 557. [CrossRef] [PubMed]
8. Sassoni, E.; D'Amen, E.; Roveri, N.; Scherer, G.W.; Franzoni, E. Durable self-cleaning coatings for architectural surfaces by incorporation of TiO_2 nano-particles into hydroxyapatite films. *Materials* **2018**, *11*, 1–16. [CrossRef] [PubMed]
9. Possenti, E.; Colombo, C.; Conti, C.; Gigli, L.; Merlini, M.; Plaisier, J.R.; Realini, M.; Sali, D.; Gatta, G.D. Diammonium hydrogenphosphate for the consolidation of building materials. Investigation of newly-formed calcium phosphates. *Constr. Build. Mater.* **2019**, *195*, 557–563. [CrossRef]
10. Possenti, E.; Colombo, C.; Bersani, D.; Bertasa, M.; Botteon, A.; Conti, C.; Lottici, P.P.; Realini, M. New insight on the interaction of diammonium hydrogenphosphate conservation treatment with carbonatic substrates: A multi-analytical approach. *Microchem. J.* **2016**, *127*, 79–86. [CrossRef]
11. Molina, E.; Rueda-Quero, L.; Benavente, D.; Burgos-Cara, A.; Ruiz-Agudo, E.; Cultrone, G. Gypsum crust as a source of calcium for the consolidation of carbonate stones using a calcium phosphate-based consolidant. *Constr. Build. Mater.* **2017**, *143*, 298–311. [CrossRef]
12. Sassoni, E.; Graziani, G.; Franzoni, E. Repair of sugaring marble by ammonium phosphate: Comparison with ethyl silicate and ammonium oxalate and pilot application to historic artifact. *Mater. Des.* **2015**, *88*, 1145–1157. [CrossRef]
13. Wang, L.; Nancollas, G.H. Calcium Orthophosphates: Crystallization and Dissolution. *Chem. Rev.* **2008**, *108*, 4628–4669. [CrossRef] [PubMed]
14. Dorozhkin, S.V. Calcium orthophosphates. *J. Mater. Sci.* **2007**, *42*, 1061–1095. [CrossRef]
15. Calore, N.; Botteon, A.; Colombo, C.; Comunian, A.; Possenti, E.; Realini, M.; Sali, D.; Conti, C. High Resolution ATR μ-FTIR to map the diffusion of conservation treatments applied to painted plasters. *Vib. Spectrosc.* **2018**, *98*, 105–110. [CrossRef]

16. Possenti, E. Inorganic Products Used in the Conservation of Cultural Heritage: Interaction with Carbonatic Substrates and Newly-Formed Crystalline Phases. Ph.D. Thesis, University of Milan, Milan, Italy, 7 February 2019.

17. Possenti, E.; Colombo, C.; Conti, C.; Gigli, L.; Merlini, M.; Plaisier, J.R.; Realini, M.; Gatta, G.D. Grazing incidence synchrotron X-ray diffraction of marbles consolidated with diammonium hydrogen phosphate treatments: Non-destructive probing of buried minerals. *Appl. Phys. A* **2018**, *124*, 383. [CrossRef]

18. Possenti, E.; Colombo, C.; Conti, C.; Gigli, L.; Merlini, M.; Plaisier, J.R.; Realini, M.; Gatta, G.D. What's underneath? A non-destructive depth profile of painted stratigraphies by synchrotron grazing incidence X-ray diffraction. *Analyst* **2018**, *143*, 4290–4297. [CrossRef] [PubMed]

19. Gulotta, D.; Bertoldi, M.; Bortolotto, S.; Fermo, P.; Piazzalunga, A.; Toniolo, L. The Angera stone. A challenging conservation issue in the polluted environment of Milan (Italy). *Environ. Earth Sci.* **2013**, *69*, 1085–1094. [CrossRef]

20. Schultheiss, S.; Sethmann, I.; Schlosser, M.; Kleebe, H.-J. Pseudomorphic transformation of Ca/Mg carbonates into phosphates with focus on dolomite conversion. *Mineral. Mag.* **2013**, *77*, 2725–2737. [CrossRef]

21. Pesonen, J.; Myllymäki, P.; Vervecken, G.; Hu, T.; Prokkola, H.; Tuomikoski, S. Use of calcined dolomite as chemical coagulant in the simultaneous removal of nitrogen and phosphorus. In Proceedings of the 6th International Conference on Sustainable Solid Waste Management, Naxos Island, Greece, 13–16 June 2018; pp. 1–8.

22. Beeson, K.C. Chemical Reactions in Fertilizer Mixtures Reactions of Diammonium Phosphate with Limestone and with Dolomite. *Ind. Eng. Chem.* **1937**, *29*, 705–708. [CrossRef]

23. Keenen, F.G.; Morgan, W.A. Rate of Dolomite Reactions in Mixed Fertilizers. *Ind. Eng. Chem.* **1937**, *29*, 197–201. [CrossRef]

24. Cavallo, A.; Bigioggero, B.; Colombo, A.; Tunesi, A. The Verbano Cusio Ossola province: A land of quarries in northern Italy (Piedmont). *Period. Mineral.* **2004**, *73*, 197–210.

25. Alessandrini, G.; Bugini, R.; Peruzzi, R. I materiali lapidei impiegati nei monumenti lombardi e i loro problemi di conservazione. In *Materiali Lapidei, Bollettino d'Arte—Ministero per i beni e le attività culturali*; Istituto Poligrafico e Zecca dello Stato: Rome, Italy, 1987; pp. 145–156.

26. Alessandrini, G. Le pietre del monumento. In *La Ca' Granda di Milano. L'intervento Conservativo sul Cortile Richiniano*; SNAM-Amilcare Pizzi: Milano, Italy, 1993; pp. 173–203. ISBN 88-366-0435-8.

27. Alessandrini, G. Lo stato di conservazione dei materiali lapidei: Morfologia e cause di degrado. In *La Ca' Granda di Milano. L'intervento Conservativo sul Cortile Richiniano*; SNAM-Amilcare Pizzi: Milano, Italy, 1993; pp. 219–239. ISBN 88-366-0435-8.

28. Riganti, V.; Rosetti, R.; Soggetti, F.; Veniale, F.; Zezza, U. *Alterazione e protezione delle pietre dei monumenti storici dell'Università di Pavia*; Società Italiana di Scienze Naturali Corso Venezia: Milano, Italy, 1978.

29. Pittaluga, D.; Fratini, F.; Nielsen, A.; Rescic, S. Industrial archaeological sites and architectonic remains: The problem of consolidation in humid areas. In Proceedings of the Scienza e Beni Culturali XXVIII, Bressanone, Italy, 10–13 July 2012; pp. 303–312.

30. Sassoni, E. Phosphate-based treatments for conservation of stone. *RILEM Tech. Lett.* **2017**, *2*, 14. [CrossRef]

31. Karampas, I.A.; Kontoyannis, C.G. Characterization of calcium phosphates mixtures. *Vib. Spectrosc.* **2013**, *64*, 126–133. [CrossRef]

32. Bhuiyan, M.I.H.; Mavinic, D.S.; Koch, F.A. Thermal decomposition of struvite and its phase transition. *Chemosphere* **2008**, *70*, 1347–1356. [CrossRef] [PubMed]

33. Gunasekaran, S.; Anbalagan, G. Thermal decomposition of natural dolomite. *Bull. Mater. Sci.* **2007**, *30*, 339–344. [CrossRef]

34. Olszak-Humienik, M.; Jablonski, M. Thermal behavior of natural dolomite. *J. Therm. Anal. Calorim.* **2015**, *119*, 2239–2248. [CrossRef]

35. Ramlogan, M.V.; Rouff, A.A. An investigation of the thermal behavior of magnesium ammonium phosphate hexahydrate. *J. Therm. Anal. Calorim.* **2016**, *123*, 145–152. [CrossRef]

36. Tansel, B.; Lunn, G.; Monje, O. Struvite formation and decomposition characteristics for ammonia and phosphorus recovery: A review of magnesium-ammonia-phosphate interactions. *Chemosphere* **2018**, *194*, 504–514. [CrossRef] [PubMed]

37. Koutsopoulos, S. Synthesis and characterization of hydroxyapatite crystals: A review study on the analytical methods. *J. Biomed. Mater. Res.* **2002**, *62*, 600–612. [CrossRef] [PubMed]

38. Dorozhkin, S.V. Amorphous calcium (ortho)phosphates. *Acta Biomater.* **2010**, *6*, 4457–4475. [CrossRef] [PubMed]

39. Dorozhkin, S.V. Calcium Orthophosphates in Nature, Biology and Medicine. *Materials* **2009**, *2*, 399–498. [CrossRef]

40. Elliott, J.C. Hydroxyapatite and Nonstoichiometric Apatites. In *Structure and Chemistry of the Apatites and Other Calcium Orthophosphates*; Elsevier: Amsterdam, The Netherlands, 1994; pp. 111–189.

41. Drouet, C. Apatite formation: Why it may not work as planned, and how to conclusively identify apatite compounds. *Biomed. Res. Int.* **2013**, *2013*, 1–12. [CrossRef] [PubMed]

42. Ariyanto, E.; Ha Ming, A.; Tushar, S. Effect of initial solution pH on solubility and morphology of struvice crystals. In Proceedings of the CHEMECA Conference, Sydney, Australia, 18–21 September 2011; pp. 1–10.

43. Ren, F.; Leng, Y.; Xin, R.; Ge, X. Synthesis, characterization and ab initio simulation of magnesium-substituted hydroxyapatite. *Acta Biomater.* **2010**, *6*, 2787–2796. [CrossRef] [PubMed]

44. Naidu, S.; Scherer, G.W. Nucleation, growth and evolution of calcium phosphate films on calcite. *J. Colloid Interface Sci.* **2014**, *435*, 128–137. [CrossRef] [PubMed]

45. Cao, X.; Harris, W. Carbonate and magnesium interactive effect on calcium phosphate precipitation. *Environ. Sci. Technol.* **2008**, *42*, 436–442. [CrossRef] [PubMed]

Comparative Study Between Ammonium Phosphate and Ethyl Silicate Towards Conservation of Prehistoric Paintings in the Magura Cave (Bulgaria)

Enrico Sassoni [1,2,*], **Elisa Franzoni** [1,2], **Milyana Stefanova** [3], **Zdravko Kamenarov** [3], **Paolo Scopece** [4] and **Emanuele Verga Falzacappa** [4]

[1]   Department of Civil, Chemical, Environmental and Materials Engineering (DICAM), University of Bologna, Via Terracini 28, 40131 Bologna, Italy; elisa.franzoni@unibo.it
[2]   Centre for Applied Research on Buildings and Construction (CIRI-EC), University of Bologna, Via del Lazzaretto 15/5, 40131 Bologna, Italy
[3]   NTConservation ltd, Blv. Al. Konstantinov 51, 1504 Sofia, Bulgaria; milyana13@yahoo.com (M.S.); kamenarov_zdravko@abv.bg (Z.K.)
[4]   Nadir srl Plasma & Polymers, Via Torino 155/b, 30172 Venezia, Italy; scopece@nadir-tech.it (P.S.); falzacappa@nadir-tech.it (E.V.F.)
*   Correspondence: enrico.sassoni2@unibo.it; Tel.: +39-051-2090-429

Abstract: This study aimed at evaluating the effectiveness and the compatibility of two alternative treatments, in view of their possible use for conservation of prehistoric paintings in the Magura cave (Bulgaria). The paintings are made of bat guano applied over limestone; therefore, two sets of laboratory specimens were considered: stone specimens and stone specimens covered with a layer of sterilized bat guano. The two investigated treatments were a commercial product based on ethyl silicate ("ES") and a solution of diammonium hydrogen phosphate ("DAP"), aimed at forming calcium phosphates. The results of the study indicated that both treatments were able to increase the mechanical properties of stone, the increase being higher for "DAP". Both consolidants caused acceptable color changes, but the "ES" treatment significantly decreased stone wettability, water absorption, and water vapor permeability, while the "DAP" treatment slightly affected those properties. In the stone + guano specimens, the presence of the guano layer affected the penetration of the consolidants, thus partly reducing their effectiveness. Compared to the stone samples, the guano layer experienced a more intense color change, alongside visible cracking. However, the adopted methodology to replicate the cave paintings was not completely successful, as the so-deposited guano layer was very prone to detachment when dry, unlike cave paintings. Future work will be dedicated to assessing the consolidant performance onto samples that resemble even more closely the conditions of the cave paintings, by improving the methodology for the guano layer deposition and by contaminating specimens with soluble salts before consolidant application.

Keywords: cave painting; inorganic consolidant; hydroxyapatite; calcium phosphate; ammonium phosphate; ethyl silicate; TEOS; non-thermal plasma; wettability

1. Introduction

The present paper aimed at investigating the effectiveness and the compatibility of two treatments that have been taken into consideration for the conservation of prehistoric paintings in the Magura cave (northwest Bulgaria). The Magura cave contains impressive prehistoric paintings, displaying both figurative and abstract compositions [1]. Religious ceremonies, hunting scenes, signs, and graphic motifs decorate one of the cave chambers—the Gallery with the paintings (Figure 1).
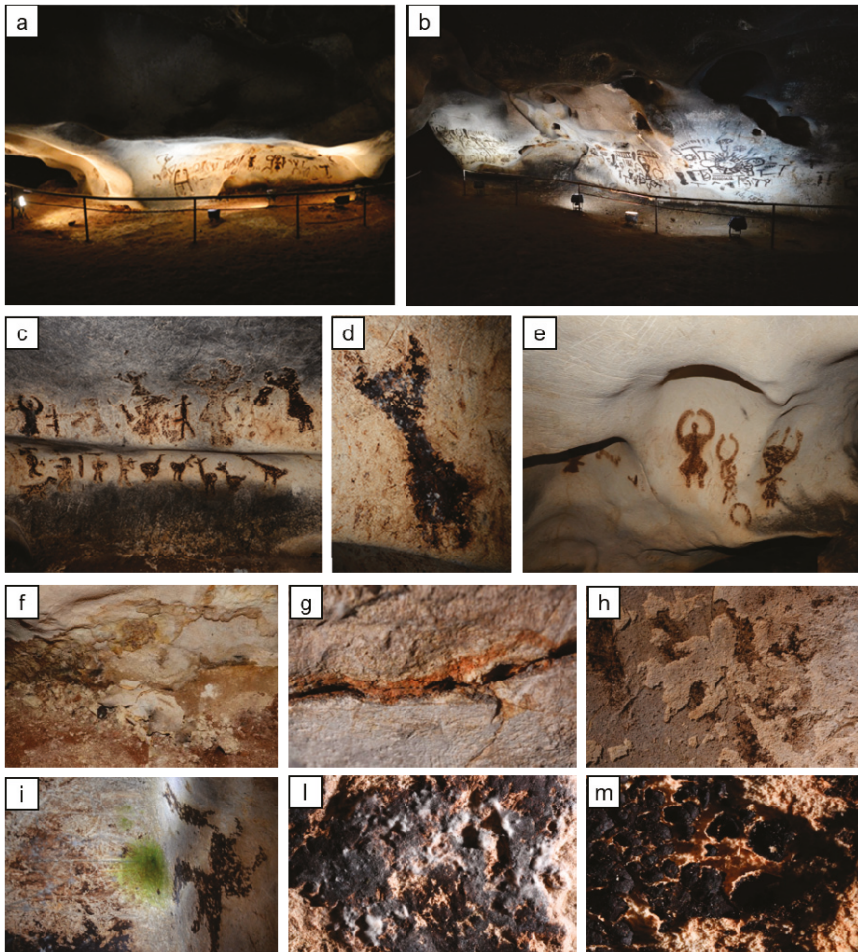
Figure 1. General view of the Gallery with the paintings in the Magura cave (Bulgaria) (**a**,**b**), details of the cave paintings (**c**,**d**,**e**), and details of the deterioration patterns ((**f**,**g**,**h**)—cracks, powdering, blistering, and fragmentation of the limestone; (**i**,**l**)—biological colonization; (**m**)—cracking and loss of the original guano painting due to the drying of the surface and powdering of the stone).

These artworks, dating back to some 5500 years ago, are made of fossilized guano of cave-dwelling bats applied over limestone [2–5]. After opening to the public in 1961, with the consequent presence of visitors and the use of artificial light, the delicate balance of environmental conditions inside the cave has been altered. Despite the cultural relevance of the Magura Cave, unfortunately, the micro-environmental data, such as temperature, relative humidity, CO_2 concentration, and atmospheric pressure, have never been professionally measured and controlled. Today, the cave suffers from biological colonization and stone pulverization, originated by crystallization of soluble salts present in rising damp from the ground. Deterioration patterns, such as green biofilm and white and black colorations over the stone/paintings surface, together with limestone powdering, blistering, and fragmentation [6] (Figure 1), led to the closure of the Gallery in May 2019.

The preservation of the cave paintings requires challenging interventions to face the growth of bio-organisms and the deterioration of the stone. As for biological growth, the use of biocides is

dangerous because they may completely alter the balance of microbial communities in the cave with negative consequences [7]. For this reason, biodeactivation by non-thermal plasma sterilization has been attempted, and some encouraging results have been obtained [8]. As for stone consolidation, the issue is particularly challenging for the following reasons:

(1)   the presence of the guano layer creating the paintings. The case of the Magura cave is different from the case of wall paintings [9] and also from the case of other prehistoric paintings, such as those in the Altamira [10] and Lascaux [11] caves. In the wall paintings, the pigments were dispersed in limewater and then applied directly onto the wet plaster (in the so-called "fresco" technique) and/or they were applied onto the dried plaster by using an organic binder, such as egg, milk, or vegetal extractives [9]. In the case of other prehistoric paintings, the pigments, usually red (Fe_2O_3), black (charcoal, soot, bone charcoal, or Mn oxides), and more rarely yellow (FeOOH) and brown (ochres), were mixed with an extender and/or a binder [10,11]. The case of the Magura cave, with paintings laid on the cave walls by bat guano having a plastic consistency similar to clay [5], is substantially different from the situations discussed above, with only a few similar cases, such as the Baylovo Cave in Bulgaria and the "Grotta dei Cervi" (Deer cave) in Italy [7]. To our knowledge, no case of consolidation of cave paintings made of bat guano has been reported in the scientific literature.

(2)   the presence of soluble salts inside the stone pores. This is an issue for two reasons: (i) salts already present inside the pores may lead to failure of the consolidation intervention, if the tip of the cracks among grains is filled with salts, so that no effective sealing of the crack tip can be achieved by the consolidant [12]. To prevent this, it is usually recommended that salts be extracted by poulticing before consolidants are applied, but this is useless in the present case, as salts are continuously supplied from the ground; (ii) salt crystallization cycles taking place after stone consolidation may lead to stress at the grain boundaries, with possible failure of the consolidation intervention if the stone tensile strength is exceeded. Experiences of application of various consolidants onto salt-laden stones, possibly later subjected to further salt crystallization cycles, have been reported in the literature, as detailed in the following.

(3)   the environmental conditions in the cave. Because of its hypogeous nature, the temperature in the cave ranges between 12 and 25 °C, while the relative humidity (RH) is constantly in the range 65–90%. Such environmental conditions may have an impact on a consolidant performance, as discussed below.

In these conditions, the selection of consolidants to be tested and possibly applied in the Magura cave is very hard, as none of the commercially available treatment seems ideal for application onto the limestone and the paintings in the cave. The two consolidants tested in this study, namely, a commercial product based on ethyl silicate and diammonium hydrogen phosphate, were selected based on the following reasoning.

Organic consolidants, such as acrylic resins, were discarded because, in the past, the use of polymeric treatments often led to enhanced deterioration to such an extent that removal of polymers applied in the past is nowadays one of the greatest issues in materials science for cultural heritage conservation [13]. The failure of organic consolidants often originates from water vapor being impeded to move from the interior of the consolidated substrate towards the exterior [14]. This risk would be particularly high in the case of the Magura cave, where water is continuously supplied from the ground, and systems currently used in building for damp reduction are not applicable.

Among inorganic treatments, nanolimes were first considered because of their good chemical-mineralogical compatibility with limestone and because they have shown a good performance when applied onto lime-based frescoes and wall paintings [9,13–16]. However, as already mentioned, a substantial difference exists between wall paintings and paintings in the Magura cave, made of bat guano. Moreover, in the case of the Magura cave, the purpose was the consolidation of the powdering stone with the bat guano painting on the surface, and not of the painting layer alone;

therefore, a consolidant able to penetrate in depth in the substrate was needed. In several cases of application of nanolimes onto stones, a poor penetration depth (<1 mm) has been reported [14]. Nanolime accumulation below the surface is likely not due to nanoparticle coagulation preventing penetration, but rather to nanoparticle re-transport towards the surface during drying [14]. When applied onto the salt-laden stone, conflicting results have been reported about the ability of nanolimes to increase stone durability to salt weathering [17,18]. In fact, in some cases, nanolimes have been reported to increase the crystallization pressure in the treated stone, as a result of the alteration in pore size distribution after consolidation, with a consequent decrease in durability [17]. Considering the limitations exhibited by nanolimes in terms of penetration depth and durability to salt weathering, which are both very important aspects for the conservation of the Magura cave limestone and paintings, nanolimes were discarded, and further options were explored.

Ammonium oxalate was considered as this treatment was specifically developed for the protection and consolidation of carbonate substrates, like wall paintings, marble, and limestone [19]. A positive aspect of the ammonium oxalate treatment is that encouraging results have been reported in the literature about its application onto salt-laden stones [20,21]. Removal of salts before application of ammonium oxalate solutions was found to be not as crucial as in the case of organic treatments because ammonium oxalate does not completely occlude pores (although forming a surface coating) [20]. However, ammonium oxalate was finally discarded because of its reduced availability in the market. The method based on barium hydroxide [19] was discarded as well due to its recommended poultice application (aimed at reducing the risk of surface whitening) and its possible reaction with nitrate salts (giving barium nitrate, a very damaging salt upon crystallization). Given the impossibility to apply the consolidant in the cave by poultice and the presence of several salts in the stone, barium hydroxide was not considered for the present application.

Ammonium phosphate was proposed years ago as an improvement of the ammonium oxalate treatment for the consolidation and protection of carbonate stones [22,23]. The treatment is based on the formation of new calcium phosphates (ideally hydroxyapatite, the least soluble calcium phosphate at pH > 4 [24]) from the reaction between an aqueous solution of ammonium phosphate and the stone [22]. This reaction occurs in 24–48 h during which the stone is kept impregnated with the ammonium phosphate solution; therefore, the environmental conditions of the cave are not expected to negatively affect the treatment success. Thanks to the low viscosity of the phosphate solution and to the absence of nanoparticles, a good penetration depth is usually achieved (>5 cm in highly porous limestone) [25]. So far, the treatment has provided good results on a variety of substrates [25], including many types of natural stones [26–32], mortars [33,34], and stuccoes [35]. Recently, the interaction between ammonium phosphate solutions and pigments used in wall paintings has been investigated, and, in most of the cases (but not in all), the treatment has been found to cause negligible color changes [36]. This is encouraging towards the use of this treatment for the conservation of wall paintings, even though the substantial difference of the Magura cave paintings remains. Another positive aspect of the ammonium phosphate treatment is that the presence of salts in the stone pores has proven to be not detrimental for the treatment success [30,37], but, of course, this depends on the amount and type of salts and on the features of the stone pore system. Moreover, accelerated durability tests have shown that ammonium phosphate treatment is able to increase the durability of treated stone to salt crystallization cycles [38–40]. Furthermore, considering the presence of hydroxyapatite in the Magura cave limestone (although not in the limestone used for the laboratory tests), the chemical-compatibility of the ammonium phosphate treatment can be considered as excellent. For all these reasons, the phosphate treatment was regarded as highly promising for application in the Magura cave and hence was investigated in this study. As described in Section 2.3.2, two alternative formulations of the phosphate treatment were initially considered, and, after some preliminary screening tests, the most promising one was chosen.

Considering that ammonium phosphate has the limitation that experience on its use dates back only to a few years ago and that only a limited number of applications onto real case studies have been reported, a possible alternative consolidant was searched. Products based on ethyl silicate were

taken into consideration as they are known to generally exhibit a good penetration depth into porous substrates [41], often sensibly higher than that of nanolimes [14]. One major limitation of ethyl silicate when applied onto carbonate stones, as would be the case in the Magura cave, is that its consolidating effectiveness is lower than in the case of silicate stones. In fact, in the latter case, chemical bonding can take place between the silicate substrate and the silica gel resulting from hydrolysis-condensation of ethyl silicate, while, in the case of carbonate stones, only physical bonding can occur [12]. Nonetheless, significant increases in mechanical properties of carbonate stones treated by ethyl silicate have been reported [42], especially when the stone contains even limited quarzitic fractions that may allow for some chemical bonding between the consolidant and the substrate [43]. To improve the performance of ethyl silicate onto carbonate stones, several routes have been investigated, such as the use of coupling agents [41] or the addition of organic molecules (e.g., polyethylene glycol chains end-capped with carboxylic acid groups [44]) or inorganic nanoparticles (e.g., amorphous calcium carbonate and amorphous calcium oxalate [45]) directly into the ethyl silicate solution. Cases of application of ethyl silicate products onto salt-laden stones have been reported in the literature, with mixed results [18,37,41,46], also due to the variable nature of the ethyl silicate products in the market in terms of oligomer size, solvent nature, catalyst, etc. When salts are present in the pores of the treated stone, the consolidating effectiveness is not dramatically diminished [18,37]. However, the alterations induced by ethyl silicate in the stone pore size distribution may increase the salt crystallization pressure, thus decreasing the resistance to salt crystallization cycles, as assessed on both initially salt-contaminated [18] and uncontaminated [38,39] stone. In comparative studies, the salt resistance of carbonate stones treated by ethyl silicate proved to be lower compared to ammonium phosphate (but still higher than untreated stone) [38,39]. Another import factor when evaluating the suitability of ethyl silicate for the case of the Magura cave is the temporary hydrophobicity induced by ethyl silicate [12]. In fact, until hydrolysis-condensation reactions are completed, the treated stone remains hydrophobic because of the presence of residual ethoxy groups [12]. Completion of hydrolysis-condensation reactions can take as long as 6–7 months [12,47,48], even though the technical data sheet of commercial products usually report that the product reaction is completed in 1 month. The hydrophobic behavior of stone treated by ethyl silicate, which generally preserves permeability to water vapor but prevents the transport of liquid water through the consolidated layer, may be an issue in the case of Magura cave, where rising damp from the ground is present. On the other hand, the high relative humidity (65–90%) inside the cave is expected to speed up the hydrolysis-condensation reactions, which is positive. To accelerate the curing of ethyl silicate, thus re-establishing a hydrophilic behavior in a shorter time, various methods have been proposed, which basically consist of supplying water [47] or water-ethanol mixtures [48] to promote hydrolysis reactions. However, such methods seem unfeasible in the case of the Magura cave, as they involve the application of a poultice onto the treated surface, which may lead to damage and detachment of the cave paintings. All things considered, even though not ideal, ethyl silicate was regarded as worthy of investigation as a possible alternative to ammonium phosphate. Among the numerous products available in the market, a commercial formulation enhanced with antimicrobial ability was used, as described in detail in Section 2.3.1.

For testing the two selected consolidants, the complex situation of the Magura cave had to be necessarily simplified, to isolate variables and better evaluate the consolidant performance. With regard to the three aspects discussed above, the following decisions were made:

(1) To evaluate the effects of the two consolidants not only on limestone but also on the cave paintings, two types of laboratory specimens were considered: (i) specimens made of a limestone similar to that in the cave and (ii) specimens made of the same limestone with a layer of sterilized bat guano deposited on top, to resemble the prehistoric paintings in the cave. The procedure for the deposition of the guano layer, described in detail in Section 2.2, was developed in such a way to likely resemble the process of creation of the paintings, even though, of course, freshly prepared samples could not be identical to cave paintings that have undergone about 5500 years of fossilization.

(2) To evaluate the effects of the two consolidants onto salt-laden samples, to be further subjected to salt crystallization cycles after consolidation, would have been ideal. However, this would have made the evaluation of the consolidants on the two types of specimens (stone and stone+guano) even more difficult, with the risk that the influence of salts in the pore and the guano layer on the stone surface could be hard to distinguish. For this reason, at the present stage of the research, the consolidants were applied onto uncontaminated specimens, which were used to evaluate the effectiveness and the compatibility of the treatments in these simplified conditions. Application onto salt-laden samples, together with the evaluation of the durability of the consolidated substrates, was left to a future stage of the research, once the performance on this simplified system has been assessed.

(3) At this stage of the research, the effects of the treatments were evaluated in laboratory conditions (T = 19–23 °C, RH = 45–55%), which were regarded as conservative with respect to the environmental conditions in the cave (T = 12–25 °C, RH = 65–90%). In fact, the higher relative humidity in the cave was expected to positively influence the rate of hydrolysis-condensation reactions of ethyl silicate (while no effect was expected on the reaction of the ammonium phosphate treatment). Nonetheless, to obtain some preliminary information on the performance of two consolidants in the real environmental conditions, specimens treated with the two consolidants were exposed in the Magura cave for 9 months, as described in detail in the following.

In the frame of the experimental choices described above, in the present paper, the performance of the two consolidants was characterized in terms of effectiveness (penetration depth, dynamic elastic modulus, and resistance to abrasion) and compatibility (alterations in color, pore size distribution, contact angle, water sorptivity, water absorption, water vapor permeability). The results obtained in the present study will be used in future research to evaluate also the durability of the two treatments, also in salt-contaminated stone.

2. Materials and Methods

2.1. Stone Specimens

Two small samples of the Magura cave limestone were available for characterization, namely, a stone piece affected by severe powdering and a hard surface crust. Although not sufficient to fully characterize the stone in the cave, these samples were characterized to select a stone for laboratory testing that could suitably resemble the limestone in the cave. The minerals present in the two samples were determined by powder X-ray diffraction (XRD), using a Philips diffractometer (Milan, Italy) with PW1830 generator and PW1820 goniometer (40 kV and 30 mA, 2θ range 3°–80°, step size 0.025 2θ, time per step 1 s). Additional minerals, present in quantities below the sensitivity of XRD, were investigated by Fourier transform infrared spectrometry (FT-IR), using a Perkin Elmer Spectrum Two spectrometer (Milan, Italy) (ATR mode, 2000–400 cm^{-1} range, spectral resolution 2 cm^{-1}, 32 scans, data interval 1 cm^{-1}). The amount of calcite in the samples was quantified by Dietrich–Frühling gas volumetric method, i.e., by measuring the CO_2 volume released by reacting the powdered sample with HCl. The open porosity of the samples was assessed by mercury intrusion porosimetry (MIP), using a Pascal 140 and 240 instrument. The Magura cave limestone was found to be mainly composed of calcite (the only mineral detected by XRD), quantified as 90.0 ± 1.8 wt.% (by gas volumetric method). Based on FT-IR, the remaining fraction was composed of hydroxyapatite and possibly traces of quartz. In terms of microstructure, the open porosity was found to range significantly between the two samples, from 2% for the hard crust to almost 48% for the powdering sample.

The stone selected for the laboratory tests was Vratsa limestone, which is quarried very close to the Magura cave (Oreshets quarry, Municipality of Vidin, Bulgaria, 20 km from the cave). In terms of mineralogical composition (assessed as above), Vratsa limestone was mainly composed of calcite (80.0 ± 0.1 wt.%), the remaining fraction being quartz (the only other phase detected by XRD and FT-IR). The open porosity of Vratsa limestone (assessed as above) exhibited some variability, ranging

from 11% to 18%. Although not identical to the cave limestone, the Vratsa limestone was considered as still suitable, as it exhibited mineralogical composition similar to the Magura cave limestone (although the minor phases were different) and open porosity that was intermediate between the values registered for the samples from the cave (which, however, were very different from each other).

Specimens of Vratsa limestone to be used for the tests (labeled "ST") were sawn in the form of prisms ($7 \times 7 \times 3$ cm^3) and cubes (5 cm side).

2.2. Stone+Guano Specimens

To resemble the cave paintings, the original guano from the Gallery with the paintings, which is home of 8 different bat species, was used. The guano has an organic matter content greater than 40%, visible chitinous insect remains and is a favorable environment for many different types of microorganisms [49,50]. For safety reasons, the original bat guano was exposed to autoclave sterilization (Laboratory of Geological Microbiology, Department of Microbiology, Sofia University St. Kliment Ohridski, Bulgaria).

The stone+guano specimens (labeled "ST+G") were prepared, starting from the "ST" specimens, by depositing a layer of sterilized bat guano on top, following the procedure illustrated in Figure 2. First, a small amount of guano was added with deionized water so as to reach a suitable consistency (guano:water ratio of 1:2 by weight). After mixing the guano with water, the obtained mixture was applied onto one face of the specimens by brush. After about 2 min, the second layer of guano was applied in the same way.

Considering that the so-deposited guano layer becomes dusty and starts to detach from the substrate when it dries, the consolidant application was carried out 30 min after the guano application to avoid the stone+guano specimens from becoming too powdery.
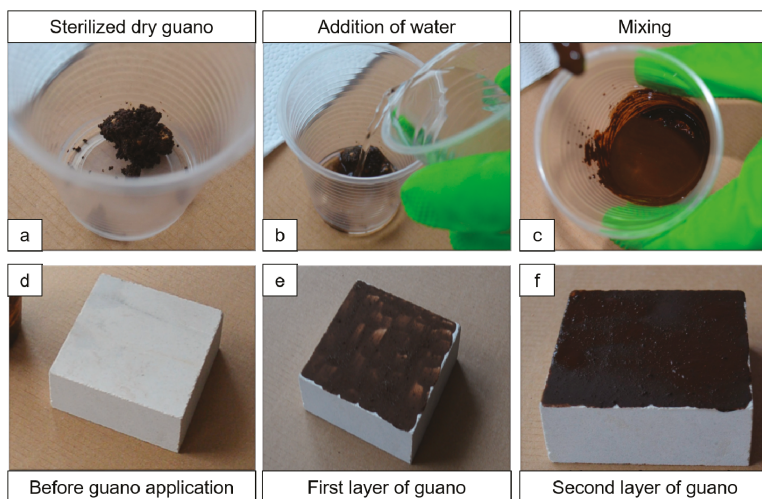
Figure 2. Procedure for guano application: sterilized dry guano (**a**) is added with water (**b**); after mixing (**c**), stone specimens (**d**) are covered with the first layer of guano (**e**) applied by brush; after about 2 min, the second layer of guano (**f**) is applied.

2.3. Consolidants

The two consolidants selected for testing were a commercial product based on ethyl silicate (labeled "ES") and diammonium hydrogen phosphate (labeled "DAP"). In both cases, the consolidants were applied by brushing onto one face of the specimens (the face already covered with the guano

layer, in the case of the "ST+G" specimens). For each consolidant, 7 prismatic and 2 cubic specimens were treated.

2.3.1. Ethyl Silicate-Based Consolidant

The commercial product "Bio Estel New" by CTS Srl (Florence, Italy) was selected. According to the manufacturer's technical data sheet, "Bio Estel New" is based on ethyl silicate and isopropyl alcohol as a solvent, and it combines consolidating ability with protective ability against microorganisms. The technical data sheet also reports that the product is suitable for application onto silicate and carbonate stones, especially underwater stones and stones in a very humid environment, and that the product reaction is completed in about 4 weeks at T = 20 °C and RH = 40–50%.

The ES consolidant was applied by brushing until apparent refusal (7 brush strokes), waiting for the product to be absorbed between two consecutive brush strokes. At the end of the consolidant application, specimens were left to cure in laboratory conditions (T = 21 ± 2 °C, RH = 50% ± 5%) for at least 4 weeks before characterization.

2.3.2. Phosphate Consolidant

For the phosphate treatment, diammonium hydrogen phosphate (DAP, $(NH_4)_2HPO_4$), calcium chloride ($CaCl_2·2H_2O$), and ethanol (EtOH), all purchased from Sigma-Aldrich (Milan, Italy, assay > 99%) were used. Based on results obtained in previous studies [22,25,51], two formulations of the phosphate treatment were initially considered for the tests: (i) 1 M DAP + 1 mM $CaCl_2$ and (ii) 0.1 M DAP + 0.1 mM $CaCl_2$ in 30 vol.% EtOH. Calcium chloride has the beneficial effect of accelerating the formation of calcium phosphates [51], while ethanol has been found to promote densification of the new calcium phosphates [52]. To identify the most promising treatment condition in the specific case of the specimens resembling paintings in the Magura cave, preliminary tests were carried on the "ST+G" specimens. The surface alteration following consolidant application, carried out 30 min after guano application, was visually evaluated. As illustrated in Figure 3, the formulation containing 0.1 M DAP + 0.1 mM $CaCl_2$ in 30 vol.% EtOH caused lower alteration (darkening and cracking) of the specimen surface, compared to the alternative formulation. Consequently, that formulation was selected and applied to the "ST" and "ST+G" specimens.
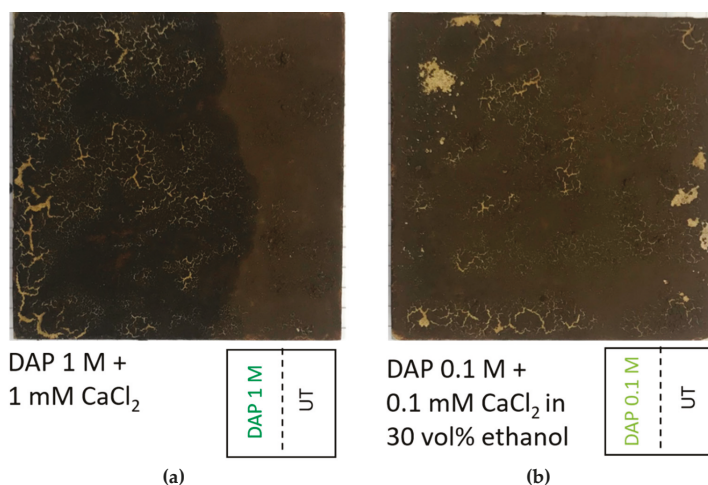
Figure 3. Alteration of the specimen surface caused by consolidant application 30 min after guano application: 1 M DAP + 1 mM $CaCl_2$ (**a**) and 0.1 M DAP + 0.1 mM $CaCl_2$ in 30 vol.% (**b**).

The "DAP" treatment was applied by brushing until apparent refusal (10 brush strokes), waiting for the product to be absorbed between two consecutive brush strokes. At the end of the consolidant application, specimens were wrapped in a plastic film to prevent evaporation and left to react for 48 h. Then, specimens were unwrapped, rinsed with deionized water (only in the case of the "ST" specimens), and left to dry at room temperature until constant weight.

2.4. Pre-treatment by Plasma

To evaluate whether penetration of the two consolidants into the stone might be enhanced, with a consequent improvement in the consolidating efficacy, part of the stone specimens was pre-treated by plasma, before consolidant application. Indeed, an improvement in wettability is a well-known effect of a wide range of plasma sources on different materials. Mainly, thanks to oxygen atoms implantation and the subsequent formation of polar groups on the treated surface, an increase in surface energy is typically observed together with a reduction in water contact angle [53].

To evaluate whether pre-treatment by plasma might be beneficial for the consolidant performance, right before consolidant application, part of the "ST" specimens was subjected to pre-treatment by plasma, carried out with a dual-frequency atmospheric plasma jet device (Stylus Plasma Noble provided by Nadir Srl, Venice, Italy) [54]. The following working parameters were adopted: 5 W power at 16 kHz, 30 W power at 27 MHz, argon gas flow as working gas at 10 L/min, and compressed air as cooling gas at 12 L/min. The 7×7 cm^2 surface of prismatic specimens were manually treated for a total exposure time of 2 min, maintaining a constant working distance of 3 mm between the plasma source and the specimen.

The effects of the plasma pre-treatment were evaluated in terms of static contact angle, amount of product absorbed, and increase in dynamic elastic modulus, assessed as described in the next paragraph.

2.5. Sample Characterization

The effectiveness and the compatibility of the two consolidants were investigated by comparing the properties of untreated ("UT") and treated specimens ("ES" and "DAP"), as described in the following.

2.5.1. Morphology of the New Phases

The morphology of the new phases formed over the treated surface was evaluated by observing samples (about $10 \times 10 \times 2$ mm^3, obtained by wet sawing from the prismatic specimens), using a field emission gun scanning electron microscope (FEG-SEM, Tescan Mira3, Brno, Czech Republic, WD = 10 mm, Voltage = 10 kV). Before SEM observation, the sample surface was made conductive by sputtering with aluminum.

2.5.2. Composition of the New Phases

The composition of the new phases formed over the treated surface was evaluated by analyzing powdered samples (obtained from the specimen surface using a spatula) by FT-IR, using the same instrument as in Section 2.1.

2.5.3. Penetration Depth

The penetration depth of the two consolidants into the "ST" and "ST+G" prismatic specimens was evaluated by fracturing them with a chisel to expose a cross-section, right at the end of the consolidant application (7 brush strokes in the case of ES, 10 in the case of DAP). The consolidant penetration depth was visually identified as the darker zone. Two replicate specimens were considered for each condition.

2.5.4. Dynamic Elastic Modulus

Dynamic elastic modulus (E_d) was measured on prismatic specimens, perpendicular and parallel to the plane of the slab (in the "ST+G" samples, perpendicular and parallel to the face covered with

guano). Given the absence of any clear anisotropy in the stone, values measured in the two directions parallel to the plane of the slab were averaged, so that, in the end, each specimen was characterized in terms of $E_{d\perp}$ and $E_{d//}$. E_d was calculated according to the formula $E_d = \rho \times v^2$, where ρ is the density and v is the ultrasonic pulse velocity. v was measured with a Matest instrument with 55 kHz transducers, using a rubber sheet to improve the contact between the transducers and the specimen. A rubber sheet instead of grease was used to improve the contact (as would be the standard procedure), in order not to stain the samples that later had to be consolidated. For instrument calibration, a standard bar with fixed traveling time was used. Five replicate specimens were tested.

2.5.5. Resistance to Abrasion

Resistance to abrasion was measured on prismatic specimens, in terms of material loss after an accelerated abrasion test, carried out following a previously developed method [55]. By partially modifying the PEI (Porcelain Enamel Institute) abrasion test, samples were tested by keeping steel spheres and corundum powder in rotatory motion over one of the 7×7 cm^2 faces of the specimens (the face already covered with the guano layer, in the case of the "ST+G" specimens), for a total of 15,000 rounds. The amount of material abraded during the test was then determined by comparing the sample weight before and after the test. Five replicate specimens were tested.

In the case of the "ST+G" samples, because guano flakes were prone to detach also from the area not directly subjected to the abrasion test, before the test all the guano-covered surface, not directly in contact with the steel spheres, was covered with scotch tape, so that no material loss could take place from that area.

2.5.6. Color Change

The color change after consolidation was measured on prismatic specimens by making use of a NH310 colorimeter. For the untreated and treated conditions, the LabCIE* color parameters (L^* = black–white, a^* = green–red, b^* = blue–yellow) were determined on duplicate specimens, repeating the measurements in three different spots for each specimen. For instrument calibration, a standard white sample supplied with the instrument was used. The color change (ΔE^*) between untreated and treated specimens was then calculated as $\Delta E^* = (\Delta L^{*2} + \Delta a^{*2} + \Delta b^{*2})^{1/2}$, considering the average L^*, a^*, and b^* values obtained for each condition.

2.5.7. Pore Size Distribution

The alterations in open porosity and pore size distribution following the treatments were determined by mercury intrusion porosimetry (MIP), using a Porosimeter 2000 by Carlo Erba (Milan, Italy) with Fisons Macropore Unit 120. MIP samples were obtained by chisel from prismatic specimens, always including the treated surface (where alterations were expected to be most pronounced). For each condition, two replicate samples were tested.

2.5.8. Static Contact Angle

For the untreated and treated conditions, the static contact angle was measured on prismatic specimens by making use of a DSA30 instrument by Krüss (Hamburg, Germany), calibrated according to its standard procedure. A drop of deionized water (4 μL volume) was released on the specimen surface, and then the drop profiles were recorded using a camera and analyzed by SCA20 software 1.0. The static contact angle was determined on duplicate specimens, repeating the measurements in three different spots for each specimen.

2.5.9. Water Sorptivity and Water Absorption

Water sorptivity (S) of untreated and treated specimens was measured on cubic specimens, according to the European Standard EN 15801 [56]. Deionized water was let penetrate the specimens

through the treated face, and the weight increase over time was periodically monitored. The amount of water absorbed by capillarity into the samples after 24 h (WA_{24h}) and 7 days (WA_{7d}) was determined. Two specimens were tested for each condition.

2.5.10. Water Vapor Permeability

The water vapor permeability of untreated and treated specimens was measured on prismatic samples and expressed in terms of water vapor diffusion resistance coefficient (μ), according to the European Standard EN 15803 [57]. A glass container was filled with a saturated aqueous solution of KNO_3 up to 3 cm from the top and the specimen was placed on top of the container, with the treated face towards the solution. The specimen was then glued to the container, and the lateral sides of the samples were sealed. The coefficient μ was calculated as $\mu = \delta_a/\delta_p$, where δ_a is the water vapor permeability of air, and δ_p is the water vapor permeability of the specimen. Two specimens were tested for each condition.

2.5.11. Field Exposure

Considering the importance of evaluating also the durability of stone consolidants [38] and that small differences in microclimatic conditions may have a strong impact on stone durability [58], untreated and treated stone specimens were exposed in the cave for 9 months (from April to December 2019) to obtain a preliminary evaluation of the effects of the specific environmental conditions inside the Magura cave (T = 12–25 °C, RH = 65–90%). The exposed samples were periodically monitored by visual observation.

3. Results and Discussion

3.1. Morphology of the New Phases

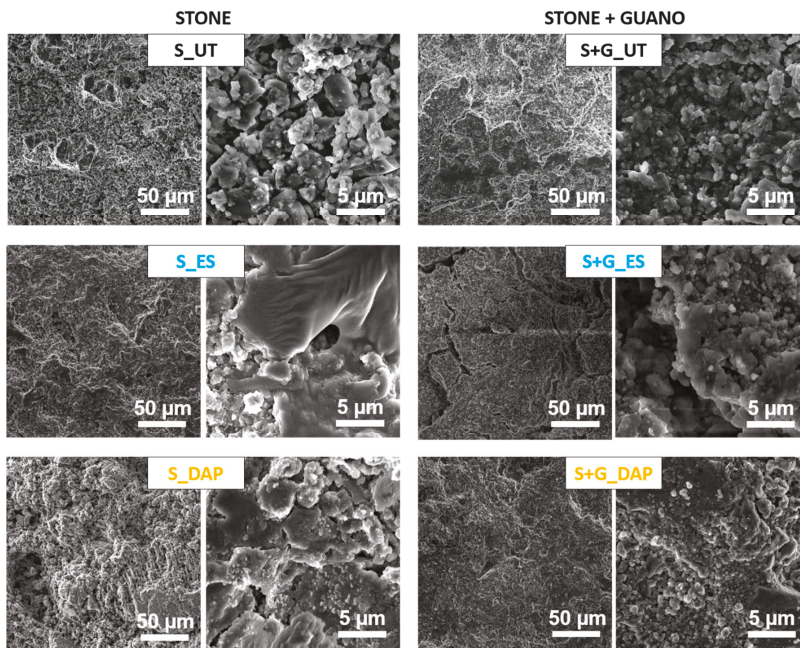The morphology of the new phases formed after treatment is illustrated in Figure 4.

Figure 4. Morphology of untreated and treated stone ("ST") and stone+guano (ST+G") specimens.

In the case of the "ST" specimens, the untreated stone was characterized by large pores among the calcite crystals. After consolidation with "ES", a coating of amorphous silica was formed, as expected [41]. Because of the porous nature of the substrate, the coating was not continuous, and bare areas were largely visible. After treatment with "DAP", small clusters of the new calcium phosphates were visible on the stone surface, which, also in this case, was not continuously coated with the new phases. Generally, new calcium phosphates formed in carbonate stones from the reaction with ammonium phosphate solutions show a flower-like morphology [25], but, in the case of dilute solutions (such as that adopted in the present case), the formation of small clusters has been reported before [59,60].

In the case of the "ST+G" specimens, observation of the untreated sample at low magnification allowed to distinguish the scales constituting the guano layer, which was cracked and prone to detachment from the substrate. After consolidation with "ES", cracks were still visible in the guano layer. The tendency of the silica gel formed from ethyl silicate to crack upon drying is well known [41]. An increase in the cohesion of the guano layer seemed to be present in the case of the "DAP" specimen, where tiny crystals, ascribable to the formation of the new calcium phosphates, were visible over the treated surface.

3.2. Composition of the New Phases

The FT-IR spectra of untreated and treated specimens are reported in Figure 5.
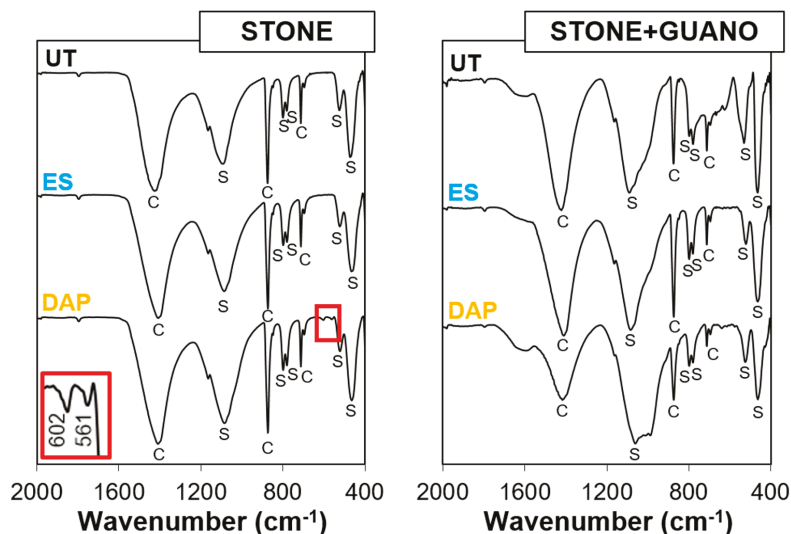
Figure 5. FT-IR spectra of untreated and treated stone ("ST") and stone+guano (ST+G") specimens. C = Calcite; S = Silica; new bands at 602 and 561 cm^{-1}, owing to the formation of new calcium phosphate phases, are highlighted in the inset.

In the "ST" specimens, bands owing calcite and silica were present in the untreated reference. After treatment with "ES", no new band was visible because "ES" led to the formation of amorphous silica, whose bands overlapped with those of the substrate. After treatment with "DAP", small new bands appeared at 602 and 561 cm^{-1}, which indicated the formation of new calcium phosphates [61]. The fact that these new bands were very small was due to the low concentration of DAP used for the treatment (0.1 M), which was consistent with a previous study where FT-IR bands of new calcium phosphates were found to be more pronounced for more concentrated DAP solutions [60]. To distinguish between formation of hydroxyapatite [HAP, $Ca_{10}(PO_4)_6(OH)_2$] and octacalcium phosphate

[OCP, $Ca_8H_2(PO_4)6 \cdot 5H_2O$], which both could be formed as the reaction product between calcareous stones and DAP solutions [51] and both have FT-IR bands at 560–563 and 600–602 cm^{-1} [61], the position of the other strong bands (at 1031 cm^{-1} for HAP and 1023 cm^{-1} for OCP [61]) should be considered. However, in the present case, no other band was clearly visible because of the overlapping with the strong band at 1080 cm^{-1} owing to quartz in the substrate. Consequently, no conclusive identification of the new phase was possible. However, the formation of either hydroxyapatite or octacalcium phosphate was expected to have a durable consolidating ability, as both minerals have lower water solubility than calcite [25,51].

In the case of the "ST+G" specimens, the spectrum of the untreated reference exhibited some new shoulders at 1580, 1000, and 700 cm^{-1} (not present in the untreated "ST" sample), which could be attributed to the guano layer. These shoulders were present also in the FT-IR spectra of the treated "ST+G" samples, which exhibited no additional clear band owing to new phase formation. In the case of "ES", this was not surprising, for the reasons discussed above. In the case of "DAP", the lack of new bands (contrary to the case of the "ST" sample) was most likely due to the very low amount of new phases formed after treatment. In fact, very little amounts of new phases are usually formed [22], especially when diluted DAP solutions are used [25]. Moreover, in the present case, the guano layer likely acted as a barrier, limiting the consolidant penetration (cf. Section 3.3) and reducing the number of new phases. Although below the detection limit of FT-IR, new phases were, however, formed after treatment, as indicated by the significant mechanical improvement (cf. Sections 3.4 and 3.5).

3.3. Penetration Depth

The penetration depth of the "ES" and "DAP" treatments into the "ST" and "ST+G" samples, measured by fracturing the samples right at the end of the consolidant application, is illustrated in Figure 6.

STONE   **STONE + GUANO**

ES   10 mm   DAP   10 mm   ES   10 mm   DAP   10 mm
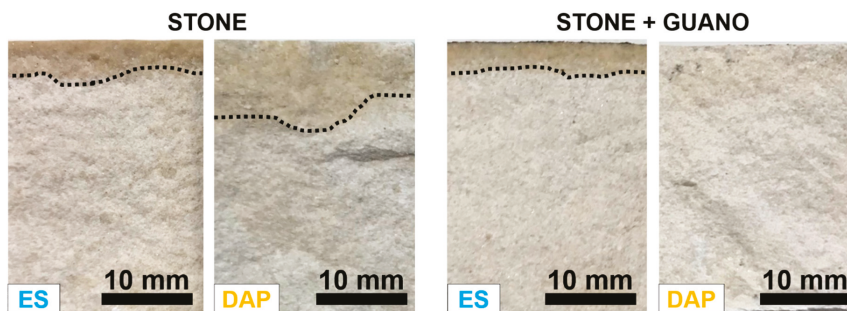
**Figure 6.** Examples of penetration depth of the treatments into the stone and stone+guano samples.

In the case of the stone specimens, the penetration depth was 4.5 ± 1 mm for "ES" and 7.0 ± 1.0 mm for "DAP", the limit of the wet fringe being more easily distinguishable in "ES" specimens. Such penetration depth of both consolidants was in line with previous results if the porosity of the substrate was considered: a penetration >10 mm was reported for both ES [42] and DAP [26,42,62] for highly porous limestones (open porosity 35–50%), while values between 3 and 5 mm were reported for less porous stones (open porosity 5–17%) [30,40]. It is worth noting that previous studies highlighted that, during curing, consolidants are progressively absorbed into finer pores [12], so that the final depth of formation of new binding phases is generally higher than assessed right at the end of the consolidant application [38,63].

In the case of the "ST+G" specimens, the penetration depth was 3.5 ± 1 mm for "ES", hence slightly lower compared to the "ST" specimens. This reduction in penetration depth was likely due to the guano layer acting as a barrier and altering the penetration into the substrate. Moreover, because

the consolidants were applied 30 min after application of the guano layer, some water used to apply the guano might have been still present in the pores of the samples, thus reducing the ability of the consolidants to penetrate in depth. In the case of "DAP", no evident sign of a wet fringe could be observed. Nonetheless, this was not an indication that no penetration took place because, otherwise, there would be no mechanical improvement, contrary to what assessed in Sections 3.4 and 3.5.

3.4. Dynamic Elastic Modulus

For untreated and treated "ST" and "ST+G" specimens, E_d values measured in the directions perpendicular and parallel to the plane of the slabs are reported in Figure 7.
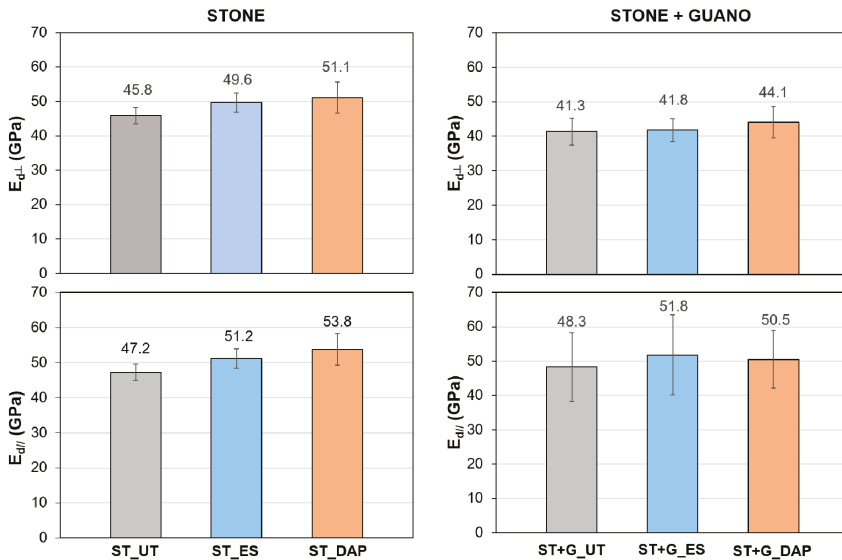
Figure 7. Dynamic elastic modulus (E_d) of untreated ("UT") and treated ("ES" and "DAP") stone ("ST") and stone+guano ("ST+G") specimens in the directions perpendicular and parallel to the plane of the slab.

In the "ST" specimens, both treatments caused an improvement in E_d, the increase being higher in the case of the "DAP" treatment. Indeed, the "ES" treatment caused an E_d increase of +8% in the perpendicular direction and +8% in the parallel direction, whereas the "DAP" treatment caused an E_d increase of +11% in the perpendicular direction and +14% in the parallel direction. The fact that the DAP treatment resulted more effective than ES was in line with several previous studies on limestone consolidation by these two consolidants: the increase in E_d was +15% for DAP and +11% for ES in Pietra Serena [28], +9–11% for DAP and +7% for ES in Arenisca Ronda [39], +90–110% for DAP and +42% for ES in Indiana limestone [22,48]. In other comparative studies, ES caused higher E_d increases than DAP: +25% for DAP and +39% for ES in Giallo di Siena [28] and +47% for DAP and +62% for ES in Globigerina limestone [42]. In any case, when comparing results obtained in different studies, it should be borne in mind that the properties of the stones tested in each study (mineralogical composition, open porosity, and pore size distribution) and the properties of the tested consolidants (concentration of the active principle, nature and amount of the solvent, application technique, etc.) play a fundamental role, determining the final outcome of the consolidating treatment.

As for the "ST+G" specimens, in the untreated condition, they exhibited a lower E_d value in the perpendicular direction compared to the "ST" specimens (41.3 ± 3.9 GPa against 45.8 ± 2.3 GPa, respectively), while, in the parallel direction, the values were much closer (48.3 ± 10.1 GPa against

47.2 ± 3.8 GPa, respectively). This was thought to be a consequence of the guano presence in the "ST+G" specimens, where the guano layer worsened the contact between the specimen and the transducers in the perpendicular direction, while no alteration was present in the parallel direction. The guano presence also slightly reduced the consolidating effectiveness. In fact, the "ES" treatment caused an E_d increase of +1% in the perpendicular direction and +7% in the parallel direction, while the "DAP" treatment caused an E_d increase of +7% in the perpendicular direction and +4% in the parallel direction. This reduction, compared to the "ST" samples, was most likely due to the guano layer, limiting the consolidant penetration in depth and thus the consolidating ability in the "ST+G" specimens.

3.5. Resistance to Abrasion

The weight losses of untreated and treated specimens after the abrasion test are reported in Figure 8.
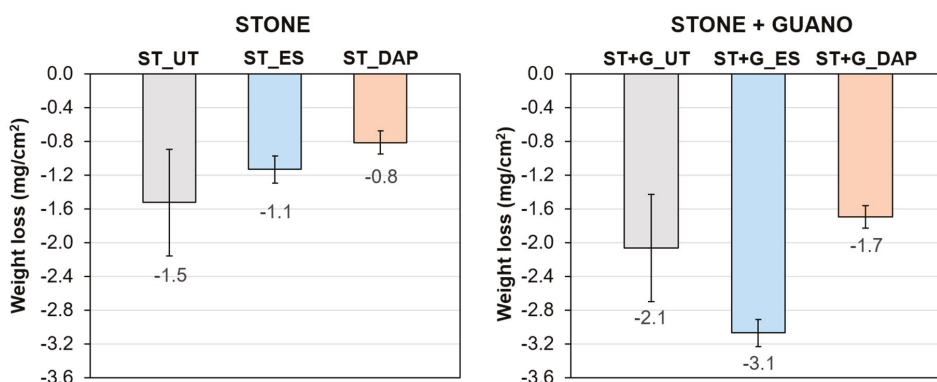
Figure 8. Weight loss after the abrasion test of untreated ("UT") and treated ("ES" and "DAP") stone ("ST") and stone+guano ("ST+G") specimens.

In the case of the "ST" specimens, both consolidants improved the stone resistance to abrasion, again the benefit being higher for the "DAP" treatment, consistent with the E_d results. Indeed, the "ES" treatment caused a reduction in weight loss by 26%, whereas the "DAP" treatment caused a reduction by 47%. The higher efficacy of DAP to increase stone resistance to abrasion was consistent with previous results obtained on marble (reduction in the weight loss by 86% for DAP and 60% for ES [64]), while substantially similar results were obtained for the two treatments on highly porous limestone (reduction in the weight loss by 37% for both DAP and ES [42]).

In the case of the "ST+G" specimens, the untreated references exhibited a higher weight loss compared to the "ST" specimen because the guano layer could be easily detached from the stone substrate. In the case of the treated specimens, as already noticed in the case of E_d, the guano layer interfered with the consolidant penetration and hardening, so that a lower benefit was found, compared to the "ST" specimens. In particular, the "DAP" treatment caused an improvement in the resistance to abrasion (weight loss reduced by 18%), while the "ES" treatment apparently worsened the resistance to abrasion. In fact, compared to the untreated condition, the "ES" treatment apparently caused an increase in weight loss by 49%. This was thought to occur because the "ES" treatment deposits a relatively high amount of new material in the porous guano layer so that the removal of the guano layer during the abrasion test results in a high weight loss.

3.6. Color Change

The appearance of an illustrative specimen for each condition of the "ST" and "ST+G" specimens is shown in Figure 9. The measured CIELab color parameters are reported in Table 1.

In the case of the "ST" specimens, the "ES" treatment caused some darkening (decrease in L^*) and shift towards red (increase in a^*). The general tendency of ethyl silicate to darken the treated stone is well known [39,41,42]. On the contrary, the "DAP" treatment caused some whitening (increase in L^*) and shift towards blue (decrease of b^*), as also assessed in previous studies [26,40,64,65]. For both treatments, the resulting color change was lower than the threshold commonly accepted for conservation treatments ($\Delta E^* = 5$ [66]), as illustrated in Figure 10. In the case of the "DAP" treatment, a color change lower than the acceptability threshold is usually experienced [25], even though more pronounced color changes have been reported in the literature [39]. However, for a given consolidant, the color change strongly depends on a multiplicity of parameters, such as the initial color of the stone, the consolidant concentration, and the application technique [39].
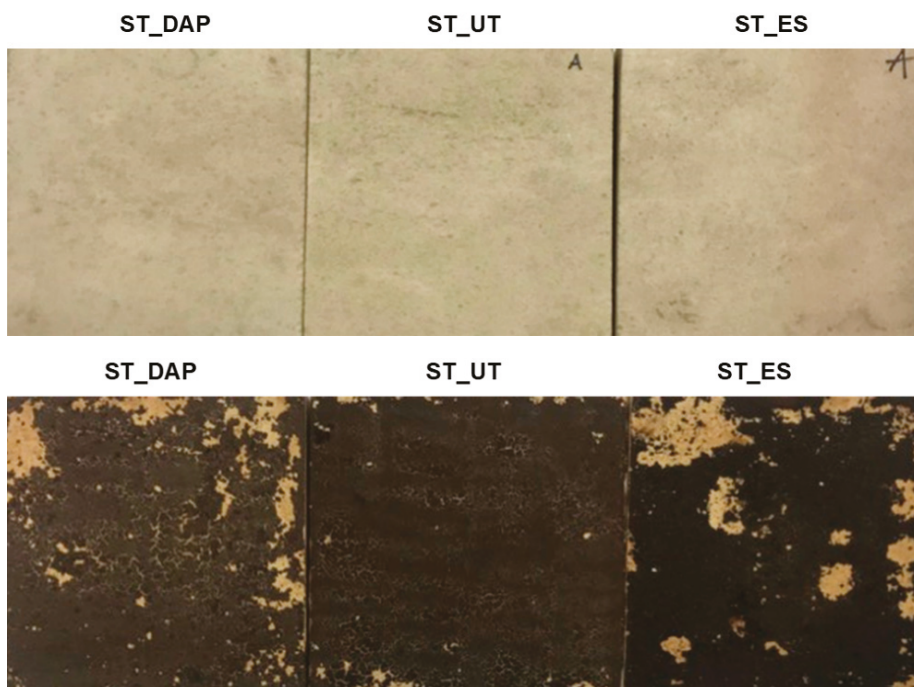
Figure 9. Comparison between the surface appearance of "DAP"-treated (**left**), "UT" (**middle**), and "ES"-treated (**right**) stone ("ST") and stone+guano ("ST+G") specimens. DAP = diammonium hydrogen phosphate; UT = untreated; ES = ethyl silicate.

Table 1. Color parameters of untreated and treated specimens.

Specimens	Condition	L^*	a^*	b^*
	UT	79.55 ± 0.76	2.86 ± 0.18	10.36 ± 0.58
ST	ES	77.20 ± 2.16	4.07 ± 0.90	10.90 ± 1.90
	DAP	81.10 ± 1.22	2.53 ± 0.23	8.98 ± 0.28
	UT	29.13 ± 1.17	6.31 ± 0.85	7.02 ± 0.29
ST+G	ES	24.91 ± 0.88	6.46 ± 1.20	4.70 ± 0.43
	DAP	32.25 ± 1.39	5.29 ± 0.55	7.24 ± 0.31

"ST" = stone, "ST+G" = stone+guano, "UT" = untreated, "ES" = ethyl silicate, "DAP" = diammonium hydrogen phosphate, L^* = black–white, a^* = green–red, b^* = blue–yellow.
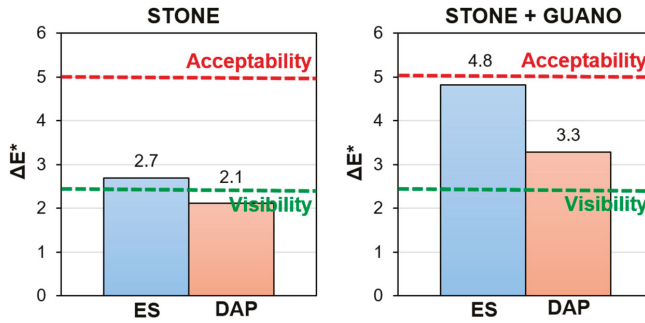
Figure 10. Color change (ΔE^*) of stone ("ST") and stone+guano ("ST+G") specimens.

In the case of the "ST+G" specimens, the color alteration after consolidation was higher than in the "ST" specimens, again because the guano layer partly interfered with the consolidant penetration into the substrate. This resulted in a considerable darkening in the case of the "ES" treatment (significant decrease in L^*) and considerable whitening in the case of "DAP" (significant increase in L^*). As reported in Figure 10, the resulting color change ΔE^* was anyway lower than the common acceptability threshold ($\Delta E^* = 5$ [66]). However, in this specific case, a general visual assessment of the alteration of the surface appearance (Figure 9) was probably more significant to evaluate the impact of the treatments because both consolidants (especially "DAP") caused some increase in the cracking of the guano layer, thus making the color measurement difficult. This increase in cracking was likely the result of combined mechanical stress originated by the brush stroke and physical stress originated by the solvents in which the consolidants were dissolved (water and ethanol in the case of DAP, isopropyl alcohol in the case of ES).

3.7. Pore Size Distribution

The pore size distribution of a representative sample for each condition is illustrated in Figure 11. In the "ST" specimens, the "DAP" treatment caused minor alterations in pore size distribution and total open porosity, which decreased from 17.9% to 14.2%. A limited reduction in open porosity after the DAP treatment was consistent with previous results on limestone consolidation by several formulations of the treatment [22,28,40,42]. The "ES" treatment caused a more pronounced reduction in open porosity (from 17.9% to 10.7%), which again was in line with the tendency reported in the literature [41,42,47]. Such different impact of the two consolidants on the pore system of the treated stone was in line with previous findings, and it was one of the major differences between the two consolidating treatments [28,42].
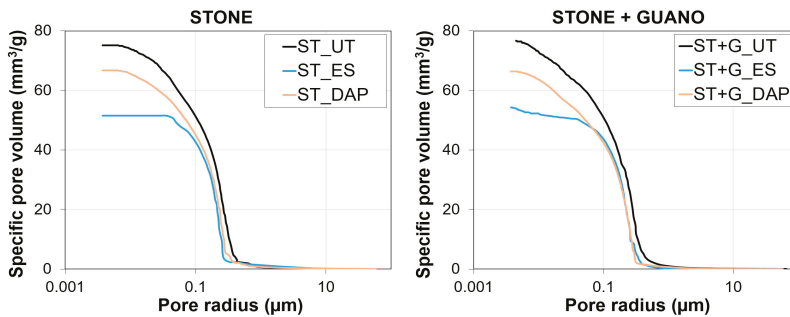

Figure 11. Pore size distributions of untreated ("UT") and treated ("ES" and "DAP") specimens of stone ("ST") and stone+guano ("ST+G").

Substantially similar behavior was registered also in the case of the "ST+G" specimens, where the presence of the guano layer apparently had very little effect on the MIP measurement, even in the untreated sample. This was a consequence of the fact that, during the MIP test, mercury can be intruded into the sample not only through the sample face covered with the guano layer but also through the other faces of the sample (free from guano), so that the influence of the guano layer is strongly reduced.

3.8. Static Contact Angle

The values of static contact angle measured for the "ST" specimens in the various conditions are summarized in Figure 12, which also displays examples of static contact angle photographed for "ST" and "ST+G" specimens.
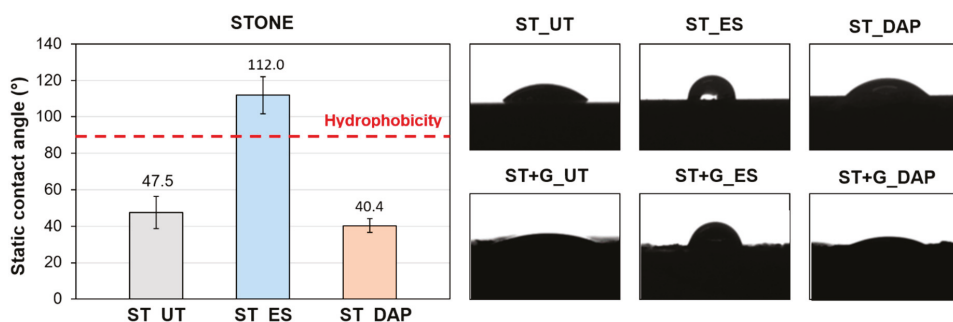
Figure 12. Values of static contact angle of untreated ("UT") and treated ("ES" and "DAP") stone specimens ("ST") and photos of the static contact angle of both "ST" and "ST+G" specimens.

The untreated "ST" sample exhibited a hydrophilic behavior, as expected (contact angle 47.5° ± 8.9°). The "DAP" treatment caused a slight alteration in the contact angle, which slightly diminished to 40.4° ± 3.9°. Such reduced alteration in stone wettability was consistent with previous results [42]. On the contrary, the "ES" treatment caused a sensible increase in the contact angle up to 112.0° ± 10.2°, so that, 8 weeks after treatment, the stone was still hydrophobic. As discussed in Section 1, products based on ethyl silicate are known to cause prolonged hydrophobicity, lasting up to 6–7 months [12,41,47]. Nonetheless, it is worthy to highlight that the technical data sheet of the commercial product used in this study states that the product reaction is complete in about 4 weeks, while curing is evidently still in progress after 8 weeks.

In the case of the "ST+G" specimens, it was impossible to quantify the static contact angle with the adopted software because the roughness of the guano layer was too high for the software to identify a straight baseline for the contact angle calculation. However, from a qualitative point of view, the same behavior observed for the "ST" samples was confirmed also for the "ST+G" samples, as illustrated in Figure 12. The "ES"-treated stone exhibited a clear hydrophobic behavior, whereas the "DAP"-treated one remained hydrophilic.

3.9. Water Sorptivity and Water Absorption

For untreated and treated specimens, the weight increase per unit area as a function of time is illustrated in Figure 13, while the resulting water sorptivity (S), water absorption after 24 h (WA_{24h}), and water absorption after 7 days (WA_{7d}) are reported in Table 2.
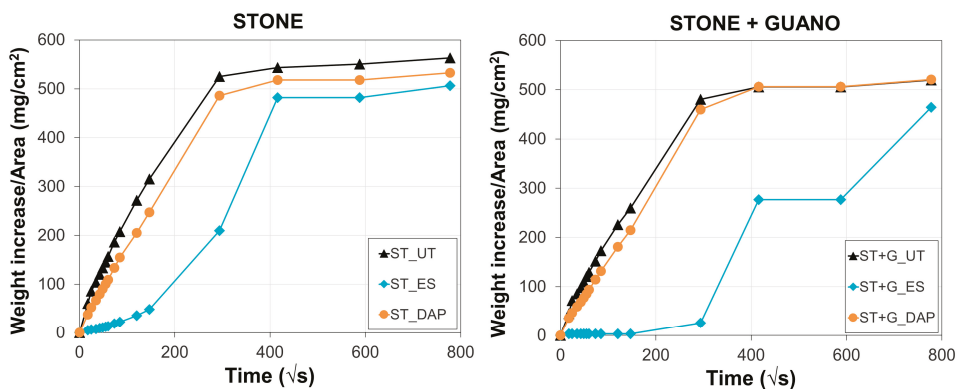
Figure 13. Water absorption as a function of time of untreated ("UT") and treated ("ES" and "DAP") stone ("ST") and stone+guano ("ST+G") specimens.

Table 2. Water transport properties of untreated and treated specimens.

Specimens	Condition	S (mg/cm$^2\sqrt{s}$)	WA$_{24h}$ (wt.%)	WA$_{7d}$ (wt.%)
	UT	1.79 ± 0.14	4.9 ± 0.4	5.2 ± 0.4
ST	ES	n.d.	1.9 ± 0.8	4.6 ± 0.1
	DAP	1.65 ± 0.06	4.5 ± 0.2	4.9 ± 0.3
	UT	1.64 ± 0.01	4.0 ± 0	4.7 ± 0
ST+G	ES	n.d.	0.2 ± 0	4.1 ± 0.1
	DAP	1.57 ± 0.05	4.2 ± 0.1	4.8 ± 0

"ST" = stone, "ST+G" = stone+guano, "UT" = untreated, "ES" = ethyl silicate, "DAP" = diammonium hydrogen phosphate, *S* = water sorptivity, *WA$_{24h}$* = water absorption after 24 h, *WA$_{7d}$* = water absorption after 7 days, n.d. = not determinable (because of the initial hydrophobic behavior).

Consistently with the slight alterations in static contact angle and pore size distribution, the "DAP" treatment caused only minor modifications in stone sorption properties, leading to minor changes in the final water absorption after 24 h (4.5 ± 0.2 wt.% for "DAP" against 4.9 ± 0.4 for "UT") and after 7 days (4.9 ± 0.3 wt.% for "DAP" against 5.2 ± 0.4 for "UT"). This was consistent with the previous results obtained on several types of stone treated by DAP [25,28,39,42].

On the contrary, the water absorption of "ES"-treated samples was initially very low, reaching a water absorption of 1.9 ± 0.8 wt.% after 24 h. After prolonged contact with water, the hydrophilic behavior of the stone was re-established, so that water absorption after 7 days was close to that of the untreated stone (4.6 ± 0.1 wt.% for "ES", 5.2 ± 0.4 for "UT"). The period during which stone remains hydrophobic (which in the field can last up to 6–7 months [47]) may threaten stone durability. Indeed, if water containing dissolved salts is trapped behind the consolidated layer, salt crystallization behind the consolidated layer may lead to detachment of this layer, thus causing failure of the conservation work [12]. For this reason, conservation treatments that do not significantly alter stone transport properties are often preferred [38].

In the case of the "ST+G" samples, the water sorptivity and the amount of water absorbed after 24 h and 7 days were a little lower, compared to the "ST" samples, likely because of the presence of the guano layer. Nonetheless, similar to the previous case, the "DAP" treatment basically caused no modification in the absorption capacity, while the "ES" treatment induced an initial hydrophobic behavior.

Because of their initial hydrophobic behavior, the sorptivity value S of the "ES"-treated specimens could not be determined.

3.10. Water Vapor Permeability

The water vapor diffusion resistance coefficient (μ) of untreated and treated "ST" specimens is reported in Table 3. The "DAP" treatment left the μ coefficient substantially unaltered, which was consistent with the modest reductions measured in previous studies on stone consolidation by DAP [40,42]. The "ES" treatment was found to cause a significant reduction in the water vapor permeability, differently from a previous study on a more porous limestone where a negligible reduction was found after treatment with ethyl silicate [42]. It is true that, also, in the present case, the vapor exchange with the environment was not completely blocked, but still a considerable reduction in water vapor permeability might be an issue for the conservation of the Magura cave paintings; hence, this aspect requires further investigation.

In the case of the "ST+G" specimens, the adopted method to test the water vapor permeability resulted as unsuitable. In fact, because the face of the specimens covered with the guano layer and treated with the consolidant was placed downwards (to ensure that the water vapor cross the consolidated layer), during the test, flakes of guano started to detach and fell into the KNO_3 solution, thus altering the reliability of the test results. For this reason, no μ values were available in the case of the "ST+G" specimens, although a behavior substantially similar to that exhibited by the "ST" specimens was expected.

Table 3. Water vapor diffusion resistance coefficient of untreated and treated stone specimens.

Specimens	Condition	μ
	UT	47.8 ± 0.7
ST	ES	82.4 ± 11.6
	DAP	45.8 ± 0.9

"ST" = stone, μ = water vapor diffusion resistance coefficient (absolute number).

3.11. Field Exposure

After exposure in the cave from April to December 2019, none of the specimens exhibited visible alteration, such as biodeterioration or pulverization. Of course, field exposure for 9 months was not enough to derive conclusive information on the long term behavior of the treated stone. Nonetheless, considering the very specific environmental conditions in the cave, this period of time was likely sufficient to trigger weathering processes, such as salt crystallization and growth of microorganisms, so the lack of visible deterioration after 9 months could be regarded as an encouraging result.

3.12. Pre-treatment by Plasma

For untreated stone specimens, the alteration in static contact angle measured 30 min after the plasma treatment (corresponding to the time between plasma pre-treatment and consolidant application) is qualitatively illustrated in Figure 14. The plasma treatment definitely modified the wettability of the stone, substantially increasing its hydrophilicity.

Nonetheless, the increase in wettability did not significantly alter the penetration depth of the consolidants, as indicated by results of consolidant uptake and mechanical strengthening reported in the following. The weight gain at the end of the consolidant application was substantially the same for specimens pre-treated or not by plasma, as illustrated in Figure 14. This was thought to be a consequence of the fact that the plasma treatment significantly modifies the wettability of the stone surface, but the walls of the pores inside the stone maintain the original properties so that the mechanism of liquid absorption in depth and the resulting penetration depth and liquid uptake are not significantly modified. Consistently, no improvement in the consolidating ability was evidenced in the case of samples pre-treated by plasma before consolidant application, as indicated by dynamic elastic modulus measurements (Figure 14).

From these results, pre-treatment by plasma looks like a promising strategy for the application of conservation treatments that are intended to affect mostly the stone surface (such as protective treatments). In the case of conservation treatments aimed at penetrating in depth into the stone (such as consolidating treatments), no clear benefit seems to derive from pre-treatment by plasma because the wettability of the stone surface is modified but, inside the pores, the wettability of the pore walls remains substantially unaltered.
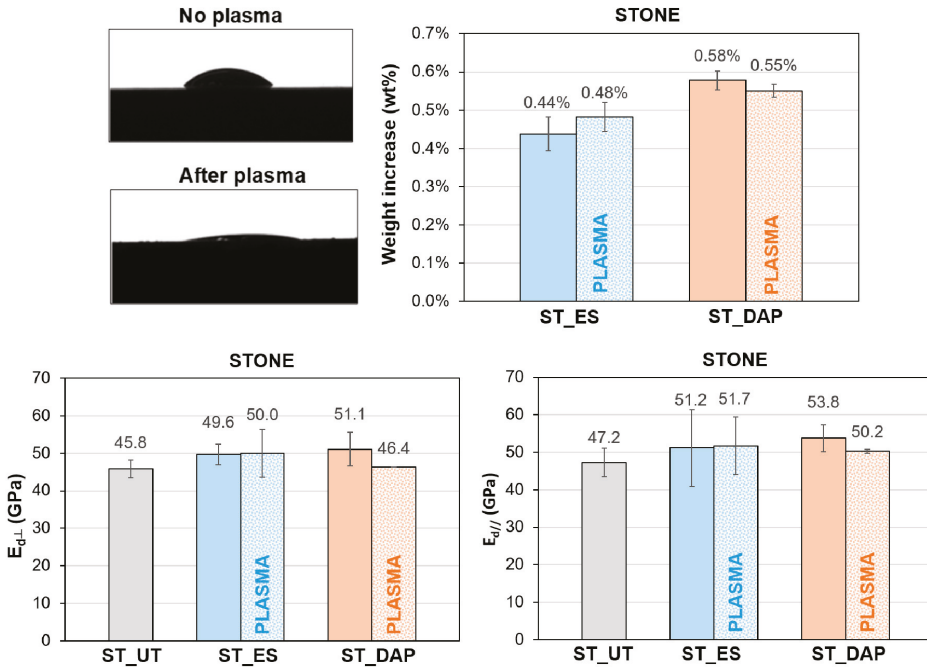
Figure 14. Effects of pre-treatment by plasma on the static contact angle of untreated stone ("ST_UT") specimens, weight increase of the stone specimens ("ST") at the end of the treatment application, and dynamic elastic modulus (E_d) of untreated ("UT") and treated ("ES" and "DAP") stone specimens ("ST"), without (solid bars) and with (dotted bars) pre-treatment by plasma, in the directions perpendicular and parallel to the plane of the slab.

4. Conclusions

Based on the results obtained in the present study, aimed at evaluating the effectiveness and the compatibility of two alternative consolidants taken into consideration for the conservation of prehistoric paintings in the Magura cave (Bulgaria), the following conclusions could be derived:

- In the case of the stone specimens, both the treatment based on ethyl silicate ("ES") and that based on ammonium phosphate ("DAP") were able to increase stone mechanical properties, the increase being higher for "DAP". Both treatments caused acceptable color changes, while a significant difference was registered in terms of alterations in water and water vapor transport properties. "DAP" left the stone hydrophilic, with negligible alterations in static contact angle and water sorptivity, while "ES" made the stone hydrophobic, even 8 weeks after the consolidant application. Moreover, "DAP" also left the water vapor permeability basically unaltered, while a reduction in permeability was caused by "ES". After exposure in the cave for 9 months, none of the treated specimens had shown evident signs of biodeterioration or pulverization, which could be regarded

as an encouraging result, even though long term data are necessary to conclusively ascertain the treatment durability.

- In the case of the stone+guano specimens, the presence of the guano layer affected the penetration of the two consolidants into the stone, thus partly reducing the consolidating effectiveness. A more intense color change was registered, compared to the stone samples, alongside cracking of the guano layer. Although more difficult to quantify, the general trend of modification in water transport properties was confirmed: "DAP" caused minor alterations, while "ES" made the stone+guano specimens hydrophobic. It was not possible to reliably determine the water vapor permeability of the stone+guano specimens by the adopted methodology, but results substantially similar to those of the stone specimens were expected (similarly to the case of the water transport properties).

- Regarding the possible benefit deriving from pre-treatment by non-thermal plasma before consolidant application, a significant decrease in the static contact angle of the stone surface was found after plasma treatment. This might be useful for the application of conservation treatments that are intended to remain mostly on the stone surface (e.g., protective treatments). Nonetheless, no significant increase in the amount of retained product or mechanical consolidation was found when pre-treatment by plasma was performed because the wettability of the stone surface was conveniently modified, but that of the pore walls remained unaltered.

All things considered, the comparison between the two investigated consolidants suggested that the "DAP" treatment had the advantage of causing higher mechanical strengthening, with lower alterations in stone transport properties, compared to the "ES" treatment. This latter aspect is very important, especially in the case of the Magura cave, where rising damp containing dissolved salts might trigger severe conservation issues if it was blocked behind a hydrophobic layer, which might be the case of the "ES" treatment. Moreover, in the case of a moist substrate (as likely the case inside the cave), the "DAP" treatment had the advantage of being applicable even if the stone pores were partly filled with water. On the contrary, the application of ES-based products would be impossible, as they react readily with water, so that deep penetration and bonding of the stone grains would be prevented.

However, the present study was based on several simplifications, which made the effects of the two treatments easier to be evaluated, but still not fully representative of the real conditions in the cave. In particular, the following aspects need to be further evaluated in future research, before any consolidant is applied onto the real artworks:

- the presence of the surface guano layer: an improved methodology of guano application onto the limestone substrate needs to be developed. In fact, the methodology adopted in this study produced specimens very prone to pulverization and detachment of the guano layer, differently from the real guano paintings in the Magura cave. To reproduce the paintings in a manner that fully resembles the condition of the real ones is extremely difficult, as the prehistoric paintings have undergone millennials of fossilization. A possible strategy to improve the reliability of the stone+guano specimens produced in the laboratory may be to subject the stone+guano specimens to accelerated aging, aimed at mimicking the natural fossilization process.

- the presence of salts in the substrate: after evaluating the effects of the two consolidants onto uncontaminated specimens, their effects onto specimens containing salts in the pores need to be evaluated, as this would be the condition in the cave (complete salts removal before the consolidant application is not feasible). To do so, the amount and nature of the salts present in the limestone cave need to be specifically investigated and characterized, so that laboratory specimens can be prepared accordingly. Then, after preliminary salt contamination and consolidation, the durability of the treated specimens to further salt weathering should be evaluated by accelerated salt crystallization cycles. This should be carried out in the current environmental conditions of the cave or, in case it is possible to control them, in the adjusted environmental conditions that would be adopted for cave conservation.

In conclusion, the present study does not complete the research needed to address the complex issue of preserving the prehistoric paintings in the Magura cave but represents the first step towards this goal.

References

1. Ivanova, S.; Gurova, M.; Spassov, N.; Hristova, L.; Tzankov, N.; Popov, V.; Marinova, E.; Makedonska, J.; Smith, V.; Ottoni, C.; et al. Magura Cave, Bulgaria: A multidisciplinary study of Late Pleistocene human palaeoenvironment in the Balkans. *Quatern Int.* **2016**, *415*, 86–108. [CrossRef]
2. Stoytchev, T. Eneolithic paintings from Magoura cave, Bulgaria. *Annu. Dep. Archaeol. NBU* **1994**, *1*, 307–320. (In Bulgarian)
3. Stoytchev, T. *Rock Art: General Classification*; Agato Press: Sofia, Bulgaria, 2005; p. 24. (In Bulgarian)
4. Nougier, R. Les "ballerines" de Magura. *Préhistoire Ariégeoise* **1977**, *XXXII*, 123–131.
5. Kunov, A.; Arnaudov, V.; Molar, M. First ^{14}C dating of the bat guano used for the ancient drawings of Magura cave, NW Bulgaria. In Proceedings of the Bulgarian Geological Society, National Conference "GEOSCIENCES 2014", Sofia, Bulgaria, 10–11 December 2014.
6. *Illustrated Glossary on Stone Deterioration Patterns = Glossaire Illustré sur les Forms D'altération de la Pierre*, 1st ed.; Vergès-Belmin, V. (Ed.) English-French ed.; Monuments & Sites no. 15; ICOMOS and (ISCS) International Scientific Committee for Stone: Paris, France, 2008.
7. Mitova, M.M.; Iliev, M.; Nováková, A.; Gorbushina, A.A.; Groudeva, V.I.; Martin-Sanchez, P.M. Diversity and biocide susceptibility of fungal assemblages dwelling in the Art Gallery of Magura Cave. *Bulg. Int. J. Speleol.* **2017**, *46*, 67–80. [CrossRef]
8. Stefanova, M.; Kamenarov, Z.; Sassoni, E.; Franzoni, E.; Ripà, M.; Patelli, A.; Scopece, P.; Verga Falzacappa, E.; Sakaj, M. Innovative solutions for prehistoric paintings -atmospheric pressure plasma and phosphate consolidant for the preservation of the Magura Cave (Bulgaria) 13–15 May 2020. *Florence (IT) Proc. Heri-Tech* **2020**, in press.
9. Chelazzi, D.; Poggi, P.; Jaidar, Y.; Toccafondi, N.; Giorgi, R.; Baglioni, P. Hydroxide nanoparticles for cultural heritage: Consolidation and protection of wall paintings and carbonate materials. *J. Colloid Interface Sci.* **2013**, *392*, 42–49. [CrossRef]
10. Valladas, H.; Cachier, H.; Maurice, P.; Bernaldo de Quirost, F.; Clottes, J.; Cabrera Valdes, V.; Uzquiano, P.; Arnold, M. Direct radiocarbon dates for prehistoric paintings at the Altamira, El Castillo and Niaux caves. *Nature* **1992**, *357*, 68–70. [CrossRef]
11. Chalmin, E.; Vignaud, C.; Menu, M. Palaeolithic painting matter: Natural or heat-treated pigment? *Appl. Phys. A* **2004**, *79*, 187–191. [CrossRef]
12. Scherer, G.W.; Wheeler, G.S. Silicate consolidants for stone. *Key Eng. Mater.* **2009**, *391*, 1–25. [CrossRef]
13. Baglioni, P.; Carretti, E.; Chelazzi, D. Nanomaterials in art conservation. *Nat. Nanotechnol.* **2015**, *10*, 287–290. [CrossRef]
14. Rodriguez-Navarro, C.; Ruiz-Agudo, E. Nanolimes: From synthesis to application. *Pure Appl. Chem.* **2018**, *90*, 523–550. [CrossRef]
15. Ambrosi, M.; Dei, L.; Giorgi, R.; Neto, C.; Baglioni, P. Colloidal Particles of Ca(OH)$_2$: Properties and Applications to Restoration of Frescoes. *Langmuir* **2001**, *17*, 4251–4255. [CrossRef]
16. Giorgi, R.; Ambrosi, M.; Toccafondi, T.; Baglioni, P. Nanoparticles for Cultural Heritage Conservation: Calcium and Barium Hydroxide Nanoparticles for Wall Painting Consolidation. *Chem. Eur. J.* **2010**, *16*, 9374–9382. [CrossRef] [PubMed]

17. Ruffolo, S.A.; La Russa, M.F.; Aloise, P.; Belfiore, C.M.; Macchia, A.; Pezzino, A.; Crisci, G.M. Efficacy of nanolime in restoration procedures of salt weathered limestone rock. *Appl. Phys. A* **2014**, *114*, 753–758. [CrossRef]

18. Ruffolo, S.A.; La Russa, M.F.; Ricca, M.; Belfiore, C.M.; Macchia, A.; Comite, V.; Pezzino, A.; Crisci, G.M. New insights on the consolidation of salt weathered limestone: The case study of Modica stone. *Bull. Eng. Geol. Environ.* **2017**, *76*, 11–20. [CrossRef]

19. Matteini, M. Inorganic treatments for the consolidation and protection of stone artefacts. *Conserv. Sci. Cult. Herit.* **2008**, *8*, 13–27.

20. Pinna, D.; Salvadori, B.; Porcinai, S. Evaluation of the application conditions of artificial protection treatments on salt-laden limestones and marble. *Construct. Build. Mater.* **2011**, *25*, 2723–2732. [CrossRef]

21. Dreyfuss, T. Interactions on site between powdering porous limestone, natural salt mixtures and applied ammonium oxalate. *Herit. Sci.* **2019**, *7*, 5. [CrossRef]

22. Sassoni, E.; Naidu, S.; Scherer, G.W. The use of hydroxyapatite as a new inorganic consolidant for damaged carbonate stones. *J. Cult. Herit.* **2011**, *12*, 346–355. [CrossRef]

23. Naidu, S.; Sassoni, E.; Scherer, G.W. New treatment for corrosion-resistant coatings for marble and consolidation of limestone. In *Jardins de Pierres—Conservation of Stone in Parks, Gardens and Cemeteries*; Stefanaggi, M., Vergès-Belmin, V., Eds.; XL Print: Paris, France, 2011; pp. 289–294.

24. Dorozhkin, S.V. Calcium orthophosphates: Occurrence, properties, biomineralization, pathological calcification and biomimetic applications. *Biomatter* **2011**, *1*, 121–164. [CrossRef]

25. Sassoni, E. Hydroxyapatite and Other Calcium Phosphates for the Conservation of Cultural Heritage: A Review. *Materials* **2018**, *11*, 557. [CrossRef] [PubMed]

26. Matteini, M.; Rescic, S.; Fratini, F.; Botticelli, G. Ammonium phosphates as consolidating agents for carbonatic stone materials used in architecture and cultural heritage: Preliminary research. *Int. J. Archit. Herit.* **2011**, *5*, 717–736. [CrossRef]

27. Yang, F.W.; Liu, Y.; Zhu, Y.C.; Long, S.J.; Zuo, G.F.; Wang, C.Q.; Guo, F.; Zhang, B.J.; Jiang, S.W. Conservation of weathered historic sandstone with biomimetic apatite. *Chin. Sci. Bull.* **2012**, *57*, 2171–2176. [CrossRef]

28. Sassoni, E.; Franzoni, E.; Pigino, B.; Scherer, G.W.; Naidu, S. Consolidation of calcareous and siliceous sandstones by hydroxyapatite: Comparison with a TEOS-based consolidant. *J. Cult. Herit.* **2013**, *14*, e103–e108. [CrossRef]

29. Graziani, G.; Sassoni, E.; Franzoni, E. Consolidation of porous carbonate stones by an innovative phosphate treatment: Mechanical strengthening and physical-microstructural compatibility in comparison with TEOS-based treatments. *Herit. Sci.* **2015**, *3*, 1–6. [CrossRef]

30. Molina, E.; Rueda-Quero, L.; Benavente, D.; Burgos-Cara, A.; Ruiz-Agudo, E.; Cultrone, G. Gypsum crust as a source of calcium for the consolidation of carbonate stones using a calcium phosphate-based consolidant. *Construct. Build. Mater.* **2017**, *143*, 298–311. [CrossRef]

31. Ma, X.; Balonis, M.; Pasco, H.; Toumazou, M.; Counts, D.; Kakoulli, I. Evaluation of hydroxyapatite effects for the consolidation of a Hellenistic-Roman rock-cut chamber tomb at Athienou-Malloura in Cyprus. *Construct. Build. Mater.* **2017**, *150*, 333–344. [CrossRef]

32. Possenti, E.; Conti, C.; Gatta, G.D.; Realini, M.; Colombo, C. Diammonium hydrogen phosphate treatment on dolostone: The role of Mg in the crystallization process. *Coatings* **2019**, *9*, 169. [CrossRef]

33. Balonis-Sant, M.; Ma, X.; Kakoulli, I. Preliminary results on biomimetic methods based on soluble ammonium phosphate precursors for the consolidation of archaeological wall paintings. In *Archaeological Chemistry VIII, ACS Symposium Series*; American Chemical Society: Washington, DC, USA, 2013; Volume 1147, pp. 419–447. [CrossRef]

34. Sassoni, E.F. Lime and cement mortar consolidation by ammonium phosphate. *Construct. Build. Mater.* **2020**, *245*, 118409. [CrossRef]

35. Sassoni, E.; Graziani, G.; Franzoni, E.; Scherer, G.W. Conversion of calcium sulfate dihydrate into calcium phosphates as a route for conservation of gypsum stuccoes and sulfated marble. *Construct. Build. Mater.* **2018**, *170*, 290–301. [CrossRef]

36. Ma, X.; Pasco, H.; Balonis, M.; Kakoulli, I. Investigation of the optical, physical, and chemical interactions between diammonium hydrogen phosphate (DAP) and pigments. *Sustainability* **2019**, *11*, 3803. [CrossRef]

37. Graziani, G.; Sassoni, E.; Scherer, G.W.; Franzoni, E. Phosphate-based treatments for consolidation of salt-bearing Globigerina limestone. *IOP Conf. Ser. Mater. Sci. Eng.* **2018**, *364*, 012082. [CrossRef]

38. Sassoni, E.; Graziani, G.; Franzoni, E. An innovative phosphate-based consolidant for limestone. Part 2: Durability in comparison with ethyl silicate. *Construct. Build. Mater.* **2016**, *102*, 931–942. [CrossRef]
39. Molina, E.; Fiol, C.; Cultrone, G. Assessment of the efficacy of ethyl silicate and dibasic ammonium phosphate consolidants in improving the durability of two building sandstones from Andalusia (Spain). *Environ. Earth Sci.* **2018**, *77*, 302. [CrossRef]
40. Shekofteh, A.; Molina, M.; Rueda-Quero, L.; Arizzi, A.; Cultrone, G. The efficiency of nanolime and dibasic ammonium phosphate in the consolidation of beige limestone from the Pasargadae World Heritage Site. *Archaeol. Anthropol. Sci.* **2019**. [CrossRef]
41. Wheeler, G. Alkoxysilanes and the Consolidation of Stone. In *Research in Conservation*; The Getty Conservation Institute: Los Angeles, CA, USA, 2005.
42. Sassoni, E.; Graziani, G.; Franzoni, E. An innovative phosphate-based consolidant for limestone. Part 1: Effectiveness and compatibility in comparison with ethyl silicate. *Construct. Build. Mater.* **2016**, *102*, 918–930. [CrossRef]
43. Maravelaki-Kalaitzaki, P.; Kallithrakas-Kontos, N.; Korakaki, D.; Agioutantis, Z.; Maurigiannakis, S. Evaluation of silicon-based strengthening agents on porous limestones. *Prog. Org. Coat.* **2006**, *57*, 140–148. [CrossRef]
44. da Fonseca, B.S.; Piçarra, S.; Pinto, A.P.F.; Montemor, M.d. Polyethylene glycol oligomers as siloxane modificators in consolidation of carbonate stones. *Pure Appl. Chem.* **2016**, *88*, 1117–1128. [CrossRef]
45. Burgos-Cara, A.; Rodríguez-Navarro, C.; Ortega-Huertas, M.; Ruiz-Agudo, E. Bioinspired Alkoxysilane Conservation Treatments for Building Materials Based on Amorphous Calcium Carbonate and Oxalate Nanoparticles. *ACS Appl. Nano Mater.* **2019**, *2*, 4954–4967. [CrossRef]
46. Moropoulou, A.; Haralampopoulos, G.; Tsiourva, T.; Auger, F.; Birginie, M. Artificial weathering and non-destructive tests for the performance evaluation of consolidation materials applied on porous stones. *Mater. Struct.* **2003**, *36*, 210–217. [CrossRef]
47. Franzoni, E.; Graziani, G.; Sassoni, E. TEOS-based treatments for stone consolidation: Acceleration of hydrolysis-condensation reactions by poulticing. *J. Sol-Gel Sci. Tech.* **2015**, *74*, 398–405. [CrossRef]
48. Naidu, S.; Liu, C.; Scherer, G.W. Hydroxyapatite-based consolidant and the acceleration of hydrolysis of silicate-based consolidants. *J. Cult. Herit.* **2015**, *16*, 94–101. [CrossRef]
49. Wurster, C.M.; Munksgaard, N.; Zwart, C.; Bird, M. The biogeochemistry of insectivorous cave guano: A case study from insular Southeast Asia. *Biogeochemisty* **2015**, *124*, 163–175. [CrossRef]
50. Shahack-Gross, R.; Berna, F.; Karkanas, P.; Weiner, S. Bat guano and preservation of archaeological remains in cave sites. *J. Archaeol. Sci.* **2004**, *31*, 1259–1272. [CrossRef]
51. Naidu, S.; Scherer, G.W. Nucleation, growth and evolution of calcium phosphate films on calcite. *J. Colloid Interface Sci.* **2014**, *435*, 128–137. [CrossRef]
52. Sassoni, E.; Graziani, G.; Franzoni, E.; Scherer, G.W. Calcium phosphate coatings for marble conservation: Influence of ethanol and isopropanol addition to the precipitation medium on the coating microstructure and performance. *Corros. Sci.* **2018**, *136*, 255–267. [CrossRef]
53. Tendero, C.; Tixier, C.; Tristant, P.; Desmaison, J.; Leprince, P. Atmospheric pressure plasmas: A review. *Spectrochim. Acta B* **2006**, *61*, 2–30. [CrossRef]
54. Patelli, A.; Verga, E.; Nodari, L.; Petrillo, S.M.; Delva, A.; Ugo, P.; Scopece, P. A customised atmospheric pressure plasma jet for conservation requirements. *IOP Conf. Ser. Mater. Sci. Eng.* **2018**, *364*, 012079. [CrossRef]
55. Sandrolini, F.; Franzoni, E.; Cuppini, G. Predictive diagnostics for decayed ashlars substitution in architectural restoration in Malta. *Mater. Eng.* **2000**, *11*, 323–337.
56. *Conservation of Cultural Property -Test Methods -Determination of Water Absorption by Capillarity*; European Standard EN 15801; European Standard EN: Brussels, Belgium, 2010.
57. *Conservation of Cultural Property -Test Methods -Determination of Water Vapor Permeability (δp)*; European Standard EN 15803; European Standard EN: Brussels, Belgium, 2010.
58. Sandrolini, F.; Franzoni, E.; Sassoni, E.; Diotallevi, P.P. The contribution of urban-scale environmental monitoring to materials diagnostics: A study on the Cathedral of Modena (Italy). *J. Cult. Herit.* **2011**, *12*, 441–450. [CrossRef]

59. Sassoni, E.; Graziani, G.; Ridolfi, G.; Bignozzi, M.C.; Franzoni, E. Thermal behavior of Carrara marble after consolidation by ammonium phosphate, ammonium oxalate and ethyl silicate. *Mater. Des.* **2017**, *120*, 345–353. [CrossRef]
60. Sassoni, E.; Andreotti, S.; Scherer, G.W.; Franzoni, E.; Siegesmund, S. Bowing of marble slabs: Can the phenomenon be arrested and prevented by inorganic treatments? *Environ. Earth Sci.* **2018**, *77*, 387. [CrossRef]
61. Karampas, I.A.; Kontoyannis, C.G. Characterization of calcium phosphates mixtures. *Vib. Spectrosc.* **2013**, *64*, 126–133. [CrossRef]
62. Franzoni, E.; Sassoni, E.; Graziani, G. Brushing, poultice or immersion? The role of the application technique on the performance of a novel hydroxyapatite-based consolidating treatment for limestone. *J. Cult. Herit.* **2015**, *16*, 173–184. [CrossRef]
63. Graziani, G.; Sassoni, E.; Scherer, G.W.; Franzoni, E. Penetration depth and redistribution of an aqueous ammonium phosphate solution used for porous limestone consolidation by brushing and immersion. *Construct. Build. Mater.* **2017**, *148*, 571–578. [CrossRef]
64. Sassoni, E.; Graziani, G.; Franzoni, E. Repair of sugaring marble by ammonium phosphate: Comparison with ethyl silicate and ammonium oxalate and pilot application to historic artifact. *Mater. Des.* **2015**, *88*, 1145–1157. [CrossRef]
65. Sassoni, E.; D'Amen, E.; Roveri, N.; Scherer, G.W.; Franzoni, E. Durable self-cleaning coatings for architectural surfaces by incorporation of TiO2 nanoparticles into hydroxyapatite films. *Materials* **2018**, *11*, 177. [CrossRef]
66. Delgado Rodrigues, J.; Grossi, A. Indicators and ratings for the compatibility assessment of conservation actions. *J. Cult. Herit.* **2007**, *8*, 32–43. [CrossRef]

MDPI